

Dynamics of Ultrasonic Motors

Vom Fachbereich Mechanik
der Technischen Universität Darmstadt
zur Erlangung des Grades eines
Doktor-Ingenieurs (Dr.-Ing.)
genehmigte

Dissertation

von

Dipl.-Ing. Thomas Sattel

aus Speyer am Rhein

Referent:	Prof. Dr. Peter Hagedorn
Korreferent:	Prof. Dr.-Ing. Jörg Wallaschek
Tag der Einreichung:	24. Juni 2002
Tag der mündlichen Prüfung:	16. Juli 2002

Darmstadt 2003

D 17

Acknowledgements

This thesis has emerged from my time as research and teaching assistant in the Dynamics Research Group at the Department of Applied Mechanics, Darmstadt University of Technology.

First of all I would like to express my sincere gratitude to Prof. Dr. Peter Hagedorn for suggesting the interesting research topic, his encouragements, useful advices and the way he laid the academic and social boundary conditions in his research group. This constitutes a great deal in bringing about this study of ultrasonic motors. Besides, I would always remember all the opportunities of meeting interesting people of various universities in different countries.

I would especially like to thank Prof. Dr.-Ing. Jörg Wallaschek for his willingness to co-promote my thesis, his suggestive advices and discussions with himself and his co-workers. I also appreciate the advices I got from Prof. Dr.-Ing. Richard Markert during my time at the Department of Applied Mechanics.

Special thanks to all colleagues, who were instrumental in doing this thesis. First of all I would like to mention my friends and former colleagues Dr.-Ing. Marcus Berg, Dr.-Ing. Kai Wolf, Prof. Dr.-Ing. Wolfgang Seemann, Dr.-Ing. Karl-Joseph Hoffmann and Stefanie Gutschmidt, MSc. All the discussions I had with them and the advices I got were helpful in one or the other way. I'm also indebted to Dipl.-Ing. Tobias Vomstein for diverse assistance and to Dr. Goutam Chakraborty for his reading and editing efforts. From many other colleagues I got also support in various ways. I acknowledge to them and to our secretaries, Renate Schreiber and Jutta Braun, who both had hands in producing good spirit in day-to-day work. I felt good in the institute during all my time there.

Darmstadt, August 2002

Thomas Sattel

In Memory of my Parents

Contents

1	Introduction	1
1.1	The working principle	2
1.2	Past and ongoing research	15
1.3	Actual problems and objective of the work	16
2	Modeling	19
2.1	Literature review	19
2.2	General modeling aspects	21
2.2.1	Outline of the USM modeling	22
2.2.2	Kinematics	23
2.2.3	Material description in an inertial frame	24
2.2.4	Material description in a moving reference frame	25
2.2.5	Time derivatives and virtual velocities	26
2.3	Contact formulation	27
2.3.1	Contact kinematics	28
2.3.2	Contact states: Normal and tangential contact	31
2.3.3	Switching conditions: Detecting temporal changes of the contact zones	32
2.4	Dynamics	34
2.4.1	Problem statement in local form	35
2.4.2	Principle of virtual power (PvP)	38
2.5	Material Laws	40
2.5.1	Stator and piezoceramic	40
2.5.2	Rotor and contact layer	43
2.6	Electric current, voltage, admittance, power and efficiency	44
2.6.1	Electric excitation	45
2.6.2	Electric current to the actor electrodes	48

2.6.3	Electric voltage on the sensor electrodes	49
2.6.4	Electric input admittance	50
2.6.5	Power and efficiency	50
2.7	A simple planar motor model	53
2.7.1	Moving reference frame	54
2.7.2	Stator	55
2.7.3	Rotor	56
2.7.4	Contact layer	57
2.7.5	Contact formulation	58
2.7.6	External forces	59
2.7.7	Scaling and non-dimension formulation	59
2.7.8	Equations of motion	62
2.7.9	Electric quantities	64
2.7.10	Comment on the electric displacement	66
2.7.11	Summary	67
3	Model Analysis	69
3.1	Introduction	69
3.2	Numerical Solution Procedure	70
3.2.1	Eigenfrequencies of stator and rotor	70
3.2.2	Contact equations	71
3.2.3	Steady-state system equations	81
3.2.4	Contact boundaries and transitions	86
3.2.5	GALERKIN discretization	88
3.2.6	Problem statement	94
3.2.7	Contact Algorithm	96
3.3	Numerical Results	99
3.4	Summary	104
4	Experiments	107
4.1	Introduction	107
4.1.1	Literature review	108
4.1.2	Objective	110
4.1.3	Measurable quantities, measuring devices and measurements	111
4.2	Resonance behavior	114
4.2.1	Resonance behavior of the stator	116
4.2.2	Resonance behavior of the motor	121

4.3	Temperature dependence	127
4.4	Steady-state behavior of the motor	128
4.4.1	Speed-torque characteristics: four quadrant operation	129
4.4.2	Speed-torque characteristics: influence of excitation frequency	132
4.4.3	Speed-torque characteristics: influence of axial preload	138
4.4.4	Speed-torque characteristics: hysteresis behavior	139
4.4.5	Vibrational behavior	140
4.4.6	Power and efficiency	149
4.5	Summary	155
5	Discussion and future work	157
	Appendix	159
A.1	Coefficient of the PDEs	159
	Bibliography	163

Chapter 1

Introduction

Ultrasonic motors (USMs) belong to the class of piezoelectric motors. In this work the term USM will be used for the motor only (power electronics and closed loop control are not included). The system, composed of the motor, power electronics and the closed loop control will be called *ultrasonic actuator* or *piezoelectric actuator*. The working principle of these motors has been well known for at least 50 years WALLASCHEK (1995, [59]). However, they gained widespread interest first with the influencing work of SASHIDA (1982, [43]). Before, piezoceramic materials with high conversion efficiency and fast electronic power control of the ultrasonic vibrations were not available. Through their specific advantages compared to conventional electro-magnetic motors they fill a gap in certain actuator applications. Advantages of USM over electromagnetic motors are their compactness, i.e. their high stall torque-mass ratio and their high torque at low rotational speed, often making speed reducing gears superfluous. Additionally, with no voltage applied, an inherent holding torque is present due to the frictional driving mechanism. It is also worthwhile to mention that their compactness and the high frequency electrical excitation make quick responses possible. But besides that, USM also offer a high potential for miniaturization. These actuators produce no magnetic field since the excitation is quasi-electrostatic. On the other hand, some drawbacks can be easily pointed out. Due to the frictional driving mechanism, the lifetime is limited and the motor may heat up drastically within minutes of operation. The complicated stator-rotor contact behavior and the temperature drift call for special control strategies. Last but not least, the electrical excitation frequencies in the ultrasonic range, the capacitive or inductive behavior of the motor out of resonance and the temperature dependence of the motor materials require sophisticated power electronics and closed loop controls. Due to the frictional driving mechanism between stator and rotor, USMs are not intended to be used as permanently driven actuators. The friction between stator and rotor causes wear and abrasion effect as well as temperature rise of the motor,

which may lead to a faster aging due to polarization degradation of the piezoceramic material.

Their potential field of application is in "short time" actuation tasks. The first mass produced USM were utilized in lens drives in autofocus cameras. In the meantime other large scale applications have been established, e.g. steering-wheel or head rest adjustment. In areas like robotics USMs are planned to be used as actuators, e.g. in robot wrists. Intensive research in the field of USM is being conducted for more than two decades now. Unlike in the early years, when research was concentrated on the invention of different vibration principles and motor designs, nowadays the focus is more on sophisticated mathematical models and towards a better understanding of motor dynamics and motor optimization.

1.1 The working principle

There are various different design and operation principles for ultrasonic motors. Depending on the design (plate-type stator, cylinder-type stator, etc.), on the kind of actuation (linear or rotational motion) or on the vibration principle (traveling-wave-type or standing-wave-type vibrations) there are different classifications of USM. A good overview is presented in the monograph of UEHA *et al.* (1993, [57]). These motors are usually driven in an ultrasonic vibration range between 20-100 kHz. Common in most

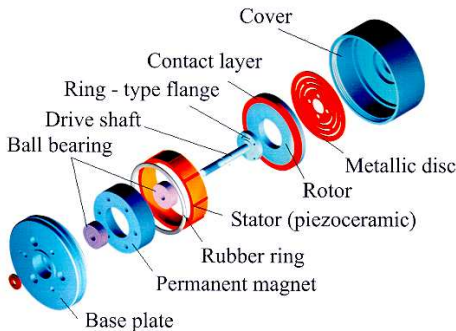


Figure 1.1: Prototype of a USM developed by Physic Instrumente; diameter 60 mm

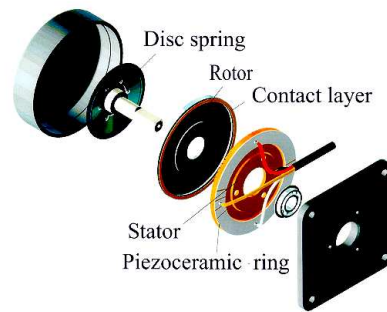


Figure 1.2: Prototype of a USM developed by Daimler-Chrysler; diameter 90 mm

of these motors is the excitation of stator vibrations so that the stator's surface points move in elliptical trajectories. In Figs. 1.1 and 1.2, two examples of rotary traveling-wave-type USM are shown; the left one with a stator in the form of a cylindrical shell

and the one on the right side with a plate-type stator. The stator of the motor in Fig. 1.1 is fully made of piezoceramic material. Appropriate electrode patterns distributed over the outer and inner circumferential surfaces of the stator are used to electrically excite mixed bending and longitudinal vibration modes. The superposition of these modes results in a traveling wave causing material points lying on the surface towards the rotor to move through an elliptical trajectory. Pressing the rotor against the stator leads to a frictional contact and thus to the rotor motion. The vibration principle for this type of motor is explained in detail by BERG (2001, [5]).

In Fig. 1.3 a slider of a linear traveling-wave-type motor is depicted. Two orthogonal bending modes are excited in the slider by the bonded piezoceramic patches. Their superposition leads to a traveling bending wave. But as it may be obvious, the geometric structure has to be adjusted appropriately to get two orthogonal bending modes with the same frequency. This is not an easy task. Pressing the slider against the support, frictional contact takes place and the slider moves along the support. Details about

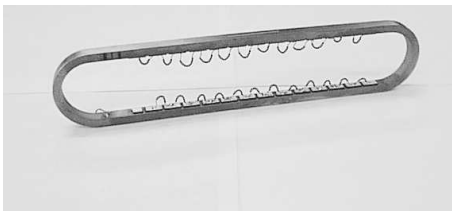


Figure 1.3: Slider of a linear ultrasonic traveling wave motor

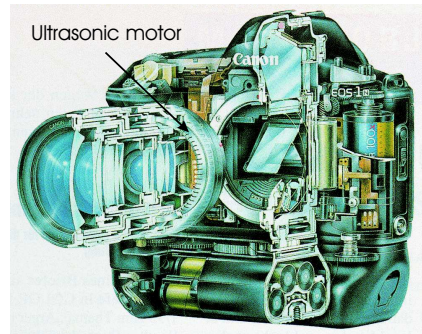


Figure 1.4: Example of a possible application of USM: Autofocus-camera

the motor design and the experimental results can be found in SATTEL & HAGEDORN (2001, [18]). A well-known example of an application of a USM technology is depicted in Fig. 1.4. The lens adjustment in the auto-focus camera is done via a USM. The working principle of an USM will be explained in detail using the motor design in Fig. 1.2 and with reference to HAGEDORN & WALLASCHEK (1992, [20])

Different options are available to generate a traveling wave. In the plate type USM shown in Fig. 1.2 two degenerate eigenmodes (bending modes) having the same eigenfrequency are excited. Both bending modes have n nodal lines and zero nodal circles. Their excitation has a spatial phase shift of $\lambda/4$ (90° in a wavelength sense) in circumferential direction. They are excited to the same amplitude, \hat{w}_s , by two excitation sources (two phase) with a temporal phase shift of 90° . The mode shapes of these orthogonal bending modes are illustrated in Fig. 1.5 (for the sake of simplicity $n = 2$).

Actually, the stator in Fig. 1.2 is excited in its eleventh bending mode, i.e. $n = 11$. If w represents the transverse deflection of the stator plate, one may express the lateral vibration of the plate's mid-plane as

$$\begin{aligned} w_s(r, \varphi, t) &= \hat{w}_s R(r) \sin n\varphi \sin \Omega t + \hat{w}_s R(r) \cos n\varphi \cos \Omega t \\ &= \hat{w}_s R(r) \cos(n\varphi - \Omega t), \end{aligned} \quad (1.1)$$

where $R(r)$, $\sin n\varphi$ and $\cos n\varphi$ are the radial and the circumferential shape functions of the orthogonal eigenmodes, respectively. For the radial mode shape the scaling $R(r_a) = 1$ is chosen, where r_a represents the plate's outer circumferential radius. Furthermore, \hat{w}_s denotes the stator vibration amplitude and Ω the excitation frequency. The superposition of the mathematical representations of the two standing waves, shifted 90° in space and time, may be transformed in a mathematical representation of a traveling wave using trigonometric identities. Eigenmodes with eigenfrequencies in the ultrasonic range are selected to achieve silent operation.

The bending deformation in the plate leads to elliptic motion of the surface points as illustrated in the side view of Fig. 1.6. This can be made obvious by considering the kinematics of surface points using KIRCHHOFF plate theory. In cylindrical coordinates the displacements of surface points may be written as

$$\mathbf{u}_P(r, \varphi, z, t) = -\frac{h_s}{2} w_{s,r}(r, \varphi, t) \mathbf{e}_r - \frac{h_s}{2r} w_{s,\varphi}(r, \varphi, t) \mathbf{e}_\varphi + w_s(r, \varphi, t) \mathbf{e}_z, \quad (1.2)$$

where $(\cdot)_{,r}$ and $(\cdot)_{,\varphi}$ are the derivatives with respect to the coordinates r and φ , respectively. The vectors $(\mathbf{e}_r, \mathbf{e}_\varphi, \mathbf{e}_z)$ define a local reference frame and h_s is the stator thickness. Inserting (1.1) into (1.2) results in an equation describing the elliptic motion. The time derivatives of the displacement function in (1.2) give the velocities of the sur-

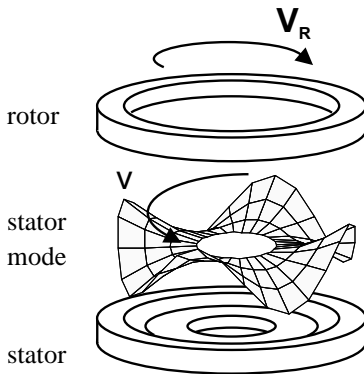


Figure 1.5: Possible stator vibration form

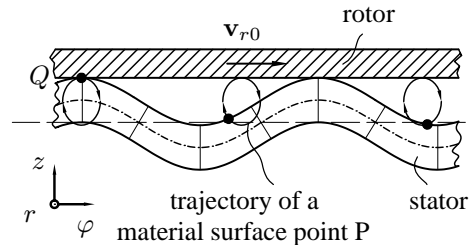


Figure 1.6: Planar sketch of the working principle of the motor in Fig. 1.5

face points. The velocity of the points Q at the wave crest may be obtained by setting $\cos(n\varphi - \Omega t) = 1$, yielding

$$\dot{\mathbf{u}}_Q = -\hat{w}_s \Omega \frac{h_s}{2} \frac{R(r)}{r} n \mathbf{e}_\varphi . \quad (1.3)$$

It turns out that the velocity at the wave crest is in the circumferential direction, i.e. in the \mathbf{e}_φ direction. But note that for all surface points not lying at the wave crest, radial velocity components exist. Such radial velocity components do not contribute to the motor drive but to dissipative effects instead. One design task, therefore, is to hold such radial velocity components as small as possible.

A ring type rotor is pressed against the stator, e.g. by a disc spring and driven by frictional contact forces acting between stator and rotor. Assuming a rigid rotor and contact at the wave crests along the outer radius r_o only, the no slip rotational speed of the rotor is given by

$$\dot{\varphi}_r = -\frac{|\dot{\mathbf{u}}_Q|}{r_o} = -\hat{w}_s \Omega \frac{h_s}{2} \frac{R(r_o)}{r_o^2} n \quad (1.4)$$

and the velocity at the outer circumference follows as

$$\mathbf{v}_{r0} = v_{r0} \mathbf{e}_\varphi = \dot{\varphi}_r r_o \mathbf{e}_\varphi . \quad (1.5)$$

Two things are noteworthy. First, a comparison of (1.3) and (1.1) shows that the traveling wave and the rotor move in opposite directions. Second, using parameters of a typical motor having an outer diameter of the stator of 60 mm and with $h_s \approx 5\text{mm}$, $r_o \approx 30\text{mm}$, $R(r_o) \approx 2\mu\text{m}$ and $n = 9$, (1.6) gives the ratio

$$\frac{\dot{\varphi}_r}{\Omega} \approx -\frac{1}{40000} \quad (1.6)$$

between the rotational speed and the excited circular frequency. This means a frequency reduction of the order of magnitude 10^4 between the circular frequency Ω and the rotational speed of the rotor!

From a motor design perspective (1.6) indicates, which design variables influence the maximum rotational speed of a motor. The stator vibration amplitudes are usually limited by the maximum strain that the piezoceramics are capable to withstand. To increase the maximum rotational speed the number of nodal lines, n , can be made larger as well as the stator thickness h_s . However, a larger stator thickness comes along with an increasing stator stiffness and thus with an increase in the eigenfrequencies in which the stator is excited. Higher excitation frequencies in the motor demand more effort in the design of the power electronics. To avoid this, notches can be milled into the stator, as illustrated in the FE-model in Fig. 1.8, which allow to increase the stator thickness h_s without a significant change of the eigenfrequencies of the stator's operational eigenmode. Surely, there is an increase of the manufacturing costs, but the notches offer an additional benefit. Wear particles will be taken apart from the contact zone between

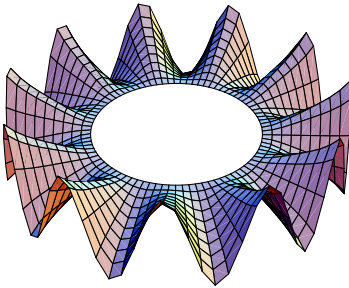


Figure 1.7: Possible stator vibration form with $n = 11$ of the motor shown in Fig. 1.2

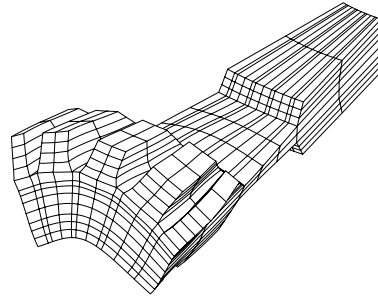


Figure 1.8: FE-Model of one sector (half wavelength) of the stator with notches, shown in Fig. 1.2

stator and rotor, as pointed out in SASHIDA *et al.* (1993, [44]). The notches also influence the eigenmodes of the stator. Without notches, the eigenmodes are harmonic and with notches they are only periodic in circumferential direction. Thus, parasitic vibration components occur. The stator teeth act almost as rigid bodies. Whether the teeth have to be considered in the contact modeling or not, depends on the perturbation of the stator's harmonic mode shape in circumferential direction. The influence of the notches on the stator kinematics is discussed in SCHMIDT (1999, [51]).

The question remains, how to excite the traveling bending wave in the stator? In Fig. 1.9 the excitation principle used in the motor in Fig. 1.2 is shown schematically. The piezoceramic ring, bonded to the lower surface of the stator is divided into oppositely polarized segments having remnant polarization P_r (see Fig. 2.6). The length of each segment is equal to half the wavelength λ of the bending mode. At the free surface of the piezoceramic ring, these segments in Fig. 1.9 are coated with a thin metallic layer acting as an electrode. An electric voltage across the piezoceramic thickness causes the segments to either elongate or shorten in the circumferential direction (φ -direction) due to the inverse piezoelectric effect. This effect is called a d_{31} -effect, since an electric field in the 3-direction (z -direction) causes mechanical strains in the 1-direction (x -direction). The excitation of two orthogonal bending modes may be achieved by various arrangements of polarization or electrodes. For a two-phase drive, one possibility is to use half of the piezoceramic ring to excite one bending mode and the other half to excite the corresponding orthogonal bending mode. This is illustrated in Fig. 1.10. There are two polarization configurations, A and B . Each configuration is used to excite one bending mode. Hence, there must be a spatial phase shift of a quarter of the wavelength λ between both configurations. The $+$ and $-$ signs in each segment indicate the orientation of the remnant polarization vector P_r with respect to the z -direction. Each polarization configuration in Fig. 1.10 is coated by a thin metallic layer acting as an electrode. But note that the two electrodes A and B are electrically isolated. Under perfect transfer be-

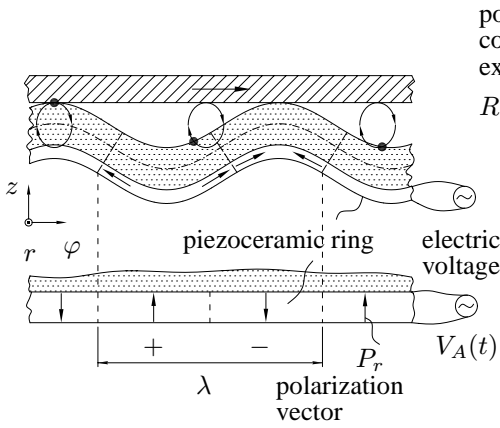


Figure 1.9: Principle of excitation of a bending mode by a piezoceramic ring

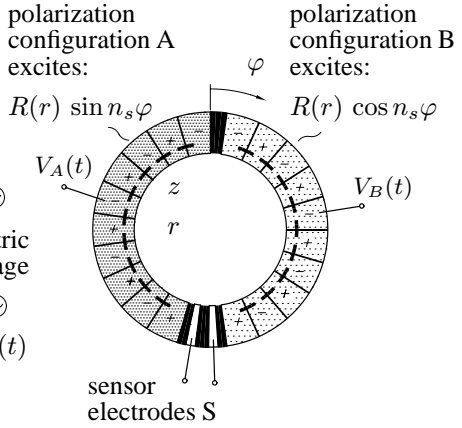


Figure 1.10: Polarization configuration of the piezoceramic ring exciting bending vibrations of the type shown in Fig. 1.7

havior (without motor imperfections), the excitation of the polarization configurations A and B by voltages $V_A(t) = \hat{V}_A \sin \Omega t$ and $V_B(t) = \hat{V}_B \cos(\Omega t + \Delta\phi_V)$, results in a lateral vibration of the stator according to (1.1). Note that the temporal phase shift of 90° in the voltage excitation is necessary to excite a pure traveling wave. Otherwise also standing wave components will be excited. Indeed, voltage signals of the form

$$V_A(t) = \hat{V}_A \sin \Omega t, \quad V_B(t) = \hat{V}_B \cos(\Omega t + \Delta\phi_V) \quad (1.7)$$

with the phase deviation $\Delta\phi_V$ cause lateral vibrations of the plate's mid plane as

$$w_s(r, \varphi, t) = \hat{w}_{sA} R(r) \sin n\varphi \sin \Omega t + \hat{w}_{sB} R(r) \cos n\varphi \cos(\Omega t + \Delta\phi_V) \quad (1.8)$$

$$= \hat{w}_{sA} R(r) \cos(n\varphi - \Omega t) + [\hat{w}_{sB} R(r) \cos(\Omega t + \Delta\phi_V) - \hat{w}_{sA} R(r) \cos(\Omega t)] \cos(n\varphi), \quad (1.9)$$

where the first term in the second equation corresponds to the traveling wave component and the second term to the standing wave component. It is readily seen that by choosing $\Delta\phi_V = 0$ for the phase deviation and $\hat{w}_{sA} = \hat{w}_{sB}$ for the vibration amplitudes of both modes a pure traveling wave results. The trajectories of stator surface points at different phase deviations, $\Delta\phi_V$, and vibration amplitudes, \hat{w}_{sA} , \hat{w}_{sB} , of both modes is illustrated in Fig. 1.11 for two time instances. The arrows indicate the positions of stator surface points along the circumference. Note that these trajectories are projected onto the (φ, z) axis and are scaled with respect to the φ -axis. The trajectories have extensions in the μm range, whereas the wavelength, λ , is in the mm range. For $\Delta\phi_V = 90^\circ$ and $\hat{w}_{sA} = \hat{w}_{sB}$ a pure standing wave is obtained.

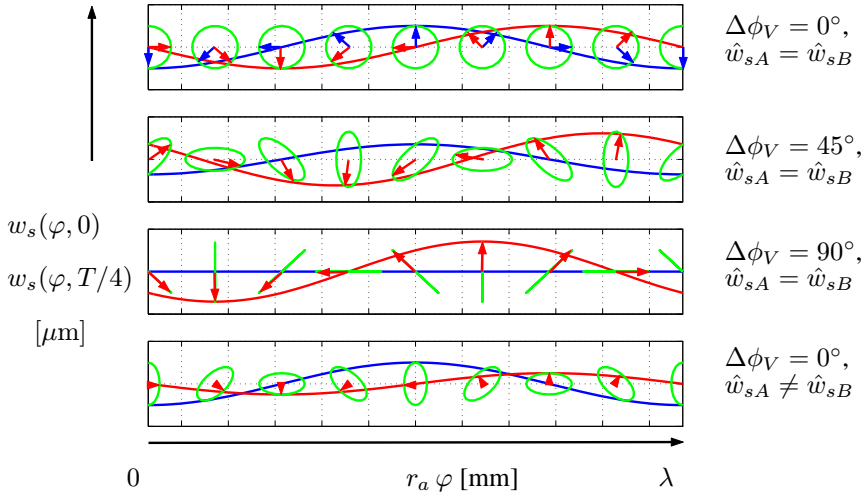


Figure 1.11: Lateral displacement of the stator's mid-plane at two time instances ($t=0$, red, and $t=T/4$, blue) and trajectories of stator surface points for different phase deviations and vibration amplitudes

The motor is driven near its resonance in the ultrasonic range. Although the near resonance motor operation needs special effort with respect to the motor and power electronic design, the out-of-resonance operation implies several drawbacks making it difficult for such kinds of actuators to compete with classic electromagnetic motors. First, out of resonance, the reactive power component can be larger than the resistive power component. Since the power electronic device has to be designed for the apparent power, a large reactive power component results in power electronic devices which may be larger in size than the motor itself. This contradicts the effort to miniaturize the USM technology. Second, the out-of-resonance operation needs high voltage excitation to reach the same vibration amplitude in the stator as with the near resonance excitation. Special application fields as e.g. consumer market devices, however, did not allow high voltage devices for safety reasons.

A typical resonance behavior of the stator's lateral vibration amplitude \hat{w}_s of a USM excited at constant voltage amplitude is shown in Fig. 1.12. In SATTEL *et al.*, 2001, [49] it was shown, that such a resonance curve with softening behavior of an USM may be caused by the non-linear stator-rotor contact. It can be explained as follows. With a rigid rotor, only point contact between stator and rotor would occur. The rotor and the contact layer are however deformable (see Fig. 1.2). Hence, under operating conditions, there are contact zones of finite area depending on the stator vibration amplitude. Therefore, the stator-rotor contact introduces a nonlinear effect. Far away from the

resonance peak the contact zones between stator and rotor are relatively large. When the excitation frequency approaches the resonant peak, the stator amplitude increases, with a corresponding decrease in the contact zones, thus resulting in decreasing contact stiffness. Therefore, the softening behavior in the resonance curve in Fig. 1.12 may be explained by a decrease in the contact stiffness between stator and rotor when the excitation frequency approaches the resonance peak. To ensure smooth and robust oper-

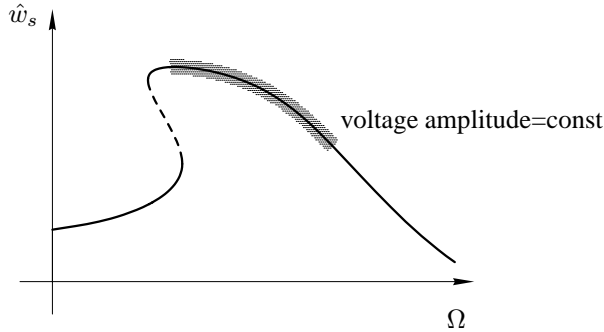


Figure 1.12: Resonance curve of stator displacement in the motor

ation, the range of the excitation frequency must be on the downslope resonance curve and sufficiently far away from the resonance peak.

Besides the mechanical behavior of motors, the electrical behavior is important from a power electronic and control point of view. The principle electrical behavior of piezoelectric motors in the vicinity of their resonance frequency is explained most easily by a simple rod model. In Fig. 1.13 an electrically excited polarized piezoceramic rod with polarization vector \mathbf{P} , free-free mechanical boundary conditions and electroded end faces is depicted, as well as an equivalent electric circuit diagram representing the electric behavior in the vicinity of the resonance frequency. The electrical quantities L_m , C_m and R_m correspond to the modal mass, the modal stiffness and the modal damping, respectively, of the rod's mechanical vibration behavior. The two impedances C_p and R_p represent the electric behavior of the piezoceramics. Details on the representation of electromechanical systems by equivalent electric circuits may be found in various books, as e.g. BERLINCOURT *et al.*, 1964, [7] or IKEDA, 1990, [24]. Exciting the rod electrically by a voltage $V(t) = \hat{V} \cos \Omega t$ in the vicinity of the eigenfrequency of the first longitudinal eigenmode, the frequency response plots of the longitudinal displacement $u(L)$ and the electric admittance

$$\underline{Y} = \frac{I}{V} \quad (1.10)$$

yield the qualitative behavior as illustrated in Fig. 1.14. The frequency response plot of the displacement shows a resonance only, whereas the electric admittance exhibit a

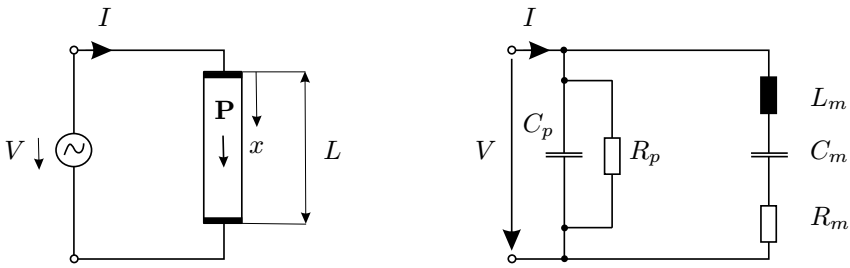


Figure 1.13: Left: Simple piezoceramic rod structure with electrodes at the end faces and free-free mechanical boundary conditions; right: equivalent electric circuit diagram near a resonance frequency

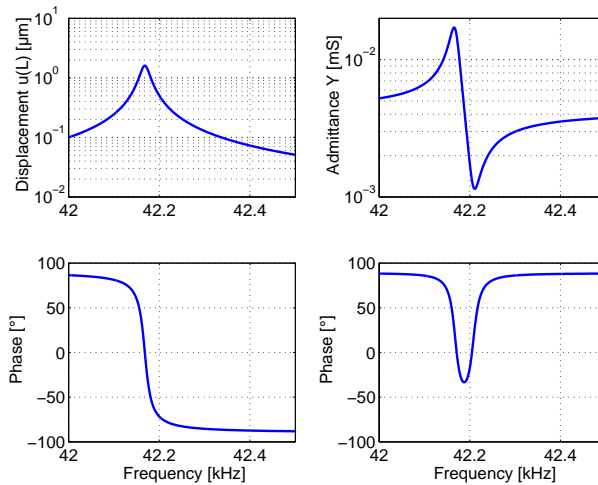


Figure 1.14: Frequency response plots of the rod's longitudinal displacement $u(L)$ and the electric admittance Y near the eigenfrequency corresponding to the first longitudinal eigenmode

resonance and an antiresonance. Neglecting damping effects and considering the free vibrating structure, i.e. without electric excitation, the resonance and antiresonance frequencies in the electric admittance plot correspond to the eigenfrequencies of the free vibrating rod at different electric boundary conditions, namely those with *short-circuited* and *open-circuited* electrodes (see Fig 1.15). In the case of short-circuited electrodes the eigenfrequency corresponds to the resonance, whereas open-circuited electrodes stiffens the system and results in a higher eigenfrequency, corresponding to the antiresonance in the frequency response plot.

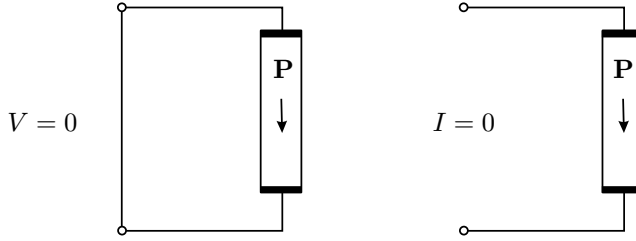
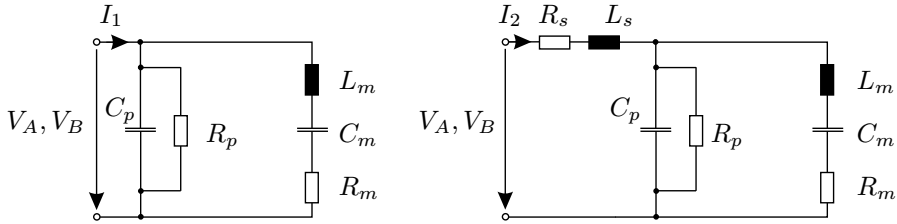


Figure 1.15: Short-circuited and open circuited electric boundary conditions of the rod

It is often argued that USMs show capacitive behavior due to the piezoceramic material, thus causing reactive power that subjects the power electronics to a high load. Since USMs are resonant driven devices it is not immediately obvious why there is a

Figure 1.16: Left: Equivalent electric circuit diagram of an USM; right: with an inductor L_s , R_s added in series

capacitive electric motor behavior. In literature a clear explanation is missing, so that a few comments seem to be necessary. In Fig. 1.16 two simple equivalent electrical circuit diagrams are plotted. The electric circuit in the left figure describes qualitatively the electric admittance of one electrical port of an USM in the vicinity of the operational resonance frequency. The electric quantities L_m , C_m and R_m correspond to the modal mass, the modal stiffness and the modal damping, respectively, of the motor's mechanical vibration behavior (Fig. 1.5). The two impedances C_p and R_p represent the electric behavior of the piezoceramics. The electrical circuit on the right side of Figs. 1.16 illustrates the electric circuit of the motor with an inductor added in series. Putting the inductance L_s in parallel to the electric circuit of the motor would also be possible. Different other more sophisticated circuit topologies for so called *resonant converters* are known, as e.g. *LC* or *LLCC* circuit topologies, as pointed out in MAAS, 2000, [34]. The electric admittance of the motor is denoted as \underline{Y}_1 and that of the motor with inductor as \underline{Y}_2 . The electric admittances for both equivalent circuits yield

$$\underline{Y}_1 := \frac{\hat{I}_1}{\hat{V}_i}, \quad \underline{Y}_2 := \frac{\hat{I}_2}{\hat{V}_i}, \quad \text{with} \quad i = \{A, B\} \quad (1.11)$$

and the graphs of both admittances are depicted in Fig. 1.17. The admittances on the right are zoom plots. Considering the electric admittance \underline{Y}_1 of only the motor, the resonance is followed by an anti-resonance. This is typical for a piezoelectric system. The

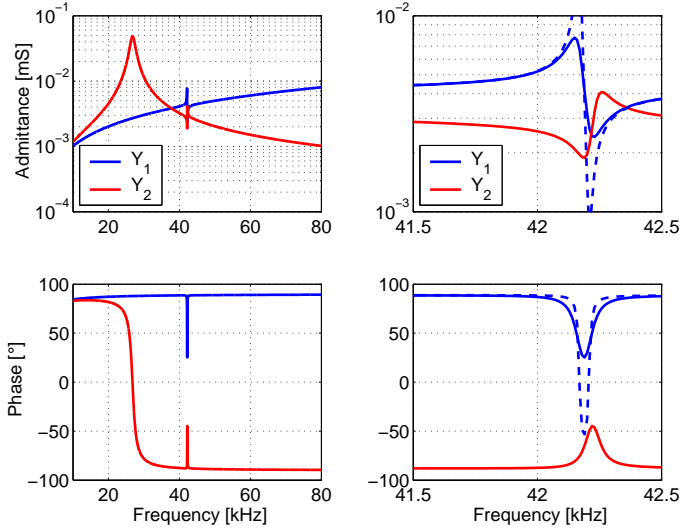


Figure 1.17: Typical electric admittance of USMs without, \underline{Y}_1 , and with an inductance in series, \underline{Y}_2 . Dashed line for low motor damping

operational resonance frequency at 42 kHz is both, an electrical and a mechanical resonance. The resonance frequency corresponds to a vibration mode when the electrodes are short circuited, whereas the anti-resonance frequency corresponds to a vibration mode with open circuited electrodes (no current flow). The solid line indicates a high frictional damping in the motor due to the rotor contact, and the dashed line describes the behavior at low frictional damping. Connecting an inductor with high enough inductance L_s , in series with the motor, results in the admittance behavior as illustrated by \underline{Y}_2 in Fig. 1.17. For frequencies above the anti-resonance frequency (≈ 43 kHz), the motor's electric admittance \underline{Y}_1 is dominated by the piezoceramic capacitance and the admittance of the motor with inductor, \underline{Y}_2 , is dominated by the inductance, thus

$$\underline{Y}_1 \approx j\Omega C_p, \quad \underline{Y}_2 \approx \frac{1}{j\Omega L_s} \quad \text{for} \quad f \geq 43 \text{ kHz} \quad (1.12)$$

hold. Indeed, the motor itself shows a high-pass filter behavior (*capacitive behavior*) at frequencies above the anti-resonance. Instead, the motor with series inductor L_s exhibits a low-pass filter behavior (*inductive behavior*). Operating a motor near its resonance with a pure sinusoidal voltage signal would not lead to a significantly different electrical behavior between both the circuits despite a phase reversal. However,

the power electronics for USMs may produce electric voltage signals with significant higher order harmonic components (pulse width modulated signals e.g.). With a capacitive behavior, \underline{Y}_1 , such higher harmonics may produce large reactive power components, whereas with an inductive behavior, \underline{Y}_2 , the reactive power components are drastically reduced. This is what is meant in literature by *capacitive behavior of USM!* There are investigations where especially the electric port behavior of USMs and the interaction of USMs and power electronics had been the focus of research.

So far, ideal motor transfer behavior was assumed to hold. Imperfections or symmetry disturbances due to manufacturing inaccuracies results in non-ideal transfer behavior of the motors. In the case of USMs using two or more degenerated eigenmodes (modes with the same eigenfrequencies), imperfections split the eigenfrequency of the degenerated modes, as pointed out e.g. in UEHA *et al.* (1993, [57], p.58-59). Ideal traveling wave operation is not possible anymore. When using single frequency excitation, there is always a standing wave component, which produces frictional damping effects only. The frequency split must be small enough so that there is a sufficient traveling wave component in the motor.

In Fig. 1.18 the principal character of speed-torque curves of USMs are sketched in a four-quadrant graphic. The motor output torque and the rotational speed are denoted by T and n , respectively. For an ideal motor, i.e. without any imperfections, the speed-torque characteristics have point symmetry with respect to the origin. Each motor characteristic has two distinguished points, the *no-load speed* at zero torque and the *stall torque* at zero speed. The curves run through three different quadrants in the graph, namely the *operation quadrant*, the *dragging quadrant* and the *braking quadrant*. In the operation quadrant the USM is loaded by an external load. In the dragging quadrant, the USM is driven by an external load and in the braking quadrant, the rotor reverses it's direction of motion due to an external load, acting as a brake. Having a closer look at the velocities of particular stator and rotor material points, this can be explained in more detail. Under simplified assumptions regarding the contact mechanism between stator and rotor, the following relations between the rotor velocity at the outer circumference and the velocities at the stator's wave crests hold in different quadrants (see also Fig. 1.6):

- operation quadrant: \mathbf{v}_{r0} is in the same direction as $\dot{\mathbf{u}}_Q$ and $|\mathbf{v}_r| \leq |\dot{\mathbf{u}}_Q|$ holds
- dragging quadrant: \mathbf{v}_{r0} is in the same direction as $\dot{\mathbf{u}}_Q$ and $|\mathbf{v}_r| \geq |\dot{\mathbf{u}}_Q|$ holds
- braking quadrant: \mathbf{v}_{r0} is in the opposite direction as $\dot{\mathbf{u}}_Q$.

The motor behavior in the dragging quadrant and in the braking quadrant have not been investigated in detail up to now, since such motor operation conditions are unusual if not unwanted. For a given motor design, there are at least four parameters influencing

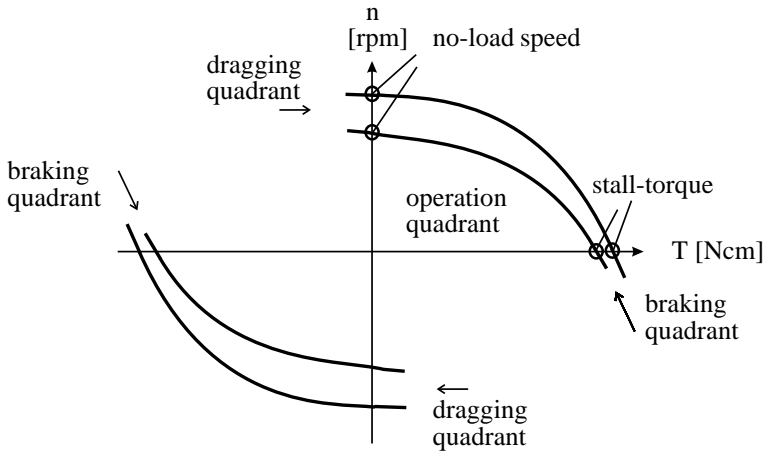


Figure 1.18: Typical speed-torque characteristics of USMs

the position of the speed-torque characteristics, namely the position of the no-load rotational speed and the stall-torque on their corresponding axes. One parameter is the axial preload, F_{axial} , exerted to press the rotor against the stator. This design parameter is easy to adjust. Within certain bounds, it influences mainly the stall-torque. Moreover, the stall-torque depends on the friction coefficient and on the contact state between stator and rotor. Since the stator-rotor contact state may exhibit a complex behavior, the stall-torque cannot be predicted *a priori*. Only an upper bound of the motor output torque can be estimated: $T_{max} = r_0 \mu F_{axial}$. The other three parameters are the control parameters excitation frequency Ω , voltage amplitudes \hat{V}_a , \hat{V}_B and phase deviation $\Delta\phi_V$. In a first approximation they influence the no-load rotational speed by changing the size, the orientation and the elliptical shape of the stator's surface point trajectories, as it is shown in Fig. 1.11. The excitation frequency, e.g., changes the vibration amplitude of the stator's transverse displacement (see Fig. 1.12) and thus results in a change in major and minor axes of the ellipse without changes of the ellipse's shape. This again changes the tangential velocity component at the stator's wave crest in (1.3). A simultaneous change of both voltage amplitudes, i.e. changing $\hat{V}_a = \hat{V}_B$, shows the same effect.

However, there are changes that cause also standing wave components which result in a change of the ellipse's shape. Different voltage amplitudes, i.e. $\hat{V}_a \neq \hat{V}_B$, as well as a phase deviation $\Delta\phi_V \neq 0^\circ$ lead to those standing wave components.

Each of these three control mechanism has its advantages and disadvantages with respect to feedback control, motor operation and motor efficiency. In the experimental part the influence of these four parameters will be investigated. A few comments on feedback control can be found in UCHINO (1997, [56]).

1.2 Past and ongoing research

There has been active research in the USM technology for more than 20 years. During this time, new working and design principles have been invented, yielding an increasing range of applications and greater industrial interest and demand for this kind of actuators. Nevertheless, besides a few applications like lens drives in autofocus cameras of Canon (see UEDA *et al.* (1993, [57])), USMs are not yet mass-produced. New applications are beginning to emerge in special areas like robotics, e.g. in the robotic manipulator 'MarsArmII' which is driven by a USM, (SCHENKER *et al.* (1997, [50])), or as a robot wrist actuator, (SCHREINER *et al.* (2000, [53])), or e.g. in active-control sticks for airplanes, (MAAS *et al.* 1999 [33]). Some applications may also be found e.g. in micro-positioning devices, as proposed in FERREIRA (1998, [11]), or in the automotive industry.

Different trends in research on USM can be recognized. One direction of research concentrates on miniaturization of these motors, aiming at piezoelectric micromotors with diameters in the millimeter range. The fundamental work of FLYNN (1997, [12]) marks the beginning in this area. The opposite direction was promoted e.g. by DaimlerChrysler Research Center in Frankfurt, Germany, (SCHREINER *et al.* (2000, [53])), where a 90 mm diameter motor with a holding torque of approximately 6 Nm was designed. To increase the USMs' torque-mass ratio, so called two-sided USMs have been designed and tested, (see GLENN & HAGOOD (1998, [15])). The motor has an outer diameter of approximately 80 mm and operates with in a vibrational mode with nine nodal lines. With an axial preload of 200 N a stall torque of 170 Ncm was obtained as well as a non-load speed of 40 rpm. The authors mentioned excessive wear of the polymer layer (friction layer) bonded to the non-rotating parts. And this was likely the cause of the lowered performance with a peak value of 13% for the motor's efficiency. The motor was operated at the frequency boundary where it became noise and inconsistent at lower frequencies. A third research direction focuses on new design principles and the fourth and last trend, which has been emerging in recent years aims at motor optimization and the development of more realistic and detailed mathematical models.

Today, the research fields in the area of USMs may be roughly divided into motor design and motor optimization where the investigations of the stator-rotor contact, including tribological issues, play an important role. Research is also conducted in piezoceramic material performance and motor control or power electronics technology. The development of appropriate mathematical models goes along with all these research activities.

One major research field is the stator-rotor contact, since this is one of the key issues for motor optimization and performance improvements. Consequently, many contributions are dedicated to contact layer materials, to the better understanding of the contact mechanics and its influence on the overall motor behavior, like the torque-speed characteristics.

1.3 Actual problems and objective of the work

The design and prototyping of USMs essentially is still an empirical process, involving many experiments and tests. More advanced and refined mathematical models would be helpful for the preliminary design and optimization of an ultrasonic actuator. Also, detailed studies of the influence of different motor parameters on the motor behavior have not yet been carried out. Today it is not a difficult task to design a stator for an USM by using commercial FE-packages and analyzing its vibrational behavior. However, choosing "good" design parameters for a rotor in contact with the stator is still in its infancy. Which rotor material should be taken or which rotor thickness should be taken to ensure stable, reliable and efficient operation are typical questions for the rotor design. Such questions cannot be answered as directly as those for the stator design variables. There has been a lot of progress towards a better understanding of the dynamic contact problem between stator and rotor, but nevertheless there is by far a good understanding of the contact mechanisms. To date, most researchers have concentrated on particular design issues like stator-rotor contact, design of controllers, compensation of reactive power using finite element models or electric analogy models for oversimplified motor behavior. Few researchers have considered complete motor models. Questions like how to choose the rotor geometry or the material parameters of the contact layer to ensure reliable and silent motor operation in the desired range of rotational speed and output torque have not been addressed in a rigorous and systematic way.

On the other hand some special problems still exist in USMs which have not been investigated from a modeling point of view. The onset of squealing, which occurs e.g. when the rotational speed falls below a certain speed threshold, is one of these problems. This phenomenon was observed in our laboratory (Dept. of Applied Mechanics, Darmstadt University of Technology) with different motors. The initial torque-speed characteristics observed in a cold motor is poor compared to that of the motor heated up by internal dissipation. Squealing occurs in a relatively broad range of rotational speeds. Another drawback of ultrasonic actuators is the speed threshold below which they don't work, depending on the speed control strategy used and the stator-rotor contact behavior. For applications requiring low rotational speed without using additional gears, a reduction of the speed threshold may be necessary. Surely, there is the possibility to drive the motors out of phase or far away from resonance, but this requires additional effort in the power electronic design, since high reactive load is present. Operating these motors near resonance can reduce the size of the power electronics drastically. A thorough modeling and theoretical investigation of the stator-rotor contact is needed for a deeper understanding of all these phenomena, more so, since the processes in the contact zone are difficult to measure.

SASHIDA (1993, [44] p. 219) commented that rotor flexibility is a 'necessary evil' in the design of USM. In his book he mentioned the necessity of rotor flexibility in the design of USM but did not give reasons for his statement. One reason could be that a

high rotor stiffness results in a greater rotor inertia, which limits the potential of these motors with respect to a fast response time compared to classical electromagnetic motors. As it is, Sashida's comment highlights another of the design problems in USM. The rotor flexibility may be one reason for stability problems in USM operation. One hypothesis is, that eigenmodes in the rotor can be excited by the frictional contact forces causing noise and reduced operability. Experimental investigations carried out together with an industrial collaborator clearly indicate, that the operativeness and reliability of USMs strongly depends on the design of the rotor. In SASHIDA (1993, [44]) some comments on stability problems in USMs are stated and our laboratory experience indicate that instability problems may occur in a wide range of motor operation (see 4.1.1).

Besides the purely mechanical phenomena observed in the motor dynamics, the electromechanical part must also be studied in detail. The compensation of reactive power due to the piezoceramic material needs particular attention. Special capacitance-inductance circuits, so called LLCC-circuits (see SCHULTE *et al.* (2000, [54])), are used between the power amplifier and the piezoceramic part of the motor to cancel out the reactive power. These circuits are also resonant systems, so that the dynamics of the complete actuator is affected.

Obviously, there is a need for more detailed modeling investigations to obtain a global picture of such actuator systems. The few motor models found in the literature usually are formulated in the time domain, they often neglect rotor flexibility or contain other simplifications. They, therefore, only give very limited information on the influence of the different design parameters on the motor dynamics.

The present work is concerned with the modeling, model analysis and experimental analysis of USMs. In the modeling part a framework for modeling the complete motors is established. The framework is formulated for a two-dimensional description of such motors. Thus, linear motors and rotary motors where the curvature can be neglected in a first approximation can be modeled within this framework. It includes a thorough description of the contact kinematics and of the contact laws. The description is done with respect to a reference frame moving with the traveling wave in the stator, as proposed in SCHMIDT *et al.* (1996, [52]). All the necessary balance laws, mechanical and electrical, are combined in the principle of virtual power. Assuming the appropriate kinematics for stator, rotor and electric displacement, the equations of motion may then be derived in a straightforward manner. In the model analysis part, a numerical solution procedure for the contact problem in USMs is proposed for the description in a moving reference frame. Numerical results will be discussed and the computed speed-torque characteristics will be compared with the measured characteristics. In the experimental part the resonance behavior and the steady-state motor behavior are investigated in detail. Also some investigations with respect to the instationary motor behavior are carried out. The objective of these experiments is to give a comprehensive qualitative picture of typical motor behavior.

Chapter 2

Modeling

2.1 Literature review

A good overview of the various design principles of USMs can be found in UEHA *et al.* (1993, [57]) while detailed information pertaining to the Shinsei USM is given in SASHIDA (1993, [44]). Piezoelectric actuator technology is also presented in parts of UCHINO (1997, [56]). In addition, some simple but helpful models of mechanical stator, electric analogy stator and stator-rotor contact are treated in these references. These models do however not describe the relation between the stator-rotor contact and the overall motor behavior. In addition, the electric analogy models lack a physical interpretation.

The working principle and the modeling and numerical vibration analysis of USM stator's of the Shinsei type are described in HAGEDORN & WALLASCHEK (1992, [20]) and HAGEDORN *et al.* (1993, [20]).

A comprehensive survey of the state-of-the-art of stator-rotor contact problems in USM is given in the review article by WALLASCHEK (1998, [58]). Only some representative literature concerning the stator-rotor contact problem are cited. ENDO & SASAKI (1986 [9]) investigate the influence of the hardness of the contact layer material on the motor operation. The authors point out that material hardness strongly influences the motor behavior. The high-frequency frictional mechanisms in USM are investigated in detail by REHBEIN & WALLASCHEK (1998, [42]). They suggest special polymer composites for the contact layer material. Using tribological experiments they also show that friction coefficients measured at high frequencies (20 kHz) are significantly smaller than those measured at low frequency. They explain the phenomenon by microimpacts

between colliding asperities. KANAZAWA *et al.* (1993, [29]) observed that the friction and wear processes in USM are less severe than those of sliding friction. They claim that the fluid dynamic effect of air appreciably influences this process. Among the papers on motor operability KAMANO *et al.* (1988, [28]) is cited, who observed a stator vibration amplitude below which the rotor doesn't operate. This phenomenon is important when designing USM as precision positioning devices. In the latter context FURUYA *et al.* (1992, [10]) mention the difficulty of operating USM at low rotational speeds. Hence, more detailed investigations concerning the appropriate control strategy are necessary and adequate (see MAAS *et al.* (1999, [33])). Motor models would be useful to this end. KAWAI *et al.* (1995, [30]) investigate experimentally the influence of rotor vibrations on the motor characteristics and state that the maximum output torque, output power and efficiency are obtained when the rotor vibration amplitude in axial direction is half that of the stator vibration amplitude. They also state that, with a proper rotor design, high rotor vibration amplitudes may be realized without squealing.

MAENO and his co-workers conducted both experimental and numerical work. In MAENO *et al.* (1992, [36]) for example, finite-element simulations of the stator-rotor contact behavior are carried out in the time domain for a Canon-USM and compared to experimental results. The authors find several stick-slip zones within one contact zone. Differences between measured friction coefficients and the values calculated by fitting measured torque-speed characteristics lead MAENO *et al.* (1992, [36]) to the hypothesis of the importance of hydrodynamic bearing effects. Numerical investigations qualitatively confirm this hypothesis. An analytic approach to solve contact problems in USM was used by ZHARII (1995, [63]). By applying the half-space method he derived analytical expressions for the normal stresses and relative velocities in the contact zones. This approach may be used to justify numerical results. The half space method was also used by LE MOAL & MINOTTI (1997, [32]). The rotor is modeled as half-space and the stator is assumed to act as rigid indenter with a wavy profile, pressed into the contact layer and rotor substrate. The inertia of stator, rotor and contact layer are however ignored.

A different approach is chosen by CAO & WALLASCHEK (1995, [8]), who focus on the contact layer bonded to the rotor substrate. A simple but useful contact model is derived for the computation of the torque-speed characteristics for different motor design parameters. A similar model was chosen by HAGEDORN *et al.* (1996, [52]). The model consists of a visco-elastic contact layer attached to a rigid rotor and an elastic stator. It is shown that the feedback of the rotor and the contact motion on the stator motion is negligible in the vicinity of resonance. Thus, the stator may be modeled as a kinematic constraint. In the same laboratory SCHMIDT (1999, [51]) and SATTEL, HAGEDORN & SCHMIDT (2001, [48]) studied the stator-rotor contact including rotor elasticity and a visco-elastic contact layer. Using COULOMB's law, several stick-slip zones were obtained in one contact zone, depending on the mechanical load. Relations between rotor stiffness, contact layer stiffness and torque-speed characteristics are com-

puted. It turns out, for example, that rotor flexibility strongly influences the flatness of the torque-speed characteristic. A stator-rotor contact model for simulations in the time domain was proposed in SATTEL & HAGEDORN (1999, [45]).

The first complete motor model relating on design parameters was proposed by HAGOOD & MACFARLAND (1995, [21]). Models of this type are important for designing the motors and controllers. A plate type stator substrate with bonded piezoceramic ring is discretized using a RITZ-Method. However, the rotor was modeled as a rigid body with one rotational and one axial degree of freedom. A pure slip law was used for the contact. Since the simulation is done in the time-domain, transient motor characteristics can be investigated. HAGEDORN *et al.* (1998, [19]) extended the motor model proposed by HAGOOD & MACFARLAND by incorporating the rotor flexibility. Additionally an analysis in the frequency domain was carried out (see HAGEDORN & SATTEL (1998, [47])). LE LETTY *et al.* (1997, [31]) developed a finite-element model together with a dynamic contact algorithm working in the time-domain.

2.2 General modeling aspects

This chapter presents a general two-dimensional framework for the modeling of ultrasonic traveling wave motors, including both, the electro-mechanical and the contact modeling but neglecting curvature of rotary motors. Previous models either take only the contact between stator and rotor into account, neglecting the electrical part of the motor, or include the electrical part, but use a very limited contact model. Notches, milled into the stator, as described in Section 1.1 and Fig. 1.8 are, however, not considered in the modeling. Their influence on stator vibration modes is discussed in SCHMIDT (1999, [51]). From the modeling point of view, it is a priori not obvious which parts and design parameters of the motor have important influence on the motor dynamics and which can be neglected. Thus, a consistent and very general derivation of the equations of motion is carried out. All simplifications are made under the aspect of the order of magnitude of the coefficients by using a scaling analysis. Neither the mass of the contact layer is neglected nor the layer is described as fibers. Non-dimensional and scaled equations are characteristics of the model presented here. Often the a priori assumption is made, that the tangential contact stress does not influence the normal contact stress. By the scaled equations it is possible to decide under which parameters such an assumption is valid. The general framework of modeling allows to transfer the modeling procedure for plate type USMs and for USMs with stators of cylindrical shape, as well. Maxwells equations are taken into account on an over average level which allows to compute and examine the influence of connected impedances. In contrary to other models, lower modes can also be considered which enables the model to determine and to represent subharmonic vibration in the solution. This is important

when investigating effects like squealing, which often occurs in the design stage and causes lots of experiments to find appropriate stator and rotor design parameters.

The contact kinematics is formulated in a continuum mechanical setting to provide flexibility in the modeling. All equations are described with respect to a reference frame moving with the traveling wave to simplify model analysis. Choosing appropriate mechanical and electric displacement shape functions, motor models of different modeling depth can be derived using the principle of virtual power. Electrical quantities like electric admittance or reactive power which are useful for the design of the power electronics are introduced. Using this general framework, a simple motor model with BERNOULLI-EULER kinematics for stator and rotor is derived giving a set of PDE's for stator, rotor, contact layer, piezoceramic and constraint equations for the stator-rotor contact. Subsequently, a scaling is carried out to neglect terms of lower order. This simple model can be used for example to investigate the influence of different design parameters on torque-speed characteristics. Also, transient analysis may be carried out by using appropriate contact algorithms. The objective of this modeling framework is to derive more sophisticated dynamic motor models in order to get a deeper qualitative understanding of motor dynamics and contact behavior in ultrasonic motors, and to work towards motor optimization tools. Furthermore, complete motor models are useful in the design of controllers for ultrasonic motors.

2.2.1 Outline of the USM modeling

In Sections 2.2.2 to 2.6 the general two-dimensional modeling framework is presented. A simple motor model is then derived in Section 2.7 using this general framework. The kinematics of stator and rotor motion is described both, in a spatial fixed frame of reference and in a reference frame moving with the traveling wave in the stator. Section 2.3 contains the notation and definitions used to describe the stator-rotor contact including the sliding velocity and the switching conditions for the detection of changes in the frictional contact states. The dynamics is treated in Section 2.4. First, the boundary value problem is formulated for these special electro-mechanical systems. The principle of virtual power is discussed together with the local balance laws. This is followed by the formulation of the constitutive laws for stator, rotor, contact layer and piezoceramic. The necessary electric quantities for the motor model are introduced in Section 2.6. These are the electric current to the actor electrodes, the electric potential at the sensor electrodes and other quantities such as the electric admittance and reactive power, which are useful for the design of the power electronics. The simple motor model derived in Section 2.7 is scaled with appropriate characteristic quantities to distinguish the quantitative important terms in the equations of motion from higher order effects.

2.2.2 Kinematics

First, the simplification of using a planar instead of a three dimensional motor model is motivated. A thin contact layer (thickness ≈ 0.1 mm) is bonded on the rotor surface at the outer radius r_a as shown in Fig. 1.2. Line contact at the outer circumference of stator and rotor is assumed, since for the width s of the contact layer $s \ll r_a$ holds. Thus, only the displacements at the outer radius are of interest. According to (1.2) and (1.1) the stator's displacement at the outer radius can be written as

$$\begin{aligned} \mathbf{u}_s(r_a, \varphi, z, t) = & -z w_{s,r}(r_a, \varphi, t) \mathbf{e}_r - \frac{z}{r_a} w_{s,\varphi}(r_a, \varphi, t) \mathbf{e}_\varphi \\ & + w_s(r_a, \varphi, t) \mathbf{e}_z, \quad \varphi \in [0, 2\pi] \end{aligned} \quad (2.1)$$

with $w_s(r_a, \varphi, t) = R(r_a) \cos(n_s \varphi - \Omega t)$. Using the coordinate transformation $x = r_a \varphi$ we get

$$\mathbf{u}_s(x, z, t) = -z w_{s,r}(x, t) \mathbf{e}_r - z w_{s,x}(x, t) \mathbf{e}_\varphi + w_s(x, t) \mathbf{e}_z, \quad x \in [0, L] \quad (2.2)$$

with the outer circumferential length $L = 2\pi r_a$, the transverse displacement

$$w_s(x, t) = R(r_a) \cos(n_s k x - \Omega t) \quad (2.3)$$

and the *fundamental wave number*

$$k = 2\pi/L = 1/r_a. \quad (2.4)$$

The radial displacement component of the stator's surface points in (2.2) is orthogonal to the circumferential direction and therefore contributes only to frictional dissipative effects between stator and contact layer and not in driving the rotor. Hence, the stator design and the eigenmodes in which the motor is driven should be chosen appropriately to get only small radial displacement components. The magnitudes of the different displacement components can be compared by substituting (2.3) into (2.2). This yields

$$\begin{aligned} \max_{\varphi \in [0, 2\pi]} |\mathbf{u}_s \cdot \mathbf{e}_r| &= \frac{h_s}{2} R'(r_a), & \max_{\varphi \in [0, 2\pi]} |\mathbf{u}_s \cdot \mathbf{e}_\varphi| &= \frac{h_s}{2} R(r_a) k, \\ \max_{\varphi \in [0, 2\pi]} |\mathbf{u}_s \cdot \mathbf{e}_z| &= R(r_a). \end{aligned} \quad (2.5)$$

If choosing the stator's geometry and bending mode properly, the radial displacement component $\max |\mathbf{u}_s \cdot \mathbf{e}_r|$ in (2.6) is small compared to the axial and circumferential ones. To this end, the number of nodal lines n_s must be high enough and R' must be sufficiently low. Equation (2.2) then is reduced to

$$\mathbf{u}_s(x, z, t) = -z w_{s,x}(x, t) \mathbf{e}_x + w_s(x, t) \mathbf{e}_z \quad x \in [0, L], \quad (2.6)$$

with periodic boundary conditions at $x = 0$ and $x = L$. The x -axis can be identified with the *circumferential direction* at the outer radius and the z -axis corresponds to the *axial direction* of a rotary USM. The z -axis will also be called *rotational axis*.

2.2.3 Material description in an inertial frame

In modeling rotary ultrasonic motors, the stator in the shape of a circular plate is substituted by a straight beam, according to the discussion leading to (2.6). Both linear and rotary motors are therefore modeled as two-dimensional bodies. The motions χ_s of the stator and χ_r of the rotor in material description with respect to an inertial reference frame $(O, \mathbf{E}_1, \mathbf{E}_2, \mathbf{E}_3)$, as depicted in Fig. 2.1, can be written as

$$\mathbf{x}_s = \chi_s(\mathbf{X}, t) = \mathbf{X} + \mathbf{u}_s(\mathbf{X}, t) = [X_i + u_{s_i}(\mathbf{X}, t)] \mathbf{E}_i, \quad \mathbf{X} \in \mathcal{B}_{0s} \quad (2.7)$$

and

$$\begin{aligned} \mathbf{x}_r = \chi_r(\mathbf{X}, t) &= \mathbf{c}_r(t) + \mathbf{X} + \mathbf{u}_r(\mathbf{X}, t) \\ &= [c_{r_i}(t) + X_i + u_{r_i}(\mathbf{X}, t)] \mathbf{E}_i, \quad \mathbf{X} \in \mathcal{B}_{0r}, \end{aligned} \quad (2.8)$$

where the unit vectors $\mathbf{E}_1, \mathbf{E}_3$ span the motor plane and \mathbf{E}_2 is perpendicular to them. In case of the rotary USM the circumferential direction coincides with X_1 -axis and the rotational axis is identified with the X_3 -axis of the reference frame in Fig. 2.1. The

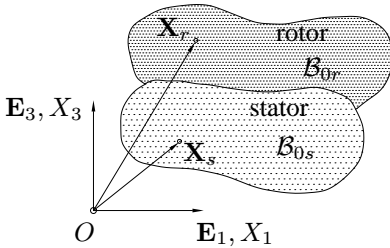


Figure 2.1: Motor model in the reference configuration $\mathbf{X} = \chi(\mathbf{X}, t_0)$

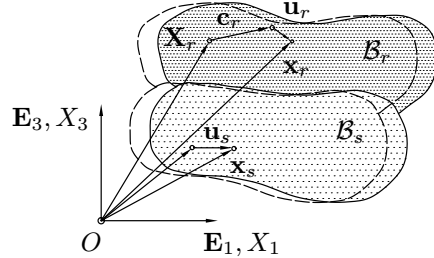


Figure 2.2: Motor model in the momentary configuration for $t > t_0$

translational rigid body motion of the rotor and the displacement fields of stator and rotor are described by $\mathbf{c}_r(t)$ and $\mathbf{u}_r(\mathbf{X}, t)$, respectively. For the sake of simplicity, $\mathbf{u}(\mathbf{X}, t)$ instead of $\mathbf{u}(X_1, X_2, X_3, t)$ is used to indicate the material coordinates. In the reference configuration, shown in Fig. 2.1, the stator and rotor occupy the volumes \mathcal{B}_{0s} , \mathcal{B}_{0r} and in the momentary configuration, as illustrated in Fig. 2.9, the volumes \mathcal{B}_s , \mathcal{B}_r respectively. If necessary, points of stator or rotor are designated by

$$\mathbf{X}_s, \quad \forall \mathbf{X} \in \mathcal{B}_{0s}, \quad \mathbf{X}_r, \quad \forall \mathbf{X} \in \mathcal{B}_{0r}.$$

For the planar motor model, the periodicity condition

$$\mathbf{u}(X_1, X_2, X_3, t) = \mathbf{u}(X_1 + L, X_2, X_3, t), \quad X_1 \in [-\infty, \infty] \quad (2.9)$$

is assumed, where L can be regarded as the circumferential length for example at the outer radius of a rotary USM (see Section 2.2.2). Throughout the paper it is assumed

that this periodicity also holds for linear motors. The vibration amplitudes in almost all ultrasonic traveling wave motors are small compared to the wavelength of the traveling wave and to the geometric dimensions of both, stator and rotor. Therefore, the assumptions of small displacements \mathbf{u} and small deformations $\text{Grad } \mathbf{u}(\mathbf{X}, t)$ are applied. For the linearized strain tensor \mathbf{S} of stator and rotor, one obtains

$$\mathbf{S} = \frac{1}{2} \left[\text{Grad } \mathbf{u}(\mathbf{X}, t) + \text{Grad}^T \mathbf{u}(\mathbf{X}, t) \right]. \quad (2.10)$$

2.2.4 Material description in a moving reference frame

A traveling wave such as $\cos(n_s k_s X_1 - \Omega t)$ is excited in the stator. Here Ω is the circular excitation frequency, k_s the fundamental wave number and n_s the number of the nodal lines in the stator. Then, also the steady state contact zones between stator and rotor travel with velocity $v_w = \Omega/(n_s k_s)$. From the modeling and model analysis point of view it is convenient to introduce a new reference frame, $(\tilde{O}, \tilde{\mathbf{E}}_1, \tilde{\mathbf{E}}_2, \tilde{\mathbf{E}}_3)$, with coordinates Y_1, Y_2, Y_3 moving with the traveling wave in the stator (see Fig. 2.3). In this reference frame, the traveling wave degenerates into a standing wave. A co-

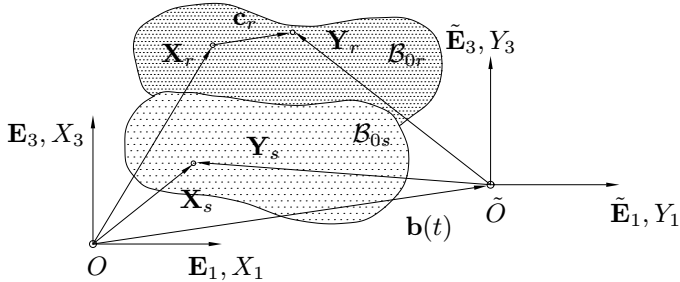


Figure 2.3: Configurations of stator and rotor with respect to inertial and moving reference frames

ordinate transformation then gives $\cos(n_s k_s X_1 - \Omega t) = \cos(n_s k_s Y_1)$. Under some simplifying assumptions, stationary motor operations, i.e. for constant rotational speed and stationary contact states, this leads to a time independent contact problem. The reduction of the dynamic contact problem to a time independent contact problem in the moving reference frame may be a good approximation in the vicinity of the resonance of the system (see Fig. 1.12). This presupposes a corresponding excitation of the stator vibrations, which will be discussed in more detail in Section 2.6.1. The two reference frames are related by $\mathbf{E}_i = \tilde{\mathbf{E}}_i$, since these undergo only an translational shift. The points of the stator \mathbf{X}_s , and of the rotor \mathbf{X}_r , transform according to

$$\mathbf{X}_s = \mathbf{b}(t) + \mathbf{Y}_s \quad \Leftrightarrow \quad X_{s_i} = b_i(t) + Y_{s_i} \quad (2.11)$$

$$\mathbf{X}_r + \mathbf{c}_r(t) = \mathbf{b}(t) + \mathbf{Y}_r \quad \Leftrightarrow \quad X_{r_i} + c_{r_i}(t) = b_i(t) + Y_{r_i}. \quad (2.12)$$

Inserting the transformation relations (2.11) and (2.12) in the displacement functions \mathbf{u} gives

$$\mathbf{u}_s(\mathbf{X}_s, t) = \mathbf{u}_s(\mathbf{b} + \mathbf{Y}_s, t) =: \tilde{\mathbf{u}}_s(\mathbf{Y}_s, t) \quad (2.13)$$

$$\mathbf{u}_r(\mathbf{X}_r, t) = \mathbf{u}_r(\mathbf{b} - \mathbf{c}_r + \mathbf{Y}_r, t) =: \tilde{\mathbf{u}}_r(\mathbf{Y}_r, t), \quad (2.14)$$

with

$$\mathbf{Y}_s(t) = \mathbf{X}_s - \mathbf{b}(t) \quad \text{and} \quad \mathbf{Y}_r(t) = \mathbf{X}_r - [\mathbf{b}(t) - \mathbf{c}_r(t)]. \quad (2.15)$$

The periodicity condition (2.9) in the inertial reference frame also holds in the moving reference frame $(O, \tilde{\mathbf{E}}_1, \tilde{\mathbf{E}}_2, \tilde{\mathbf{E}}_3)$

$$\tilde{\mathbf{u}}(Y_1, Y_2, Y_3, t) = \tilde{\mathbf{u}}(Y_1 + L, Y_2, Y_3, t). \quad (2.16)$$

The strain tensor (2.10) becomes

$$\tilde{\mathbf{S}} = \frac{1}{2} \left[\text{Grad } \tilde{\mathbf{u}}(\mathbf{Y}, t) + \text{Grad}^T \tilde{\mathbf{u}}(\mathbf{Y}, t) \right]. \quad (2.17)$$

2.2.5 Time derivatives and virtual velocities

Next, the velocities and accelerations of stator and rotor points must be calculated. The abbreviation $(\dot{\cdot}) \equiv \frac{d}{dt}$ is used to indicate the total time derivative with respect to the inertial reference frame $(0, \mathbf{E}_1, \mathbf{E}_2, \mathbf{E}_3)$. It follows that

$$\mathbf{v}_s(\mathbf{X}_s, t) = \dot{\chi}_s(\mathbf{X}_s, t) = \dot{\mathbf{u}}_s(\mathbf{X}_s, t) \quad (2.18)$$

$$\dot{\mathbf{v}}_s(\mathbf{X}_s, t) = \ddot{\chi}_s(\mathbf{X}_s, t) = \ddot{\mathbf{u}}_s(\mathbf{X}_s, t) \quad (2.19)$$

for the stator and

$$\mathbf{v}_r(\mathbf{X}_r, t) = \dot{\chi}_r(\mathbf{X}_r, t) = \dot{\mathbf{c}}_r + \dot{\mathbf{u}}_s(\mathbf{X}_r, t) \quad (2.20)$$

$$\dot{\mathbf{v}}_r(\mathbf{X}_r, t) = \ddot{\chi}_r(\mathbf{X}_r, t) = \ddot{\mathbf{c}}_r + \ddot{\mathbf{u}}_s(\mathbf{X}_r, t) \quad (2.21)$$

for the rotor. For the material time derivatives of the displacement fields expressed in terms of the moving reference frame coordinates, the chain rule is applied and the partial time derivative with respect to the inertial reference frame is indicated by the symbol $(\overset{\circ}{\cdot}) \doteq \frac{\partial}{\partial t}$. It follows

$$\tilde{\mathbf{v}}_s = \overset{\circ}{\mathbf{u}}_s - \text{Grad } \tilde{\mathbf{u}}_s \cdot \dot{\mathbf{b}} \quad (2.22)$$

$$\dot{\tilde{\mathbf{v}}}_s = \overset{\circ}{\overset{\circ}{\mathbf{u}}}_s - 2 \text{Grad } \overset{\circ}{\mathbf{u}}_s \cdot \dot{\mathbf{b}} + \text{Grad} \left[\text{Grad } \tilde{\mathbf{u}}_s \cdot \dot{\mathbf{b}} \right] \cdot \dot{\mathbf{b}} - \text{Grad } \tilde{\mathbf{u}}_s \cdot \ddot{\mathbf{b}} \quad (2.23)$$

and

$$\tilde{\mathbf{v}}_r = \dot{\mathbf{c}}_r + \overset{\circ}{\tilde{\mathbf{u}}}_r - \text{Grad } \tilde{\mathbf{u}}_r \cdot (\dot{\mathbf{b}} - \dot{\mathbf{c}}_r) \quad (2.24)$$

$$\begin{aligned} \dot{\tilde{\mathbf{v}}}_r = & \ddot{\mathbf{c}}_r + \overset{\circ\circ}{\tilde{\mathbf{u}}}_r - 2 \text{Grad } \overset{\circ}{\tilde{\mathbf{u}}}_r \cdot [\dot{\mathbf{b}} - \dot{\mathbf{c}}_r] + \text{Grad} \left[\text{Grad } \tilde{\mathbf{u}}_r \cdot [\dot{\mathbf{b}} - \dot{\mathbf{c}}_r] \right] \cdot (\dot{\mathbf{b}} - \dot{\mathbf{c}}_r) \\ & - \text{Grad } \tilde{\mathbf{u}}_s \cdot [\ddot{\mathbf{b}} - \ddot{\mathbf{c}}_r] \end{aligned} \quad (2.25)$$

for stator and rotor, respectively. Using the velocity expressions given above, the strain rate tensor $\dot{\tilde{\mathbf{S}}}$ can be expressed as

$$\dot{\tilde{\mathbf{S}}} = \frac{1}{2} \left[\text{Grad } \tilde{\mathbf{v}} + \text{Grad}^T \tilde{\mathbf{v}} \right] . \quad (2.26)$$

The equations of motion are derived using the principle of virtual power. To this end, the virtual velocities are needed

$$\delta \tilde{\mathbf{v}}_s = \delta \overset{\circ}{\tilde{\mathbf{u}}}_s \quad (2.27)$$

$$\delta \tilde{\mathbf{v}}_r = \delta \dot{\mathbf{c}}_r + \delta \overset{\circ}{\tilde{\mathbf{u}}}_s + \text{Grad } \tilde{\mathbf{u}}_r \cdot \delta \dot{\mathbf{c}}_r . \quad (2.28)$$

Note that the variation of $\dot{\mathbf{b}}$ is zero since \mathbf{b} is the prescribed motion of the moving reference frame relative to the inertial reference frame. The virtual strain rate tensor

$$\delta \dot{\tilde{\mathbf{S}}} = \frac{1}{2} \left[\text{Grad } \delta \tilde{\mathbf{v}} + \text{Grad}^T \delta \tilde{\mathbf{v}} \right] \quad (2.29)$$

is needed for the formulation of the principle of virtual power in the often-used short form.

2.3 Contact formulation

The vibration amplitudes in ultrasonic motors are in the range of microns and the wavelengths in stators are typically in the range of millimeters. Several experiments, as carried out by FLYNN (1997, [12]), or ENDO & SASAKI (1986, [9]), for example, show that the surface finishing of both stator and rotor or contact layer, in addition to the hardness of the materials, can drastically influence the motor performance. ODEN & MARTINS (1985, [39]) note that, depending on the method of surface finishing, the peak height of surface asperities may vary between $0.05\mu\text{m}$ to $50\mu\text{m}$ while the spacing

between them ranges from $0.5\mu\text{m}$ - 50 mm resulting in an average slope of the asperities usually of the order $5^\circ - 10^\circ$. It is therefore not surprising that the surface roughness, described for example as 'root mean square' in ODEN & MARTINS (1985, [39]) or JOHNSON (1985, [27]), has to be low enough to ensure that only the wave crests of the traveling waves are in contact with the rotor. The motor performance would otherwise seriously deteriorate since the velocity profile of the valley of the traveling wave is opposite to that of the wave crest (see Fig. 1.6). The contact surfaces are therefore lapped flat and then polished with appropriate lapping paper. In FLYNN (1997, [12]), averaged surface roughnesses in the order of $10^{-2}\mu\text{m}$ of 8mm-diameter motors operating at vibration amplitudes in the micron range were obtained after lapping and polishing the surfaces. MAENO & BOGY (1992, [36]) mentioned a maximum surface roughness between 50-100 nm for a Canon ultrasonic motor whereas HONDA & KATO (1993, [23]), state surface roughnesses of 600 nm for a rotor and 50 nm for a stator.

Depending on the modeling objective one has to choose appropriate contact models and appropriate contact formulations from the numerous options available in contact mechanics. Since the focus is on deformation effects in the stator, rotor and the contact layer (see Fig. 1.2) and on the phenomenology of motor dynamics, a continuum based approach for the contact formulation is chosen, according to WRIGGERS (1995, [62]), or ODEN & MARTINS (1985, [39]), for example. This method of modeling allows so called *conformal contact* (see JOHNSON (1985, [27])), as is the case in many USMs and its formulation is general enough to derive motor models for a variety of motor designs. As for the contact model, a simple *non-penetration condition* is used for the normal contact and COULOMB's law with *stick-slip transitions* is used to account for the tangential contact. Reasons to choose these contact laws are stated below. Other, more sophisticated contact models, such as nonlinear penetration laws for high-pressure contact are mentioned in WRIGGERS (1995, [62]) or ODEN & MARTINS (1985, [39]). Possible other friction mechanisms, such as hydrodynamic bearing effects proposed in MAENO & BOGY (1991, [35]), due to the high frequency motion of surface particles and the small gap between non-contacting surface points of stator and rotor, are not considered. Also, small scale frictional mechanisms as micro-impacts between surface asperities, as suggested by REHBEIN & WALLASCHEK (1998, [42]), to explain the decrease of the 'apparent' coefficient of friction at high frequencies (ultrasonic range) can only be considered by adjusting the macroscopic coefficient of friction. To this end, in a first approximation the surface properties are assumed, including wear effects, to be contained both, in the stiffness of the contact layer and in the friction coefficient.

2.3.1 Contact kinematics

The objective of this section is the formulation and definition of contact kinematic quantities, such as the *gap function* and the *relative velocity* of two contacting surface points. In the following, all quantities and variables referring to the surface of stator or rotor are

denoted by a hat symbol ($\hat{\cdot}$). For each rotor material point $\hat{\mathbf{X}}_r$ of the rotor surface, a sta-

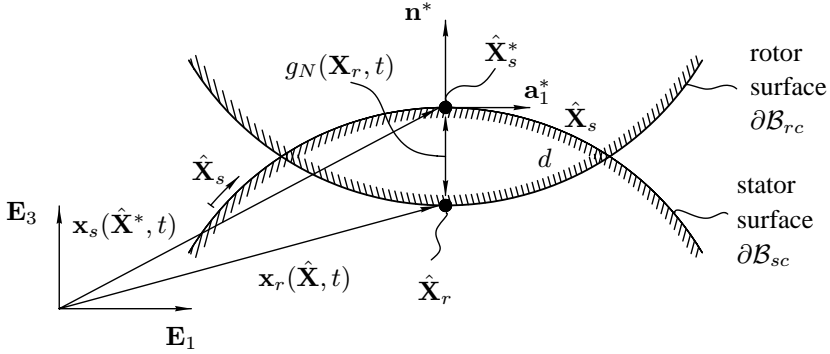


Figure 2.4: Definition of the contact gap

tor surface point $\hat{\mathbf{X}}_s^*$ is associated, which can be determined by minimizing the distance $d(\hat{\mathbf{X}}_r, \hat{\mathbf{X}}_s, t)$ (see Fig. 2.4) between surface points

$$d(\hat{\mathbf{X}}_r, \hat{\mathbf{X}}_s, t) = \min_{\hat{\mathbf{X}}_s \in \partial\mathcal{B}_{sc}} \| \mathbf{x}_r(\hat{\mathbf{X}}_r, t) - \mathbf{x}_s(\hat{\mathbf{X}}_s, t) \| . \quad (2.30)$$

The pair $(\hat{\mathbf{X}}_r, \hat{\mathbf{X}}_s^*)$ represents a contact pair and it should be noted that the stator surface point $\hat{\mathbf{X}}_s^*(\hat{\mathbf{X}}_r, t)$ is a function of the rotor contact point $\hat{\mathbf{X}}_r$ and time and is found by solving the necessary condition for a minimum

$$\frac{\partial}{\partial \hat{\mathbf{X}}_s} d(\hat{\mathbf{X}}_r, \hat{\mathbf{X}}_s, t) \Big|_{\hat{\mathbf{X}}_s = \hat{\mathbf{X}}_s^*} = 0 . \quad (2.31)$$

All field variables referring to the contact point $\hat{\mathbf{X}}_s^*$ will be denoted by a star, $(\cdot)^*$. A local coordinate system is defined at the stator surface point $\hat{\mathbf{X}}_s^*$ with the tangent unit vectors

$$\mathbf{a}_1^* = \frac{\partial \hat{\mathbf{x}}_s(\hat{\mathbf{X}}_s^*, t)}{\partial X} \approx \mathbf{E}_1, \quad \mathbf{a}_2^* = \mathbf{E}_2 \quad (2.32)$$

and the outside normal vector

$$\mathbf{n}^* = \frac{\mathbf{a}_x^* \times \mathbf{a}_y^*}{\| \mathbf{a}_x^* \times \mathbf{a}_y^* \|} \approx \mathbf{E}_3, \quad (2.33)$$

according to the assumptions of small displacements and planar motor models. If referring to the contact kinematics or the contact forces, we will speak of the *normal* and *tangential direction* \mathbf{n}^* and \mathbf{a}_1^* , respectively. The gap function can then be defined as

$$\begin{aligned} g_N(\hat{\mathbf{X}}_r, t) &:= [\mathbf{x}_r(\hat{\mathbf{X}}_r, t) - \mathbf{x}_s(\hat{\mathbf{X}}_s^*, t)] \cdot \mathbf{n}^* = [\mathbf{u}_r(\hat{\mathbf{X}}_r, t) - \mathbf{u}_s(\hat{\mathbf{X}}_s^*, t)] \cdot \mathbf{n}^* \\ &= [\hat{\mathbf{u}}_r - \hat{\mathbf{u}}_s^*] \cdot \mathbf{n}^* . \end{aligned} \quad (2.34)$$

The gap function can be written in terms of the moving reference coordinates

$$\tilde{g}_N(\mathbf{Y}_r, t) = [\hat{\mathbf{u}}_r - \hat{\mathbf{u}}_s^*] \cdot \mathbf{n}^* \quad (2.35)$$

with

$$\text{separation : } \tilde{g}_n > 0, \quad \text{penetration : } \tilde{g}_N < 0.$$

The gap velocity follows as

$$\dot{g}_N = [\hat{\mathbf{v}}_r - \hat{\mathbf{v}}_s^*] \cdot \mathbf{n}^* \quad (2.36)$$

in terms of coordinates with respect to the interial reference frame and as

$$\dot{\hat{g}}_N(\hat{\mathbf{Y}}, t) = [\hat{\mathbf{v}}_r - \hat{\mathbf{v}}_s^*] \cdot \mathbf{n}^* \quad (2.37)$$

in terms of coordinates of the moving reference frame. The variation of the gap velocity leads to

$$\delta \dot{\hat{g}}_N(\hat{\mathbf{Y}}, t) = [\delta \hat{\mathbf{v}}_r - \delta \hat{\mathbf{v}}_s^*] \cdot \mathbf{n}^*. \quad (2.38)$$

Substituting (2.22) and (2.24) into (2.37) yields

$$\dot{\hat{g}}_N = \left[\dot{\mathbf{c}}_r + \overset{\circ}{\hat{\mathbf{u}}}_r - \text{Grad } \hat{\mathbf{u}}_r \cdot (\dot{\mathbf{b}} - \dot{\mathbf{c}}_r) - \overset{\circ}{\hat{\mathbf{u}}}_s + \text{Grad } \hat{\mathbf{u}}_s \cdot \dot{\mathbf{b}} \right] \cdot \mathbf{n}^* \quad (2.39)$$

The virtual gap velocity is needed for the principle of virtual velocity which can be written as

$$\delta \dot{\hat{g}}_N = \left[\delta \dot{\mathbf{c}}_r + \delta \overset{\circ}{\hat{\mathbf{u}}}_r + \text{Grad } \hat{\mathbf{u}}_r \cdot \delta \dot{\mathbf{c}}_r - \delta \overset{\circ}{\hat{\mathbf{u}}}_s \right] \cdot \mathbf{n}^* \quad (2.40)$$

Here, the variation $\delta \dot{\mathbf{b}} = 0$ since the motion of the moving reference frame in Fig. 2.3 (see also Eqn. (2.11) and (2.12)) is prescribed. Since a COULOMB friction law is used, the kinematics of the tangential contact is written at the velocity level, yielding the relative velocity

$$\hat{\mathbf{v}}_{rel} = \dot{\hat{g}}_T \mathbf{a}_x^* := [\hat{\mathbf{v}}_s(\mathbf{Y}_s^*, t) - \hat{\mathbf{v}}_r(\mathbf{Y}_r, t)] \cdot \mathbf{a}_x^* \quad (2.41)$$

and the virtual relative velocity

$$\delta \hat{\mathbf{v}}_{rel} = \delta \dot{\hat{g}}_T \mathbf{a}_x^* := [\delta \hat{\mathbf{v}}_s^* - \delta \hat{\mathbf{v}}_r] \cdot \mathbf{a}_x^* \quad (2.42)$$

Note, that according to definition (2.41), the relative velocity is positive for stator tangential velocities exceeding rotor tangential velocities, i.e. for a driven rotor surface point.

2.3.2 Contact states: Normal and tangential contact

The contact stress at the stator surface, $\hat{\mathbf{T}}^s$, is divided into normal and tangential components, according to the local coordinate system shown in Fig. 2.4

$$\hat{\mathbf{T}}^{s*} = \hat{\mathbf{T}}_N^{s*} + \hat{\mathbf{T}}_T^{s*} = \tilde{T}_N \mathbf{n}^* + \tilde{T}_T \mathbf{a}_1^* . \quad (2.43)$$

T_N and T_T will be called the *normal* and *tangential contact stress*, respectively. The following equation holds at a contact point

$$\hat{\mathbf{T}}^r = -\hat{\mathbf{T}}^{s*} , \quad (2.44)$$

where $\hat{\mathbf{T}}^r$ is the contact stress at the rotor surface. It is distinguished between contact and non-contact states by using the gap function \tilde{g}_N and the normal contact stress \tilde{T}_N . Instead of a material contact law for the normal contact, i.e. a functional relation between normal contact stress and gap function, $\hat{\mathbf{T}} = f(\tilde{g}_N)$ (see WRIGGERS (1995, [62]) or ODEN & MARTINS (1985, [39])), a non-penetration condition is chosen

$$\begin{aligned} \text{no contact} & : \quad \left(\tilde{g}_N > 0 \quad \wedge \quad \tilde{T}_N = 0 \right) \\ \text{contact} & : \quad \left(\tilde{g}_N = 0 \quad \wedge \quad \tilde{T}_N \leq 0 \right) . \end{aligned} \quad (2.45)$$

This geometric contact formulation is motivated by the order of magnitude of the normal contact stress between stator and rotor surfaces and the averaged surface roughness of the contact surfaces. The normal contact stress usually is in the range of only several N/mm² in USMs, and the averaged surface roughness is assumed to be at least one order of magnitude smaller than the vibration amplitude in the stator. This indicates that a small penetration only can be assumed between the centerlines (see Johnson (1985, [27] pp. 406)) of the rough surfaces of stator and rotor (small compared to the stator vibration amplitude). Thus, a geometric non-penetration condition seems to be valid.

For tangential contact COULOMB'S law with identical coefficients of friction and stiction is assumed. It should be noted, that this is merely an assumption and is not evident from experimental results with USM or appropriate polymer-metal contact pairs. REHBEIN & WALLASCHEK (1998, ([42]), for example, measured a difference between sticking coefficients μ_{stick} and apparent coefficients of friction, μ_{slip} , for sliding contact carrying out various polymer-metal contact experiments at high frequency. LE MOAL *et al.* (1997, [32]), conducted tribological experiments with the Shinsei USM. They measured a sliding friction coefficient increasing with the relative sliding velocity to a limit friction coefficient. No details about the experiments were however given. WRIGGERS (1995, [62]), distinguish between elastic sticking and plastic sliding. The tangential slip g_T is split into an elastic part g_T^e and a plastic (slip) part g_T^s . The elastic

part describes the reversible micro-displacements of the asperities during sticking and results in a constitutive relation of the type

$$\tilde{T}_T = c_T \tilde{g}_T^e$$

between the tangential contact stress and the tangential displacement where c_T is the tangential contact stiffness between asperities.

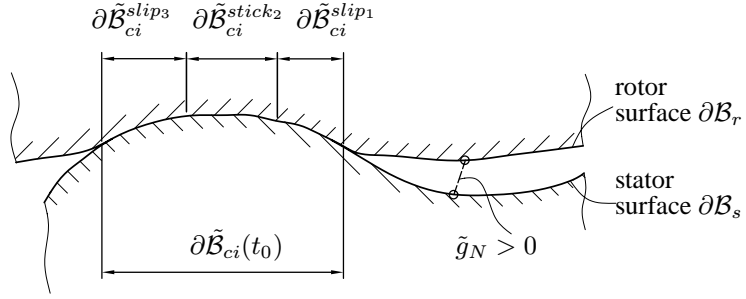
As outlined above, in USM applications the contact surfaces are finished to obtain an averaged surface roughness much smaller than the vibration amplitude. Also, the averaged slope of asperities usually is of the order of $5^\circ - 10^\circ$ only. This provides a first explanation for the high tangential contact stiffness c_T , since the asperities may undergo very small tangential displacements only. In the limit case, for $c_T \rightarrow \infty$, COULOMB's law results. ODEN & MARTINS (1985, [39] p. 530) state that the macroscopically observed apparent dependence of the coefficient of friction on relative velocity may, at least in certain cases, also be explained by a more refined modeling, e.g. by taking into account oscillations in the normal direction. It must however be noted that their statements are based on experiments with metal-metal contact. There seems to be no reason not to use COULOMB's law in the form

$$|\tilde{T}_T| \leq \mu \tilde{T}_n \quad \text{with} \quad \begin{cases} \text{if } |\tilde{T}_T| < \mu \tilde{T}_n & \text{then } \dot{\tilde{g}}_T = 0 : \text{ stick} \\ \text{if } |\tilde{T}_T| = \mu \tilde{T}_n & \text{then } \dot{\tilde{g}}_T \neq 0 : \text{ slip} \end{cases} . \quad (2.46)$$

Condition $\dot{\tilde{g}}_T = 0$ is a tangential constraint equation which has to be fulfilled for sticking. Also smoothed friction laws, such as proposed by ODEN & MARTINS (1985, [39]) for example, or stated in WRIGGERS (1995, [62]), may be applied. In some cases smoothed friction laws are used to simplify computation.

2.3.3 Switching conditions: Detecting temporal changes of the contact zones

In the dynamic stator-rotor contact problem of USMs, the surface points run through a series of different contact states with a changing number of contact constraints. Firstly, it is assumed that the system state as known, so that also the contact state at time t_0 is given. Let there be a total of I contact zones $\partial\tilde{\mathcal{B}}_{ci}$, $i \in \{1, \dots, I\}$ at time t_0 and consider e.g. the i -th contact zone $\partial\tilde{\mathcal{B}}_{ci}$, as illustrated in Fig. 2.5. Additionally, it is assumed that three subzones exist at time t_0 with one sticking contact subzone, $\tilde{\mathcal{B}}_{ci}^{stick_2}$, and two slipping contact subzones, $\tilde{\mathcal{B}}_{ci}^{slip_1}$, $\tilde{\mathcal{B}}_{ci}^{slip_3}$. At time $t > t_0$ it must be checked whether new contact zones occur, $\partial\tilde{\mathcal{B}}_{c(I+1)}$, or old ones grow, shrink or disappear. The switching conditions for normal contact between stator and rotor are:

Figure 2.5: Example of a contact zone, \mathcal{B}_{ci} , between stator and rotor

$$\begin{array}{lll}
 \text{contact:} & \tilde{g}_N = 0 \quad \wedge \quad \tilde{T}_N < 0 & \forall \hat{\mathbf{Y}}_r \in \partial\tilde{\mathcal{B}}_{ci}(t_0) \\
 \Downarrow & & \Downarrow \\
 \text{switching condition:} & \text{check whether for } t > t_0 & \exists \hat{\mathbf{Y}}_r \in \partial\tilde{\mathcal{B}}_{ci}(t_0) \\
 & & \text{with } \boxed{\tilde{T}_N(\hat{\mathbf{Y}}_r, t) = 0} \\
 \Downarrow & & \Downarrow \\
 \text{no contact:} & \tilde{g}_N > 0 \quad \wedge \quad \tilde{T}_N = 0 & \forall \hat{\mathbf{Y}}_r \in \partial\tilde{\mathcal{B}}_{ci}(t_0) \setminus \partial\tilde{\mathcal{B}}_{ci}(t) .
 \end{array}$$

Here $\tilde{g}_N = 0$ is a constraint equation which has to be released ($\tilde{g}_N > 0$) for all contact points at which the switching condition $\tilde{T}_N = 0$ (see the box), holds. The reverse switching condition, as stated below, indicates if two surface points come into contact at time $t > t_0$:

$$\begin{array}{lll}
 \text{no contact:} & \tilde{g}_N > 0 \quad \wedge \quad \tilde{T}_N = 0 & \forall \hat{\mathbf{Y}}_r \in \partial\tilde{\mathcal{B}}_r \setminus \cup_{i=1}^I \partial\tilde{\mathcal{B}}_{ci}(t_0) \\
 \Downarrow & & \Downarrow \\
 \text{switching condition:} & \text{check whether for } t > t_0 & \exists \hat{\mathbf{Y}}_r \in \partial\tilde{\mathcal{B}}_r \setminus \cup_{i=1}^I \partial\tilde{\mathcal{B}}_{ci}(t_0) \\
 & & \text{with } \boxed{\tilde{g}_N(\hat{\mathbf{Y}}_r, t) = 0} \\
 \Downarrow & & \Downarrow \\
 \text{contact:} & \tilde{g}_N = 0 \quad \wedge \quad \tilde{T}_N < 0 & \forall \hat{\mathbf{Y}}_r \in \cup_{i=1}^{I+J} \partial\tilde{\mathcal{B}}_{ci}(t) ,
 \end{array}$$

for J new contact zones emerging at $t > t_0$. Different contact states, with alternating stick and slip subzones may occur in each contact zone. To account for a change from stick to slip states between two contact surface points, the tangential stress $|\tilde{T}_T|$ has to reach the sliding friction stress $\mu \tilde{T}_N$. The procedure to detect a change of tangential contact states can therefore be written as:

$$\begin{array}{ll}
\text{stick:} & \dot{\tilde{g}}_T = 0 \quad \wedge \quad |\tilde{T}_T| < \mu \tilde{T}_N \quad \forall \hat{\mathbf{Y}}_r \in \partial \tilde{\mathcal{B}}_{ci}^{stick_j}(t_0) \\
\downarrow & \downarrow \\
\text{switching:} & \text{check whether for } t > t_0 \quad \exists \hat{\mathbf{Y}}_r \in \partial \tilde{\mathcal{B}}_{ci}^{stick_j}(t_0) \\
\text{condition} & \text{with } \boxed{|\tilde{T}_T| - \mu \tilde{T}_N = 0} \\
\downarrow & \downarrow \\
\text{slip:} & \dot{\tilde{g}}_T \neq 0 \quad \wedge \quad |\tilde{T}_T| = \mu \tilde{T}_N \quad \forall \hat{\mathbf{Y}}_r \in \partial \tilde{\mathcal{B}}_{ci}^{stick_j}(t_0) \setminus \partial \tilde{\mathcal{B}}_{ci}^{stick_j}(t)
\end{array}$$

In a similar manner, the reverse formulation indicating the transition from slip to stick, can be stated as follows:

$$\begin{array}{ll}
\text{slip:} & \dot{\tilde{g}}_T \neq 0 \quad \wedge \quad |\tilde{T}_T| = \mu \tilde{T}_n \quad \forall \hat{\mathbf{Y}}_r \in \partial \tilde{\mathcal{B}}_{ci}^{slip_j}(t_0) \\
\downarrow & \downarrow \\
\text{switching:} & \text{check whether for } t > t_0 \quad \exists \hat{\mathbf{Y}}_r \in \partial \tilde{\mathcal{B}}_{ci}^{slip_j}(t_0) \\
\text{condition} & \text{with } \boxed{\dot{\tilde{g}}_T(\hat{\mathbf{Y}}_r, t) = 0} \\
\downarrow & \downarrow \\
\text{stick:} & \dot{\tilde{g}}_T = 0 \quad \wedge \quad |\tilde{T}_T| < \mu \tilde{T}_n; \quad \forall \hat{\mathbf{Y}}_r \in \partial \tilde{\mathcal{B}}_{ci}^{slip_j}(t_0) \setminus \partial \tilde{\mathcal{B}}_{ci}^{slip_j}(t)
\end{array}$$

As mentioned above, frictional problems are evolutionary, the state at time t follows from the history of frictional states beginning at time t_0 . To solve a contact problem at hand, an initial contact configuration must be known (e.g. if the motor is at rest, there is contact over the complete stator surface) and the contact algorithm needs to keep track of kinematic ($\dot{\tilde{g}}_N = 0$, $\dot{\tilde{g}}_T = 0$) and dynamic ($\tilde{T}_N = 0$, $|\tilde{T}_T| - \mu \tilde{T}_N = 0$) switching conditions of stick-slip and contact forces. At each time increment Δt the switching conditions have to be checked and contact constraints have to be set or released. Therefore, a numerical *contact search algorithm* for the stator-rotor contact is needed. Such an algorithm must determine unknown contact zones, $\partial \tilde{\mathcal{B}}_{ci}$, and unknown contact subzones, $\partial \tilde{\mathcal{B}}_{ci}^{stick}$, $\partial \tilde{\mathcal{B}}_{ci}^{slip}$, as well as temporal changes in the contact zones.

2.4 Dynamics

The principle of virtual power is used to derive the equations of motion of USMs. It provides an easy way to account on one hand for special kinematic fields, such as BERNOULLI-EULER kinematics or the kinematics of the friction layer. On the other hand the electromechanical boundary conditions are obtained as a by-product without additional effort. Starting from the local balance laws and the appropriate boundary conditions of the quasi-electrostatic approximation of VOIGT's theory of linear piezoelectricity, the principle of virtual power for electromechanical systems is formulated, incorporating mechanical contact contributions. The boundary value problem is stated in Section 2.4.1 and in Section 2.4.2 the principle of virtual power is given.

2.4.1 Problem statement in local form

Without loss of generality the equations of the quasi-electrostatic approximation of VOIGT's theory of linear piezoelectricity (see MAUGIN (1988, [13], p.218)) for the description in the material framework and pp. 222 for the linear theory) are written in coordinates of the moving reference frame $(\tilde{O}, \tilde{\mathbf{E}}_1, \tilde{\mathbf{E}}_2, \tilde{\mathbf{E}}_3)$ (see Figure 2.3). When using different (inertial) reference frames it is necessary to distinguish between the reference frame a variable is described in and the reference frame a variable's derivative is derived with respect to (see Section 2.2.5). The independent variables (\mathbf{Y}, t) in the field description will be dropped in the remainder of this section. The three balance laws used in modeling ultrasonic motors are the balance of momentum (see BECKER & BÜRGER (1975, [2]))

$$\rho \dot{\tilde{\mathbf{v}}} = \text{Div } \tilde{\mathbf{T}}, \quad \mathbf{Y} \in \tilde{\mathcal{B}}, \quad (2.47)$$

the balance of charges, referred also as COULOMB's law (see JACKSON (1975, [26] pp. 14 and 218))

$$\text{Div } \tilde{\mathbf{D}} = \tilde{\rho}_{free} \equiv 0, \quad \mathbf{Y} \in \tilde{\mathcal{B}}_{sp}. \quad (2.48)$$

where $\tilde{\mathbf{D}}$ is the electric displacement in C/mm² and $\tilde{\rho}_{free}$ in C/mm³ is the charge density of the free charges which is equal to zero in an ideal dielectric media and the continuity law for free charges and currents (see JACKSON (1975, [26] p. 218))

$$\text{Div } \mathbf{J} + \frac{\partial \rho_{free}}{\partial t} = 0, \quad (2.49)$$

with the electric current density \mathbf{J} of free charges in C/(s mm²). Equation (2.49) is written with respect to the inertial reference frame (without tilde) since the electric current, needed to calculate the input electric power, is determined by appropriate surface integration over the electrodes, which are fixed in the inertial reference frame. The usage of (2.49) is explained in detail in Section 2.6.2.

REMARK: The electromagnetical balance laws are written in the rationalized MKSA (meter, kilogram, seconds, ampere) system (see JACKSON (1975, [26] p. 818)). The electric displacement is a calculative quantity, representing an abbreviation of $\tilde{\mathbf{D}} := \epsilon_0 \tilde{\mathbf{E}} + \tilde{\mathbf{P}} + \dots$, where ϵ_0 is the dielectric constant in a vacuum and $\tilde{\mathbf{P}}$ is the polarization vector, describing the macroscopically averaged effect of electric field induced separation (displacement) of the centers of positive and negative charges in a crystal lattice. This effect is also called the electric dipole effect. Higher order electric effects, such as electric quadrupoles, are completely negligible in most materials (see JACKSON (1975, [26], p.232)). Thus, $\tilde{\mathbf{D}} := \epsilon_0 \tilde{\mathbf{E}} + \tilde{\mathbf{P}}$ is in excellent agreement with physics for almost all materials. Note that in the microscopic description of MAXWELL's equations, i.e.

without an spatial averaging process, all charges are considered individually. In such a description, no electric displacement and polarization vector occurs. The only fields are then the microscopic electric field, magnetic field, volume charge distribution and electric current density. As a result of the spatial averaging process, "molecules can be viewed as a collection of point multipoles located at one fixed point in the molecule". By this averaging process, the polarization vector is introduced. And, for the sake of simplicity in the representation of the formulas and description of charge boundary conditions (i.e. $\mathbf{D} \mathbf{n} = -\sigma$, where σ is the surface charge density) a mathematical quantity, the electric displacement \mathbf{D} , is defined as stated above. The derivation of the macroscopic MAXWELL equations from the microscopic equations can be found in JACKSON (1975, [26], pp. 226).

Material laws can be formulated either using the polarization vector, as $\tilde{\mathbf{P}}(\tilde{\mathbf{E}})$ for example, or the electric displacement $\tilde{\mathbf{D}}(\tilde{\mathbf{E}})$. It is also clear that inverse laws, like $\tilde{\mathbf{E}}(\tilde{\mathbf{D}})$, can be formulated. Due to the reasons stated above, it is common to describe the material laws as relations between electric displacement and electric field.

The strain-displacement relation (2.17) and the electric field-potential relation for quasi-static electric fields can be written as

$$\tilde{\mathbf{S}} = \frac{1}{2} \left[\text{Grad } \tilde{\mathbf{u}} + \text{Grad}^T \tilde{\mathbf{u}} \right], \quad \mathbf{Y} \in \tilde{\mathcal{B}} \quad (2.50)$$

$$\tilde{\mathbf{E}} = -\text{Grad } \tilde{\Phi}, \quad \mathbf{Y} \in \tilde{\mathcal{B}}_{sp}. \quad (2.51)$$

Two types of mechanical boundary conditions may exist. Let the displacement be specified on section $\partial\mathcal{B}_u$, while surface tractions are specified on $\partial\mathcal{B}_T$:

$$\tilde{\mathbf{u}} = \hat{\tilde{\mathbf{u}}}, \quad \mathbf{Y} \in \partial\tilde{\mathcal{B}}_u, \quad (2.52)$$

$$\tilde{\mathbf{T}} \cdot \hat{\tilde{\mathbf{n}}} = \hat{\tilde{\mathbf{T}}}, \quad \mathbf{Y} \in \partial\tilde{\mathcal{B}}_T. \quad (2.53)$$

The prescribed quantities are the stress vector $\hat{\tilde{\mathbf{T}}}$ and the displacement $\hat{\tilde{\mathbf{u}}}$. The vector $\hat{\tilde{\mathbf{n}}}$ is the outer normal vector of the surface considered. Due to the nature of the contact problem at hand, intermediate conditions between stator and rotor/slider have been formulated in Section 2.3.2, (2.45), (2.46), and (2.44), which will be stated again here:

$$\begin{aligned} \hat{\tilde{\mathbf{T}}}^r &= -\hat{\tilde{\mathbf{T}}}^{s*}, & \mathbf{Y} \in \partial\tilde{\mathcal{B}}_{ci}, \\ \hat{g}_N &= 0, & \mathbf{Y} \in \partial\tilde{\mathcal{B}}_{ci}, & i \in \{1, \dots, I\}, \\ \hat{g}_T &= 0, & \mathbf{Y} \in \partial\tilde{\mathcal{B}}_{ci}^{stick}, & i \in \{1, \dots, I\}. \end{aligned} \quad (2.54)$$

The surface of the piezoceramic is covered by electrodes and the electric potential is specified by

$$\tilde{\Phi} = \hat{\tilde{\Phi}}, \quad \mathbf{Y} \in \partial\tilde{\mathcal{B}}_{\Phi}, \quad (2.55)$$

where the term $\hat{\Phi}$ describes a given time dependent spatial distribution of the electric potential at the surface electrodes, applied to excite vibrations modes in the stator of an USM.

REMARK: It is possible to justify the use of the quasi-electrostatic approximation (2.49) and (2.51) of Maxwell's equations through some simple scaling arguments. The quasi-electrostatic approximation neglects the coupling of the electric and magnetic fields, $\tilde{\mathbf{E}}$ and $\tilde{\mathbf{B}}$, respectively, and considers this coupling as a second order effect. One line of argument to neglect the electromagnetic coupling in many piezoceramic applications is based on the comparison of the wavelength λ_{em} of electromagnetic waves with that of mechanical waves, λ_{mech} , at a common excitation frequency Ω of a specified piezoelectric boundary-value problem. Consider the phase velocity c_0 of electromagnetic waves in vacuum, the phase velocity c_{em} of electromagnetic waves in piezoceramic nondispersive matter and c_{mech} as the phase velocity of mechanical waves in the same matter. The relation $c_0 > c_{em} \gg c_{mech}$ holds and from it follows $k_{em} \ll k_{mech}$ for the wave numbers or $\lambda_{em} \gg \lambda_{mech}$ for the wavelength, respectively. The length L may be used as the characteristic length scale of a motor. Considering mechanical waves of the order $\lambda_{mech}/L \approx 0.1$, it follows that $\lambda_{em}/L \gg 1$. This allows for a quasi-static approximation. For a proof see MAUGIN (1988, [13] p. 235), for example.

Finally, material laws relating stress $\tilde{\mathbf{T}}$ and electric field $\tilde{\mathbf{E}}$ to strain $\tilde{\mathbf{S}}$ and electric displacement $\tilde{\mathbf{D}}$ are required. Since isothermal conditions are assumed in the remainder of the paper, terms involving temperature and entropy are neglected, i.e. the thermodynamical background is ignored. From the modeling point of view, it is more convenient to choose $(\tilde{\mathbf{T}}, \tilde{\mathbf{E}})$ as dependent variables instead of $(\tilde{\mathbf{T}}, \tilde{\mathbf{D}})$ since this simplifies the modeling procedure, as explained in the next section. The relations

$$\tilde{\mathbf{T}}(\tilde{\mathbf{S}}, \tilde{\mathbf{D}}), \quad \tilde{\mathbf{E}}(\tilde{\mathbf{S}}, \tilde{\mathbf{D}}) \quad \mathbf{Y} \in \tilde{\mathcal{B}}_{sp} \quad (2.56)$$

are used for a ceramic material. A simple elastic material law is assumed for the stator and rotor substrate occupying the volumes $\tilde{\mathcal{B}}_s \setminus \tilde{\mathcal{B}}_{sp}, \tilde{\mathcal{B}}_r \setminus \tilde{\mathcal{B}}_{rc}$, respectively

$$\tilde{\mathbf{T}}(\tilde{\mathbf{S}}), \quad \mathbf{Y} \in \left(\tilde{\mathcal{B}}_s \setminus \tilde{\mathcal{B}}_{sp} \right) \cup \left(\tilde{\mathcal{B}}_r \setminus \tilde{\mathcal{B}}_{rc} \right), \quad (2.57)$$

while a visco-elastic material law

$$\tilde{\mathbf{T}}(\tilde{\mathbf{S}}, \dot{\tilde{\mathbf{S}}}), \quad \mathbf{Y} \in \tilde{\mathcal{B}}_{rc} \quad (2.58)$$

is assumed for the rotor contact layer. The detailed forms of the above material laws are specified in Section 2.5. The problem formulation given above contains the four field variables, $\tilde{\mathbf{T}}, \tilde{\mathbf{S}}(\tilde{\mathbf{v}}), \tilde{\mathbf{E}}$ and $\tilde{\mathbf{D}}$. In the next section the principle of virtual power is formulated by choosing the velocity $\tilde{\mathbf{v}}$ and the electric displacement rate $\dot{\tilde{\mathbf{D}}}$ as independent variables.

2.4.2 Principle of virtual power (PvP)

The pairs $(\tilde{\mathbf{T}}, \tilde{\mathbf{v}})$ and $(\tilde{\mathbf{E}}, \dot{\tilde{\mathbf{D}}})$ represent the conjugate field variables of mechanical and electrical power, respectively. A weak form of the local balance laws in Section 2.4.1 is derived in a formal procedure by using the pairs $(\tilde{\mathbf{T}}, \delta\tilde{\mathbf{v}})$ and $(\tilde{\mathbf{E}}, \delta\dot{\tilde{\mathbf{D}}})$. To this end, both, the balance of momentum (2.47) and the electric field-voltage relation (2.51) are multiplied with their virtual counterparts, the virtual velocity $\delta\tilde{\mathbf{v}}$ and virtual electric displacement rate $\delta\dot{\tilde{\mathbf{D}}}$, respectively. Applying the product rule and the GAUSS theorem one gets

$$\mathcal{P}_{inertia} + \mathcal{P}_{inner} + \mathcal{P}_{contact} = \mathcal{P}_{mech} + \mathcal{P}_{elec} \quad (2.59)$$

with

$$\mathcal{P}_{inertia} = \int_{\tilde{\mathcal{B}}} \rho \dot{\tilde{\mathbf{v}}} \cdot \delta\tilde{\mathbf{v}} d\tilde{V}, \quad (2.60)$$

$$\mathcal{P}_{inner} = \int_{\tilde{\mathcal{B}}} \tilde{\mathbf{T}} : \delta\dot{\tilde{\mathbf{S}}} d\tilde{V} + \int_{\tilde{\mathcal{B}}_{sP}} \tilde{\mathbf{E}} \cdot \delta\dot{\tilde{\mathbf{D}}} d\tilde{V}, \quad (2.61)$$

$$\mathcal{P}_{contact} = - \int_{\partial\tilde{\mathcal{B}}_c} \tilde{T}_N \delta\dot{g}_N d\tilde{A} + \int_{\partial\tilde{\mathcal{B}}_c} \tilde{T}_T \delta\dot{g}_T d\tilde{A}, \quad (2.62)$$

$$\mathcal{P}_{mech} = \int_{\partial\tilde{\mathcal{B}}_s} \hat{\mathbf{T}} \cdot \delta\hat{\tilde{\mathbf{v}}} d\tilde{A}, \quad \mathcal{P}_{elec} = \int_{\partial\tilde{\mathcal{B}}_\Phi} \hat{\Phi} \hat{\mathbf{n}} \cdot \delta\dot{\tilde{\mathbf{D}}} d\tilde{A}. \quad (2.63)$$

Equation (2.59) will now be understood as a fundamental principle, the principle of virtual power (PvP).

The term $\tilde{\mathbf{T}} : \delta\dot{\tilde{\mathbf{S}}}$ in the virtual power of the inner mechanical forces, \mathcal{P}_{inner} , is obtained from the equality $\tilde{\mathbf{T}} : \text{Grad} \delta\tilde{\mathbf{v}} = \tilde{\mathbf{T}} : \delta\dot{\tilde{\mathbf{S}}}$, by applying the identity $\tilde{\mathbf{T}} : \text{Grad} \delta\tilde{\mathbf{v}} \equiv \tilde{\mathbf{T}}^T : \text{Grad}^T \delta\tilde{\mathbf{v}}$ and using the symmetry of the stress tensor $\tilde{\mathbf{T}} = \tilde{\mathbf{T}}^T$.

The virtual power of the mechanical forces acting on the stator and the rotor is broken up into the virtual power of the prescribed forces, \mathcal{P}_{mech} , acting upon the stator and into the virtual power of contact forces, $\mathcal{P}_{contact}$, acting between stator and rotor. The virtual power of the contact forces in (2.62) is derived by separating stator and rotor and applying the contact forces at both contact regions:

$$\mathcal{P}_{contact} = \int_{\partial\tilde{\mathcal{B}}_{sc}} \hat{\mathbf{T}}^{s*} \cdot \delta\hat{\tilde{\mathbf{v}}}_s^* d\tilde{A} + \int_{\partial\tilde{\mathcal{B}}_{rc}} \hat{\mathbf{T}}^r \cdot \delta\hat{\tilde{\mathbf{v}}}_r d\tilde{A}. \quad (2.64)$$

Substituting (2.44) and (2.43) into (2.64), rearranging the terms and substituting the virtual velocity terms with (2.38) and (2.41), results in (2.62).

Note that, if contact occurs, $\delta\dot{g}_N = 0$ holds in the contact zone and thus $\dot{g}_N = 0$ establishes a kinematical constraint to be fulfilled. Similarly, if sticking occurs within a contact subzone, $\delta\dot{g}_T = 0$ holds, yielding the tangential constraint condition $\dot{g}_T = 0$. These constraint conditions follow from (2.40) and (2.42).

The relation $\delta\dot{\mathbf{D}} \cdot \tilde{\mathbf{n}} = -\delta\tilde{\sigma}$ holds for the term \mathcal{P}_{elec} , where $\tilde{\sigma}$ is the surface charge density. The minus sign stems from the convention of orientation of electric quantities at system interfaces. The virtual electric displacement rate satisfies $\delta\dot{\mathbf{D}} = \delta\dot{\mathbf{D}}$ as in (2.27).

REMARK: It is possible to formulate other equivalent principles. A principle which is called principle of mixed virtual power, for example, uses the pairs $(\tilde{\mathbf{T}}, \delta\tilde{\mathbf{v}})$ and $(\tilde{\mathbf{D}}, \delta\tilde{\mathbf{E}})$. The term *mixed* indicates that displacement quantities $\delta\tilde{\mathbf{v}}$ and force quantities $\delta\tilde{\mathbf{E}}$ are used as independent variables. The weak form for the mixed PvP is obtained by multiplying the electric field-potential relation (2.51), with the virtual displacement rate, and the balance of charges (2.48) with the virtual electric potential. Some terms change in this mixed PvP and are indicated in Tab. 2.1. Depending on the type of principle, the appropriate material laws have to be used as indicated in the table.

Principle	\mathcal{P}_{inner}	\mathcal{P}_{elec}	Boundary Constraint	Compatibility Conditions	Material Law
PvP	$\int_{\mathcal{B}_{sp}} \left[\tilde{\mathbf{T}} : \delta\dot{\mathbf{S}} + \tilde{\mathbf{E}} \cdot \delta\dot{\mathbf{D}} \right] dV$	$\int_{\partial\mathcal{B}_{0\Phi}} \tilde{\Phi} \tilde{\mathbf{n}} \cdot \delta\dot{\mathbf{D}} dA$	$\dot{\mathbf{D}} \cdot \tilde{\mathbf{n}} = -\tilde{\sigma}, \quad \partial\mathcal{B}_{\sigma}$ $\tilde{\mathbf{u}} = \hat{\mathbf{u}}, \quad \partial\mathcal{B}_{\tilde{\mathbf{u}}}$	$\text{Div } \tilde{D} = 0$ $\text{rot}^T \text{rot } \tilde{\mathbf{u}} = 0$	$\tilde{\mathbf{T}}(\tilde{\mathbf{S}}, \tilde{\mathbf{D}})$ $\mathbf{E}(\tilde{\mathbf{S}}, \tilde{\mathbf{D}})$
Mixed PvP	$\int_{\mathcal{B}_{sp}} \left[\tilde{\mathbf{T}} : \delta\dot{\mathbf{S}} + \tilde{\mathbf{D}} \cdot \delta\tilde{\mathbf{E}} \right] dV$	$\int_{\partial\mathcal{B}_{\sigma}} \dot{\mathbf{D}} \cdot \tilde{\mathbf{n}} \delta\tilde{\Phi} dA$	$\Phi = \hat{\Phi}, \quad \partial\mathcal{B}_{\Phi}$ $\tilde{\mathbf{u}} = \hat{\mathbf{u}}, \quad \partial\mathcal{B}_{\tilde{\mathbf{u}}}$	$\tilde{\mathbf{E}} = -\text{grad } \tilde{\varphi}$ $\text{rot}^T \text{rot } \tilde{\mathbf{u}} = 0$	$\tilde{\mathbf{T}}(\tilde{\mathbf{S}}, \tilde{\mathbf{E}})$ $\mathbf{D}(\tilde{\mathbf{S}}, \tilde{\mathbf{E}})$
Compl. PvP	$\int_{\mathcal{B}_{sp}} \left[\dot{\mathbf{S}} : \delta\mathbf{T} + \dot{\mathbf{D}} \cdot \delta\mathbf{E} \right] dV$	$\int_{\partial\mathcal{B}_{\sigma}} \dot{\mathbf{D}} \cdot \mathbf{n} \delta\Phi dA$	$\Phi = \hat{\Phi}, \quad \partial\mathcal{B}_{\Phi}$ $\tilde{\mathbf{T}} \cdot \tilde{\mathbf{n}} = \hat{\mathbf{T}}, \quad \partial\mathcal{B}_{\tilde{\mathbf{T}}}$	$\tilde{\mathbf{E}} = -\text{grad } \tilde{\varphi}$ $\text{Div } \tilde{\mathbf{T}} = 0$	$\tilde{\mathbf{S}}(\tilde{\mathbf{T}}, \tilde{\mathbf{E}})$ $\mathbf{D}(\tilde{\mathbf{T}}, \tilde{\mathbf{E}})$

Table 2.1: Different forms of the principle of virtual power

There are two fundamental electric boundary conditions, portions $\partial\tilde{\mathcal{B}}_\Phi$ on which the electric potential $\hat{\Phi}$ is specified and portions $\partial\tilde{\mathcal{B}}_\sigma$ on which a surface charge $\tilde{\sigma}$ is specified. In general, boundary conditions may be of a mixed type with electric potential and surface charge interrelated by a load impedance. In ultrasonic motors there exist almost only regions where the electric potential is specified. The sensor electrodes would be regions on which the surface charge is prescribed, because the sensor potential normally is measured with high-impedance circuits and neglectable current. In the case of neglectable currents the surface charge remains constant, while the electric potential will vary. However, the area of the sensor electrodes is small compared to the surface area where the electric potential is prescribed. Therefore, the sensor electrode part in USMs is neglected. If the PvP is applied, the prescribed electric potential enters the principle through the term \mathcal{P}_{elec} in (2.63). On the other hand, if the mixed PvP is applied, the prescribed electric potential has to be considered as a boundary constraint. In structural dynamics, where structural members like beams, plates or shells are used and the polarization is in the thickness direction, the PvP has some advantage over the Mixed PvP. This is due to the fact, that, after carrying out the integration over the thickness of the beam or plate model in the PvP, the specified electric potential enters the PvP as a right-hand side inhomogeneity in the equations of motion, whereas in the Mixed PvP the specified electric potential has to be considered as an additional constraint, or must be incorporated into the principle via LAGRANGE multipliers. Note, that a complementary principle of virtual power can only be formulated in statics and not in dynamics, since the velocity in the inertia term enters the principle as an independent variable.

REMARK: When using the PvP to derive equations of motion, displacement fields must be chosen so as to satisfy exactly, or in a good approximation, the mechanical compatibility condition $\text{rot}^T \text{rot } \tilde{\mathbf{u}} = \mathbf{0}$ and the electric compatibility condition $\text{Div } \tilde{\mathbf{D}} = 0$, see Tab. 2.1.

2.5 Material Laws

2.5.1 Stator and piezoceramic

Stators in ultrasonic motors can be made up completely or partially of ceramics. In the latter, the ceramic is bonded to the metallic stator substrate. Making the stator entirely out of ceramics guarantees high energy density with respect to the motor volume and avoids the bonding of ceramics. However, it also results in higher geometric misalignment due to the special manufacturing process of piezoceramic material. The excitation of a harmonic traveling wave is based on two degenerate eigenmodes and this requires

good geometric alignment. For a metallic stator substrate, HOOKE's law

$$\mathbf{T} = \mathbf{c}_s : \mathbf{S} \quad \Leftrightarrow \quad T_{ij} = c_{ijkl} S_{kl} \quad (2.65)$$

is used with the stiffness coefficients

$$c_{ijkl} = \frac{E_s}{1 + \nu_s} \left(\delta_{ik} \delta_{jl} + \frac{\nu_s}{1 - 2\nu_s} \delta_{ij} \delta_{mk} \delta_{ml} \right), \quad (2.66)$$

where δ_{ij} is the Kroneker symbol and E_s and ν_s are Young's modulus and Poisson ratio, respectively. For a piezoceramic material in the linear range of application one of several representations described in literature, e.g. IKEDA (1990, [24] p. 16), is

$$\begin{aligned} \mathbf{T} &= \mathbf{c}^D : \mathbf{S} - (\mathbf{h})^T \cdot \mathbf{D} & \Leftrightarrow & \quad T_{ij} = c_{ijkl}^D S_{kl} - h_{mij} D_m \\ \mathbf{E} &= \mathbf{h} : \mathbf{S} + \beta^S \cdot \mathbf{D} & \Leftrightarrow & \quad E_i = -h_{ikl} S_{kl} + \beta_{ij}^S D_j \end{aligned} \quad (2.67)$$

with the coefficients for the stiffness, electromechanical coupling and the dielectric impermeability, respectively (see GHANDI (1997, [14]))

$$\begin{aligned} c_{ijkl} &= (\delta_{kl} c_3 + 2a_k a_l c_5) a_i a_j + (2\delta_{kl} c_1 + a_k a_l c_3) \delta_{ij} + 2c_2 \delta_{il} \delta_{jk} \\ &\quad + c_4 (\delta_{il} a_k a_j + \delta_{jk} a_l a_i), \\ h_{mij} &= h_1 (\delta_{mi} a_j + \delta_{mj} a_i) + (\delta_{ij} h_2 + a_i a_j h_3) a_m, \\ \beta_{ij} &= b_1 \delta_{ij} + 2b_2 a_i a_j. \end{aligned} \quad (2.68)$$

The above illustrates a material law for a linear planar isotropic piezoelectric ceramic with 10 different material constants. The scalar constants c_1, \dots, c_5 , are related to the material stiffness, h_1, h_2, h_3 and b_1, b_2 are related to the electromechanical coupling and the material dielectric properties, respectively. The coefficient $a_i \equiv \delta_{ri}$ indicates the direction r of polarization in the ceramics. The superscript \mathbf{D} and \mathbf{S} in (2.67) indicate material constants measured at constant electric displacement D or constant strain S . A so-called engineering notation is often used in the literature (IEEE STANDARD (1987, [1]), MAUGIN (1988, [13])), which makes use of symmetry properties of the material coefficients of piezoelectric ceramics leading to a compressed notation:

ij or kl	p or q		
11	→	1	$T_{ij} \rightarrow T_p$
22	→	2	
33	→	3	$S_{ij} \rightarrow S_p$ for $i = j, p=1,2,3$
23 or 32	→	4	
31 or 13	→	5	$2S_{ij} \rightarrow S_p$ for $i \neq j, p=1,2,3$.
12 or 21	→	6	

Now, the constitutive equations (2.67) with (2.68) can be written in short form

$$\begin{aligned}
T_p &= c_{pq}^D S_q - h_{kp} D_k, \\
E_i &= -h_{ip} S_p + \beta_{ik}^S D_k,
\end{aligned} \tag{2.69}$$

where c_{pq}^D , h_{kp} and β_{ik}^S are the standard piezoelectric constants found in the literature and in published data sheets of measured material properties. In matrix notation the short form representation (2.69) of piezoelectric ceramics, which have transversal isotropy with respect to the polarization axis is

$$\begin{bmatrix} T_1 \\ T_2 \\ T_3 \\ T_4 \\ T_5 \\ T_6 \end{bmatrix} = \begin{bmatrix} c_{11}^D & c_{12}^D & c_{13}^D & 0 & 0 & 0 \\ c_{12}^D & c_{11}^D & c_{13}^D & 0 & 0 & 0 \\ c_{13}^D & c_{13}^D & c_{33}^D & 0 & 0 & 0 \\ 0 & 0 & 0 & c_{44}^D & 0 & 0 \\ 0 & 0 & 0 & 0 & c_{44}^D & 0 \\ 0 & 0 & 0 & 0 & 0 & c_{66}^D \end{bmatrix} \begin{bmatrix} S_1 \\ S_2 \\ S_3 \\ S_4 \\ S_5 \\ S_6 \end{bmatrix} + \begin{bmatrix} 0 & 0 & h_{31} \\ 0 & 0 & h_{31} \\ 0 & 0 & h_{33} \\ 0 & h_{15} & 0 \\ h_{15} & 0 & 0 \\ 0 & 0 & 0 \end{bmatrix} \begin{bmatrix} D_1 \\ D_2 \\ D_3 \end{bmatrix} \tag{2.70}$$

with $c_{66}^D = \frac{1}{2}(c_{11}^D - c_{12}^D)$ and

$$\begin{bmatrix} E_1 \\ E_2 \\ E_3 \end{bmatrix} = \begin{bmatrix} 0 & 0 & 0 & 0 & h_{15} & 0 \\ 0 & 0 & 0 & h_{15} & 0 & 0 \\ h_{31} & h_{31} & h_{33} & 0 & 0 & 0 \end{bmatrix} \begin{bmatrix} S_1 \\ S_2 \\ S_3 \\ S_4 \\ S_5 \\ S_6 \end{bmatrix} + \begin{bmatrix} \beta_{11}^S & 0 & 0 \\ 0 & \beta_{11}^S & 0 \\ 0 & 0 & \beta_{33}^S \end{bmatrix} \begin{bmatrix} D_1 \\ D_2 \\ D_3 \end{bmatrix} \tag{2.71}$$

As a convention in engineering notation the Z- or 3-axis is used as the polarization axis, giving $a_i = \delta_{3i}$.

REMARK: The linear material laws (2.67) with (2.68) and (2.69) are valid only in the vicinity of the remanent polarization P_r , depicted in Fig. 2.6. Using for example the strain $\tilde{\mathbf{S}}$ and the electric field $\tilde{\mathbf{E}}$ as independent variables, the polarization $\tilde{\mathbf{P}}(\tilde{\mathbf{E}}, \tilde{\mathbf{S}})$ follows and it is clear that both, strain and electric field, must be low enough for a linear material law to hold.

REMARK: Piezoelectric ceramics, often called piezoceramics, are made up of isotropic ferroelectric ceramics by means of a polarization procedure using a strong electric field (UCHINO (1997, [56] pp. 51)). The bulk isotropic ferroelectric ceramic possesses no net piezoelectric property in the vicinity of the unloaded state, since the grains and the domains in the material are randomly oriented, so that the crystals produce no net macroscopic polarization. Depending on the temperature, the proportion of Zr and

Ti in the ceramics and the contamination with other atoms the randomly oriented grains in the ferroelectric belong to different crystal systems and crystal classes (e.g. tetragonal, rhombohedral). Exerting a strong homogeneous external electric field aligns the microscopic polarization in the direction of the external field due to the rearrangement of the domain walls within the grains. A macroscopic polarization of the isotropic ferroelectric ceramics occurs. If the strong electric field is removed, a remnant polarization is kept and a transversely isotropic piezoelectric ceramic material is obtained, where the axis of net polarization is perpendicular to the plane of isotropy. The bulk material has a material law equivalent to that of a single hexagonal crystal of the crystal class $6mm$ (see NYE (1985 [38], pp. 295) for the classification of crystals). Each piezoceramic material possesses this special material behavior but note that this is only a macroscopic equivalence. The crystals in the piezoceramic material are not of the crystal class $6mm$!

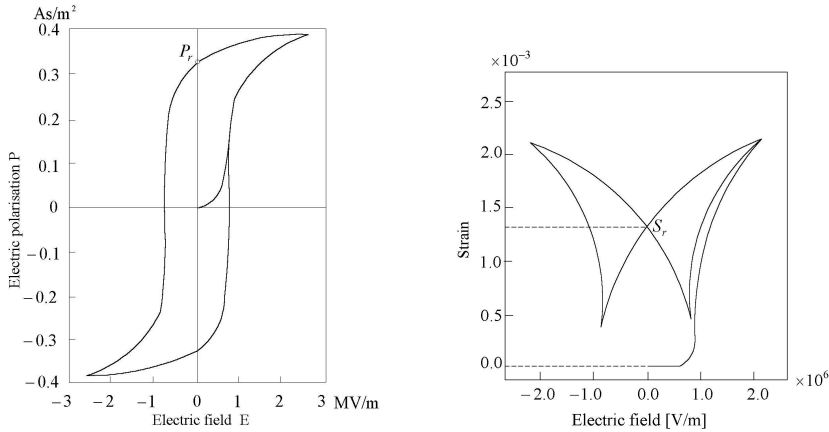


Figure 2.6: Response of an initially unpoled piezoceramic material to a cyclic electric field

2.5.2 Rotor and contact layer

For the rotor HOOKE's law is used

$$\mathbf{T} = \mathbf{c}_r : \mathbf{S} \quad \Leftrightarrow \quad T_{ij} = c_{ijkl} S_{kl} \quad (2.72)$$

and, for the sake of simplicity, the contact layer bonded to the rotor as shown in Fig. 1.2 is modeled by assuming a linear visco-elastic material law of the Kelvin-Voigt type

(see Eq.(2.58))

$$\mathbf{T} = \mathbf{c}_{rc} : (\mathbf{S} + \vartheta_{rc} \dot{\mathbf{S}}) \quad \Leftrightarrow \quad T_{ij} = c_{ijkl} (S_{kl} + \vartheta_{rc} \dot{S}_{kl}) \quad (2.73)$$

with the stiffness coefficients

$$c_{ijkl} = \frac{E_{rc}}{1 + \nu_{rc}} \left(\delta_{ik} \delta_{jl} + \frac{\nu_{rc}}{1 - 2\nu_{rc}} \delta_{ij} \delta_{mk} \delta_{ml} \right) \quad (2.74)$$

and the viscous damping ϑ_{rc} term. In ultrasonic motors a special contact material between stator and rotor is often used to increase the maximum output torque to prevent unwanted noise or to improve the efficiency of energy conversion between stator and rotor. Several experimental investigations, as for example in REHBEIN & WALLASCHEK (1998, [42]), have been conducted with different polymers. UEHA *et al.* (1993, [57] pp. 288) cite some data pertaining to the dynamic elastic modulus E_{rc} , the tangent loss coefficient $\tan \delta_{rc}$, measured at a frequency of 50 kHz and the friction coefficient μ , of various polymers which have been tested in a Shinsei ultrasonic motor. Next the loss tangent $\tan \delta_{rc}$ has to be related to the viscous damping coefficient ϑ_{rc} . For a one-dimensional material model (2.73) can be reduced to

$$\begin{aligned} T_{11} &= E_{rc} S_{11} + \vartheta_{rc} E_{rc} \dot{S}_{11} , & S_{11} &= \hat{S}_{11} e^{j\Omega t} \\ &\Rightarrow \hat{T}_{11} &= E_{rc} (1 + j\vartheta_{rc} \Omega) \hat{S}_{11} \end{aligned} \quad (2.75)$$

and the loss tangent follows from

$$\tan \delta_{rc} = \vartheta_{rc} \Omega . \quad (2.76)$$

2.6 Electric current, voltage, admittance, power and efficiency

In this section the definitions of the electric quantities needed for a complete motor model are given. In a first step, we consider appropriated electrode patterns for the excitation of the bending modes in the stator. Most ultrasonic motors have a two-phase excitation (see UEHA *et al.* (1993, [57])) and only those are considered here. Two types of electrodes on the piezoceramic surface are distinguished, actor electrodes A , B , delivering the electric energy to the piezoceramic material and a sensor electrode S , measuring the voltages due to the deformation of the piezoceramic material, as shown in Fig. 2.7 (see also Fig. 1.10 for the electrode configuration of the Shinsei motor). Electrodes are thin metallic layers on the piezoceramic material which are assumed to have a neglectible thickness and behave as ideal conductors. They are therefore modeled as material discontinuities at the piezoceramic surfaces.

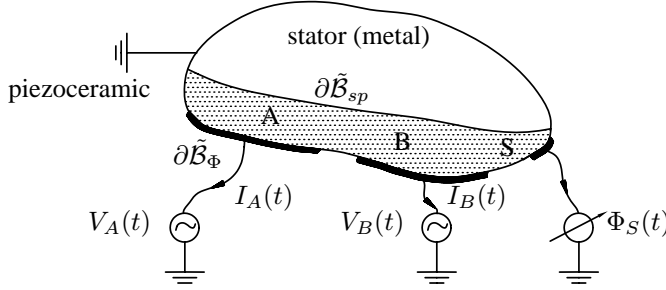


Figure 2.7: Schematic representation of the stator with actor electrodes A , B and sensor electrode S , electroded surface $\partial\mathcal{B}_\Phi$ and stator substrate surface $\partial\mathcal{B}_{sp}$

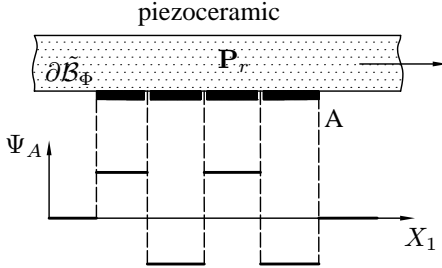


Figure 2.8: Electrode A , grouped, with spatial variation of electric potential shape function Ψ_A . See also Fig. 1.9 and Fig. 1.10

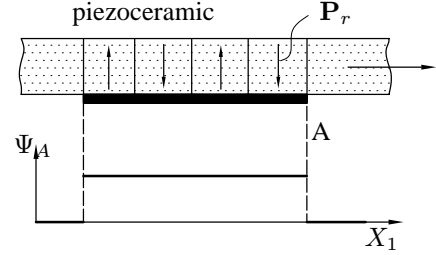


Figure 2.9: Electrode A with spatial homogenous electric potential shape function Ψ_A . See also Fig. 1.9 and Fig. 1.10

2.6.1 Electric excitation

The electric excitation may be realized in two different ways. Either by using a homogeneous polarized ceramic and grouped electrodes as depicted in Fig. 2.8 or by means of an alternating polarized ceramic with one electrode, as illustrated in Fig. 2.9. Both possibilities can be regarded as equivalent in their net effect of exciting particular eigenmodes in the stator. Thus, from the modeling point of view the former possibility seems to be more attractive since it is easier to implement. The potential $\hat{\Phi}$ at the electrode boundary $\partial\mathcal{B}_\Phi$ requires shape functions Ψ to take the spatial variation into account, as shown in Fig. 2.8. For a two-phase excitation, the electric potential at the electrode surface is described by

$$\hat{\Phi}(\mathbf{X}, t) = \Psi_A(X_1) V_A(t) + \Psi_B(X_1) V_B(t), \quad \mathbf{X} \in \partial\mathcal{B}_\Phi \quad (2.77)$$

with the electric voltages V_A and V_B and the potential shape functions Ψ_A and Ψ_B .

Ultrasonic motors are excited usually either by sinusoidal voltages or, for the sake of simplicity in the design of the power electronics, by rectangular voltages. To this end, the voltages may be described as

$$V_A(t) = \sum_{i=1}^{\infty} \hat{V}_{Ai} \sin i\Omega t, \quad V_B(t) = \sum_{i=1}^{\infty} \hat{V}_{Bi} \cos(i\Omega t + \Delta\phi_V), \quad (2.78)$$

with the fundamental circular frequency Ω as the excitation frequency of the motor and $\Delta\phi_V$ as the phase between the time signals, respectively.

The potential shape function for electrode A according to Fig. 2.8 can be expressed in terms of a Fourier expansion

$$\Psi_A(X_1) = \sum_{m=1}^{\infty} [\Psi_{ASm} \sin mkX_1 + \Psi_{ACm} \cos mkX_1], \quad k = \frac{2\pi}{L}, \quad (2.79)$$

with the fundamental wave number k of the spatial discretization and length L corresponding to the outer circumferential length of the stator, for example. A similar expression holds for electrode B .

The electric voltage is the input signal and the electric current the output signal. The electric current signals may have a different fundamental frequency ω and a phase difference α to the electric voltage signals, since USM are highly nonlinear dynamical systems eventually providing subharmonic responses in the current signal. Therefore, if a steady state motor operation is assumed, the current signals are of the type

$$I_A(t) = \sum_{j=1}^{\infty} \hat{I}_{Aj} \sin(j\Omega t + \alpha_{Aj}), \quad I_B(t) = \sum_{j=1}^{\infty} \hat{I}_{Bj} \cos(j\Omega t + \alpha_{Bj}). \quad (2.80)$$

Nevertheless, the current signals I_A, I_B contain the circular frequency component Ω . Assuming $p\omega = \Omega$ for the p -th component of the Fourier series in (2.80), the current signals therefore contain $p - 1$ subharmonic oscillation components. The number p has to be calculated after solving the steady-state problem for the motor.

For the description of the electric potential $\hat{\Phi}$ on the electrodes the voltages (2.78) and the electric shape functions (2.79) are inserted into the equation (2.77) for the electrode surface. All terms causing excitation of undesired modes may be lumped in a term $R(X_1, t)$, leading to the abbreviated form of electric potential

$$\begin{aligned} \hat{\Phi}(\mathbf{X}, t) = & \Psi_{ASn_s} \hat{V}_{A1} \sin n_s k X_1 \sin \Omega t \\ & + \Psi_{BCn_s} \hat{V}_{B1} \cos n_s k X_1 \cos(\Omega t + \Delta\phi_V) + R(X_1, t), \end{aligned} \quad (2.81)$$

where $\sin n_s k X_1$ and $\cos n_s k X_1$ in the first two terms represent the two orthogonal eigenmodes of the stator in which the motor is driven near resonance, n_s being the

number of nodal diameters. Note that $R(X_1, t)$ describes all of the undesired sub- and superharmonic excitations caused by both non-harmonic electric voltages $V_A(t)$ and $V_B(t)$ and rectangular electric shape functions Ψ_A, Ψ_B , respectively (see Fig. 2.8). In the case of an excitation frequency in the vicinity of a motor resonance (see Fig. 1.12), the forced vibrations in the stator due to the sub- and superharmonic terms in $R(X_1, t)$ can be neglected, in a first approximation. For the sake of simplicity it is set $\Psi_{ASn_s} = \Psi_{BCn_s} = 1$, without restricting the model derivation and model analysis. Equation (2.81) results in

$$\hat{\Phi}(\mathbf{X}, t) = \hat{V}_{A1} \sin n_s k X_1 \sin \Omega t + \hat{V}_{B1} \cos n_s k X_1 \cos(\Omega t + \Delta\phi_V). \quad (2.82)$$

Rearranging the terms in (2.82) and using trigonometric identities yields

$$\begin{aligned} \hat{\Phi}(\mathbf{X}, t) &= \hat{V}_{A1} \cos(n_s k X_1 - \Omega t) \\ &+ \left[\hat{V}_{B1} \cos(\Omega t + \Delta\phi_V) - \hat{V}_{A1} \cos(\Omega t) \right] \cos(n_s k X_1). \end{aligned} \quad (2.83)$$

For an electric excitation $\hat{\Phi}(\mathbf{X}, t)$ of a harmonic traveling wave $\hat{V}_{A1} = \hat{V}_{B1}$ and $\Delta\phi_V = 0^\circ$ or $\Delta\phi_V = 180^\circ$ is chosen, depending on the direction of operation of the rotor

$$\hat{\Phi}(\mathbf{X}, t) = \hat{V}_{A1} \cos(n_s k X_1 \mp \Omega t). \quad (2.84)$$

Setting $\hat{V}_{A1} = \hat{V}_{B1}$ and $\Delta\phi_V = 90^\circ$ results in the standing wave

$$\hat{\Phi}(\mathbf{X}, t) = \hat{V}_{A1} [\sin(n_s k X_1) + \cos(n_s k X_1)] \sin(\Omega t). \quad (2.85)$$

The motor has four electric input quantities, namely the excitation frequency Ω , the voltage amplitudes $\hat{V}_{A1}, \hat{V}_{B1}$ and the phase $\Delta\phi_V$ between the voltage signals.

To substitute for the coordinates of the moving reference frame the transformation rule (2.11) is inserted into (2.83). Choosing b_1 appropriately yields

$$\boxed{\hat{\Phi}(\mathbf{Y}, t) = \hat{V}_{A1} \cos(nkY_1) + \left[\hat{V}_{B1} \cos(\Omega t + \Delta\phi_V) - \hat{V}_{A1} \cos(\Omega t) \right] \cdot \cos(n_s k(Y_1 - b_1(t)))} \quad (2.86)$$

with

$$b_1(t) := v_w t = \frac{\Omega}{n_s k} t, \quad (2.87)$$

where Y_1 is a coordinate of the moving reference frame ($\tilde{O}, \tilde{\mathbf{E}}_1, \tilde{\mathbf{E}}_2, \tilde{\mathbf{E}}_3$). Under the excitation conditions $\hat{V}_{A1} = \hat{V}_{B1}$ and $\Delta\phi_V = 0$, (2.86) takes the form

$$\hat{\Phi}(\mathbf{Y}, t) = \hat{V}_{A1} \cos(nkY_1). \quad (2.88)$$

One may wonder where the excitation frequency comes into play. This becomes clear from the time derivatives of the displacements in (2.22) and (2.23), which contain not only the vector \mathbf{b} but also its derivatives. The excitation frequency therefore enters the problem via the field variables.

2.6.2 Electric current to the actor electrodes

To derive an expression for the electric current, the balance of charges, Eq. (2.48) in the inertial reference representation (without tilde), is substituted into the continuity law of charges and current (2.49), yielding the local and global forms of KIRCHHOFF's law:

$$\text{Div}(\mathbf{J} + \dot{\mathbf{D}}) = 0 \quad \Leftrightarrow \quad \oint_{\partial\mathcal{B}_{\Phi}} [\mathbf{J} + \dot{\mathbf{D}}] d\mathbf{A} = 0. \quad (2.89)$$

The electric current at the electrodes A, B, S is defined according to

$$I_i(t) := \oint_{\partial\mathcal{B}_{\Phi_i}} \mathbf{J}(\mathbf{X}, t) d\mathbf{A}, \quad i = A, B, S, \quad (2.90)$$

with the closed surfaces $\partial\mathcal{B}_{\Phi_{A,B,S}}$ around the electrodes A, B and S as indicated in Fig. 2.10. Using (2.89) and (2.90) the electric current may be expressed as

$$I_A = - \oint_{\partial\mathcal{B}_{\Phi_A}} \dot{\mathbf{D}} d\mathbf{A} \approx - \int_{\partial\mathcal{B}_{\Phi_{Ae}}} \dot{\mathbf{D}} d\mathbf{A} - \int_{\partial\mathcal{B}_{\Phi_{Ap}}} \dot{\mathbf{D}} d\mathbf{A} \quad (2.91)$$

if the side areas are neglected. Since the electric field \mathbf{E}_e in an ideal electrode is zero for

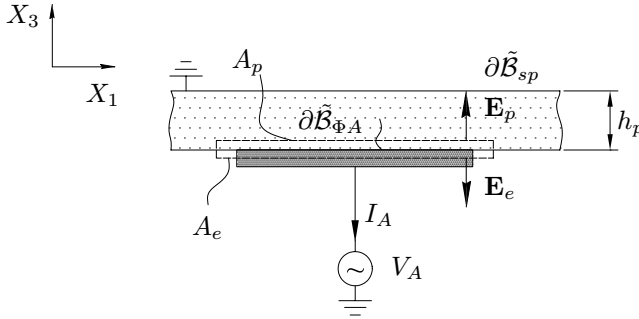


Figure 2.10: Schematic illustration of the electric current calculation at electrode A . $\partial\mathcal{B}_{\Phi_S}$: surface of discontinuity between piezoceramic and electrode, $\partial\mathcal{B}_{\Phi_{sp}}$: surface of discontinuity between piezoceramic and metallic stator substrate.

quasi-electrostatic applications, the term $\int_{\partial\mathcal{B}_{\Phi_{A1}}} \dot{\mathbf{D}} d\mathbf{A}$ is also zero. Thus, the electric current is

$$I_i = - \int_{\partial\mathcal{B}_{\Phi_i}} \dot{\mathbf{D}} d\mathbf{A} \quad i = A, B, S \quad (2.92)$$

with $\partial\mathcal{B}_{\Phi_{Ap}} = \partial\mathcal{B}_{\Phi_i}$.

The contact problem is solved in coordinates of the moving reference frame giving $\tilde{\mathbf{D}}(\mathbf{Y}, t)$ as a result. Therefore, the integral in (2.91) is transformed into a representation with respect to the moving reference frame

$$\boxed{I_i = - \int_{\partial \tilde{\mathcal{B}}_{\Phi_i}(t)} \left[\overset{\circ}{\tilde{\mathbf{D}}} - \text{Grad } \tilde{\mathbf{D}} \cdot \dot{\mathbf{b}} \right] d\tilde{\mathbf{A}} \quad i = A, B, S} \quad . \quad (2.93)$$

Here, the time derivative of the electric displacement is carried out in a manner equivalent to the time derivatives of the displacement (see Eq. (2.22)).

2.6.3 Electric voltage on the sensor electrodes

By measuring the electric potential Φ_S at the sensor electrode with respect to a reference potential, as illustrated in Fig. 2.7, changes in the mechanical state of a piezoceramic structure may be detected. The electric potential Φ_S is measured with a voltage measuring device having a high input resistor, which results in a small current signal I_S ($I_S \ll I_A, I_B$) and a small electric power loss. Thus, in good approximation the current flow to or from the sensor electrode can be neglected. Equation (2.92) yields the integral constraint condition

$$\boxed{0 = - \int_{\partial \mathcal{B}_{\Phi_S}} \dot{\mathbf{D}} \, d\mathbf{A}} \quad . \quad (2.94)$$

The electric potential at the sensor electrodes follows from the solution of the equations of motion under the integral constraint equation (2.94). An expression for the electric potential is obtained from the material law (2.67) and the electric-field potential relation (2.51), which are stated here again:

$$\mathbf{E}_p = \mathbf{h} : \mathbf{S} + \beta^S \cdot \mathbf{D} \quad , \quad \mathbf{E}_p = -\text{Grad } \Phi \quad , \quad (2.95)$$

together with the transition condition at a surface of discontinuity

$$(\mathbf{E}_e - \mathbf{E}_p) \times \mathbf{n} = 0 \quad \text{at} \quad \partial \mathcal{B}_{\Phi_S} \quad .$$

It is distinguished between the electric field in the piezoceramic material and in the electrode by using the symbols \mathbf{E}_e and \mathbf{E}_p , respectively. In (2.96) \mathbf{n} is the surface normal vector. Since the electric field in the electrode is zero, one gets

$$\mathbf{E}_p \times \mathbf{n} = 0 \quad \text{at} \quad \partial \mathcal{B}_{\Phi_S} \quad . \quad (2.96)$$

For an example on how to obtain the electric potential at a sensor electrode assume that the sensor electrode lies in the $X_1 - X_2$ plane. The normal vector is then oriented along the X_3 -direction. Using condition (2.96) gives $E_1 = E_2 = 0$ for the electric field components. The electric field is therefore different from zero at the surface. Equations (2.95) simplify to

$$\begin{aligned} E_{3p} &= -\Phi_{,3} = -h_{3p} S_p + \beta_{33}^S D_3 \\ \Rightarrow \quad \Phi_S(X_1, X_2, X_3, t) &= \int (h_{3p} S_p - \beta_{33}^S D_3) dX_3 + C \end{aligned} \quad (2.97)$$

according to the simple form of the material law (2.69). The known strain fields S_p and electric displacement field D_3 must be integrated with respect to X_3 over the piezoceramic height h_p (see Fig. 2.10). The integration constant C is obtained by specifying the electric potential equal to zero at the boundary $\partial\mathcal{B}_{sp}$ in Fig. 2.10. The electric voltage at the sensor electrode then yields $\Phi_S(X_1, X_2, h_p, t)$ with $(X_1, X_2) \in \partial\mathcal{B}_{\Phi_S}$.

2.6.4 Electric input admittance

Quantities like the electric impedance or admittance of USM are necessary in the design process of the power electronics. As these quantities characterize steady-state behavior of linear systems at harmonic excitation, one must carefully interpret them when characterizing non-linear systems since they contain only filtered information about the system at hand. In accordance to what has been stated in Section 2.6, a *fundamental complex admittance* at the electrode A is defined as follows

$$\underline{Y}_{A1}(\Omega) := \frac{\hat{I}_{A1}(\Omega)}{\hat{V}_{A1}} e^{j\alpha_{A1}(\Omega)} = Y_{A1}(\Omega) e^{j\alpha_{A1}(\Omega)}, \quad (2.98)$$

where $Y_{A1}(\Omega)$ and $\alpha_{A1}(\Omega)$ are known as the admittance and phase, respectively. In (2.98), \hat{V}_{A1} is the voltage amplitude of the fundamental frequency of electric excitation according to (2.78) and $\hat{I}_{A1}(\Omega)$ is the spectral component of the electric current signal with the same circular frequency Ω . Since the system at hand is nonlinear and a multi-input system, the current amplitude and phase depend not only on the circular frequency Ω , but also on the amplitudes \hat{V}_A, \hat{V}_B of the periodic voltage signals $V_A(t)$ and $V_B(t)$, for example.

2.6.5 Power and efficiency

The power balance of the proposed motor model follows from

$$P_{in}(t) = P_{out}(t) + P_{loss}(t) + P_{inner}(t), \quad (2.99)$$

where P_{in} , P_{out} , P_{loss} and P_{inner} are the electrical input power, the mechanical output power, the power loss due to several loss mechanisms and the inner power due to elastic deformation and electric energy storage, respectively. The electric input power delivered by the two electrodes A , B are given as

$$P_{in}(t) := P_{elec}(t) = V_A(t) I_A(t) + V_B(t) I_B(t) \quad (2.100)$$

and the mechanical output power by a motor is the product of drive force and output speed

$$P_{out}(t) := P_{mech}(t) = F(t) \dot{c}_{rx}(t) . \quad (2.101)$$

The power loss is composed of several dissipative sources due to the presence of slip contact between stator and rotor, the visco-elastic material of the contact layer, the losses in the piezoceramic and a viscous damping mechanism of the rotor due to a rubber layer between rotor and disc spring, as shown in Fig. 1.5. To this end, the different losses are divided as follows

$$P_{loss}(t) := P_{slipcontactloss}(t) + P_{contactlayerloss}(t) + P_{piezoceramicloss}(t) + P_{rotorloss}(t) . \quad (2.102)$$

The individual losses are stated in the following. In the contact zone, the losses can be written as

$$P_{slipcontactloss}(t) := \int_{\partial \tilde{\mathcal{B}}_c^{slip}} \tilde{\mathbf{T}}_T \dot{\tilde{\mathbf{g}}}_T d\tilde{\mathbf{A}} , \quad (2.103)$$

while for the contact layer and the piezoceramic material it is set

$$P_{contactlayerloss}(t) := \int_{\tilde{\mathcal{B}}_{rc}} \tilde{\mathbf{T}}_{loss} : \dot{\tilde{\mathbf{S}}} d\tilde{V} = \int_{\tilde{\mathcal{B}}_{rc}} (\mathbf{c}_{rc} : \vartheta_{rc} \dot{\tilde{\mathbf{S}}}) : \dot{\tilde{\mathbf{S}}} d\tilde{V} \quad (2.104)$$

$$P_{piezoceramicloss}(t) := \int_{\tilde{\mathcal{B}}_p} \tilde{\mathbf{T}}_{loss} : \dot{\tilde{\mathbf{S}}} d\tilde{V} = \int_{\tilde{\mathcal{B}}_{sp}} (\mathbf{c}_{sp} : \vartheta_{sp} \dot{\tilde{\mathbf{S}}}) : \dot{\tilde{\mathbf{S}}} dV , \quad (2.105)$$

where $\tilde{\mathbf{T}}_{loss}$ represents that part of the stress belonging to the dissipative processes in the material (see Eq.(2.73)). The losses $P_{rotorloss}$ in the rubber layer are described in the detailed modeling procedure in Section 2.7.3.

Power consumption and mechanical output power usually are specified as averaged quantities over one period of the lowest fundamental circular frequency of the motor in steady-state operation. The voltage signals V_A and V_B in (2.78) are the electrical input quantities, with the fundamental circular excitation frequency Ω . In non-linear systems it may happen that the response to an input quantity contains not only the frequency components of the input signal but also other sub- or superharmonic frequency components. For the steady-state motor dynamics it is assumed, that the motor quantities

contain only multiples of the fundamental circular frequency Ω . The active input power is then be defined to

$$\langle P_{in} \rangle := \frac{2\pi}{\Omega} \int_0^{\frac{\Omega}{2\pi}} [V_A(t) I_A(t) + V_B(t) I_B(t)] dt . \quad (2.106)$$

Note, that at unsteady motor operation subharmonic frequency components may occur. If Ω is used in (2.106), subharmonic components in the current signal will erroneously contribute to the active input power. The active output power is

$$\langle P_{out} \rangle := \frac{2\pi}{\Omega} \int_0^{\frac{\Omega}{2\pi}} F(t) \dot{c}_{rx}(t) dt , \quad (2.107)$$

where $F(t)$ represents the driving force of the motor. The definition of the motor efficiency yields

$$\eta := \frac{\langle P_{out} \rangle}{\langle P_{in} \rangle} . \quad (2.108)$$

Note that this efficiency contains the two-stage energy conversion from electrical energy to deformation energy in the first stage, and from deformation energy to mechanical output energy in the second stage.

Another issue important in actuator design is the capacitive behavior of the ceramics giving rise to a reactive power. This has to be considered in the design of the power electronics. The reactive power is defined as follows

$$\langle Q \rangle := \sqrt{\langle S_A \rangle^2 - \langle P_{inA} \rangle^2} + \sqrt{\langle S_B \rangle^2 - \langle P_{inB} \rangle^2} , \quad (2.109)$$

with the apparent power components

$$\langle S_i \rangle := V_{\text{eff}i} I_{\text{eff}i} , \quad i = \{A, B\} , \quad (2.110)$$

where $V_{\text{eff}i}$ and $I_{\text{eff}i}$ are the effective voltages and currents, respectively. Assuming that the main part of the electric energy is stored in the spectral component of the fundamental circular frequency Ω , the fundamental reactive power component yields

$$Q_\Omega = \frac{1}{2} [\hat{V}_{A1} \hat{I}_{A1} \sin \alpha_{A1} + \hat{V}_{B1} \hat{I}_{B1} \sin \alpha_{B1}] . \quad (2.111)$$

2.7 A simple planar motor model

The objective in this section is to derive a simple physical motor model relying on the geometrical and material data of a typical plate-type USM (e.g. Shinsei USR60), as far as these are available. A simple motor model is chosen here, which should nevertheless lead to a good qualitative agreement between model and experimental results. The model should be able to capture the main phenomena observable in experiments such as the nonlinear resonance curve or the onset of squealing in some operation ranges. For the sake of simplicity, the notches milled into the stator of some types of USM are ignored. A benefit of the notches is that wear particles created by the friction between stator and rotor can escape from the contact region, thus ensuring homogeneous and constant friction states during motor operation. The main effect of neglecting the stator notches in the model is to increase the eigenfrequencies of the eigenmodes used for motor operation. To adjust the eigenfrequency of the excited mode in the stator model to that of the physical motor, Young's modulus and mass density of the stator model are adjusted appropriately. This doesn't change or restrict the qualitative features of the motor model. The motor geometry and operation mode in the Shinsei USR60 lends itself to the use of a BERNOULLI-EULER kinematics for both, the stator with piezoceramic, and also for the rotor, as outlined in Section 2.2.2. Basics on BERNOULLI-EULER beam theory and solution methods for dynamical problems can be found in HAGEDORN (1988, [17]), for example. For the contact layer a simple kinematic relation (see Fig. 2.13) is chosen, that allows for shearing and compression. The reference configuration of the motor model is shown in Fig. 2.11. Reference frame $(O, \mathbf{E}_1, \mathbf{E}_3)$ is laboratory fixed, whereas reference frame $(\tilde{O}, \tilde{\mathbf{E}}_1, \tilde{\mathbf{E}}_3)$ moves with the velocity $\dot{b}_1(t) = v_w$ of the traveling wave to the right. In the reference configuration, stator and rotor occupy regions \mathcal{B}_{0s}

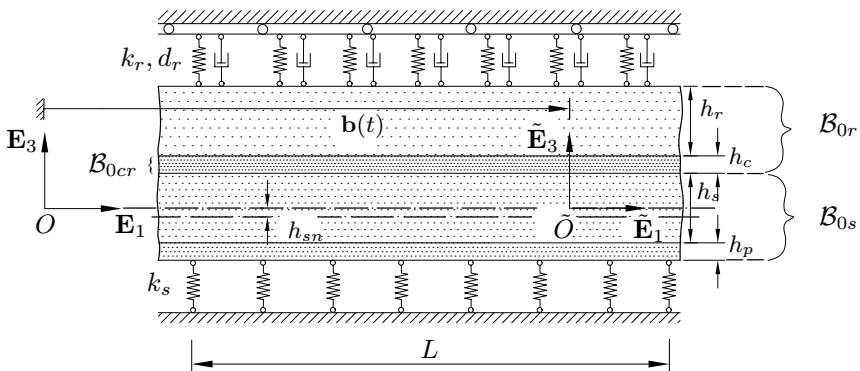


Figure 2.11: Motor model in the reference configuration

and \mathcal{B}_{0r} , respectively. The region of the piezoceramic part is denoted as \mathcal{B}_{0sp} and that of the contact layer as \mathcal{B}_{0cr} . The region of the stator substrate and the rotor substrate

are therefore identified by $\mathcal{B}_{0s} \setminus \mathcal{B}_{0sp}$ and $\mathcal{B}_{0r} \setminus \mathcal{B}_{0rc}$, respectively. The heights of stator, piezoceramic, rotor and contact layer are denoted as h_s , h_p , h_r and h_{rc} , respectively. The radial width of the contact zone between stator and rotor in the motor shown in Fig. 1.2 is small compared to the radius of the stator (see also what has been stated at the beginning of Section 2.2.2). This width is denoted as s in our linear model. Since the stator consists of a metallic stator substrate and a piezoceramic portion, the neutral plane is different from the X_1 -axis in Fig. 2.11 by a distance h_{sn} . The stator is supported by an elastic foundation with stiffness k_s and the rotor support is a visco-elastic foundation with stiffness k_r and damping constant d_r . The damping of the rotor support may come from the rubber layer between disc spring and metallic rotor, as shown in Fig. 1.2. In Fig. 2.12 the motor model is illustrated in the momentary configuration with external load F and axial preload p .

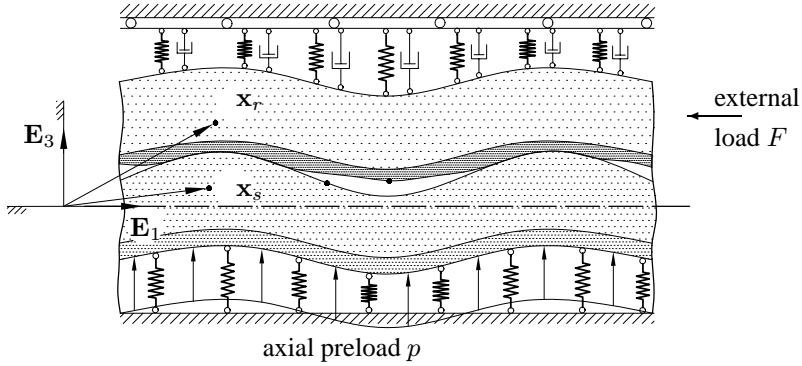


Figure 2.12: Simple motor model in the momentary configuration

2.7.1 Moving reference frame

The relations between the coordinates of the different reference frames for stator and rotor was presented in Section 2.2.4. According to (2.11) these are

$$X_{s_1} = b_1(t) + Y_{s_1}, \quad Y_{s_2} = Y_{s_2}, \quad X_{s_3} = Y_{s_3}, \quad (2.112)$$

$$X_{r_1} + c_{r_1}(t) = b_1(t) + Y_{r_1}, \quad X_{r_2} = Y_{r_2}, \quad X_{r_3} = Y_{r_3}. \quad (2.113)$$

It is remembered, that the velocity v_w of the moving reference frame with respect to the laboratory fixed reference frame was chosen to satisfy

$$b_1(t) = v_w t = \frac{\Omega}{n_s k} t, \quad (2.114)$$

where k is the fundamental wave number defined in (2.4) and n_s the number of nodal diameters of the eigenform excited in a ring type stator (see (2.87)).

2.7.2 Stator

The BERNOULLI-EULER kinematics for the stator with a piezoceramic section may be written as

$$\begin{aligned} \mathbf{x}_s &= \chi_s(\mathbf{X}, t) = \mathbf{X}_s + \mathbf{u}_s(\mathbf{X}_s, t) = \begin{bmatrix} X_1 \\ X_2 \\ X_3 \end{bmatrix} + \begin{bmatrix} -(X_3 + h_{sn}) w'_s(X_1, t) \\ 0 \\ w_s(X_1, t) \end{bmatrix} \\ \forall \mathbf{X} &\in \mathcal{B}_{0s}, \end{aligned} \quad (2.115)$$

in fixed reference frame coordinates. Using the transformation (2.112) for the displacement function \mathbf{u}_s , the description in terms of the coordinates of the moving reference frame follows

$$\tilde{\mathbf{u}}_s(\mathbf{Y}, t) = \begin{bmatrix} -(Y_3 + h_{sn}) \tilde{w}'_s(Y_1, t) \\ 0 \\ \tilde{w}_s(Y_1, t) \end{bmatrix}, \quad \forall \mathbf{Y} \in \tilde{\mathcal{B}}_s. \quad (2.116)$$

Throughout the paper, the prime $(\cdot)'$ represents the derivative with respect to the coordinate X_1 or Y_1 . The distance h_{sn} of the neutral axis from the X_1 -axis is computed by

$$\int_{-\frac{h_s}{2} + h_p}^{\frac{h_s}{2}} \tilde{T}_{11} d\tilde{A} = 0 \quad \Rightarrow \quad h_{sn}, \quad (2.117)$$

but for the sake of simplicity it is assumed that the stiffness of the piezoceramic ring equals the stiffness of the stator substrate and that the mass density of the piezoceramic material equals the mass density of the stator substrate. This is without loss of generality with respect to the qualitative behavior of the motor model. The distance of the neutral axis to the laboratory fixed frame then becomes

$$h_{sn} = \frac{h_p}{2}. \quad (2.118)$$

The kinematics in (2.116) leads to

$$\tilde{S}_{12} = 0, \quad \tilde{S}_{13} = 0, \quad \tilde{S}_{23} = 0, \quad \text{and} \quad \tilde{S}_{22} = 0, \quad \tilde{S}_{33} = 0. \quad (2.119)$$

The normal stresses \tilde{T}_{22} , \tilde{T}_{33} and the shear stresses \tilde{T}_{23} , \tilde{T}_{21} are neglected in addition to the electric field \tilde{E}_1 , \tilde{E}_2

$$\tilde{T}_{22} = 0, \quad \tilde{T}_{33} = 0, \quad \tilde{T}_{23} = 0, \quad \tilde{T}_{21} = 0, \quad \tilde{E}_1 = 0, \quad \tilde{E}_2 = 0. \quad (2.120)$$

For a BERNOULLI-EULER beam model representing a plain stress assumption the material law

$$\boxed{\tilde{T}_{11} = E_s \tilde{S}_{11} \quad \forall \mathbf{Y} \in \tilde{\mathcal{B}}_s \setminus \tilde{\mathcal{B}}_{sp}} \quad (2.121)$$

can be derived from (2.65) and (2.66). By similarly applying a planar stress assumption and assuming for the strain components in (2.119)₂ to be unequal zero and insert (2.119)₁ and (2.120) into the material laws (2.70), (2.71), the material laws for the piezoceramic part of the BERNOULLI-EULER beam stator model yield

$$\boxed{\begin{array}{ll} \tilde{T}_{11} = \bar{c}_{11}^D \tilde{S}_{11} + \bar{h}_{31} \tilde{D}_3 & \tilde{E}_3 = \bar{h}_{31} \tilde{S}_{11} + \bar{\beta}_{33} \tilde{D}_3 \\ \tilde{T}_{13} = h_{15} \tilde{D}_1 & \tilde{E}_1 = \beta_{11} \tilde{D}_1 \end{array}} \quad \forall \mathbf{Y} \in \tilde{\mathcal{B}}_{sp} \quad .(2.122)$$

Note that the material constants indicated by a bar correspond to a planar stress assumption and are different from their counterparts without a bar. The strain components are computed by inserting (2.116) into (2.17).

The compatibility condition for the electric displacement follows from the balance of charges, (2.48), together with the assumptions for the electric field in (2.120)

$$\text{Div } \tilde{\mathbf{D}} = 0 \quad \Rightarrow \quad \frac{\partial \tilde{D}_3}{\partial Y_3} = 0 \quad \Rightarrow \quad \tilde{D}_3 = \tilde{D}_3(Y_1, t) \quad (2.123)$$

and states that the electric displacement component \tilde{D}_3 depends only on the Y_1 -coordinate.

2.7.3 Rotor

The rotor substrate deformation is also described by a BERNOULLI-EULER kinematics. The motion of the rotor substrate is therefore written according to (2.8) as

$$\mathbf{x}_r = \chi_r(\mathbf{X}, t) = \mathbf{c}_r(t) + \mathbf{X}_r + \mathbf{u}_r(\mathbf{X}_r, t), \quad \forall \mathbf{X} \in \mathcal{B}_{0r} \setminus \mathcal{B}_{0cr} \quad (2.124)$$

$$= \begin{bmatrix} c_{rx}(t) \\ 0 \\ 0 \end{bmatrix} + \begin{bmatrix} X_1 \\ X_2 \\ X_3 \end{bmatrix} + \begin{bmatrix} -(X_3 - h_{rn}) w'_r(X_1, t) \\ 0 \\ w_r(X_1, t) \end{bmatrix}, \quad (2.125)$$

where h_{rn} is the distance to the rotors neutral axis (see Fig. 2.11)

$$h_{rn} = \frac{h_s}{2} + h_c + \frac{h_r}{2}, \quad (2.126)$$

which is located at mid-thickness of the rotor substrate for $h_c \ll h_r$. The displacement written in coordinates of the moving reference frame follows as

$$\tilde{\mathbf{u}}_r(\mathbf{Y}, t) = \begin{bmatrix} -(Y_3 - h_{rn}) \tilde{w}'_r(Y_1, t) \\ 0 \\ \tilde{w}_r(Y_1, t) \end{bmatrix}, \quad \forall \mathbf{Y} \in \tilde{\mathcal{B}}_r \setminus \tilde{\mathcal{B}}_{rc}. \quad (2.127)$$

The rotor material law can be written in a manner analogous to that of the stator as

$$\boxed{\tilde{T}_{11} = E_r \tilde{S}_{11}} \quad \forall \mathbf{Y} \in \tilde{\mathcal{B}}_r \setminus \tilde{\mathcal{B}}_{rc} \quad . \quad (2.128)$$

2.7.4 Contact layer

The kinematics of the displacements in the contact layer is composed out of a superposition of the BERNOLLI-EULER kinematics, the compression displacement w_c and the shear displacement u_c as shown in Fig. 2.13. The description of the contact layer

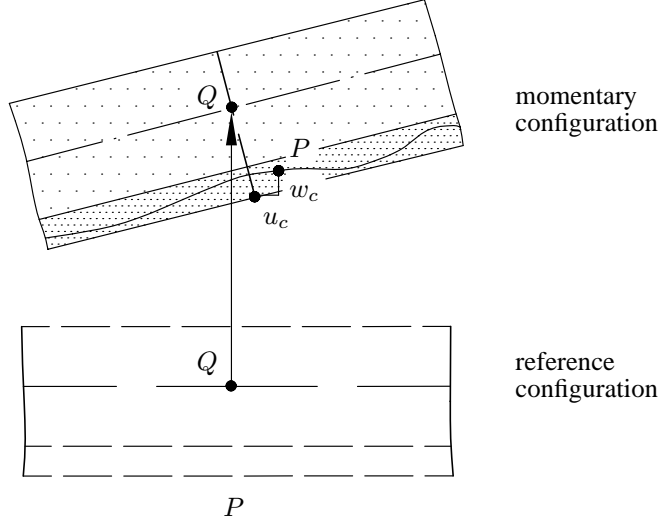


Figure 2.13: Kinematics of the contact layer

motion in the reference configuration may then be written as

$$\begin{aligned} \mathbf{x}_{rc} = \chi_{rc}(\mathbf{X}, t) &= \begin{bmatrix} c_{rx}(t) \\ 0 \\ 0 \end{bmatrix} + \begin{bmatrix} X_1 \\ X_2 \\ X_3 \end{bmatrix} +, \\ &+ \begin{bmatrix} -(X_3 - \bar{h}) w'_r(X_1, t) + u_c(X_1, t) \\ 0 \\ w_r(X_1, t) + w_c(X_1, t) \end{bmatrix}, \quad \forall \mathbf{X} \in \mathcal{B}_{0rc} \end{aligned} \quad (2.129)$$

with

$$\tilde{\mathbf{u}}_{rc}(\mathbf{Y}, t) = \begin{bmatrix} -(Y_3 - h_{rc}) \tilde{w}'_r(Y_1, t) + \tilde{u}_c(Y_1, t) \\ 0 \\ \tilde{w}_r(Y_1, t) + \tilde{w}_c(Y_1, t) \end{bmatrix}, \quad \forall \mathbf{Y} \in \tilde{\mathcal{B}}_{rc}. \quad (2.130)$$

Inserting the displacement (2.130) into the strain-displacement relation (2.17) yields

$$\tilde{S}_{22} = 0, \quad \tilde{S}_{12} = 0, \quad \tilde{S}_{23} = 0. \quad (2.131)$$

for the strain components. The normal stress \tilde{T}_{22} and the shear stress \tilde{T}_{23} are neglected:

$$\tilde{T}_{22} = 0, \tilde{T}_{23} = 0. \quad (2.132)$$

The material law for the contact layer with this special kinematic results in

$$\begin{aligned} \tilde{T}_{11} = & \frac{E_{rc}}{(1 + \nu_{rc})(1 - 2\nu_{rc})} \left[(1 - \nu_{rc}) (\tilde{S}_{11} + \vartheta_{rc} \dot{\tilde{S}}_{11}) + \right. \\ & \left. + \nu_{rc} (\tilde{S}_{33} + \vartheta_{rc} \dot{\tilde{S}}_{33}) \right] \end{aligned} \quad (2.133)$$

$$\begin{aligned} \tilde{T}_{33} = & \frac{E_{rc}}{(1 + \nu_{rc})(1 - 2\nu_{rc})} \left[(1 - \nu_{rc}) (\tilde{S}_{33} + \vartheta_{rc} \dot{\tilde{S}}_{33}) + \right. \\ & \left. + \nu_{rc} (\tilde{S}_{11} + \vartheta_{rc} \dot{\tilde{S}}_{11}) \right] \end{aligned} \quad (2.134)$$

$$\tilde{T}_{13} = \frac{2E_{rc}}{1 + \nu_{rc}} \left[\tilde{S}_{13} + \vartheta_{rc} \dot{\tilde{S}}_{13} \right]. \quad (2.135)$$

2.7.5 Contact formulation

Recalling what has been stated in Section 2.3.1, it is proceeded by computing the relation between the corresponding contact points ($\hat{\mathbf{X}}_r, \hat{\mathbf{X}}_s^*$) of stator and rotor contact layer. To this end, the minimum distance function (2.30) is evaluated assuming small displacements, resulting in the approximation

$$\mathbf{X}_s^* \approx \mathbf{c}_r + \mathbf{X}_r \quad \Rightarrow \quad \mathbf{Y}_s^* \approx \mathbf{Y}_r, \quad (2.136)$$

where the transformation rules (2.11) and (2.12) have been used. The gap function (2.35) becomes

$$\tilde{g}_N = \tilde{w}_r(Y_r, t) + \tilde{w}_c(Y_r, t) - \tilde{w}_s(Y_r, t), \quad (2.137)$$

and the gap velocity (2.39) yields

$$\dot{\tilde{g}}_N = \dot{\tilde{w}}_r + \dot{\tilde{w}}_c + (\tilde{w}'_r + \tilde{w}'_c) (\dot{c}_{rx} - v_w) - \dot{\tilde{w}}_s + \tilde{w}'_s v_w. \quad (2.138)$$

From the definition of the relative velocity between two contacting points, (2.41), one gets

$$\begin{aligned} \dot{\tilde{g}}_T = & - \left(\frac{h_p}{2} + \frac{h_s}{2} \right) \dot{\tilde{w}}'_s - \dot{c}_{rx} - \dot{\tilde{w}}_c - \left(h_c + \frac{h_r}{2} \right) \dot{\tilde{w}}'_r \\ & + (v_w - \dot{c}_{rx}) \left(\tilde{w}'_c + \left(h_c + \frac{h_r}{2} \right) \tilde{w}''_r \right) + \left(\frac{h_p}{2} + \frac{h_s}{2} \right) v_w \tilde{w}''_s. \end{aligned} \quad (2.139)$$

2.7.6 External forces

The active forces applied to the motor are the axial prestress \tilde{p} pressing the rotor against the stator and the external load F acting on the rotor as illustrated in Fig. 2.12. Both active forces enter the principle of virtual power through the first part in (2.63). For the stress components one gets

$$\hat{\tilde{T}}_{33} = \tilde{p}_{axial}(Y_1) \quad \forall \mathbf{Y} \in \partial\tilde{\mathcal{B}}_s \quad (2.140)$$

for the axial prestress and

$$\hat{\tilde{T}}_{11} = \frac{F(t)}{s h_r} \quad (2.141)$$

for the load in the Y_1 -direction.

2.7.7 Scaling and non-dimension formulation

The equations of motion will be derived via the principle of virtual power. It turns out that the derivation is rather cumbersome but straightforward. By use of the mathematical toolbox MATHEMATICA, a good part of this may be done automatically. Despite the fact that a relatively simple motor model has been chosen, the resulting PDEs are quite lengthy. For comparing the magnitudes of the different terms in the equations of motion, the equations are written in a non-dimensional form. This procedure allows us to identify and neglect terms of lower order. An overview of all the design parameters used in the simple model is given in Fig. 2.14.

The physically independent quantities are scaled as follows

$$\bar{t} = [\Omega] t, \quad \bar{Y}_1 = \frac{Y_1}{[\lambda]}. \quad (2.142)$$

The reference circular frequency $[\Omega]$ is the circular eigenfrequency of the stator's eigenmode, used for the motor operation. The reference wavelength $[\lambda]$ is computed by $[\lambda] = L/n_s$. Here L is the circumferential length of the stator at the outer radius (see Fig. 1.5). A reference stator vibration amplitude $[\hat{w}_s]$ is used for the scaling of the displacement field variables. This yields the following non-dimensional quantities

$$\bar{w}_s = \frac{\tilde{w}_s}{[\hat{w}_s]}, \quad \bar{c}_{rx} = \frac{c_{rx}}{[\hat{w}_s]}, \quad \bar{w}_r = \frac{\tilde{w}_r}{[\hat{w}_s]}, \quad \bar{u}_c = \frac{\tilde{u}_c}{[\hat{w}_s]}, \quad \bar{w}_c = \frac{\tilde{w}_c}{[\hat{w}_s]}. \quad (2.143)$$

Axial preload and contact stresses may be scaled with a reference axial prestress $[p_{axial}]$, to yield

$$\bar{p}_{axial} = \frac{\tilde{p}_{axial}}{[p_{axial}]}, \quad \bar{T}_N = \frac{\tilde{T}_N}{[p_{axial}]}, \quad \bar{T}_T = \frac{\tilde{T}_T}{[p_{axial}]} \quad (2.144)$$

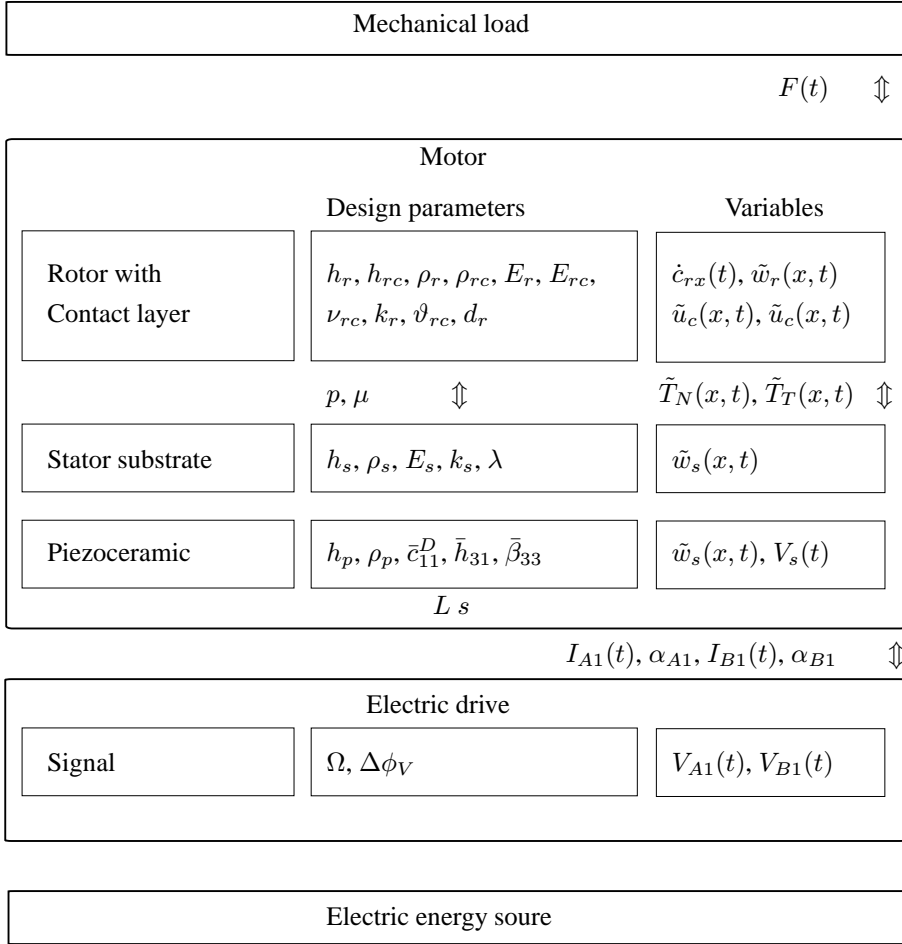


Figure 2.14: Overview of the design parameters and motor variables of the simple motor model, used in this study

and for the electric quantities reference quantities are taken for the electric displacement and voltage amplitude, $[\hat{D}], [\hat{V}]$

$$\bar{D}_3 = \frac{\tilde{D}_3}{[\hat{D}]}, \quad \bar{V} = \frac{\hat{V}}{[\hat{V}]}, \quad \bar{\Phi} = \frac{\tilde{\Phi}}{[\hat{V}]} . \quad (2.145)$$

The characteristic electric displacement is chosen, using the one-dimensional material law for the characteristic quantities, $[\hat{E}_3] = \bar{h}_{31}[\hat{S}_{11}] + \bar{\beta}_{33}[\hat{D}_3]$, ignoring the strain

influence on the electric field and choosing $[\hat{E}_3] = [\hat{V}]/h_p$. This results in $[\hat{D}_3] = [\hat{V}]/(h_p\bar{\beta}_{33})$.

Additionally, a non-dimensional excitation frequency is introduced

$$\bar{\Omega} = \frac{\Omega}{[\Omega]}. \quad (2.146)$$

Table 2.2 lists parameter values of a typical USM, which can be used as reference data for a numerical analysis and as data inserted into the PDE's to neglect terms of lower order.

<i>system parameter</i>	<i>symbol</i>	<i>value</i>	<i>dimension</i>
stator height (with teeth)	h_s	$5 \cdot 10^{-3}$	m
rotor height	h_r	$3 \cdot 10^{-3}$	m
piezoceramic height	h_p	$1 \cdot 10^{-3}$	m
contact layer height	h_c	$1 \cdot 10^{-4}$	m
stator mass density	ρ_s	$8 \cdot 10^3 *$	$\frac{kg}{m^3}$
rotor mass density	ρ_r	$3 \cdot 10^3$	$\frac{kg}{m^3}$
piezoceramic mass density	ρ_p	$8 \cdot 10^3$	$\frac{kg}{m^3}$
contact layer mass density	ρ_{rc}	$3 \cdot 10^2$	$\frac{kg}{m^3}$
stator Young's modulus	E_s	$1 \cdot 10^{11} *$	$\frac{N}{m^2}$
rotor Young's modulus	E_r	$7 \cdot 10^{10}$	$\frac{N}{m^2}$
piezoceramic Young's modulus	\bar{c}_{11}^D	$9 \cdot 10^{10}$	$\frac{N}{m^2}$
contact layer Young's modulus	E_{rc}	$3 \cdot 10^9$	$\frac{N}{m^2}$
elastic foundation stiffness	k_s, k_r	$1 \cdot 10^6$	$\frac{N}{m}$
damping constant	d_r	$2 \cdot 10^2$	$\frac{kg}{s}$
damping constant	$\tan \delta_{rc}$	$1 \cdot 10^{-1}$	
damping constant contact layer	ϑ_{rc}	$4 \cdot 10^{-7}$	s
electromechanic coupling	\bar{h}_{31}	$-2 \cdot 10^8$	$\frac{N}{C}$
dielectric constant	$\bar{\beta}_{33}$	$9 \cdot 10^7$	$\frac{Nm^2}{C^2}$

Table 2.2: Data of a typical USM (Shinsei USR60). Data's with *-symbol will be adjusted to approximately fit the eigenfrequency of the stator model with that of the physical stator having notches, since the notches have been neglected in the stator model

Approximate values of the design parameters are stated in Fig. 2.2. Some of these parameters can be easily measured, others are adopted from the literature (see e.g. HERZOG, (1993, [22]), or LE MOAL & MINOTTI (1997, [32]) or estimated by means of the data of the piezoceramic material. In this figure, values for three of the typical scaling variables are also given. With the data given in Tab. 2.2, the equations of motion will be scaled and terms of order of magnitude smaller than $1 \cdot 10^{-3}$ will be neglected. Table 2.3 lists the scaling parameters.

<i>scaling parameter</i>	<i>symbol</i>	<i>value</i>	<i>dimension</i>
reference eigenfrequency	$[\Omega]$	$3 \cdot 10^5$	$\frac{\text{rad}}{\text{s}}$
reference wavelength	$[\lambda]$	$2 \cdot 10^{-2}$	m
reference stator amplitude	$[\hat{w}_s]$	$1 \cdot 10^{-6}$	m
reference axial load	$[p_{axial}]$	$2.7 \cdot 10^5$	$\frac{\text{N}}{\text{m}^2}$
reference dielectric displacement	$[\hat{D}]$	$5.3 \cdot 10^{-4}$	$\frac{\text{C}}{\text{m}^2}$
reference voltage amplitude	$[\hat{V}]$	100	Volts

Table 2.3: Scaling parameters reflecting typical quantities of a Shinsei USR60 motor

2.7.8 Equations of motion

The velocities, virtual velocities, strain components and virtual strain rate components of the stator and rotor motion can be derived, using the formulas in the general modeling framework in Section 2.2.5. Inserting them into the principle of virtual power and doing some partial integrations and manipulations leads to the equations of motion of the motor model where all terms of order of magnitude smaller than $5 \cdot 10^{-3}$ have been neglected. The equations of motion represent a one-dimensional model of length

$$\bar{Y}_1 \in [0, n_s] \quad (2.147)$$

with the number n_s of nodal points or nodal lines for a rotary USM. All field variables \bar{f} depend on the coordinate \bar{Y}_1 and the time \bar{t} , giving $\bar{f}(\bar{Y}_1, \bar{t})$. The prime (\cdot)' now indicates the derivative with respect to the coordinate \bar{Y}_1 , and the circle ($\dot{\cdot}$) the partial time derivative with respect to \bar{t} . The non-dimensionalized equations of motion may then be stated as follows

- Stator equation:

$$S_1 \overset{\infty}{\bar{w}}_s + S_2 \overset{\infty}{\bar{w}}_s'' + S_3 \overset{\circ}{\bar{w}}_s + S_4 \overset{\circ}{\bar{w}}_s' + S_5 \overset{\circ}{\bar{w}}_s''' + S_6 \bar{w}_s + S_7 \bar{w}_s' + S_8 \bar{w}_s'' + S_9 \bar{w}_s'''' +$$

$$S_{10} \bar{T}_N + S_{11} \bar{T}'_T = -S_{12} \bar{D}''_3 - S_{13} \bar{p}_{axial} , \quad \forall \bar{Y}_1 \in [0, n_s] \quad (2.148)$$

- rotor equation of rigid body motion

$$R_{r1} \overset{\circ}{\bar{c}}_{rx} + R_{r7} \overset{\circ}{\bar{w}}''_r + R_{r8} \bar{w}'_r + R_{r11} \overset{\circ}{\bar{u}}_c + R_{r13} \overset{\circ}{\bar{u}}'_c + R_{r15} \bar{u}'_c + R_{r16} \bar{u}''_c + R_{r17} \bar{w}'_c + R_{r20} \bar{T}'_T = -R_{r22} F , \quad \forall \bar{Y}_1 \in [0, n_s] \quad (2.149)$$

- rotor equation of flexural motion

$$\overset{\circ}{\bar{w}}_r + R_{f3} \overset{\circ}{\bar{w}}_r + R_{f4} \overset{\circ}{\bar{w}}'_r + R_{f7} \bar{w}_r + R_{f8} \bar{w}'_r + R_{f9} \bar{w}''_r + R_{f11} \bar{w}''''_r + R_{f25} \bar{T}_N + R_{f26} \bar{T}'_T = 0 , \quad \forall \bar{Y}_1 \in [0, n_s] \quad (2.150)$$

- contact layer equation in the \bar{Y}_1 direction

$$L_{u9} \overset{\circ}{\bar{u}}_c + \bar{u}_c + L_{u13} \bar{u}'_c + L_{u19} \bar{T}'_T = 0 , \quad \forall \bar{Y}_1 \in [0, n_s] \quad (2.151)$$

- contact layer equation in the \bar{Y}_3 direction

$$L_{w11} \overset{\circ}{\bar{w}}_c + L_{w14} \bar{w}_c + L_{w15} \bar{w}'_c + L_{w18} \bar{T}'_N = 0 , \quad \forall \bar{Y}_1 \in [0, n_s] \quad (2.152)$$

- electric displacement equation in the Y_1 -direction

$$E_1 = 0 , \quad \forall \bar{Y}_1 \in [0, n_s]$$

- electric displacement in the \bar{Y}_3 -direction

$$P_1 \hat{\Phi}'' + P_2 \bar{D}''_3 + P_3 \bar{w}''''_s = 0 , \quad \forall \bar{Y}_1 \in [0, n_s] . \quad (2.153)$$

The contact formulation in Section 2.7.5 may be written as

- contact gap:

$$\bar{g}_N = \bar{w}_c + \bar{w}_r - \bar{w}_s = 0 , \quad \forall \bar{Y}_1 \in \partial \bar{B}_{ci} \quad (2.154)$$

- contact gap velocity:

$$\dot{\bar{g}}_N = -\dot{\bar{w}}_s + G_2 \bar{w}'_s + \dot{\bar{w}}_r + G_4 \bar{w}'_r + \dot{\bar{w}}_c + G_6 \bar{w}'_c = 0, \quad \forall \bar{Y}_1 \in \partial \bar{\mathcal{B}}_{ci} \quad (2.155)$$

- relative velocity for tangential contact:

$$\dot{\bar{g}}_T = SS_1 \dot{\bar{w}}'_s + SS_2 \bar{w}''_s - \dot{\bar{c}}_{rx} + SS_4 \dot{\bar{w}}'_r + SS_5 \bar{w}''_r - \dot{\bar{u}}_c + SS_7 \bar{u}'_c = 0, \\ \forall \bar{Y}_1 \in \partial \bar{\mathcal{B}}_{ci}^{stick} \quad (2.156)$$

- Friction law:

$$\bar{T}_T = \mu \text{sign}(\dot{\bar{g}}_T) \bar{T}_N, \quad \forall \bar{Y}_1 \in \partial \bar{\mathcal{B}}_{ci}^{slip}. \quad (2.157)$$

The coefficients S_i , R_{ri} , R_{fi} , L_{ui} , L_{wi} , P_i , G_i and SS_i are given in Appendix A.1. The notation of the coefficients is taken for convenience as the abbreviations of the stator equation of motion (S), the rotor equation of motion (R) and so on.

2.7.9 Electric quantities

The non-dimensionalization of the electric potential (2.86) is obtained by substituting the relations (2.142), (2.145) and (2.146). This yields

$$\hat{\Phi}(\bar{\mathbf{Y}}, \bar{t}) = \hat{V}_{A1} \cos(2\pi \bar{Y}_1) + \left[\hat{V}_{B1} \cos(\bar{\Omega} \bar{t} + \Phi) - \hat{V}_{A1} \cos(\bar{\Omega} \bar{t}) \right] \\ \cdot \cos(2\pi(\bar{Y}_1 - \bar{b}_1(\bar{t}))) \quad (2.158)$$

with

$$\bar{b}_1(\bar{t}) = \frac{b_1(t)}{[\lambda]} = \frac{\bar{\Omega}}{2\pi} \bar{t}. \quad (2.159)$$

The sensor electrodes occupy only a small portion of the piezoceramic part of the stator. They are important for sensing the stator vibrations for control purposes, but their direct effect on the motor dynamics is negligible. Thus, only actor electrodes will be modeled here. Under this simplification, the electric potential is assumed to act along the whole piezoceramic surface $\partial \mathcal{B}_\Phi$. The two electrodes A and B are applied to different regions

$$\partial \mathcal{B}_{\Phi A} = [0, \frac{L}{2}] \times [0, s] \quad \text{and} \quad \partial \mathcal{B}_{\Phi B} = [\frac{L}{2}, L] \times [0, s]. \quad (2.160)$$

Both electrode surfaces are defined in coordinates of the moving reference frame using (2.11). In non-dimensional notation they are characterized as

$$\begin{aligned}\partial\bar{\mathcal{B}}_{\Phi A}(t) &= [-\bar{b}_1(\bar{t}), \frac{n_s}{2} - \bar{b}_1(\bar{t})] \\ \partial\bar{\mathcal{B}}_{\Phi B}(t) &= [\frac{n_s}{2} - \bar{b}_1(\bar{t}), n_s - \bar{b}_1(\bar{t})].\end{aligned}\quad (2.161)$$

The non-dimensional expressions for the electric current to the electrodes A and B in (2.93) are similarly obtained as

$$\begin{aligned}\bar{I}_A &= - \int_{-\bar{b}_1(\bar{t})}^{n_s/2-\bar{b}_1(\bar{t})} \left[\overset{\circ}{D}_3 - \hat{D}'_3 \overset{\cdot}{b}_1 \right] d\bar{Y}_1, \\ \bar{I}_B &= - \int_{n_s/2-\bar{b}_1(\bar{t})}^{n_s-\bar{b}_1(\bar{t})} \left[\overset{\circ}{D}_3 - \hat{D}'_3 \overset{\cdot}{b}_1 \right] d\bar{Y}_1,\end{aligned}\quad (2.162)$$

with

$$\bar{I}_A = \frac{\hat{I}_A}{s [\hat{D}] [\lambda] [\Omega]} \quad \text{and} \quad \bar{I}_B = \frac{\hat{I}_B}{s [\hat{D}] [\lambda] [\Omega]}.\quad (2.163)$$

The non-dimensional electric current is obtained substituting the expression (2.153) of the electric displacement in the \bar{Y}_3 -direction in both equations (2.162). The electric current to electrode A for example can be calculated from

$$\bar{I}_A(t) = \frac{1}{P_2} \int_{-\bar{b}_1(\bar{t})}^{n_s/2-\bar{b}_1(\bar{t})} \left[P_1 \overset{\circ}{\Phi} + P_3 \overset{\circ}{w}'' - (P_1 \overset{\wedge}{\Phi}' + P_3 \bar{w}''') \bar{b}_1 \right] d\bar{Y}_1, \quad (2.164)$$

with the coefficients P_1 to P_3 defined in Appendix A.1.

The electric input admittance defined in (2.98) simplifies to

$$\bar{Y}_{A1}(\bar{\Omega}) := \frac{\hat{I}_{A1}(\bar{\Omega})}{\hat{V}_{A1}} e^{j\alpha_{A1}(\bar{\Omega})} = \hat{Y}(\bar{\Omega}) e^{j\alpha_{A1}(\bar{\Omega})}.\quad (2.165)$$

The losses in the motor can be obtained according to Section 2.6.5. The slip loss between stator and rotor follows from substituting the friction law (2.157) and the relative velocity (2.156) into (2.103):

$$\bar{P}_{slipcontact}(\bar{t}) = \int_{\partial\bar{\mathcal{B}}_c^{slip}} \mu \text{sign}(\dot{\bar{g}}_T) \bar{\lambda}_N \dot{\bar{g}}_T d\bar{A}.\quad (2.166)$$

The expression for losses in the contact layer is rather lengthy and will not be given here. The losses $P_{piezoceramicloss}(t)$ in the piezoceramic material are neglected in the following.

The active output power is calculated as

$$\langle \bar{P}_{out} \rangle = \frac{\Omega}{2\pi[\Omega]} \int_0^{\frac{2\pi[\Omega]}{\Omega}} \bar{F}(\bar{t}) \dot{\bar{c}}_{rx}(\bar{t}) d\bar{t} . \quad (2.167)$$

The active input power, the efficiency and the reactive power yield

$$\langle \bar{P}_{in} \rangle = \frac{\Omega}{2\pi[\Omega]} \int_0^{\frac{2\pi[\Omega]}{\Omega}} \bar{V}_A(\bar{t}) \bar{I}_A(\bar{t}) d\bar{t} . \quad (2.168)$$

$$\bar{\eta} = \frac{\langle \bar{P}_{out} \rangle}{\langle \bar{P}_{in} \rangle} \quad (2.169)$$

$$\bar{Q}_\Omega = \frac{1}{2} [\hat{V}_{A1} \hat{I}_{A1} \sin \alpha_{A1} + \hat{V}_{B1} \hat{I}_{B1} \sin \alpha_{B1}] . \quad (2.170)$$

2.7.10 Comment on the electric displacement

A simplified model should always be consistent with the underlying general theory. From the basic mechanical literature it is well known that the BERNOULLI-EULER (BE) theory gives good results compared to the exact solutions obtained from the theory of elasticity if only for example $h/\lambda \ll 1$. Let us examine the consistency of the BE theory with the theory of elasticity. In BE beam theory the shear stress T_{xy} is neglected and only the stress component T_{xx} in axial direction is considered to be important. For a given T_{xx} the shear stress T_{xy} can however be computed from the theory of elasticity. In the theory of elasticity one can show that $h/\lambda \ll 1$ in fact leads to $\max T_{xy}/\max T_{xx} \ll 1$ (and also to $\max U_{shear}/\max U_{bend} \ll 1$). BE theory is therefore consistent with the theory of elasticity. For electromechanical models, such a consistency, must not only hold for the stresses but also for the electric field components, for example. Therefore, for the model developed here, the consistency

$$\frac{\max \tilde{E}_1}{\max \tilde{E}_3} \ll 1 \quad (2.171)$$

must hold. In modeling the stator, the assumptions $\tilde{E}_1 = 0$, $\tilde{E}_2 = 0$ were made, see (2.120). Thus \tilde{E}_3 is the only remaining electric field component. To compute the electric potential, one can use the material law (2.122) and the electric field-electric potential relation

$$\tilde{E}_3 = \frac{\partial \tilde{\Phi}}{\partial Y_3} = \bar{h}_{31} \tilde{S}_{11} + \bar{\beta}_{33} \tilde{D}_3 , \quad \tilde{E}_3 = -\tilde{\Phi}_{,3} . \quad (2.172)$$

Integrating with respect to Y_3 and matching the boundary condition at $\partial\mathcal{B}_{sp}$ (see Fig. 2.7) yields

$$\tilde{\Phi}(Y_1, Y_3, t) = \frac{\bar{h}_{31}}{2} \left[Y_3^2 - \frac{h_s^2}{4} \right] \bar{w}_s''(Y_1, t) - \bar{\beta}_{33}^S \left[Y_3 + \frac{h_s}{2} \right] D_3(Y_1, t). \quad (2.173)$$

The electric field-electric potential relation (2.51) leads to

$$E_1 = -\frac{\partial\tilde{\Phi}}{\partial Y_1} \neq 0, \quad E_2 = -\frac{\partial\tilde{\Phi}}{\partial Y_2} \neq 0, \quad E_3 = -\frac{\partial\tilde{\Phi}}{\partial Y_3} \neq 0, \quad (2.174)$$

which is inconsistent with the assumption pertaining to the electric field components. It may be shown very easily by non-dimensionalizing the ratio (2.171) that for the proposed model the relation

$$\frac{\max \bar{E}_1}{\max \bar{E}_3} \approx \frac{h_p}{[\lambda]} \quad (2.175)$$

is valid, thus if the ratio between the height of the piezoceramic part of the stator and the wavelength is small enough, the inner consistency in (2.171) is satisfied. Clearly, this is not a sufficient condition but nevertheless suffices as an initial indicator to check the validity of the model assumptions.

2.7.11 Summary

In this chapter the basic equations for modeling USM have been presented, focusing on key issues like the formulation of the equations with respect to a moving reference frame, the contact mechanics, or the modeling of piezoceramics. The principle of virtual power for electro-mechanical systems, extended by terms representing the mechanical contact between stator and rotor, has been stated in order to generate the equations of motion, the electric equations as well as the contact constraints. The framework of the basic equations allows to derive planar motor models for different motor designs. This has been done exemplary for a plate-type motor, for which a simple planar model has been derived. The model assumptions and simplifications in the presented framework are listed below:

- Planar motor model, assuming a small strip of contact layer at the outer radius and neglecting the curvature and radial motion of surface points in rotary motors.
- Teeth only indirectly considered by using the stator height in the model as the height of the physical stator with teeth but adjusting the Young's modulus and the mass density of the stator model to get approximately the same eigenfrequency in the stator model and the physical stator.

- Isothermal process assumed, i.e. no long time scale effects due to temperature drift is considered.
- Instead of modeling non-homogenous polarization (see Figs. 1.10, 2.8 and 2.9) periodic shape functions for the electric potential are assumed to simplify computation.
- No material non-linearity of the piezoceramic is considered.
- Properties of the contacting surfaces are subsumed in the friction coefficient, no inner variables accounting for surface roughness are introduced.
- No distinction between sticking and sliding friction coefficient is made.

For the simple planar motor model, proposed in Section 2.7, further assumptions have been made, which will be summarized here:

- Longitudinal displacements in stator and rotor are ignored.
- A lossless piezoceramic material is assumed.
- No sensor electrodes are incorporated.
- No geometric imperfections are modeled, such as for example wavyness of the surface, non-coincidence of the eigenfrequencies of only nearly orthogonal eigenmodes.

It turned out, that, although the model is held simple, the equations of motion are rather lengthy and cumbersome to generate by hand. Therefore, a symbolic toolbox have been used to derive the model equations. To exploit only terms of leading order in the equations of motion, dimensionless quantities were introduced. A scaling procedure have been carried out to neglect terms of lower order. The proposed simple motor model extends those already used in different aspects. First, it is a electromechanical model in contrary to many models, where only the mechanical parts have been modeled, or the mechanical parts have been represented by equivalent electrical circuits. Second, it includes rotor flexibility as well as the kinematics and dynamics of the contact layer bonded to the rotor. Third, the model is not restricted to given kinematics of the stator, but allows to excite the stator by voltages and get electric currents as output quantities. It is possible to connect the motor model with models of power electronic models to analyze the dynamics of the whole system.

Chapter 3

Model Analysis

3.1 Introduction

In this chapter, a numerical solution procedure for the contact problem of USMs is proposed and some results of numerical analysis will be presented. The design process of USMs is usually based on the analysis of the eigenfrequencies and the eigenmodes of the stator. A lot of work has been done to understand the vibrational behavior of the stator. The situation is different when it comes to modeling of the motor behavior. Here, only a few models have been proposed and only some analysis results have been presented (see Section 2.1 for a literature review). Some numerical results on the stator-rotor contact problem were obtained by time integration of Finite-Element-Models. CAO & WALLASCHEK (1995, [8]) and SCHMIDT (1999, [51]) started to give a deeper insight into the contact behavior between stator and rotor using more sophisticated structural dynamic models. Also, equivalent electric circuit models have been investigated capturing the essential motor behavior. To come towards design rules for the motor, the models need to be more sophisticated. The computation of frequency response curves, speed-torque characteristics and electric admittances e.g. allows to estimate important motor characteristics without actually building prototypes. Questions like how to choose the ratio between stator vibration amplitude and wavelength or how to choose the rotor design parameters for a given stator design have not yet been investigated intensively. Therefore, contact models and model analysis algorithms are necessary which can give qualitative insights into the motor dynamics and which allow parameter studies in reasonable time compared to numerical time simulation of Finite-Element-Models.

In the first part of this chapter a numerical solution procedure is presented. At a constant load, transients of motor dynamics usually settle down within a few milliseconds due to different damping mechanism. Thus, the focus is on the analysis of the

steady-state motor dynamics. Since the concept of a moving reference frame is used, the steady-state analysis can be reduced to solving a time independent contact problem. This drastically simplifies the analysis compared to the time consuming FEM analysis. First the computation of the eigenfrequencies of stator and rotor is discussed. Then, the steady-state system equations are formulated for the simple motor model derived in Section 2.7. The equations to compute the normal and tangential contact behavior are given and the contact boundary conditions as well as the initial conditions are specified. Using a Galerkin method, the set of ODE's is then spatially discretized. All equations are transformed into a matrix notation. Due to the contact interaction between stator and rotor, stiffness matrices occur in the system equations which have to be updated whenever the contact state changes. The system equations thus have an alterable structure. For the contact algorithm the principle incremental solution procedure is briefly explained. A flow diagram of the contact algorithm gives an overview on the computation procedure. In the section containing numerical results, the difficulties encountered during the numerical analysis of the contact zones are discussed and computed speed-torque characteristics are compared to measured ones. Also, a result of a time domain analysis is presented.

3.2 Numerical Solution Procedure

3.2.1 Eigenfrequencies of stator and rotor

For interpretation of the results of numerical analysis, knowledge of the eigenfrequencies of stator and rotor are of importance since the stator is excited in two orthogonal eigenmodes with the same frequency. Replacing the electric displacement on the right side of the stator equation (2.148) with the equation of the electric displacement in (2.153) and neglecting the contact forces and the external forces result in

$$S_1 \overset{\circ}{\bar{w}}_s + S_2 \overset{\circ\circ}{\bar{w}}_s + S_3 \overset{\circ}{\bar{w}}_s + S_4 \overset{\circ}{\bar{w}}_s' + S_5 \overset{\circ\circ\circ}{\bar{w}}_s + S_6 \bar{w}_s + S_7 \bar{w}_s' + S_8 \bar{w}_s'' + \left[S_9 - S_{12} \frac{P_3}{P_2} \right] \bar{w}_s''' = 0, \quad \forall \bar{Y}_1 \in [0, n_s]. \quad (3.1)$$

Note, that the term $S_{12} \frac{P_3}{P_2}$ in (3.1) represents influence of the piezoceramic part on bending stiffness of the stator. Since periodic boundary conditions at $\bar{Y}_1 = 0$ and $\bar{Y}_1 = n_s$ are assumed, the wavenumbers of the eigenmodes are known a priori to be

$$\bar{k}_i = (i - 1) \frac{2\pi}{n_s}, \quad i = 1, 2, \dots \quad (3.2)$$

To each wavenumber corresponds the wave velocity

$$\bar{v}_i = \frac{\bar{\omega}_i}{\bar{k}_i}, \quad \text{with} \quad \bar{v}_i = \frac{v_i}{[\Omega][\lambda]}. \quad (3.3)$$

The terms S_4, S_5, S_7-S_9 in (3.1) depend on the velocity of the traveling reference frame

$$v_w = \frac{[\Omega]}{n_s k} \bar{\Omega} \quad (3.4)$$

and thus on the circular frequency $\bar{\Omega}$. There are two ways to compute the eigenfrequencies. One is to solve the eigenvalue problem in a spatially fixed reference frame by setting $v_w = 0$. Consequently, the terms with the coefficients containing the wave velocity v_w vanish. Inserting an ansatz of the type $\tilde{w} = e^{j\bar{k}_i \bar{Y}_1} e^{j\bar{\omega}_i \bar{t}}$ into (3.1) gives an equation for the $\bar{\omega}_i$ for each \bar{k}_i . The other way of computing eigenfrequencies is to look at the steady state condition where the time dependent terms in (3.1) vanish. Using an ansatz of the type $\tilde{w} = e^{j\bar{k}_i \bar{Y}_1}$ and substituting (3.4) into (3.1) gives the eigenfrequencies $\bar{\Omega}_i$. These are related to the eigenfrequencies $\bar{\omega}_i$ of the modes via

$$\bar{\omega}_i = \frac{i-1}{n_s} \bar{\Omega}_i, \quad i = 2, 3, \dots, \quad (3.5)$$

where it is taken into consideration that the wave velocity v_w in (3.4) corresponds to the $(n_s + 1)$ th mode in the stator (the operational mode).

3.2.2 Contact equations

The most important characteristic of USMs are the speed-torque curves, i.e. the motor features under steady-state motor operation. Transient characteristics like start and stop behavior may be important, too. However, the first step towards a better understanding of the motor dynamics and the influence of important design parameters, e.g. the rotor geometry and material, must be an analysis of the steady-state motor behavior. The numerical solution procedure is then carried out for steady-state, i.e. all time derivatives in the system equations (2.148)-(2.157) vanish, except for the rotor rigid body displacement \bar{c}_{rx} in the driving direction. The motor equations for steady-state are, the stator equation

$$\begin{aligned} S_6 \bar{w}_s + S_7 \bar{w}'_s + S_8 \bar{w}''_s + \left[S_9 - S_{12} \frac{P_3}{P_2} \right] \bar{w}'''_s + S_{10} \bar{T}_N + S_{11} \bar{T}'_T \\ = -S_{12} \bar{D}''_3 - S_{13} \bar{p}_{axial}, \quad \forall \bar{Y}_1 \in [0, n_s] \end{aligned} \quad (3.6)$$

the rotor equation of rigid body motion

$$\begin{aligned} R_{r8} \bar{w}'_r + R_{r15} \bar{u}'_c + R_{r16} \bar{u}''_c + R_{r17} \bar{w}'_c + R_{r20} \bar{T}_T = -R_{r22} F, \\ \forall \bar{Y}_1 \in [0, n_s] \end{aligned} \quad (3.7)$$

the rotor equation of flexural motion

$$\begin{aligned} R_{f7} \bar{w}_r + R_{f8} \bar{w}'_r + R_{f9} \bar{w}''_r + R_{f11} \bar{w}'''_r + R_{f25} \bar{T}_N + R_{f26} \bar{T}'_T = 0, \\ \forall \bar{Y}_1 \in [0, n_s] \end{aligned} \quad (3.8)$$

the contact layer equation in the \bar{Y}_1 direction

$$\bar{u}_c + L_{u13} \bar{u}'_c + L_{u19} \bar{T}_T = 0, \quad \forall \bar{Y}_1 \in [0, n_s] \quad (3.9)$$

the contact layer equation in the \bar{Y}_3 direction

$$L_{w14} \bar{w}_c + L_{w15} \bar{w}'_c + L_{w18} \bar{T}_N = 0, \quad \forall \bar{Y}_1 \in [0, n_s] \quad (3.10)$$

the contact gap

$$\bar{g}_N = \bar{w}_c + \bar{w}_r - \bar{w}_s, \quad \text{with} \quad (3.11)$$

$$\bar{g}_N = 0, \quad \forall \bar{Y}_1 \in \partial \bar{\mathcal{B}}_{ci} \quad \text{and} \quad \bar{g}_N > 0, \quad \forall \bar{Y}_1 \in \partial \bar{\mathcal{B}}_{nci} \quad (3.12)$$

the relative velocity for tangential contact

$$\dot{\bar{g}}_T = SS_2 \bar{w}''_s - \dot{\bar{c}}_{rx} + SS_5 \bar{w}''_r + SS_7 \bar{u}'_c \quad \text{with} \quad (3.13)$$

$$\dot{\bar{g}}_T = 0 \quad \forall \bar{Y}_1 \in \partial \bar{\mathcal{B}}_{ci}^{stick} \quad \text{and} \quad \dot{\bar{g}}_T \neq 0 \quad \forall \bar{Y}_1 \in \partial \bar{\mathcal{B}}_{ci}^{slip} \quad (3.14)$$

and the friction law

$$\bar{T}_T = \mu \text{sign}(\dot{\bar{g}}_T) \bar{T}_N, \quad \forall \bar{Y}_1 \in \partial \bar{\mathcal{B}}_{ci}^{slip}. \quad (3.15)$$

The interaction between stator, rotor and contact layer is expressed via the normal contact stresses

$$\bar{T}_N \equiv \begin{cases} \bar{T}_N^* & \text{if } \bar{Y}_1 \in \partial \bar{\mathcal{B}}_{ci} \\ 0 & \text{if } \bar{Y}_1 \notin \partial \bar{\mathcal{B}}_{nci} \end{cases}, \quad (3.16)$$

and the tangential contact stress

$$\bar{T}_T \equiv \begin{cases} \bar{T}_T^{stick} & \text{if } \bar{Y}_1 \in \partial \bar{\mathcal{B}}_{ci}^{stick_j} \quad \wedge \quad \dot{\bar{g}}_T = 0 \\ \text{sign}(\dot{\bar{g}}_T) \mu \bar{T}_N^* & \text{if } \bar{Y}_1 \in \partial \bar{\mathcal{B}}_{ci}^{slip_j} \quad \wedge \quad \dot{\bar{g}}_T \neq 0 \\ 0 & \text{if } \bar{Y}_1 \notin \partial \bar{\mathcal{B}}_{ci} \end{cases}, \quad (3.17)$$

with $i = 1, \dots, N_c$ contact zones and $j = 1, \dots, N_{cti}$ stick and slip sub-zones, within each contact zone. The different contact zones are illustrated in Fig. 2.5.

The motor input quantities are the electric excitation, which are given according to (2.158) as

$$\hat{\Phi}(\bar{\mathbf{Y}}, \bar{t}) = \hat{V}_{A1} \cos(2\pi \bar{Y}_1), \quad (3.18)$$

and the rigid body speed of the rotor as

$$\dot{\bar{c}}_{rx} := \bar{v}_r. \quad (3.19)$$

Note, that the assumption is made that higher harmonic spatial components caused by the rectangular shaped electric potential as illustrated in Fig. 2.10 are negligible, since the motor is driven near it's operational resonance. Thus, higher harmonic components in the stator due to the electric excitation are assumed to be small.

There are four given or prescribed quantities, namely the frequency of excitation $\bar{\Omega}$, the amplitude of the electric voltage \bar{V}_{A1} , the axial prestress p_{axial} , and the rotor velocity \bar{v}_r . Note, that the rotor velocity is used instead of the motor output force as independent variable to simplify the computational effort. The unknown quantities are the displacements $\bar{w}_s(\bar{Y}_1)$, $\bar{w}_r(\bar{Y}_1)$, $\bar{w}_c(\bar{Y}_1)$, $\bar{u}_c(\bar{Y}_1)$, the contact stresses $\bar{T}_N(\bar{Y}_1)$ and $\bar{T}_T(\bar{Y}_1)$, the contact gap $\bar{g}_N(\bar{Y}_1)$, the relative velocity $\dot{\bar{g}}_T(\bar{Y}_1)$ the contact boundaries $\{p_{ei}, p_{bi}\}$ for $i = 1, \dots, N_c$ as well as the transition points with coordinates p_{tij} for $j = 1, \dots, N_{cti}$, defining transitions from stick to slip and vice versa. The bending wave runs from left to right with the wave velocity v_w while due to the stator kinematics, the rotor moves in the opposite direction with rotor velocity \bar{v}_r . The beginning of a contact zone is defined as that boundary at which material points approach each other (coordinates p_{bi}). Analogously, the end of a contact zone is defined as that boundary at which material points separate from each other (coordinates p_{ei}). The contact bound-

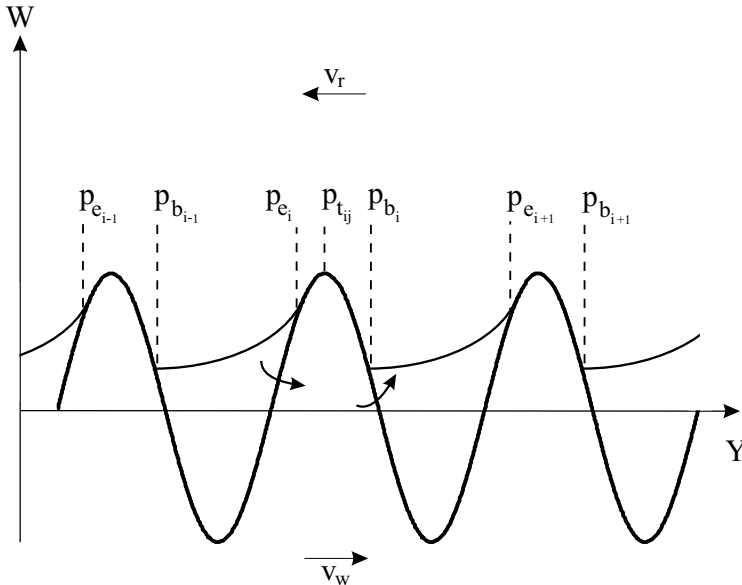


Figure 3.1: Stator and rotor deformation and contact boundaries

aries are illustrated in Fig. 3.1. The various contact subzones are labeled by the type of contact. According to Fig. 2.5 the various subzones are named as follows: The contact

zones, $\partial\mathcal{B}_{ci}$, and the non-contact zones $\partial\mathcal{B}_{nci}$ correspond to

$$\partial\mathcal{B}_{ci} = [p_{ei}, p_{bi}], \quad \partial\mathcal{B}_{nci} = [p_{bi}, p_{e(i+1)}], \quad (3.20)$$

respectively. It is assumed that N_c contact zones exist, with $i = 1, \dots, N_c$, whereas $N_c = 1$ is possible. For both types of subzones, the relations

$$\partial\mathcal{B}_{rc} = \left(\bigcup_{i=1}^{N_c} \partial\mathcal{B}_{ci} \right) \cup \left(\bigcup_{i=1}^{N_c} \partial\mathcal{B}_{nci} \right) \quad \text{and} \quad \partial\mathcal{B}_{ci} \cap \partial\mathcal{B}_{nci} = \emptyset,$$

hold. The contact zones are divided into stick- and slip-subzones by the transition coordinates, which are bounded by the boundaries of the contact zone. The computation of the tangential contact stress distribution starts at the beginning of a contact zone. This is the reason why the numeration of these subzones starts at the beginning of a contact zone and ends at the end of a contact zone. The stick-subzones may belong to the following sections of the stator or rotor contact surface

$$\begin{aligned} \partial\bar{\mathcal{B}}_{ci}^{\text{stick}_1} &= [p_{ti1}, p_{bi}] \quad \vee \quad \partial\bar{\mathcal{B}}_{ci}^{\text{stick}_{j+1}} = [p_{ti(j+1)}, p_{tij}] \\ &\vee \quad \partial\bar{\mathcal{B}}_{ci}^{\text{stick}_{N_{cti}}} = [p_{ei}, p_{ti(N_{cti}+1)}]. \end{aligned} \quad (3.21)$$

Analogously, the slip-subzones may belong to the sections

$$\begin{aligned} \partial\bar{\mathcal{B}}_{ci}^{\text{slip}_1} &= [p_{ti1}, p_{bi}] \quad \vee \quad \partial\bar{\mathcal{B}}_{ci}^{\text{slip}_{j+1}} = [p_{ti(j+1)}, p_{tij}] \\ &\vee \quad \partial\bar{\mathcal{B}}_{ci}^{\text{slip}_{N_{cti}}} = [p_{ei}, p_{ti(N_{cti}+1)}]. \end{aligned} \quad (3.22)$$

It is assumed, that each contact zone consists of $N_{ct_i} + 1$ stick or slip subzones, with $j = 1, \dots, N_{ct_i} + 1$. For the stick- and slip-subzones the relations

$$\partial\bar{\mathcal{B}}_{ci} = \bigcup_{j=1}^{N_{ct_i}} \partial\bar{\mathcal{B}}_{ci}^{\text{stick}/\text{slip}_j} \quad \text{and} \quad \partial\mathcal{B}_{ci}^{\text{stick}_j} \cap \partial\mathcal{B}_{ci}^{\text{slip}_k} = \emptyset, \quad \forall j \neq k.$$

hold.

Before the discretization method is carried out, the motor equations are rearranged and partially solved to reduce the number of unknowns. The objective now is to express both displacements of the contact layer, $\bar{w}_c(\bar{Y}_1)$, $\bar{u}_c(\bar{Y}_1)$, and the contact stresses in terms of the stator and rotor displacements. Therefore, the contact conditions have to be considered in more detail.

Normal contact Two cases must be distinguished, the contact state and the non-contact state. In the case of contact, $\bar{g}_N = 0$ holds and according to the gap function in (3.11), the lateral contact layer displacement can be expressed as

$$\bar{w}_c = \bar{w}_s - \bar{w}_r . \quad (3.23)$$

Substituting (3.23) back into the equation of the lateral contact layer displacement (3.10) results in an expression for the normal contact stress

$$\bar{T}_N^* = -\frac{1}{L_{w18}} [L_{w14} (\bar{w}_s - \bar{w}_r) + L_{w15} (\bar{w}'_s - \bar{w}'_r)] , \quad \forall \bar{Y}_1 \in \partial\mathcal{B}_{ci} . \quad (3.24)$$

In the case of non-contact, $\bar{T}_N = 0$ holds for the contact stress. The equation of the contact layer in the \bar{Y}_3 direction, (3.10), reduces to a homogeneous ODE

$$L_{w14} \bar{w}_c + L_{w15} \bar{w}'_c = 0 , \quad \forall \bar{Y}_1 \notin \partial\mathcal{B}_{ci} . \quad (3.25)$$

The solution of this equation is

$$\bar{w}_c = C_{wi}^{free} e^{-\frac{L_{w14}}{L_{w15}} \bar{Y}_1} , \quad \forall \bar{Y}_1 \in [p_{bi}, p_{ei+1}] \notin \partial\mathcal{B}_{ci} . \quad (3.26)$$

The solution (3.26) is valid for two neighboring contact zones. Substituting (3.26) into (3.11) yields

$$\bar{g}_N = C_{wi}^{free} e^{-\frac{L_{w14}}{L_{w15}} \bar{Y}_1} + \bar{w}_r(\bar{Y}_1) - \bar{w}_s(\bar{Y}_1) > 0 , \quad \forall \bar{Y}_1 \in \partial\mathcal{B}_{nci} . \quad (3.27)$$

As it has been shown, the normal contact stress \bar{T}_N^* , the contact layer displacement \bar{w}_c , and the contact gap can be expressed in terms of the stator and rotor displacements, \bar{w}_s , \bar{w}_r , respectively. Consequently, additional unknowns such as the integration constants C_{wi}^{free} , $i = 1, \dots, N_c$ enter the equations of motion, which have to be determined by the contact boundary conditions. This will be discussed in a subsequent paragraph.

Tangential contact A similar procedure as that for the normal contact will be carried out for the tangential contact. The objective is the same, to express the tangential contact layer displacement \bar{u}_c and the tangential contact stress \bar{T}_T in terms of the stator and rotor displacement. In the case of contact, $\bar{g}_N = 0$, between two different contact situations must be distinguished, the stick and the slip tangential contact state.

Where two surfaces stick, the relative velocity is zero, i.e. $\dot{\bar{g}}_T = 0$ is valid. The tangential displacement of the contact layer can be expressed in terms of the stator and rotor displacements by integrating (3.13)

$$\bar{u}_c^{stick} = \frac{1}{SS_7} [\bar{v}_r \bar{Y}_1 - SS_2 \bar{w}'_s - SS_5 \bar{w}'_r] + C_{ui}^{stickj} \quad \forall \bar{Y}_1 \in \partial\bar{\mathcal{B}}_{ci}^{stickj} . \quad (3.28)$$

Substituting (3.28) into (3.9) gives an expression for the tangential stress in terms of the stator and rotor displacement

$$\begin{aligned} \bar{T}_T^{stick} &= -\frac{1}{L_{u19} SS_7} [\bar{v}_r \bar{Y}_1 - SS_2 \bar{w}'_s - SS_5 \bar{w}'_r + L_{u13} (\bar{v}_r - SS_2 \bar{w}''_s - SS_5 \bar{w}''_r)] \\ &\quad - \frac{1}{L_{u19}} C_{ui}^{stickj} , \quad \forall \bar{Y}_1 \in \partial\bar{\mathcal{B}}_{ci}^{stickj} . \end{aligned} \quad (3.29)$$

Under slip-contact conditions, $\dot{g}_T = \dot{g}_T^{slip} \neq 0$ holds. Inserting the friction law (3.15) into (3.9) yields an inhomogeneous ODE for the displacement \bar{u}_c

$$\bar{u}_c^{slip} + L_{u13} (\bar{u}_c^{slip})' = -L_{u19} \mu \text{sign}(\dot{g}_T) \bar{T}_N^*, \quad \forall \bar{Y}_1 \in \partial \bar{\mathcal{B}}_{ci}^{slip_j}. \quad (3.30)$$

The solution consists of the superposition of a particular solution and the solution of the homogeneous equation

$$\bar{u}_c^{slip} = \bar{u}_{ch}^{slip} + \bar{u}_{cp}^{slip}, \quad \text{with} \quad \bar{u}_{ch}^{slip} = C_{ui}^{slip_j} e^{-\frac{1}{L_{u13}} \bar{Y}_1}, \quad \forall \bar{Y}_1 \in \partial \bar{\mathcal{B}}_{ci}^{slip_j}. \quad (3.31)$$

The right hand side of (3.30) can be modified by inserting (3.24)

$$\begin{aligned} \bar{u}_{cp}^{slip} + L_{u13} (\bar{u}_{cp}^{slip})' &= \frac{L_{u19}}{L_{w18}} \mu \text{sign}(\dot{g}_T) [L_{w14} (\bar{w}_s - \bar{w}_r) + L_{w15} (\bar{w}'_s - \bar{w}'_r)] \\ &\quad \forall \bar{Y}_1 \in \partial \bar{\mathcal{B}}_{ci}^{slip_j}. \end{aligned} \quad (3.32)$$

The right hand side of (3.32) is a function of the stator and rotor displacement. Thus, a particular solution $\bar{u}_{cpi}^{slip_j}$ can be obtained depending on the stator and rotor displacements. Analogously, the tangential contact stress for slipping surfaces, i.e. the friction law (3.15) follows as

$$\begin{aligned} \bar{T}_T^{slip} &= -\frac{\mu \text{sign}(\dot{g}_T)}{L_{w18}} [L_{w14} (\bar{w}_s - \bar{w}_r) + L_{w15} (\bar{w}'_s - \bar{w}'_r)], \\ &\quad \forall \bar{Y}_1 \in \partial \bar{\mathcal{B}}_{ci}^{slip_j}. \end{aligned} \quad (3.33)$$

Other, more sophisticated friction laws may be implemented by substituting the term $\mu \text{sign}(\dot{g}_T)$ by the corresponding functional dependence of the friction coefficient $\mu(\dot{g}_T)$. The relative velocity results in

$$\dot{g}_T^{slip} = SS_2 \bar{w}_s'' + SS_5 \bar{w}_r'' + SS_7 (\bar{u}_c^{slip})' - \bar{v}_r \quad (3.34)$$

with \bar{u}_c^{slip} taken from (3.31) and (3.32).

In the case of non-contact, $\bar{T}_T = 0$ holds and the contact layer equation (3.9) degenerates to a simple homogeneous ODE with the solution

$$\bar{u}_c^{free} = C_{ui}^{free} e^{-\frac{1}{L_{u13}} \bar{Y}_1}, \quad \forall \bar{Y}_1 \in [p_{bi}, p_{ei+1}]. \quad (3.35)$$

The contact layer displacements \bar{u}_c , \bar{w}_c and the contact stresses \bar{T}_N^* , \bar{T}_T^{stick} and \bar{T}_T^{slip} have been expressed in terms of the stator and rotor displacements \bar{w}_s and \bar{w}_r , respectively. This reduced the number of field variables and thus, the computation time. However, additional unknowns, namely the integration constants $C_{ui}^{stick_j}$ and $C_{ui}^{slip_j}$, appear. Notably, the contact problem has to be solved incrementally, since due to the frictional contact the equations cannot be solved simultaneously. At each load step increment or increment of the excitation frequency, for example, the normal contact problem is solved under constant tangential contact conditions (\bar{u}_c , \bar{T}_T). After that, the tangential contact condition is updated and the integration constant will be determined.

Contact boundary conditions Besides the field variables, also the contact boundaries (p_{ei}, p_{bi}) as well as the integration constants C_{wi}^{free} , C_{ui}^{free} , $C_{ui}^{slip_j}$, and $C_{ui}^{stick_j}$ are unknown. To solve the equations of motion, additional conditions have to be formulated at the contact boundaries. The variables (p_{ei}, p_{bi}) and C_{wi}^{free} are related to the normal contact. Therefore, three types of boundary equations are necessary. First, the integration constant C_{wi}^{free} is determined. At the end of the $i + 1$ th contact zone, the gap function (3.83)

$$\bar{g}_N(p_{ei+1}) \equiv C_{wi}^{free} e^{-\frac{L_{w14}}{L_{w15}} p_{ei+1}} + \bar{w}_r(p_{ei+1}) - \bar{w}_s(p_{ei+1}) = 0 \quad (3.36)$$

must be satisfied. The integration constant becomes

$$C_{wi}^{free} = [\bar{w}_s(p_{ei+1}) - \bar{w}_r(p_{ei+1})] e^{-\frac{L_{w14}}{L_{w15}} p_{ei+1}}. \quad (3.37)$$

The other boundary conditions result in equations for the boundary values (p_{ei}, p_{bi}) . At the beginning of the contact zone, the gap function must vanish

$$\begin{aligned} \bar{g}_N(p_{bi}) &\equiv [\bar{w}_s(p_{ei+1}) - \bar{w}_r(p_{ei+1})] e^{-\frac{L_{w14}}{L_{w15}} (p_{bi} + p_{ei+1})} \\ &+ \bar{w}_r(p_{bi}) - \bar{w}_s(p_{bi}) = 0. \end{aligned} \quad (3.38)$$

whereas, at the end of the contact zone the normal contact stress reaches zero

$$\begin{aligned} \bar{T}_N^*(p_{ei}) &\equiv -\frac{1}{L_{w18}} [L_{w14} (\bar{w}_s(p_{ei}) - \bar{w}_r(p_{ei})) \\ &+ L_{w15} (\bar{w}'_s(p_{ei}) - \bar{w}'_r(p_{ei}))] = 0. \end{aligned} \quad (3.39)$$

As the next step, the boundary conditions for the tangential contact will be stated. Using the incremental solution procedure, the normal contact state, i.e. the contact boundaries (p_{ei}, p_{bi}) are assumed to be known. In the updating procedure, the tangential contact state is computed at constant normal contact state. For the tangential contact state, conditions for the determination of the integration constants C_{ui}^{free} , $C_{ui}^{slip_j}$, and $C_{ui}^{stick_j}$ must be given.

Transition conditions from stick to slip and vice versa With the knowledge of the normal contact stress at an incremental change of the external quantities, the updating of the tangential contact stress needs the equations stated in the foregoing paragraph. At this step the stator and rotor displacements \bar{w}_s and \bar{w}_r are known. So is also the normal contact stress \bar{T}_N^* . The rotor velocity \bar{v}_r is given. The unknown parameters, such as the contact layer displacement \bar{u}_c and the tangential contact stress \bar{T}_T are computed next. Since Coulomb's friction law is used, stick and slip zones must be distinguished. Therefore, the conditions of the transition points P_{tij} between stick and slip regions need to be formulated in order to determine the integration constants $C_{ui}^{stick_j}$ and $C_{ui}^{slip_j}$. The strategy is to pass through the contact state from the beginning of contact (at p_{bi}) through the end of contact (at p_{ei}). During passage, it must be verified whether a transition from

stick to slip or vice versa occurs. Two limiting frictional stresses exist, a *braking limit stress* and a *driving limit stress*

$$\text{braking limit stress: } \bar{T}_T^{l+}(\bar{Y}_1) := \mu |\bar{T}_N^*(\bar{Y}_1)|, \quad (3.40)$$

$$\text{driving limit stress: } \bar{T}_T^{l-}(\bar{Y}_1) := -\mu |\bar{T}_N^*(\bar{Y}_1)|, \quad (3.41)$$

where braking and driving are considered with respect to the rotor rigid body motion \bar{v}_r . The normal contact stress $\bar{T}_N^*(\bar{Y}_1)$ is given by (3.24). The determination of *transition points* P_{tij} , $i = 1, \dots, N_{pi}$ between stick- and slip-subzones starts at the beginning of the contact zone, at points P_{bi} . Three cases must be distinguished.

First, the transition from stick to slip will be determined, i.e under the assumption that the stick contact state is known, the integration constant C_{ui}^{slipj} for the slip contact state is found. The coordinate p_{tij} where the transition from stick to slip takes place, is located by the *indicator function*

$$f(p_{tij}) \equiv |\bar{T}_T^{stick}(p_{tij})| - |\mu \bar{T}_N^*(p_{tij})| = 0. \quad (3.42)$$

The explicit expression of the indicator function is given by inserting (3.29) and (3.24) into (3.42). The contact layer displacement in tangential direction under stick-condition gives

$$\bar{u}_c^{stick}(p_{tij}) = \bar{u}_{c0}^{stick}. \quad (3.43)$$

The integration constant is then determined from the condition of continuous transition of the displacement

$$\bar{u}_c^{slip}(p_{tij}) = \bar{u}_{c0}^{stick}, \quad (3.44)$$

resulting in

$$C_{ui}^{slip(j+1)} = [\bar{u}_{c0}^{stick} - \bar{u}_{cp}^{slip}(p_{tij})] e^{\frac{p_{tij}}{L_{u13}}}. \quad (3.45)$$

Second, the transition from slip to stick is formulated under the assumption that the slip contact state is known. The *indicator function* is given by (3.34) and the transition coordinate p_{tij} is determined by the vanishing of

$$\dot{g}_T^{slip}(p_{tij}) \equiv SS_2 \bar{w}_s''(p_{tij}) + SS_5 \bar{w}_r''(p_{tij}) + SS_7 (\bar{u}_c^{slip})'(p_{tij}) - \bar{v}_r = 0. \quad (3.46)$$

The contact layer displacement in tangential direction under slip-condition gives

$$\bar{u}_c^{slip}(p_{tij}) \equiv \bar{u}_{c0}^{slip} \quad (3.47)$$

at the transition point. The integration constant is then again determined by the condition of continuous transition of the displacement

$$\bar{u}_c^{stick}(p_{tij}) = \bar{u}_{c0}^{slip}, \quad (3.48)$$

with $\bar{u}_c^{stick}(p_{tij})$ taken from (3.28). The integration constant becomes

$$C_{ui}^{stick(j+1)} = \bar{u}_{c0}^{slip} + \frac{1}{SS_7} [SS_2 \bar{w}'_s(p_{tij}) + SS_5 \bar{w}'_r(p_{tij}) - \bar{v}_r p_{tij}] . \quad (3.49)$$

Third, the transition from stick- or slip-contact to no-contact needs to be derived. In this case, the transition point is already known, namely the end-points of the contact zones, P_{ei} . The contact layer displacement at the end of the last contact subzone is known and is either a stick or a slip subzone

$$\bar{u}_c^{slip}(p_{ei}) = \bar{u}_{c0}^{slip} \quad \text{or} \quad \bar{u}_c^{stick}(p_{ei}) = \bar{u}_{c0}^{stick} . \quad (3.50)$$

The integration constant of the solution for the non-contact state of the contact layer is determined from

$$\bar{u}_c^{free}(p_{ei}) = \bar{u}_{c0}^{slip/stick} . \quad (3.51)$$

The integration constant is given by (3.35) as

$$C_{ui}^{free} = \bar{u}_{c0}^{slip/stick} e^{\frac{L_w 14}{L_w 15} p_{ei}} . \quad (3.52)$$

Motor output force and maximum rotational speed After the solution of the contact problem for a given set of external variables (voltage, excitation frequency and rotational speed), the corresponding motor output force can be computed by rearranging (3.7)

$$F = -\frac{1}{R_{r22}} [R_{r8} \bar{w}'_r + R_{r15} \bar{u}'_c + R_{r16} \bar{u}''_c + R_{r17} \bar{w}'_c + R_{r20} \bar{T}_T] , \quad \forall \bar{Y}_1 \in [0, n_s] . \quad (3.53)$$

A scaling analysis, using the characteristic data from Tab. 2.2 and the reference data from Tab. 2.2, shows that the coefficient R_{r20}/R_{r22} is much greater than the others. In very good approximation the motor force is given by

$$F = -\frac{1}{n_s} \frac{R_{r20}}{R_{r22}} \sum_{i=1}^{N_c} \int_{p_{ei}}^{p_{bi}} \bar{T}_T d\bar{Y}_1 , \quad (3.54)$$

where the integration is carried out between the different stick and slip subzones.

The maximum rotational speed of the motor would be achieved in point contact between the wave crests of the bending wave in stator and rotor. For such an idealized condition the rotor together with the contact layer must behave like a rigid body. The velocity of stator surface points for the simple motor model is given by substituting (2.116) and (2.118) into (2.22)

$$\bar{v}_{rmax} = \left[\frac{h_s}{2} + \frac{h_p}{2} \right] v_w \max [\bar{w}''_s]_{\bar{Y}_1 \in [0, n_s]} . \quad (3.55)$$

With the scaling parameters in Tab. 2.2 and the typical data in Tab. 2.2, the maximum rotational speed reads as follows

$$\bar{v}_{rmax} = 0.25 \hat{w}_s , \quad (3.56)$$

where \hat{w}_s is the dimensionless amplitude of the harmonic stator vibration. The dimensional form is obtained using (3.19) and the scaling rules (2.142), (2.143) as

$$v_{rmax} \approx 100 \frac{\text{rpm}}{\mu\text{m}} \hat{w}_s . \quad (3.57)$$

The maximum rotational speed gives an upper bound for the no-load rotational speed of the motor. For the no-load rotational speed \bar{v}_{r0} ,

$$\bar{v}_{r0} < \bar{v}_{rmax} \quad (3.58)$$

holds. The no-load rotational speed is unknown beforehand, since the tangential contact distribution along the contact zones are unknown.

Initial conditions The frictional contact between stator and rotor demands an incremental solution procedure, since frictional processes are history dependent. Beginning with a known contact state, a control parameter (e.g. excitation frequency, electric voltage) is changed by an increment. Then, the normal contact state is determined. Hereby, the tangential contact state stays unchanged. In a second step, the tangential contact state is updated with the new normal contact state remaining unchanged. Using such an incremental procedure, the incremental steps of the control parameter must be small enough to ensure only small changes in the tangential contact state. To begin with an initial contact state any known state already obtained during an contact computation can be used. Also, the contact state at rest, where no traveling wave excitation is present, can be taken as initial contact state. For this contact state, the equations (3.6) to (3.17) reduce to

the stator equation

$$S_6 \bar{w}_s + S_{10} \bar{T}_N = -S_{13} \bar{p}_{axial} , \quad \forall \bar{Y}_1 \in [0, n_s] \quad (3.59)$$

the rotor equation of rigid body motion

$$F = -\frac{1}{n_s} \frac{R_{r20}}{R_{r22}} \int_0^{n_s} \bar{T}_T d\bar{Y}_1 \quad (3.60)$$

the rotor equation of flexural motion

$$R_{f7} \bar{w}_r + R_{f25} \bar{T}_N = 0 , \quad \forall \bar{Y}_1 \in [0, n_s] \quad (3.61)$$

the contact layer equation in the \bar{Y}_1 direction

$$\bar{u}_c + L_{u19} \bar{T}_T = 0 , \quad \forall \bar{Y}_1 \in [0, n_s] \quad (3.62)$$

the contact layer equation in the \bar{Y}_3 direction

$$L_{w14} \bar{w}_c + L_{w18} \bar{T}_N = 0, \quad \forall \bar{Y}_1 \in [0, n_s] \quad (3.63)$$

the contact gap

$$\bar{g}_N = \bar{w}_c + \bar{w}_r - \bar{w}_s \quad \text{with} \quad \bar{g}_N = 0 \quad (3.64)$$

and the relative velocity for tangential contact

$$\dot{\bar{g}}_T = 0 \quad \forall \bar{Y}_1 \in \partial \bar{\mathcal{B}}_{ci}^{stick_j}. \quad (3.65)$$

For a given axial preload \bar{p}_{axial} the initial contact state can be easily determined as

$$\Rightarrow \bar{w}_s^{(0)}, \bar{w}_r^{(0)}, \bar{w}_c^{(0)}, \bar{u}_c^{(0)}. \quad (3.66)$$

Electrical Quantities Having the solution, the motor force F in (3.7) can be calculated, giving the speed-force characteristics (\bar{v}_r - F -characteristics). The speed-torque characteristics (n - T -characteristics, see Fig. 1.18) and the speed-force characteristics are related to each other by the radius of the stator and rotor. Also, electrical quantities can be calculated. For example the electric current is

$$\bar{I}_A(\bar{t}) := -\frac{1}{P_2} \int_{-\bar{b}_1(\bar{t})}^{n_s/2-\bar{b}_1(\bar{t})} \left[P_1 \hat{\Phi}' + P_3 \bar{w}_s''' \right] \bar{b}_1(\bar{t}) d\bar{Y}_1, \quad (3.67)$$

with $\bar{b}_1(\bar{t})$ defined in (2.159).

3.2.3 Steady-state system equations

In Section 3.2.2 the field variables of normal stress, tangential stress, contact gap, relative velocity and contact layer displacements were derived. They were expressed in terms of stator and rotor displacement variables and integration constants. The integration constants of these field variables were readily obtained using continuity conditions of the contact layer displacements at the contact boundaries and the transition points.

In this section the steady-state equations are summarized and the initial state as well as the contact topology is formulated. Then, a description of the contact search equations follows. Finally, the equations to compute contact boundaries and contact transition points are presented.

Stator and rotor equations

The stator and the rotor equations of motion are given by (3.6) and (3.8) as

$$\begin{aligned} S_6 \bar{w}_s + S_7 \bar{w}'_s + S_8 \bar{w}''_s + \left[S_9 - S_{12} \frac{P_3}{P_2} \right] \bar{w}''''_s + S_{10} \bar{T}_N + S_{11} \bar{T}'_T \\ = -S_{12} \bar{D}''_3 - S_{13} \bar{p}_{axial} , \quad \forall \bar{Y}_1 \in [0, n_s] \end{aligned} \quad (3.68)$$

$$\begin{aligned} R_{f7} \bar{w}_r + R_{f8} \bar{w}'_r + R_{f9} \bar{w}''_r + R_{f11} \bar{w}''''_r + R_{f25} \bar{T}_N + R_{f26} \bar{T}'_T = 0 , \\ \forall \bar{Y}_1 \in [0, n_s] , \end{aligned} \quad (3.69)$$

respectively. The motor output force, given in (3.54), is

$$F = -\frac{1}{n_s} \frac{R_{r20}}{R_{r22}} \sum_{i=1}^{N_c} \int_{p_{ei}}^{p_{bi}} \bar{T}_T(\bar{Y}_1) d\bar{Y}_1 , \quad (3.70)$$

and can be computed for a known tangential contact stress distribution $\bar{T}_T(\bar{Y}_1)$.

Contact field variables

Besides the stator and rotor equations, there are the contact field variables, which consist of the kinematic field variables, namely, the contact layer displacement, the contact gap and the relative velocity as well as the normal and tangential contact stress between stator and rotor surfaces. These field variables were derived in Section 3.2.2 together with expressions for the corresponding integration constants. Here, the field variables are summarized.

Normal contact state The normal contact layer displacement was splitted into parts describing the displacement in contact zones, (3.23), and in non-contact zones, (3.26). Substitution of the integration constant by (3.37) results in

$$\bar{w}_c(\bar{Y}_1) = \begin{cases} \bar{w}_s - \bar{w}_r & , \quad \forall \bar{Y}_1 \in \partial \mathcal{B}_{ci} \\ \left[\bar{w}_s(p_{ei+1}) - \bar{w}_r(p_{ei+1}) \right] e^{\frac{L_{w14}}{L_{w15}}(p_{ei+1} - \bar{Y}_1)} & , \quad \forall \bar{Y}_1 \in \partial \mathcal{B}_{nci} \end{cases} . \quad (3.71)$$

Summarizing the expressions for the contact gap function in the different contact areas, yields

$$\bar{g}_N(\bar{Y}_1) = \begin{cases} 0 & , \quad \forall \bar{Y}_1 \in \partial \mathcal{B}_{ci} \\ \left[\bar{w}_s(p_{ei+1}) - \bar{w}_r(p_{ei+1}) \right] e^{\frac{L_{w14}}{L_{w15}}(p_{ei+1} - \bar{Y}_1)} & . \quad (3.72) \\ +\bar{w}_r(\bar{Y}_1) - \bar{w}_s(\bar{Y}_1) > 0 & , \quad \forall \bar{Y}_1 \in \partial \mathcal{B}_{nci} \end{cases}$$

Similarly, the normal contact stress in the different contact zones is complementary to the gap function, giving

$$\bar{T}_N(\bar{Y}_1) = \begin{cases} -\frac{1}{L_{w18}} \left[L_{w14} (\bar{w}_s - \bar{w}_r) + L_{w15} (\bar{w}'_s - \bar{w}'_r) \right], & \forall \bar{Y}_1 \in \partial\mathcal{B}_{ci} \\ 0 & , \forall \bar{Y}_1 \in \partial\mathcal{B}_{nci} \end{cases} . \quad (3.73)$$

By inspection of (3.72) and (3.73) the complementary character of the gap function and the normal stress gets obvious

$$\bar{g}_N(\bar{Y}_1) \geq , \quad \bar{T}_N(\bar{Y}_1) \leq , \quad \bar{g}_N(\bar{Y}_1) \bar{T}_N(\bar{Y}_1) = 0 . \quad (3.74)$$

This is the so-called non-penetration condition or KUHN-TUCKER condition for frictionless contact problems (see WRIGGERS (1995, [62], p.10).

Tangential contact state Summarizing the tangential contact layer displacements in the different contact subzones given by (3.28), (3.31) and (3.35) yields

$$\bar{u}_c(\bar{Y}_1) = \begin{cases} \frac{1}{SS_7} [\bar{v}_r \bar{Y}_1 - SS_2 \bar{w}'_s - SS_5 \bar{w}'_r] + C_{ui}^{stick_j} & , \forall \bar{Y}_1 \in \partial\bar{\mathcal{B}}_{ci}^{stick_j} \\ C_{ui}^{slip_j} e^{-\frac{1}{L_{u13}} \bar{Y}_1} + \bar{u}_{cp}^{slip}(\bar{Y}_1) & , \forall \bar{Y}_1 \in \partial\bar{\mathcal{B}}_{ci}^{slip_j} \\ C_{ui}^{free} e^{-\frac{1}{L_{u13}} \bar{Y}_1} & , \forall \bar{Y}_1 \in \partial\bar{\mathcal{B}}_{nci} \end{cases} . \quad (3.75)$$

The relative velocity becomes

$$\dot{\bar{g}}_T(\bar{Y}_1) = \begin{cases} 0 & , \forall \bar{Y}_1 \in \partial\bar{\mathcal{B}}_{ci}^{stick_j} \\ SS_2 \bar{w}''_s + SS_5 \bar{w}''_r + SS_7 (\bar{u}_c^{slip})' - \bar{v}_r & , \forall \bar{Y}_1 \in \partial\bar{\mathcal{B}}_{ci}^{slip_j} \end{cases} , \quad (3.76)$$

using (3.34) and the tangential contact stress is given by combination of (3.29) and (3.33):

$$\bar{T}_T(\bar{Y}_1) = \begin{cases} 0 & , \forall \bar{Y}_1 \in \partial\bar{\mathcal{B}}_{nci} \\ -\frac{1}{L_{u19} SS_7} \left[\bar{v}_r \bar{Y}_1 - SS_2 \bar{w}'_s - SS_5 \bar{w}'_r \right. \\ \quad \left. + L_{u13} (\bar{v}_r - SS_2 \bar{w}''_s - SS_5 \bar{w}''_r) \right] - \frac{1}{L_{u19}} C_{ui}^{stick_j} & , \forall \bar{Y}_1 \in \partial\bar{\mathcal{B}}_{ci}^{stick_j} \\ \mu \text{sign}(\dot{\bar{g}}_T^{slip}) \left[L_{w14} (\bar{w}_s - \bar{w}_r) + L_{w15} (\bar{w}'_s - \bar{w}'_r) \right] & , \forall \bar{Y}_1 \in \partial\bar{\mathcal{B}}_{ci}^{slip_j} . \end{cases} \quad (3.77)$$

It should be noted, that the integration constants $C_{ui}^{stick_j}$, $C_{ui}^{slip_j}$ and C_{ui}^{free} are not substituted, since the topology (stick-slip sequences) of the tangential field variables, (3.75)-(3.77), are not known a priori. They have to be determined by continuity conditions of the tangential contact layer displacement u_c at the boundaries of the contact subzones (see Section 3.2.4).

Initial state and contact topology

For a given system state (e.g. the state at rest, see (3.66)), all state variables are known. This includes the integration constants of the field variables

$$C_{ui}^{stick_j}, \quad C_{ui}^{slip_j}, \quad C_{ui}^{free} \quad \text{with} \quad i = 1, \dots, N_c; \quad j = 1, \dots, N_{ct_i} + 1, \quad (3.78)$$

the displacements of stator, rotor and contact layer

$$\bar{w}_s(\bar{Y}_1), \quad \bar{w}_r(\bar{Y}_1), \quad \bar{w}_c(\bar{Y}_1) = f_w(\bar{w}_s(\bar{Y}_1), \bar{w}_r(\bar{Y}_1)), \quad \bar{u}_c(\bar{Y}_1) = f_u(\bar{w}_s(\bar{Y}_1), \bar{w}_r(\bar{Y}_1)),$$

where \bar{w}_c and \bar{u}_c are expressed as functions of the stator and rotor displacements and the topology of the contact state, respectively, and the coordinates of the contact boundaries and the transition points

$$\{p_{ei}, p_{bi}\}, \quad \{p_{ti1}, \dots, p_{tij}, \dots, p_{ti(N_{ct_i})}\} \quad \text{with} \quad i = 1, \dots, N_c. \quad (3.79)$$

Contact search equations

Topological changes in the contact states occur when stator and rotor surface points come into contact, separate or new stick-slip contact subzones appear. Such events result in a change of the number of integration constants, (3.78) and boundary and transition points, (3.79), respectively. Contact search equations are necessary to indicate new contact topologies. Additionally, they give first approximations of the coordinates of the contact boundaries and the transition points. In this section, the topological changes of normal and tangential contact states are studied and the necessary contact search equations are presented. The different variations of contact states are described according to Section 2.3.3.

Normal contact It is distinguished between contact processes which generate new contact zones and those where contact zones vanish. The first type of contact processes corresponds to mechanisms where stator and rotor surface points in a contact zone begin to separate or where stator and rotor surface points within a non-contact zone approach each other. The second type describes contact processes where contact zones vanish either by merging of neighboring contact zones or by shrinking of contact zones to zero length. In both cases the contact topology changes.

New subzones: Separation and Approach Separation of stator and rotor surface points occurs when the normal contact stress in a contact zone becomes positive, i.e. if tensile stresses occur

$$\bar{T}_N^*(\bar{Y}_1) < 0 \quad \Rightarrow \quad \bar{T}_N^*(\bar{Y}_1) > 0, \quad \bar{Y}_1 \in \partial\mathcal{B}_{ci} = [p_{ei}, p_{bi}]. \quad (3.80)$$

For the new non-contact subzone

$$\bar{T}_N^*(\bar{Y}_1) = 0, \quad \bar{Y}_1 \in [p_{bi}, p_{e(i+1)}], \quad (3.81)$$

is valid, where $\{p_{bi}, p_{e(i+1)}\}$ are the new contact boundaries. On the contrary, an approach of surface points takes place under a change of sign in the contact gap function, i.e. if penetration occurs

$$\bar{g}_N(\bar{Y}_1) > 0 \quad \Rightarrow \quad \bar{g}_N(\bar{Y}_1) < 0, \quad \bar{Y}_1 \in [p_{bi}, p_{e(i+1)}] \not\subset \partial\mathcal{B}_{ci}. \quad (3.82)$$

In the new contact zone, $[p_{e(i+1)}, p_{b(i+1)}]$,

$$\bar{g}_N(\bar{Y}_1) = 0, \quad \forall \bar{Y}_1 \in [p_{e(i+1)}, p_{b(i+1)}]. \quad (3.83)$$

holds.

Vanishing subzones: Merging and Shrinking On the one hand, contact zones vanish if neighboring contact zones merge, i.e. if contact boundaries of different contact zones approach each other:

$$\partial\mathcal{B}_{ci} = [p_{ei}, p_{bi}], \quad \partial\mathcal{B}_{c(i+1)} = [p_{e(i+1)}, p_{b(i+1)}] : \quad p_{bi} \rightarrow p_{e(i+1)}.$$

On the other hand, contact zones also vanish if contact boundaries of the same contact zone approach each other, i.e. the contact length shrinks to zero

$$\partial\mathcal{B}_{ci} = [p_{ei}, p_{bi}] : \quad p_{ei} \rightarrow p_{bi}.$$

Tangential contact The contact search for transition coordinates p_{tij} between stick- and slip-subzones starts at the contact boundaries p_{bi} . Under the assumption of sticking, it is checked, whether the sticking condition is valid or violated. The sign of the indicator function $f(\bar{Y}_1)$ in (3.42) determines, which tangential contact state

$$f(p_{bi}) < 0 \quad \text{begin with stick in the } i\text{-th contact zone}$$

or

$$f(p_{bi}) > 0 \quad \text{begin with slip in the } i\text{-th contact zone,}$$

is valid at the beginning of a contact zone. To find transitions from stick to slip or vice versa each contact zone is checked from the beginning (coordinate p_{bi}) towards the end (coordinate p_{ei}) for the first zero of each active indicator function:

$$\begin{aligned} \text{stick} \rightarrow \text{slip} & : \quad f(\bar{Y}_1) < 0 \quad \rightarrow \quad f(\bar{Y}_1) > 0 \\ \text{slip} \rightarrow \text{stick} & : \quad \dot{g}_T(\bar{Y}_1) > 0 \quad \rightarrow \quad \dot{g}_T(\bar{Y}_1) < 0, \quad \text{or} \\ \text{slip} \rightarrow \text{stick} & : \quad \dot{g}_T(\bar{Y}_1) < 0 \quad \rightarrow \quad \dot{g}_T(\bar{Y}_1) > 0. \end{aligned}$$

at each case. The indicator function $\dot{g}_T(\bar{Y}_1)$ is stated in (3.46).

3.2.4 Contact boundaries and transitions

The contact search equations in Section 3.2.3 are used to find the contact topology. The exact values of the contact boundaries and the transition coordinates between stick and slip-subzones are subsequently determined by solving a set of boundary and transition equations, which are stated below.

Normal contact

The contact boundary conditions for normal contact have already been derived in (3.2.2). At the beginning and the end of contact zones (3.38) and (3.39) must be fulfilled, leading to

$$\begin{aligned} \bar{g}_N(p_{bi}) &\equiv [\bar{w}_s(p_{ei+1}) - \bar{w}_r(p_{ei+1})] e^{-\frac{L_{w14}}{L_{w15}}(p_{bi} - p_{ei+1})} \\ &+ \bar{w}_r(p_{bi}) - \bar{w}_s(p_{bi}) = 0, \end{aligned} \quad (3.84)$$

$$\begin{aligned} \bar{T}_N^*(p_{ei}) &\equiv -\frac{1}{L_{w18}} [L_{w14} (\bar{w}_s(p_{ei}) - \bar{w}_r(p_{ei})) \\ &+ L_{w15} (\bar{w}'_s(p_{ei}) - \bar{w}'_r(p_{ei}))] = 0. \end{aligned} \quad (3.85)$$

Tangential contact

Two sets of equations are required to determine the integration constants, (3.78) and the transition coordinates, (3.79), of the tangential contact state. One set of equations is delivered by continuity conditions of the tangential displacement u_c at the contact boundaries and transition points. This is used to determine the integration constants. In each contact zone the following equations hold:

$$\bar{u}_{ci}^{state2}(p_{bi}) = \bar{u}_{ci}^{free}(p_{bi}) \quad (3.86)$$

$$\begin{aligned} &\vdots \\ \bar{u}_{ci}^{state(j+1)}(p_{tij}) &= \bar{u}_{ci}^{statej}(p_{tij}) \end{aligned} \quad (3.87)$$

$$\begin{aligned} &\vdots \\ \bar{u}_{c(i-1)}^{free}(p_{ei}) &= \bar{u}_{ci}^{stateN_{cti}-1}(p_{ei}), \end{aligned} \quad (3.88)$$

where $state \in \{\text{stick}, \text{slip}\}$. It should be mentioned here, that besides these general contact states, also degenerate contact states exist. In the case of full contact between

stator and rotor and various stick/slip subzones, the equations

$$\bar{u}_{c1}^{state_2}(p_{t11}) = \bar{u}_{c1}^{state_1}(p_{t11}) \quad (3.89)$$

$$\begin{aligned} & \vdots \\ \bar{u}_{c1}^{state_{(j+1)}}(p_{t1j}) &= \bar{u}_{c1}^{state_j}(p_{t1j}) \end{aligned} \quad (3.90)$$

$$\begin{aligned} & \vdots \\ \bar{u}_{c1}^{state_{N_{cti}+1}}(p_{t1(N_{cti})}) &= \bar{u}_{c1}^{state_{N_{cti}}}(p_{t1(N_{cti})}) \end{aligned} \quad (3.91)$$

$$\bar{u}_{c1}^{state_{N_{cti}+1}}(0) = \bar{u}_{c1}^{state_1}(n_s) \quad (3.92)$$

must be used instead. Two other degenerate contact states are full contact, $\bar{g}_N(\bar{Y}_1) = 0$, $\forall \bar{Y}_1 \in [0, n_s]$, with either pure slip-condition or pure stick-condition. For pure slip, the periodicity condition

$$\bar{u}_{c1}^{slip_1}(0) = \bar{u}_{c1}^{slip_1}(n_s) \quad (3.93)$$

must be fulfilled, thus $C_{u1}^{slip_1} = 0$ holds and only the particular solution

$$\bar{u}_{c1}^{slip_1}(\bar{Y}_1) = \bar{u}_{cp1}^{slip_1}(\bar{Y}_1) \quad (3.94)$$

remains. In case of pure stick a similar periodicity condition holds

$$\bar{u}_{c1}^{stick_1}(0) = \bar{u}_{c1}^{stick_1}(n_s) . \quad (3.95)$$

This requires the rotor speed to vanish, i.e. $\bar{v}_r = 0$. Without stator and rotor bending deformation, there is no tangential displacement and the integration constant vanishes:

$$u_c(\bar{Y}_1) = 0, \quad \text{for} \quad w'_s = w'_r = 0 \quad \Rightarrow \quad C_{u1}^{stick_1} = 0 . \quad (3.96)$$

The coordinates p_{tij} of the contact transition points P_{tij} are obtained by computing the zeros of the indicator functions, (3.42) and (3.46), respectively. Inserting (3.29) and (3.24) into (3.42) yields the equation for transition from stick to slip tangential contact

$$\begin{aligned} f(p_{tij}) &\equiv \left| \frac{1}{L_{u19} SS_7} [\bar{v}_r p_{tij} - SS_2 \bar{w}'_s - SS_5 \bar{w}'_r + L_{u13} (\bar{v}_r - SS_2 \bar{w}''_s - SS_5 \bar{w}''_r)] \right. \\ &\quad \left. + \frac{1}{L_{u19}} C_{ui}^{stick_j} \right| - \left| \frac{\mu}{L_{w18}} [L_{w14} (\bar{w}_s - \bar{w}_r) + L_{w15} (\bar{w}'_s - \bar{w}'_r)] \right| = 0 . \end{aligned} \quad (3.97)$$

Analogously, inserting (3.31) in (3.46) results in the equation for transition from slip to stick tangential contact

$$\begin{aligned} \dot{\bar{g}}_T^{slip}(p_{tij}) &\equiv SS_2 \bar{w}''_s(p_{tij}) + SS_5 \bar{w}''_r(p_{tij}) - \frac{SS_7}{L_{u13}} C_{ui}^{slip_j} e^{-\frac{p_{tij}}{L_{u13}}} \\ &\quad + (\bar{u}_{cp}^{slip})'(p_{tij}) - \bar{v}_r = 0 . \end{aligned} \quad (3.98)$$

Equations (3.97) and (3.98) are called *contact transition equations*.

3.2.5 GALERKIN discretization

In Section 3.2.2, the set of ODE's for steady-state motor operation have been given, (3.6)-(3.19). For the numerical solution procedure, a spatial GALERKIN-discretization will be carried out.

Shape-functions

Rotary USMs exhibit a spatial periodicity having a fundamental wave length corresponding to the dimensionless length n_s (see Section 3.2.1). Therefore, it is reasonable to use global, periodic shape-functions for the displacement of stator and rotor

$$\chi_k(Y) = \begin{cases} 1 & \text{if } k = 1 \\ \cos\left(\frac{k}{2} \frac{2\pi}{n_s} \bar{Y}_1\right) & \text{if } k \text{ is even} \\ \sin\left(\frac{k-1}{2} \frac{2\pi}{n_s} \bar{Y}_1\right) & \text{if } k \text{ is odd} \end{cases}, \quad \text{with } k = 2, \dots, 2N_s + 1. \quad (3.99)$$

The stator and rotor displacements are expressed by

$$\bar{w}_s(\bar{Y}_1) = \sum_{k=1}^{2N_s+1} q_{sk} \chi_k(\bar{Y}_1), \quad \bar{w}_r(\bar{Y}_1) = \sum_{k=1}^{2N_s+1} q_{rk} \chi_k(\bar{Y}_1), \quad (3.100)$$

with the state variables q_{sk} and q_{rk} . Contact forces, by themselves, must be considered as local quantities. Thus, the discretization method has to take into account the local character of the contact forces and as a result the local deformations of the contact layer. As pointed out in Section 3.2.2, the normal displacement of the contact layer \bar{w}_c in the contact zones can be expressed by the stator and rotor displacements. Together with the contact layer displacement outside the contact zones, its displacement can be summarized as given in (3.71). The situation is different for the tangential contact layer displacement \bar{u}_c . In the contact region, the tangential contact layer displacement must satisfy an inhomogeneous ODE, (3.32). The ansatz

$$\bar{u}_{cp}^{slip}(\bar{Y}_1) = \text{sign}(\dot{g}_T) \sum_{k=1}^{2N_s+1} q_{ck} \chi_k(\bar{Y}_1), \quad \bar{Y}_1 \in \partial\mathcal{B}_{ci}^{stick_j} \quad (3.101)$$

is chosen to find the particular solution of the tangential contact layer displacement within a slip-subzone. As it was stated earlier, the objective is to express both displacement variables of the contact layer in terms of the stator and rotor displacements. Therefore, the state variables q_{ck} in the ansatz (3.101) must be expressed by the state variables of stator and rotor, q_{sk} and q_{rk} , respectively. In order to do so, (3.101) together with (3.100) are substituted into (3.32). Sorting and comparing the state variables results in expressions for the q_{ck} . The relations in the different contact and non-contact regions are summarized in (3.75).

Vector notations

The displacement field variables are written in vector notation as

$$\mathbf{u}(\bar{Y}_1) = [\bar{w}_s(\bar{Y}_1), \bar{w}_r(\bar{Y}_1), \bar{w}_c(\bar{Y}_1), \bar{u}_c(\bar{Y}_1)] . \quad (3.102)$$

Similarly, the coordinates of the contact state are assembled in vector form as

$$\mathbf{C} = [C_{u1}^{free_1}, C_{u1}^{state_1}, \dots, C_{u1}^{state_{N_{ct1}+1}}, \dots, C_{u2}^{free_1}, C_{u2}^{state_1}, \dots, C_{u(N_c)}^{state_{N_{ct}(N_c)+1}}]^T . \quad (3.103)$$

A vector notation is chosen also for the coordinates of the contact topology

$$\begin{aligned} \mathbf{p}_N &= [\mathbf{p}_{N1}^T, \dots, \mathbf{p}_{NN_c}^T]^T = [p_{e1}, p_{b1}, \dots, p_{ei}, p_{bi}, \dots, p_{eN_c}, p_{bN_c}]^T \\ \mathbf{p}_T &= [\mathbf{p}_{T1}^T, \dots, \mathbf{p}_{TN_c}^T]^T = [p_{t11}, p_{t12}, \dots, p_{tij}, \dots, p_{(N_c)(1)}, p_{(N_c)(N_{ctN_c})}]^T , \end{aligned} \quad (3.104)$$

with $\mathbf{p}_{Ni} = [p_{ei}, p_{bi}]^T$ and $\mathbf{p}_{Ti} = [p_{ti1}, \dots, p_{tiN_{cti}}]^T$. The vectors of the state variables are assembled as

$$\mathbf{q}_s = [q_{s0}, \dots, q_{s(2N_s+1)}]^T, \quad \mathbf{q}_r = [q_{r0}, \dots, q_{r(2N_s+1)}]^T \quad (3.105)$$

and the composed vector of all state variables is written as

$$\mathbf{q} = [\mathbf{q}_s^T, \mathbf{q}_r^T]^T . \quad (3.106)$$

Introduction of a matrix notation for the shape functions

$$\boldsymbol{\chi} = [\chi_1(\bar{Y}_1), \dots, \chi_{2N_s+1}(\bar{Y}_1)], \quad \bar{w} = \boldsymbol{\chi} \mathbf{q} \quad (3.107)$$

results in a vector notation of the discretized displacement variables.

Discretization of the system equations

The next step in the discretization procedure is the integration of the stator and rotor equations of motion, given in (3.68) and (3.69), respectively. The procedure is explained for the stator equation, the discretization of the rotor equation follows in an analogous manner. The stator stiffness matrix \mathbf{K}_s is obtained by the integration procedure

$$\begin{aligned} \mathbf{K}_s \mathbf{q} &: \int_0^{n_s} \mathcal{K}_s[\bar{w}_s(\bar{Y}_1)] \chi_k(\bar{Y}_1) d\bar{Y}_1 \\ K_{skl} &= \int_0^{n_s} \mathcal{K}_s[\chi_l(\bar{Y}_1)] \chi_k(\bar{Y}_1) d\bar{Y}_1 . \end{aligned} \quad (3.108)$$

The symbol \mathcal{K}_s represents the functional of all terms in (3.6) containing the displacement variable \bar{w}_s . For the terms with the normal contact stresses two *normal contact stiffness matrices* \mathbf{K}_{cNss} and \mathbf{K}_{cNsr} , for one contact zone, are given by

$$\begin{aligned} \mathbf{K}_{cNss}(\mathbf{p}_{Ni}) \mathbf{q} &: \int_{p_{ei}}^{p_{bi}} \mathcal{T}_{Nss}[\bar{w}_s(\bar{Y}_1)] \chi_k(\bar{Y}_1) d\bar{Y}_1 \\ K_{cNsskl}(p_{ei}, p_{bi}) &= \int_{p_{ei}}^{p_{bi}} \mathcal{T}_{Nss}[\chi_l(\bar{Y}_1)] \chi_k(\bar{Y}_1) d\bar{Y}_1, \end{aligned} \quad (3.109)$$

$$\begin{aligned} \mathbf{K}_{cNsr}(\mathbf{p}_{Ni}) \mathbf{q} &: \int_{p_{ei}}^{p_{bi}} \mathcal{T}_{Nsr}[\bar{w}_r(\bar{Y}_1)] \chi_k(\bar{Y}_1) d\bar{Y}_1 \\ K_{cNsrkl}(p_{ei}, p_{bi}) &= \int_{p_{ei}}^{p_{bi}} \mathcal{T}_{Nsr}[\chi_l(\bar{Y}_1)] \chi_k(\bar{Y}_1) d\bar{Y}_1, \end{aligned} \quad (3.110)$$

with the functionals

$$\mathcal{T}_{Nss}[\bar{w}_s(\bar{Y}_1)] = -\frac{1}{L_{w18}} [L_{w14}(\bar{w}_s) + L_{w15}(\bar{w}'_s)], \quad (3.111)$$

$$\mathcal{T}_{Nsr}[\bar{w}_r(\bar{Y}_1)] = -\frac{1}{L_{w18}} [L_{w14}(-\bar{w}_r) + L_{w15}(-\bar{w}'_r)]. \quad (3.112)$$

The *tangential contact stiffness matrices*, $\mathbf{K}_{cTss}^{stick}(\mathbf{p}_{Ni}, \mathbf{p}_{Tj})$, $\mathbf{K}_{cTsr}^{stick}(\mathbf{p}_{Ni}, \mathbf{p}_{Tj})$ for the case of sticking and $\mathbf{K}_{cTss}^{slip}(\mathbf{p}_{Ni}, \mathbf{p}_{Tj})$, $\mathbf{K}_{cTsr}^{slip}(\mathbf{p}_{Ni}, \mathbf{p}_{Tj})$ for the case of slipping can be obtained in an analogous manner. The components of the tangential stiffness matrices $\mathbf{K}_{cTss}^{stick}$ and $\mathbf{K}_{cTsr}^{stick}$, for example, are derived as

$$\mathbf{K}_{cTss}(\mathbf{p}_{Ni}, \mathbf{p}_{Tj}) \mathbf{q} : \int_{p_{tij}}^{p_{ti(j+1)}} \mathcal{T}_{Tss}[\bar{w}_s(\bar{Y}_1)] \chi_k(\bar{Y}_1) d\bar{Y}_1 \quad (3.113)$$

$$K_{cTsskl}(\mathbf{p}_{Ni}, \mathbf{p}_{Tj}) = \int_{p_{tij}}^{p_{ti(j+1)}} \mathcal{T}_{Tss}[\chi_l(\bar{Y}_1)] \chi_k(\bar{Y}_1) d\bar{Y}_1,$$

$$\mathbf{K}_{cTsr}(\mathbf{p}_{Ni}, \mathbf{p}_{Tj}) \mathbf{q} : \int_{p_{tij}}^{p_{ti(j+1)}} \mathcal{T}_{Tsr}[\bar{w}_r(\bar{Y}_1)] \chi_k(\bar{Y}_1) d\bar{Y}_1 \quad (3.114)$$

$$K_{cTsrkl}(\mathbf{p}_{Ni}, \mathbf{p}_{Tj}) = \int_{p_{tij}}^{p_{ti(j+1)}} \mathcal{T}_{Tsr}[\chi_l(\bar{Y}_1)] \chi_k(\bar{Y}_1) d\bar{Y}_1,$$

with the functionals

$$\mathcal{T}_{Tss}[\bar{w}_s(\bar{Y}_1)] = \frac{SS_2}{L_{u19} SS_7} [(\bar{w}_s)'' + L_{u13}(\bar{w}_s)'''], \quad (3.115)$$

$$\mathcal{T}_{Tsr}[\bar{w}_r(\bar{Y}_1)] = \frac{1}{L_{u19} SS_7} [-\bar{v}_r + SS_5(\bar{w}_r)'' + L_{u13}(\bar{w}_r)''']. \quad (3.116)$$

Note, that the boundaries of the integrals in (3.113) and (3.114) can also be contact boundary coordinates p_{ei}, p_{bi} .

The rotor stiffness matrix \mathbf{K}_r , the *normal contact stiffness matrices* \mathbf{K}_{cNrs} and \mathbf{K}_{cNrr} and the *tangential contact stiffness matrices*, $\mathbf{K}_{cTrs}^{stick}(\mathbf{p}_{Ni}, \mathbf{p}_{Tj})$, $\mathbf{K}_{cTrs}^{slip}(\mathbf{p}_{Ni}, \mathbf{p}_{Tj})$, and $\mathbf{K}_{cTrr}^{stick}(\mathbf{p}_{Ni}, \mathbf{p}_{Tj})$, $\mathbf{K}_{cTrr}^{slip}(\mathbf{p}_{Ni}, \mathbf{p}_{Tj})$ are built up in a similar way, by integrating the rotor equation of motion, (3.8).

System equations in matrix notation

The system matrix is composed of the stator and rotor stiffness matrices and the normal contact matrices

$$\mathbf{K} = \begin{bmatrix} \mathbf{K}_s & \mathbf{0} \\ \mathbf{0} & \mathbf{K}_r \end{bmatrix}, \quad \mathbf{K}_{cNi} = \begin{bmatrix} \mathbf{K}_{cNss}(\mathbf{p}_{Ni}) & \mathbf{K}_{cNsr}(\mathbf{p}_{Ni}) \\ \mathbf{K}_{cNrs}(\mathbf{p}_{Ni}) & \mathbf{K}_{cNrr}(\mathbf{p}_{Ni}) \end{bmatrix}, \quad (3.117)$$

as well as the tangential stiffness matrices for sticking

$$\mathbf{K}_{cT}^{stick}(\mathbf{p}_{Ni}, \mathbf{p}_{Tj}) = \begin{bmatrix} \mathbf{K}_{cTss}^{stick}(\mathbf{p}_{Ni}, \mathbf{p}_{Tj}) & \mathbf{K}_{cTsr}^{stick}(\mathbf{p}_{Ni}, \mathbf{p}_{Tj}) \\ \mathbf{K}_{cTrs}^{stick}(\mathbf{p}_{Ni}, \mathbf{p}_{Tj}) & \mathbf{K}_{cTrr}^{stick}(\mathbf{p}_{Ni}, \mathbf{p}_{Tj}) \end{bmatrix}, \quad (3.118)$$

and the tangential stiffness matrices for slipping, yielding \mathbf{K}_{cT}^{slip} . The system matrix equation can be written as

$$\left[\mathbf{K} + \mathbf{K}_{cN}(\mathbf{p}_N) + \mathbf{K}_{cT}^{stick}(\mathbf{p}_N, \mathbf{p}_T) + \mathbf{K}_{cT}^{slip}(\mathbf{p}_N, \mathbf{p}_T) \right] \mathbf{q} = \mathbf{F}, \quad (3.119)$$

with

$$\mathbf{K}_{cN}(\mathbf{p}_N) = \sum_{i=1}^{N_c} \mathbf{K}_{cN}(\mathbf{p}_{Ni}), \quad (3.120)$$

$$\mathbf{K}_{cT}^{stick}(\mathbf{p}_N, \mathbf{p}_T) = \sum_{i=1}^{N_c} \sum_{j=1}^{N_{cti}+1} \mathbf{K}_{cT}^{stick}(\mathbf{p}_{Ni}, \mathbf{p}_{Tj}), \quad (3.121)$$

$$\mathbf{K}_{cT}^{slip}(\mathbf{p}_N, \mathbf{p}_T) = \sum_{i=1}^{N_c} \sum_{j=1}^{N_{cti}+1} \mathbf{K}_{cT}^{slip}(\mathbf{p}_{Ni}, \mathbf{p}_{Tj}). \quad (3.122)$$

Contact boundary and transition equations in matrix notation

Since (3.119) contains the unknown contact boundary variables \mathbf{p}_N , \mathbf{p}_T , additional equations are needed. Those have been stated in Section 3.2.4. The *contact boundary equations*, according to (3.38) and (3.39), can be assembled in matrix form as

$$\mathbf{Z}_N(\mathbf{p}_N) \mathbf{q} = \begin{bmatrix} \bar{g}_N(p_{b1}) \\ \bar{T}_N^*(p_{e1}) \\ \vdots \\ \bar{g}_N(p_{bN_c}) \\ \bar{T}_N^*(p_{eN_c}) \end{bmatrix} = \mathbf{0}. \quad (3.123)$$

Substituting the displacement variables in (3.107) and (3.38) by (3.39) yields the constraint matrix

$$\mathbf{Z}_N(\mathbf{p}_N) = \begin{bmatrix} Z_{11}^{gN} & Z_{12}^{gN} \\ Z_{11}^{TN} & Z_{12}^{TN} \\ \vdots & \vdots \\ Z_{(N_c)1}^{gN} & Z_{(N_c)2}^{gN} \\ Z_{(N_c)1}^{TN} & Z_{(N_c)2}^{TN} \end{bmatrix}, \quad (3.124)$$

with

$$\begin{aligned} Z_{11}^{gN} &= \chi(p_{e2}) e^{-\frac{L_{w14}}{L_{w15}}(p_{b1}-p_{e2})} - \chi(p_{b1}), & Z_{12}^{gN} &= -Z_{11} \\ &\vdots & & \\ Z_{(N_c)1}^{TN} &= -\frac{1}{L_{w18}}(L_{w14}\chi(p_{eN_c}) + L_{w15}\chi'(p_{eN_c})), & Z_{(N_c)2}^{TN} &= -Z_{(2N_c)1}. \end{aligned} \quad (3.125)$$

Besides contact boundary equations, there are *tangential displacement continuity conditions* which are formulated in (3.86)-(3.88). Substituting the ansatz, (3.100), and sorting with respect to the unknown variables yields the discrete form of the continuity equations

$$\mathbf{Z}_{c1}(\mathbf{p}_N, \mathbf{p}_T) \mathbf{C} = \mathbf{Z}_{c2}(\mathbf{p}_N, \mathbf{p}_T) + \mathbf{Z}_{c3}(\mathbf{p}_N, \mathbf{p}_T) \mathbf{q}. \quad (3.127)$$

The coefficients of the matrices \mathbf{Z}_{c1} , \mathbf{Z}_{c3} and the vector \mathbf{Z}_{c2} in (3.127) cannot be stated a priori, since they depend on the sequence of stick-slip transitions in each contact zone.

The last set of equations, which is necessary to solve the contact problem, is constituted by the *contact transition conditions*, represented by (3.97) and (3.98). Inserting the GALERKIN-Ansatz, (3.100), into both equations, yields

$$\begin{bmatrix} f(p_{t11}) \\ \dot{g}_T^{slip}(p_{t11}) \\ \vdots \\ f(p_{tij}) \\ \dot{g}_T^{slip}(p_{tij}) \\ \vdots \\ f(p_{t(N_c)(N_{tc_{N_c}})}) \\ \dot{g}_T^{slip}(p_{t(N_c)(N_{tc_{N_c}})}) \end{bmatrix} \equiv \mathbf{Z}_I(\mathbf{p}_T, \mathbf{C}, \mathbf{q}) = \mathbf{0}. \quad (3.128)$$

Contact search equations in matrix notation

To check for changes of the contact topology, a discretization of the contact surface $\partial\mathcal{B}_{rc}$ is needed. The length of the motor n_s is spatially discretized in equidistant points, according to

$$\bar{Y}_{1k} = (k-1) \Delta \bar{Y}_1, \quad \Delta \bar{Y}_1 = \frac{n_s}{N_y}, \quad k = 1, \dots, N_y + 1. \quad (3.129)$$

The discretized form of the normal contact stress in (3.73) can be written as

$$\bar{T}_N(\bar{Y}_{1k}) = \begin{cases} \mathbf{N}_{T_N}(\bar{Y}_{1k}) \mathbf{q} & , \quad \forall \bar{Y}_{1k} \in \partial\mathcal{B}_{ci} \\ 0 & , \quad \forall \bar{Y}_{1k} \in \partial\mathcal{B}_{nci} \end{cases}, \quad (3.130)$$

with the normal stress shape vector

$$\mathbf{N}_{T_N}(\bar{Y}_{1k}) = \frac{1}{L_{w18}} \left[\left(-L_{w14} \boldsymbol{\chi}(\bar{Y}_{1k}) - L_{w15} \boldsymbol{\chi}'(\bar{Y}_{1k}) \right) \right. \\ \left. \left(L_{w14} \boldsymbol{\chi}(\bar{Y}_{1k}) + L_{w15} \boldsymbol{\chi}'(\bar{Y}_{1k}) \right) \right]. \quad (3.131)$$

Similarly, the discrete form of the contact gap function writes

$$\bar{g}_N(\bar{Y}_{1k}) = \begin{cases} 0 & , \quad \forall \bar{Y}_{1k} \in \partial\mathcal{B}_{ci} \\ \mathbf{N}_{g_N}(\bar{Y}_{1k}) \mathbf{q} & , \quad \forall \bar{Y}_{1k} \in \partial\mathcal{B}_{nci} \end{cases}, \quad (3.132)$$

with the contact gap vector

$$\mathbf{N}_{g_N}(\bar{Y}_{1k}) = \left[\left(e^{\frac{L_{w14}}{L_{w15}}(p_{ei+1}-Y_{1k})} \boldsymbol{\chi}(p_{ei+1}) - \boldsymbol{\chi}(\bar{Y}_{1k}) \right) \right. \\ \left. \left(-e^{\frac{L_{w14}}{L_{w15}}(p_{ei+1}-Y_{1k})} \boldsymbol{\chi}(p_{ei+1}) + \boldsymbol{\chi}(\bar{Y}_{1k}) \right) \right]. \quad (3.133)$$

Other quantities, like the indicator functions (3.42), (3.46) or the tangential stresses, are derived in an analogous manner. Since the principle of the procedure has been outlined above, the details are not given here. Only the matrix formulations are presented.

The discrete version of the tangential contact layer displacement in (3.75) is

$$\bar{u}_c(\bar{Y}_{1k}) = \begin{cases} \mathbf{N}_u^{stick}(\bar{Y}_{1k}) \mathbf{q} + \frac{1}{SS_7} \bar{v}_r \bar{Y}_{1k} + C_i^{stickj} & , \quad \forall \bar{Y}_{1k} \in \partial\bar{\mathcal{B}}_{ci}^{stickj} \\ C_{ui}^{slipj} e^{-\frac{\bar{Y}_{1k}}{L_{u13}}} + \mathbf{N}_u^{slip}(\bar{Y}_{1k}) \mathbf{q} & , \quad \forall \bar{Y}_{1k} \in \partial\bar{\mathcal{B}}_{ci}^{slipj} \\ C_{ui}^{free} e^{-\frac{1}{L_{u13}} \bar{Y}_{1k}} & , \quad \forall \bar{Y}_{1k} \in \partial\bar{\mathcal{B}}_{ci}^{free} \end{cases}. \quad (3.134)$$

To build up the shape vector \mathbf{N}_u^{slip} in (3.134), the particular solution of (3.32) is required, (see (3.101)). The relative velocity, (3.76), is expressed in its discrete form as

$$\dot{\bar{g}}_T(\bar{Y}_{1k}) = \begin{cases} 0 & , \quad \forall \bar{Y}_{1k} \in \partial\bar{\mathcal{B}}_{ci}^{stick_j} \\ \mathbf{N}_{\dot{\bar{g}}_T}^{slip}(\bar{Y}_{1k}) \mathbf{q} - \bar{v}_r & , \quad \forall \bar{Y}_{1k} \in \partial\bar{\mathcal{B}}_{ci}^{slip_j} \end{cases} . \quad (3.135)$$

The tangential contact stress, (3.77), results in the matrix formulation

$$\bar{T}_T(\bar{Y}_{1k}) = \begin{cases} 0 & , \quad \forall \bar{Y}_{1k} \in \partial\bar{\mathcal{B}}_{nci} \\ \mathbf{N}_{\bar{T}_T}^{stick}(\bar{Y}_{1k}) \mathbf{q} - \frac{1}{L_{u19}} \left[\frac{1}{SS_7} \bar{v}_r (\bar{Y}_{1k} + L_{u13}) C_{ui}^{stick_j} \right] & , \quad \forall \bar{Y}_{1k} \in \partial\bar{\mathcal{B}}_{ci}^{stick_j} \\ \mu \text{sign}(\dot{\bar{g}}_T) \mathbf{N}_{\bar{T}_T}^{slip}(\bar{Y}_{1k}) \mathbf{q} & , \quad \forall \bar{Y}_{1k} \in \partial\bar{\mathcal{B}}_{ci}^{slip_j} \end{cases} . \quad (3.136)$$

The discretized indicator functions to detect the transition points P_{tij} from stick to slip or vice versa become

$$f(\bar{Y}_{1k}) = \left| \mathbf{N}_{\bar{T}_T}^{stick}(\bar{Y}_{1k}) \mathbf{q} - \frac{1}{L_{u19}} \left[\frac{1}{SS_7} \bar{v}_r (\bar{Y}_{1k} + L_{u13}) + C_i^{stick_j} \right] \right| - \left| \mu \mathbf{N}_{T_N}(\bar{Y}_{1k}) \mathbf{q} \right| \quad (3.137)$$

$$\dot{\bar{g}}_T^{slip} = \mathbf{N}_{\dot{\bar{g}}_T}^{slip}(\bar{Y}_{1k}) \mathbf{q} - \bar{v}_r . \quad (3.138)$$

3.2.6 Problem statement

In this section, the problem formulation for the discretized equations is given in a comprehensive form:

Given are the external quantities,

$$\mathbf{\Lambda} = [\bar{V}_A, \bar{\Omega}, p_{axial}, \bar{v}_r] ,$$

the design parameters (see Tab. 2.2)

$$\mathbf{\Gamma} = [h_s, h_r, h_p, h_c, \rho_s, \rho_r, \dots] ,$$

and the initial system state

$$\mathbf{q}^{(0)}, \quad \mathbf{p}_N^{(0)}, \quad \mathbf{p}_T^{(0)}, \quad \mathbf{C}^{(0)} . \quad (3.139)$$

An initial state can be the state at rest, for example. The solution of this motor state is given in (3.66). Find solutions for the system state variables

$$\mathbf{q}^{(1)}, \quad \mathbf{p}_N^{(1)}, \quad \mathbf{p}_T^{(1)}, \quad \mathbf{C}^{(1)}. \quad (3.140)$$

and for the external load F for a quasi-static incremental change of any of the external quantities or one of the system parameters in the following non-linear matrix equations:

The system equations, taken from (3.119), which are given as

$$\left[\mathbf{K} + \mathbf{K}_{cN}(\mathbf{p}_N) + \mathbf{K}_{cT}^{stick}(\mathbf{p}_N, \mathbf{p}_T) + \mathbf{K}_{cT}^{slip}(\mathbf{p}_N, \mathbf{p}_T) \right] \mathbf{q} = \mathbf{F}, \quad (3.141)$$

with the constraint equations at the contact boundaries, (3.123), the continuity equations of tangential contact layer displacement, (3.127), and the equations of transition conditions between stick- and slip-subzones, (3.128),

$$\mathbf{Z}_N(\mathbf{p}_N) \mathbf{q} = \mathbf{0}, \quad (3.142)$$

$$\mathbf{Z}_{c1}(\mathbf{p}_N, \mathbf{p}_T) \mathbf{C} = \mathbf{Z}_{c2}(\mathbf{p}_N, \mathbf{p}_T) + \mathbf{Z}_{c3}(\mathbf{p}_N, \mathbf{p}_T) \mathbf{q}, \quad (3.143)$$

$$\mathbf{Z}_I(\mathbf{p}_T, \mathbf{C}, \mathbf{q}) = \mathbf{0}, \quad (3.144)$$

respectively. After an incremental change of one of the external or the design parameters, it must be checked whether a change of the contact state occurs. Separation between stator and contact layer surface points is detected, if the normal stress function gives a tensile stress

$$\text{contact} \rightarrow \text{non-contact} : \quad \exists \bar{Y}_{1k} \in \partial \mathcal{B}_{ci}, \quad \bar{T}_N(\bar{Y}_{1k}) > 0. \quad (3.145)$$

Oppositely, a contact approach in the non-contact subzones is detected if the gap function shows penetration (3.132)

$$\text{non-contact} \rightarrow \text{contact} : \quad \exists \bar{Y}_{1k} \in \partial \mathcal{B}_{ci}, \quad \bar{g}_N(\bar{Y}_{1k}) < 0. \quad (3.146)$$

The indicator functions to detect the transition points P_{tij} from stick to slip or vice versa become

stick \rightarrow slip :

$$\exists \bar{Y}_{1k} \in \partial \mathcal{B}_{ci}^{stick_j} \quad f(\bar{Y}_{1k}) > 0, \quad (3.147)$$

slip \rightarrow stick :

$$\exists \bar{Y}_{1k} \in \partial \mathcal{B}_{ci}^{slip_j} \quad \dot{\bar{g}}_T^{slip} < 0 \rightarrow \dot{\bar{g}}_T^{slip} > 0 \quad \text{or}, \quad (3.148)$$

$$\exists \bar{Y}_{1k} \in \partial \mathcal{B}_{ci}^{slip_j} \quad \dot{\bar{g}}_T^{slip} > 0 \rightarrow \dot{\bar{g}}_T^{slip} < 0. \quad (3.149)$$

Note, that the excitation frequency $\bar{\Omega}$ and the rotor speed \bar{v}_r are hidden in the stiffness and constraint matrices, whereas the excitation voltage and the axial prestress are

arranged in the vector of the external forces, \mathbf{F} ! The nonlinearity of the contact problem results, on the one hand, from the contact boundary variables. The coordinates p_{ei} and p_{bi} occur as arguments of trigonometric and exponential functions in (3.141) and (3.142). On the other hand, a nonlinearity is given by the frictional contact matrices. The stiffness matrix in (3.141) is a structural variable matrix, since the number of contact matrices during the contact process is not constant.

3.2.7 Contact Algorithm

Incremental solution procedure and updating Usually in USM modeling, the influence of the tangential contact on the normal contact is neglected. This a priori assumption needs a scaling analysis to be verified. The scaling procedure, which is carried out now, shows that this negligence is not suitable with the characteristic motor parameters given. For the following estimation, the terms of the contact stresses in the stator equation (3.6) are compared.

For a slip contact condition, i.e. $|\bar{T}'_T| = \mu |\bar{T}'_N|$ the ratio between both terms can be estimated as follows

$$\left| \frac{S[11]}{S[10]} \right| \frac{|\bar{T}'_T|}{|\bar{T}'_N|} = \frac{3}{5} \frac{h_s}{[\lambda]} \frac{|\bar{T}'_T|}{|\bar{T}'_N|} \frac{|\bar{T}'_T|}{|\bar{T}'_T|} = \frac{3}{5} \frac{h_s}{[\lambda]} \mu \frac{|\bar{T}'_T|}{|\bar{T}'_T|}. \quad (3.150)$$

For the operation mode ($i = 2n_s$), $|\bar{T}'_T|$ may be written as $2\pi |\bar{T}'_T|$ (see 3.99), (3.150) yielding

$$\frac{S[11]}{S[10]} \frac{|\bar{T}'_T|}{|\bar{T}'_N|} = \frac{3}{5} \frac{h_s}{[\lambda]} 2\pi \mu \approx 0.95 \mu. \quad (3.151)$$

In REHBEIN (1998, [41] p.32) friction coefficients for steel/polymer are in the range from 0.1 to 0.5. Therefore, the tangential contact influence is in the same order of magnitude as the normal contact influence. For superharmonics the ratio between tangential and normal contact influence increases because of increasing ratio $|\bar{T}'_T| / |\bar{T}'_T|$.

An appreciable strategy to cope with interaction between normal and tangential contact stress is to use an incremental updating procedure. The control parameter, like the excitation frequency or the electric voltage, must be change in sufficiently small steps. The normal contact stress is computed using the tangential contact stress from the previous control parameter increment. If the increments are chosen sufficiently small, the tangential contact stress from the previous increment is an accurate approximation for the tangential contact stress in the actual increment.

Algorithm The contact algorithm is as follows:

1. Give the initial state:

$$\mathbf{q}^{(0)}, \quad \mathbf{p}_N^{(0)}, \quad \mathbf{p}_T^{(0)}, \quad \mathbf{C}^{(0)},$$

the external parameters $\Lambda^{(i)}$ and the system and contact matrices

$$\mathbf{K}(\Lambda^{(i)}), \quad \mathbf{K}_{cN}(\mathbf{p}_N^{(0)}; \Lambda^{(i)}), \quad \mathbf{K}_{cT}^{stick}(\mathbf{p}_N^{(0)}, \mathbf{p}_T^{(0)}; \Lambda^{(i)}), \quad \mathbf{K}_{cT}^{slip}(\mathbf{p}_N^{(0)}, \mathbf{p}_T^{(0)}; \Lambda^{(i)})$$

2. Change one of the external parameters incrementally: $\Lambda^{(i+1)}$

3. LOOP over iterations: for $m = 0, \dots$, convergence

- (a) Compute: $\mathbf{q}^{(m+1)} = \mathbf{K}_{total}^{-1}(\mathbf{p}_N^{(m)}, \mathbf{p}_T^{(m)}; \Lambda^{(i+1)}) \mathbf{F}(\Lambda^{(i+1)})$

- (b) Determine a change in the contact topology:
GOTO 4: SUBROUTINE NORMAL

- (c) Determine a change in the contact topology:
GOTO 5: SUBROUTINE TANGENTIAL

- (d) Solve: $\mathbf{Z}_N(\mathbf{p}_N; \Lambda^{(i)}) \mathbf{q}^{(m+1)} = \mathbf{0} \Rightarrow \mathbf{p}_N^{(m+1)}$
with Newton-Raphson e.g.

- (e) Compute: $\mathbf{C}^{(m+1)} = \mathbf{Z}_{c1}^{-1}(\mathbf{p}_N^{(m+1)}, \mathbf{p}_T^{(m)}; \Lambda^{(i+1)})$.

$$\left[\mathbf{Z}_{c2}^{-1}(\mathbf{p}_N^{(m+1)}, \mathbf{p}_T^{(m)}; \Lambda^{(i+1)}) + \mathbf{Z}_{c3}^{-1}(\mathbf{p}_N^{(m+1)}, \mathbf{p}_T^{(m)}; \Lambda^{(i+1)}) \mathbf{q}^{(m+1)} \right]$$

- (f) Solve: $\mathbf{Z}_I(\mathbf{p}_T, \mathbf{C}^{(m+1)}, \mathbf{q}^{(m+1)}; \Lambda^{(i+1)}) = \mathbf{0} \Rightarrow \mathbf{p}_T^{(m+1)}$
with Newton-Raphson e.g.

- (g) Check:

$$\| \tilde{\mathbf{q}}^{(m+1)} - \tilde{\mathbf{q}}^{(m)} \| < TOL_q$$

$$\| \tilde{\mathbf{p}}_N^{(m+1)} - \tilde{\mathbf{p}}_N^{(m)} \| < TOL_N$$

$$\| \tilde{\mathbf{p}}_T^{(m+1)} - \tilde{\mathbf{p}}_T^{(m)} \| < TOL_T$$

- (h) $m = m + 1$, end LOOP

4. SUBROUTINE NORMAL:

Determine a change in the topology of the normal contact:

- (a) $\exists \bar{Y}_{1k} \in \partial \mathcal{B}_{ci}^{(m)} : T_N^* = \mathbf{N}_{T_N}(\bar{Y}_{1k}; \Lambda^{(i+1)}) \mathbf{q}^{(m+1)} > 0$

- (b) $\exists \bar{Y}_{1k} \in \partial \mathcal{B}_{nci}^{(m)} : g_N^* = \mathbf{N}_{g_N}(\bar{Y}_{1k}; \Lambda^{(i+1)}) \mathbf{q}^{(m+1)} < 0$

- (c) $\Rightarrow \partial\mathcal{B}_{ci}^{(m+1)}, \partial\mathcal{B}_{ci}^{(m+1)}, i = 1, \dots, N_c^{(m+1)}$
- (d) if $N_c^{(m+1)} = N_c^{(m)} \rightarrow$ no topological change in normal contact $\rightarrow \mathbf{p}_{Nstart}$
GOTO 5
- (e) if $N_c^{(m+1)} \neq N_c^{(m)} \rightarrow$ topological change in normal contact $\rightarrow \mathbf{p}_{Nstart}$
update contact matrix \mathbf{K}_{cN} and the matrices $\mathbf{Z}_N, \mathbf{Z}_{c1}, \mathbf{Z}_{c2}, \mathbf{Z}_{c3}$
- (f) GOTO 5

5. SUBROUTINE TANGENTIAL:

Determine a change in the topology of the tangential contact, use $\mathbf{q}^{(m+1)}$:

- (a) Check whether contact zones at p_{bi}^{start} starts with stick or slip
 - i. Compute $C_{ui}^{stick(1)}$ using (3.49)
 - ii. Compute $f(\bar{Y}_{1k})$ using $C_{ui}^{stick(1)}$ and (3.137)
 - iii. Check if $f(\bar{Y}_{1k}) < 0 \rightarrow$ contact zone begins with stick, GOTO 5.(c) ii.
 - iv. Check if $f(\bar{Y}_{1k}) > 0 \rightarrow$ contact zone begins with slip, GOTO 5.(b) i.
- (b) Slip to stick transitions:
 - i. Compute $C_{ui}^{slip(j+1)}$ using (3.45) at p_{tij}
 - ii. Check if $\dot{g}_T^{slip}(\bar{Y}_{1k})$ changes sign using (3.138), for $\bar{Y}_{1k} \in \partial\mathcal{B}_{ci}^{slip_{j+1}}$
 - iii. Compute $u_c^{slip}(p_{ti(j+1)})$ at the new transition point using (3.134)
 - iv. If p_{ei} is reached, then GOTO 5.(d), else $j = j + 1$, 5.(c)
- (c) Stick to slip transitions:
 - i. Compute $C_{ui}^{stick(j+1)}$ using (3.49) at p_{tij}
 - ii. Check if $f(\bar{Y}_{1k}) > 0$ using (3.137), for $\bar{Y}_{1k} \in \partial\mathcal{B}_{ci}^{stick_{j+1}}$
 - iii. Compute $u_c^{stick}(p_{ti(j+1)})$ at the new transition point using (3.134)
 - iv. If p_{ei} is reached, then GOTO 5.(d), else $j = j + 1$, 5.(b)
- (d) $\Rightarrow \partial\mathcal{B}_{ci}^{slip^{(m+1)}}, \partial\mathcal{B}_{ci}^{stick^{(m+1)}}$
- (e) topological change: if yes, then GOTO 5.(f) else GOTO 3.(d)
- (f) update contact matrices $\mathbf{K}_{cT}^{slip}, \mathbf{K}_{cT}^{stick}$ and the matrices $\mathbf{Z}_N, \mathbf{Z}_{c1}, \mathbf{Z}_{c2}, \mathbf{Z}_{c3}, \mathbf{Z}_I$
- (g) GOTO 3

3.3 Numerical Results

In the following, some typical characteristic features of the USM model, obtained by numerical analysis will be discussed. One of the most important aspects in the design of USMs is their resonant operation mode. The stator-rotor contact plays a crucial role in this regard, as it has already pointed out by SASHIDA (1993, [44] p. 219) and HAGEDORN & SATTEL (1998, [47]). Therefore, the computational analysis of USM models also needs special attention. For the set of motor and scaling parameters, given in Tables 2.2 and 2.3 the eigenfrequencies of the stator, rotor, and stator and rotor pressed together (without separation) are listed in Tab. 3.1. For the numerical analysis, an operation mode of the stator having three wave length is chosen. The eigenfrequency $\bar{\Omega}_3^*$ of

<i>scaled eigenfrequency</i>	<i>stator</i>	<i>rotor</i>	<i>stator and rotor</i>	
			1st.	2nd.
$\bar{\Omega}_1$	0.36	0.50	0.38	15.89
$\bar{\Omega}_2$	0.69	0.99	0.75	7.96
$\bar{\Omega}_3^*$	1	1.48	1.08	5.42
$\bar{\Omega}_4$	1.27	1.97	1.38	4.33
$\bar{\Omega}_5$	1.51	2.46	1.62	3.90
$\bar{\Omega}_6$	1.70	2.96	1.80	3.86

Table 3.1: Scaled eigenfrequencies $\bar{\Omega}_i$ of the stator, rotor, and stator and rotor both pressed together. The parameters are chosen from Tab. 2.2; * corresponds to the eigenfrequency of the operational vibration mode

the stator's operation mode (with three nodes) is scaled to 1. The rotor eigenmode with the same number of nodes has a higher eigenfrequency of 1.48. If stator and rotor are pressed together (without separation), the eigenmode with the same number of nodes has an eigenfrequency of 1.08. Therefore, pressing a rotor onto the stator causes a stiffening effect which results in a frequency shift of 8% with respect to the eigenfrequency of the stator. Comparison of these computational results with experimental data (in Fig. 4.11) shows a good agreement with respect to the stiffening effect caused by the rotor. An axial preload of 250 N causes a stiffening of approximately 10%. The stiffening in Fig. 4.11 depends on the axial preload. This is either caused by a non-linear contact stiffness or by the separation between stator and rotor during the frequency sweep at lower axial preloads.

A resonance diagram at full contact between stator and rotor is illustrated in Fig. 3.2. At full contact between stator and rotor the rotor does not move, since driving and braking contact zones eliminate each other. Nevertheless, the investigation of this contact

state gives good insight into the contact behavior from a computational analysis point of view. The stator vibration amplitude \hat{w}_s is plotted versus the stator length \bar{Y} and the excitation frequency $\bar{\Omega}$. The stator is electrically excited in its vibration mode having three nodes. This is a steady-state result in a reference frame moving with the traveling bending wave. At resonance, a drastic spatial shift of the wave crests occurs. In partial contact, such a spatial phase shift also occurs so that the phase shift of the contact zones (see Fig. 3.1) is similar. This is illustrated in the contour plot shown in Fig. 3.3. The wave crests shift over half the wavelength of the stator mode. For the computa-

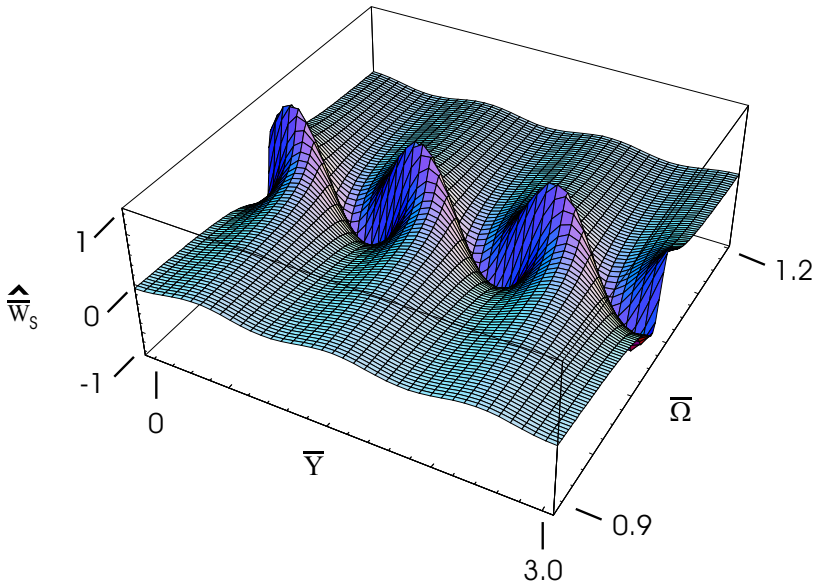


Figure 3.2: Stator displacement over stator length and excitation frequency; full contact between stator and rotor

tional analysis of the stator-rotor contact in USMs, this may cause difficulties in finding the contact zones during the contact iteration process. Therefore, special contact algorithms for spatial contact problems at resonance, like they occur in USMs, are needed. The contact algorithm, proposed in Section 3.2.7 removes such difficulties.

In USMs the excitation frequency is chosen to be above the motor's resonance frequency (see also Fig. 1.12). The same is done for the computation of speed-torque characteristics. The contact force distribution at different points along torque-speed characteristics has been analyzed and discussed in detail in SCHMIDT (1999, [51]) and SATTEL, HAGEDORN & SCHMIDT (2001 [49]) for different parameters of the contact layer. The dependence of the qualitative appearance of the speed-torque characteristics on the friction law will be discussed now. For the computation, $N_s = 15$ has

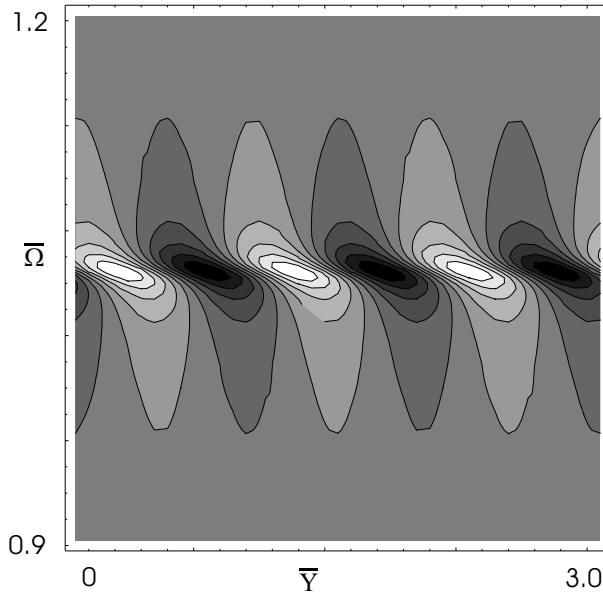


Figure 3.3: Contour plot of Fig. 3.2

been chosen for the number of vibration modes. In Fig. 3.4 two different friction laws are illustrated. Friction law 1 assumes pure slip between the contacting bodies with a constant coefficient of friction, whereas friction law 2 represents a smoothed Coulomb friction law. At high values of the slope coefficient α , friction law 2 shows a good representation of stick-slip effects, as it is pointed out in OESTREICH (1998, [40]). An one degree of freedom oscillator was modeled there. Using these friction laws, no distinction between stick and slip contact zones needs to be made. Thus, (3.147) and (3.148) can be ignored in the computation process. Instead, for all tangential contact states friction law 1 is represented by (3.4). When using friction law 2 at each iteration step of the contact algorithm, a numerical integration is necessary. Here a simple trapezoidal integration rule is used. For both friction laws, speed-torque characteristics are computed and fitted to measured data. Only the parameters of the friction laws are adjusted to fit the measured data. The motor parameters are chosen from Tab. 2.2, the excitation frequency was chosen to be in the vicinity of the resonance frequency. In Fig. 3.5, three speed-torque characteristics are plotted. Two of them are measured at different motor operation temperatures, the third one is computed. It is important to note that the motor behavior at room temperature is quite different from that at higher temperatures. A discussion on temperature effects is given in Section 4.3.

For comparison between numerical and experimental results, the model data are trans-

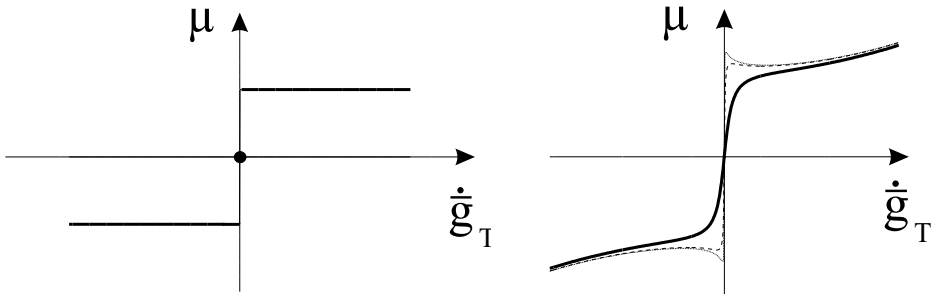


Figure 3.4: Left: friction law 1: $\mu \operatorname{sign} \dot{\sigma}_T$; right: friction law 2: $\frac{2}{\pi} (\mu_0 + a \dot{\sigma}_T^2) \arctan(\alpha \dot{\sigma}_T)$

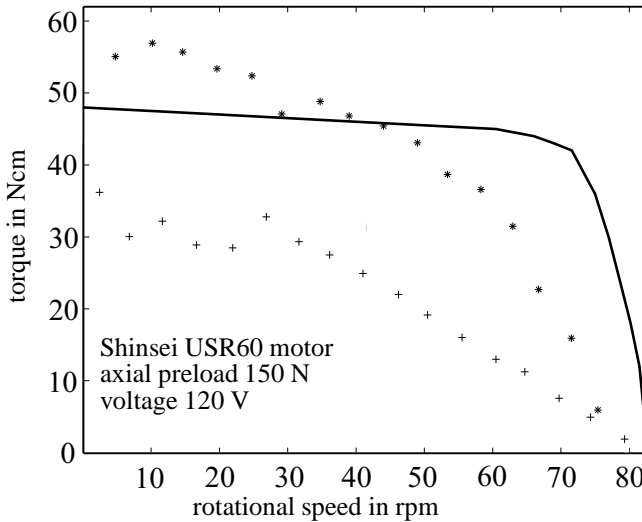


Figure 3.5: Speed-torque characteristics: (*) measured data at high temperature (80°C), (+) measured data at room temperature and (–) computed data with friction law 1

formed into a dimensional form. The friction coefficient of friction law 1 was chosen to fit the speed-torque characteristic at high temperature. It is not possible to get a good approximation of the measured curves. Starting at no-load speed, with increasing load the drop in the rotational speed is small, but at 45 Ncm load torque, the speed-torque

characteristic suddenly drops. The situation is different when using friction law 2. The result is plotted in Fig. 3.6.

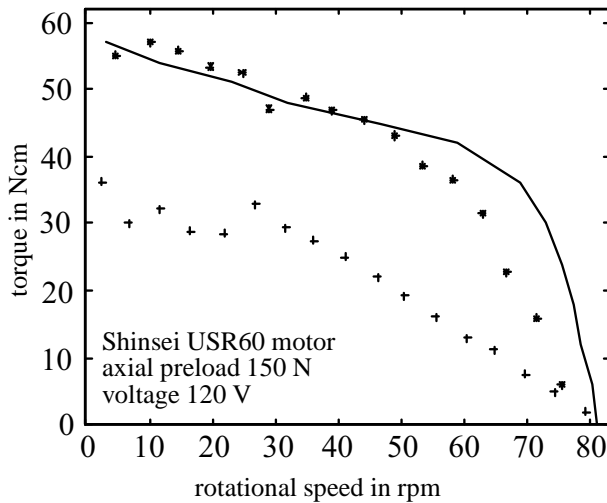


Figure 3.6: Speed-torque characteristics: (*) measured data at high temperature (80°C), (+) measured data at room temperature and (-) computed data with friction law 2

The difference between both friction laws is obvious. The smooth friction law 2 approximates stick-slip behavior. There is no sudden drop in the rotational speed at high load torques.

In addition to the computation of the speed-torque characteristics, also time simulations have been carried out. During time simulations, the mass and stiffness matrices have been generated according to the procedure outlined in Section 3.2.5. For the sake of simplification, the time derivatives in the contact layer equations (3.9) and (3.10) have been neglected. Simulation of the motor behavior in the operation quadrant (see Fig. 1.18) shows normal vibration behavior of stator and rotor. Simulations in the dragging quadrant show a beating phenomenon in the state variables of the stator. A simulation result is shown in Fig. 3.7. The two upper diagrams represent the oscillation behavior of the state variables of the two orthogonal operational bending modes of the stator. The lower two diagrams show zoomed plots. In Fig. 3.8, a measured time history of the stator vibration amplitude is depicted. The measurements were carried out with a laser vibrometer. Details on the experiments can be found in Fig. 4.2. The discussion about the experiments on the beating phenomenon is given in Section 4.4.5. It is worthwhile to note that the model is able to capture such phenomena.

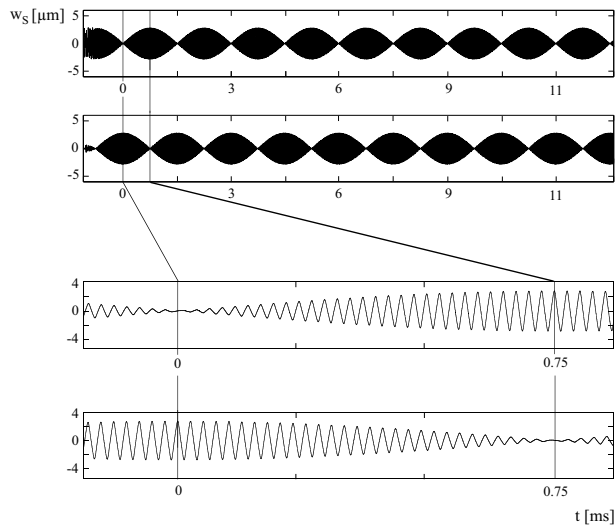


Figure 3.7: Simulated beating phenomenon in the dragging quadrant of a speed-torque characteristic

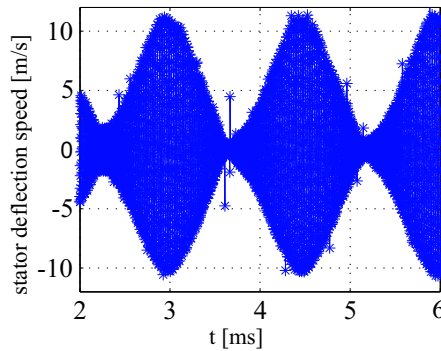


Figure 3.8: Simulated beating phenomenon in the dragging quadrant of a speed-torque characteristic

3.4 Summary

A contact algorithm has been developed which accounts for the dynamic contact problem in USMs. The model and the contact algorithm are general enough to investigate motor models with different numbers of nodes for the stator operation mode. Especially the subharmonic modes, i.e. modes having wavelength larger than the wavelength of

the operation mode, can be considered. To investigate effects like squealing, consideration of such modes may be necessary. The result of a simple scaling analysis is that normal and tangential contact stresses influence each other and cannot be considered separately. This is in contrast to what has been used and stated in other model analyses. The results of the frequency responses showed that for resonant contact problems of spatially distributed structures large spatial shifts of the contact zones occur in the vicinity of the resonance. In previous works, this has led to difficulties in finding the contact boundaries. In the traveling wave reference frame the contact zones shifts as much as half of the wavelength of the stator vibration amplitude. Therefore, the contact algorithm has to be modified correspondingly. The comparison between computed speed-torque characteristics using a slip friction law and a smoothed Coulomb friction law showed that the smoothed friction law gives a better representation of the qualitative shape of the speed-torque characteristics. In many of the analyzed contact models, a pure slip law has been used. The time simulation of a motor operation in the dragging quadrant results in a beating phenomenon in the stators state variables of the operation mode. Such a beating phenomenon has been observed also experimentally. The previously suggested models cannot capture such a phenomenon.

Chapter 4

Experiments

4.1 Introduction

This chapter outlines the results of detailed experimental studies of a typical USM. The experiments are performed to give a complete picture of the motor behavior which is essential for understanding the dynamics of such kind of motors. This is important not only for furnishing mechanical design guidelines, but also for designing control and power electronics. Many key features of traveling wave type USMs, like typical speed-torque characteristics, the jump phenomenon or rotational speed threshold have already been reported separately. What has been done are measurements focusing on particular average motor characteristics, like speed-torque characteristics or input and output power. Additional information like vibration amplitudes of stator and rotor, phase relation between voltage and electric current, or temperature behavior are not given. Thus, what is missing is a more comprehensive and detailed picture of the motor dynamics. Since the contact behavior between stator and rotor plays an important role with respect to the motor characteristics, knowledge of the vibrational behavior may contribute to formulations of design rules of USM.

The behavior in the contact zone cannot be measured directly, thus designers rely on sophisticated contact models or motor models. A spectra of various experiments can help to optimize the parameters of such a model capturing the significant phenomena. Additionally, the experimental results may be used to validate existing mathematical models.

First, the state of the art of a traveling wave type USM is given in Section 4.1.1, focusing on experimental results only. The detailed objective is stated in Section 4.1.2, pointing out which additional contributions will be made. Section 4.1.3 introduces the

various measurable quantities, measurement techniques and devices and the explanation of the test bench for measuring speed-torque characteristics. The essentials of the experimental results are summarized in Sections 4.2-4.4. First, resonance behavior of stator and motor are presented, followed by a short comment on temperature dependence of motor characteristics. The chapter ends with the main results of steady-state motor behavior.

4.1.1 Literature review

The present literature review focuses on the state of the art with respect to essential experimental results on traveling wave type USM. A vast amount of experiments has been conducted to investigate salient features of different motors at both, steady-state and/or transient operating conditions. These include motor features as speed-torque characteristics, average input and output power, efficiency or start-stop properties. The reader is referred to UEHA *et al.* (1993, [57]) or SASHIDA (1993, [44]) for a rough overview on qualitative features of different kinds of motors. Motor characteristics may be actively influenced by three control parameters, namely the electric excitation voltage, the excitation frequency and the phase between the electric input signals. In addition, there is one design parameter which is easy to adjust, namely the axial preload. These four parameters together may be varied to investigate the motor characteristics of a particular motor.

Most of the published experimental data on steady-state motor characteristics were obtained by operating the motor with feedback controllers and/or resonant converters (see FURUYA *et al.* (1992, [10])). Typically, all speed-torque characteristics drop from the no-load speed to a stall torque as illustrated in Fig. 1.18. In UEHA *et al.* (1993, [57]), the speed-torque characteristics at different input power or rather different excitation voltage levels are plotted. With increasing excitation voltage, the speed-torque curves shift to higher no-load speeds. Depending on the specific motor under investigation, some speed-torque curves end abruptly at a maximum load-torque. However, this maximum load-torque is not the stall torque of the motor. This indicates that the characteristics have been measured in a torque-controlled operation mode, see e.g. HERZOG (1993, [22], p. 78). A sudden breakdown in the rotational speed is observed (FURUYA *et al.* (1992, [10])) in a plate type USM if the excitation voltage passes certain lower values. For example, the excitation voltage is decreased from an effective value of more than 100 V at 140 rpm down to an effective value of 60 V at 100 rpm, when the rotational speed suddenly collapsed and the motor stopped. The authors showed that this voltage threshold is load dependent. In the same work the variation of the excitation frequency is also considered in which case the rotor motion is continuous, even at low rotation speeds. A shift of the phase between the voltage signals results also in a continuous reduction of the rotational speed down to a few rpm. It was concluded from the experimental results in FURUYA *et al.* (1992, [10]) that at low no-load rotational speed

operation the excitation frequency instead of the excitation voltage should be varied to ensure continuous reduction of rotational speed. But from a power electronics point of view a variation of the frequency leads to higher reactive loads. Following this line of argument, a hybrid control concept is proposed in MAAS *et al.* (1999, [33]), combining the advantages of voltage and phase variation. At high no-load rotational speeds the motor is controlled by a variation in the voltage signal, whereas at low no-load rotational speeds a phase variation is used. The experiments were carried out with an AWM90 motor of DaimlerChrysler (see Fig.1.2). The influence of axial preload on the speed-torque characteristics of the same type of motor was also reported (SCHREINER *et al.* (2000, [53])). However, the results characterize the motor together with the control unit. It is mentioned that hard contact layer material at high axial preload lead to parasitic vibrations, also in the audible range. In WHATMORE (2001, [60]) the experimental results of a plate-type motor with 8 nodal diameters are presented. It is observed, that the no-load rotational speed drops with increasing axial preload while the stall torque increases. For each axial preload there is a maximum no-load speed with respect to the excitation frequency. For small size motors like those designed and manufactured by FLYNN (1997, [12], p. 137) an optimum of the stall torque with respect to the axial preload is described, whereas the no-load speed decreases monotonically.

Only few data are available of the stator and rotor vibration amplitudes at steady-state motor operation. In reference MAENO *et al.* (1992, [36]) a Canon-type USM is examined and the stator and rotor vibrational behavior for a particular steady-state operating condition are measured. In MAAS *et al.* (1999, [33]) the stator motion is controlled to achieve a constant vibration amplitude of $1\ \mu\text{m}$ along the speed-torque characteristics.

The resonance behavior of USM is much better examined and understood. In many papers the typical non-linear resonance curves of USM (e.g. in UEHA *et al.* (1993, [57] p.71)) or more clearly in MAAS *et al.* (1999, [33] p. 112) with the jump phenomenon are presented. The frequency response curves of the vibration amplitude are important looking from a control perspective. From a power electronics point of view the electric admittance curves of motors at high voltage amplitudes are relevant, since compensating reactive power components in electric signals reduce the loading of power electronic components like semiconductor devices. In WHATMORE (2001, [60]) electric admittance curves at high voltage excitation levels are presented for a plate-type stator with 8 nodal lines. The curves exhibit a non-linear resonance behavior. With increasing voltage amplitude the stator admittance decreases. Unfortunately, the reported electric admittances of the assembled motor were measured at low electric voltage.

An often-cited advantage of USMs is their silent operation due to ultrasonic frequency drive and their gearless mechanism. This is true when the rotor geometry, the axial preload and the excitation frequency are properly chosen. The rotor geometry usually is determined by numerous empirical studies. In the early stage of motor design the occurrence of stability problems are not unusual. Unstable motor operation have

been observed by several authors. In UEHA *et al.* (1993, [57], p. 68, 99, 102, 200, 288) unstable operating conditions are reported for different motors; some accompanying with vibrations in the audible range. A degradation of the friction layer material was observed in HERZOG (1993, [22]), which leads to squealing after several hours of operation of a Shinsei USR60 motor. Using a laser-vibrometer, SATTEL & HAGEDORN (2000, [46]) measured the vibrations of stator and rotor during unstable motor operation. They observed the 2nd and 4th order of subharmonics of the excitation frequency in the vibration signals of the rotor. SCHREINER *et al.* (2000, [53]) pointed out that the rotor design has a significant influence on the onset of squeal in the motor. They mentioned that damping of the rotor vibrations by layered springs reduces possible vibrations in the audible range.

The consequence of frictional contact between stator and rotor is an increase in motor temperature during operation up to more than 100°C. IZUNO (1992, [25]) mentioned the drift of motor characteristics due to a temperature influence. SATTEL & HAGEDORN (1999, [45]) found a strong dependence of the speed-torque characteristics on temperature. The speed-torque characteristics of Shinsei USR60 motors at room temperature show a significant lower level in the output torque than those characteristics with the motor already heated up to more than 70°C. It must be noted that the measurements have been carried out applying feedback control (Shinsei control unit). Temperature fluctuations influence the mechanical as well as the electrical characteristics of the motor. In UEHA *et al.* (1993, [57] p. 50) the shift of electric admittance of a stator due to a temperature rise is shown. And notably, piezoceramic material characteristics like the electric capacity exhibit a strong dependence on the temperature.

Manufacturing imperfections may be another aspect responsible for motor deficiency. Giving only two examples of possible imperfections, it is referred to UEHA *et al.* (1993, [57] p. 58) where hints are given on the influence of non-degeneracy of eigenmodes, and HERZOG (1993, [22]) where non-uniform motion of the rotor caused by a tilt compared to about 5-10 μm are mentioned.

4.1.2 Objective

From the literature review it turns out that still some open questions on the dynamics of USM exist. To answer these questions, which have not rigorously been addressed yet, the following experimental studies will be carried out:

- Measurements of speed-torque curves of the motor only, without feedback control and without resonant converters. The motor behavior is what is focused on.
- Measurements of speed-torque characteristics in the speed-controlled mode. It seems that published data have been measured in a torque controlled mode of the test rigs.

- Investigation on the influence of the axial preload on speed-torque characteristics and overall motor dynamics.
- Measurements of stator and rotor vibration amplitudes along the speed-torque characteristics. On the one hand, the influence of the load-torque on the vibration amplitudes of stator and rotor is obtained. On the other hand, the overall dynamics of the motor is better understood from examining the vibrational behavior of both, stator and rotor.
- Measurements of frequency response curves of the vibration amplitude and the electric admittance. The phase of the electric admittance at high voltage signals indicates the high significance of the reactive power components.
- Detection of the onset of squealing at different excitation frequencies and axial preloads. This effect has been mentioned but there are almost no experimental data available. Deeper knowledge of this phenomenon may help to gain sophisticated design rules for both, stator, rotor and the contact layer.
- Measurements of the motor temperature at different load-torque levels. Some material parameters like those of the piezoceramic or the contact layer may vary drastically within the operational temperature range. Thus, motor characteristics will be influenced by the temperature level.

The experimental focus is on *steady-state operation* and *resonance behavior* of USM. Different motors have been tested in our laboratory, as depicted in Figs. 1.1, 1.2 and 1.3, for example. In the following, only the results obtained for the Shinsei USR60 motor are presented. The motor has good operation features and its experimental data are often used to develop, verify and improve contact models of USMs. Besides, some theoretical and a lot of experimental studies have been carried out in past for the Shinsei USR60 motor and similar motors, see HAGOOD & MACFARLAND (1995, [21]), LE MOAL & MINOTTI (1997, [32]) or FURUYA *et al.* (1992, [10]), for example. Three motors of this type have been used for the experiments.

4.1.3 Measurable quantities, measuring devices and measurements

All electrical and mechanical quantities, which can be measured from a motor by the available laboratory equipments are summarized in Tab. 4.1. In the following sections the devices used to measure or control these quantities are briefly explained. The relation of these experimental quantities to the quantities of the model are found in Section 2.7.8 and in Fig. 2.14. The torque T of the motor corresponds to the force \bar{F}_{motor} of the model. Similarly, the rotational speed n is related to the rigid body speed \tilde{c}_{rx} of the motor model. Note, that controlling the current would also have been possible but was not used in the experiments presented here. Adjusting $\Delta\phi_V \in \{0^\circ, 180^\circ\}$ results in

quantities	controlled	not controlled
electrical input quantities	$V_A, V_B, \Omega, \Delta\phi_V$	
electrical output quantities		I_A, I_B
axial preload	$F_{axial} (p_{axial})$	
mechanical output quantities	$T (\bar{F}_{motor})$	$n (\dot{\bar{c}}_{rx})$
	$n (\dot{\bar{c}}_{rx})$	$T (\bar{F}_{motor})$
inner quantities		$\dot{w}_s(x^*, t), \dot{w}_r(x^*, t)$
temperature		ϑ

Table 4.1: Measurable quantities of the USM splitted into variables which are controlled and not controlled while taking measurements

a traveling wave excitation with clockwise or counter-clockwise rotor motion, respectively, whereas $\Delta\phi_V \in \{-90^\circ, 90^\circ\}$ gives a standing wave excitation with rotational speed $n = 0$ rpm, as obviously seen from (1.8).

The motors were driven in two different operation modi, a standing wave operation at $\Delta\phi_V \approx 90^\circ$ and a traveling wave operation at $\Delta\phi_V \approx 0^\circ$. However, fixing the phase deviation of the excitation voltages to zero (i.e. $\Delta\phi_V \approx 0^\circ$) does not guarantee a pure traveling wave operation. Motor imperfections may prevent such ideal operating mode to be achieved. Therefore, the traveling wave condition is checked from the phase difference of the current signals $I_A(t)$ and $I_B(t)$. This is explained in detail in Section 4.4.6.

The Shinsei USR60 has two electrode systems (see Fig.1.10). Usually an electrical voltage signal with amplitude of 120 V effective is delivered. The resonance frequency of the stator is approximately 40 kHz. To deliver the voltage signals $V_A(t)$, $V_B(t)$ up to 150 V amplitude, two voltage amplifiers are utilized. These are designed especially for capacitive or inductive loads. Thus, they are capable of resisting high reactive loads due to the motor behavior. The cut-off frequency of the amplifiers are at 100 kHz. The phase difference between the two voltage signals is generated by a phase shifter (laboratory fabricated) which is connected between the output channel of the signal generator and the two voltage amplifiers. The phase shifter also has a cut-off frequency of 100 kHz. Note that the phase deviation $\Delta\phi_V$ is defined as the phase deviation between the sine and the cosine signal as described in (1.7). To obtain the excitation frequency response plots a gain-phase analyzer (HP 4296) is used. Using this analyzer together with the voltage amplifiers and a current probe, the electric admittances at different voltage levels can be measured. The excitation frequency at steady-state operation is most easily adjusted using a separate signal generator.

As mentioned earlier, a deeper understanding of the motor dynamics is possible

knowing the vibrational behavior of both, stator and rotor. A two-channel out-of-plane laser-vibrometer was utilized for that purpose. This device is capable of measuring the speeds of material surface points in the direction of the laser beam, as illustrated in Fig. 4.2. Since the outer diameter of the rotor is a little smaller than the one of the stator, it is possible to measure both, stator and rotor vibrations simultaneously in the assembled motor. Orienting the laser beams perpendicular to the stator and rotor surfaces, the out-of-plane velocities (lateral velocities) $\dot{w}_s(x^*, t)$, $\dot{w}_r(x^{**}, t)$ can be measured, as illustrated in Fig. 4.2. It is noteworthy that the corner frequency of the laser vibrometer is at 100 kHz, making it possible to detect the first higher harmonic component (80 kHz) in the stator or the rotor if present. For a harmonic signal of 40 kHz vibration amplitudes down to 0.1 μm can be detected. From design and modeling point of view the displacement signals $w_s(x^*, t)$, $w_r(x^{**}, t)$ and especially the displacement amplitudes $\hat{W}_s(\Omega, x^*)$, $\hat{W}_r(\Omega, x^{**})$ are of prime interest. The speed signals can be split up in their Fourier components by an FFT. The Fourier components of the speed signal $\hat{\dot{W}}_k(\Omega_k, x^*)$ are related to the Fourier component of the displacement signal by

$$\hat{\dot{W}}_k(\Omega_k, x^{*/**}) = \frac{\hat{W}_k(\Omega_k, x^{*/**})}{j\Omega_k}. \quad (4.1)$$

The underscore in (4.1) denotes a complex quantity.

The temperature of the motor was measured by a non-contacting temperature sensor. The sensor technique is based on the emission of infrared radiation in a band of 8 to 14 μm wavelength. For various metals the emission coefficients of the measured surfaces are tabulated, but it is recommended to calibrate the sensor by a two point measurement.

To measure torque-speed characteristics, a special test rig for USMs was developed. Details about the rig and its features are found in BERG *et al.* (1998 [6]) and BERG (2001, [5]). A short description is, however, given below. Contrary to other existing test rigs this one allows not only a torque controlled measuring mode but also a speed controlled mode. A sketch of the test rig is shown in Fig. 4.1. The axial preload, F_{axial} , is exerted by an electrically driven cylinder whose maximum limit is 500 N. To measure the axial preload a force sensor equipped with four strain gauges is located between the electrically driven cylinder and the USM. The external load unit consists of a permanently excited DC-motor with an external proprietary control unit. This electro-motor has a maximum torque of 5 Nm which is much more than the Shinsei USR60 can withstand in real life application. The measurement of the rotational speed was realized by a DC-generator, integrated in the external load unit. A torque sensor is located between the USM and the external load unit. The control of the various test rig devices together with a I/O-card, the speed and the torque controller is housed in a test rig control box. This box communicates with a PC's I/O-card which is controlled by a HPVEE program for the settings of the measurements.

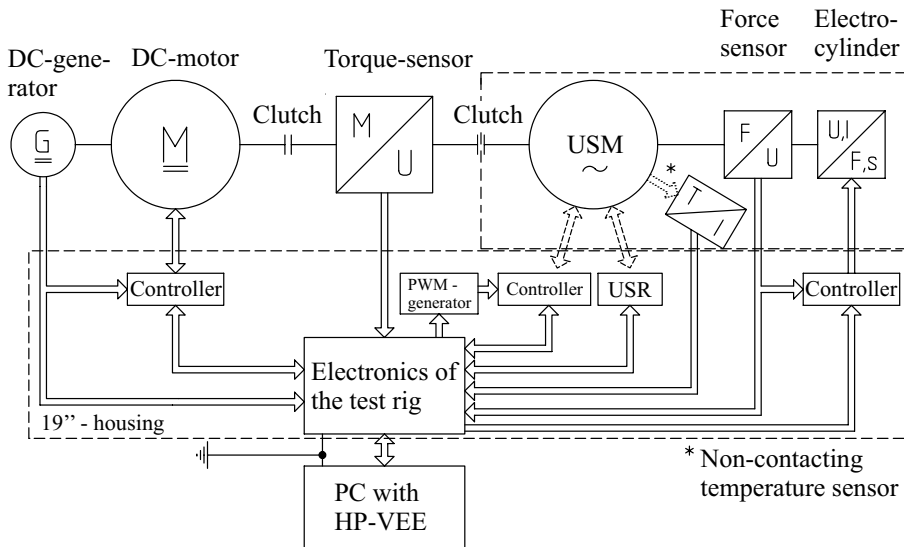


Figure 4.1: Sketch of the test rig for measuring speed-torque characteristics

4.2 Resonance behavior

This section is about the investigation of the vibrational behavior of the stator itself and the motor in the vicinity of their operational resonances. Therefore different frequency response plots have been measured. Fig. 4.2 shows a schematic of the experimental setup used throughout of all the following experiments. Both electrode systems of the piezoceramic ring (see Fig. 1.10) have been excited by harmonic electrical voltages $V_A(t)$ and $V_B(t)$. The phase deviation $\Delta\phi_V$ between the voltage signals have been set to 0° or 90° depending on the chosen kind of excitation, traveling or a standing wave excitation. The electric currents, $I_A(t)$ and $I_B(t)$, in the two circuits have been measured by either using the impedance analyzer at low voltage signals or the gain-phase analyzer together with current probes for the high voltage excitation. To detect the lateral vibration of the stator (bending vibration), a laser beam was focused on the top surface of the stator at its outer circumference. Some of the measurements were carried out for the motor, i.e. stator with rotor, at different axial preloads. Since the outer diameter of the stator is somewhat larger compared to that of the rotor, fortunately it was possible to measure the stator vibration amplitude even when the motor is assembled.

For all following measurements two kinds of frequency response plots have been

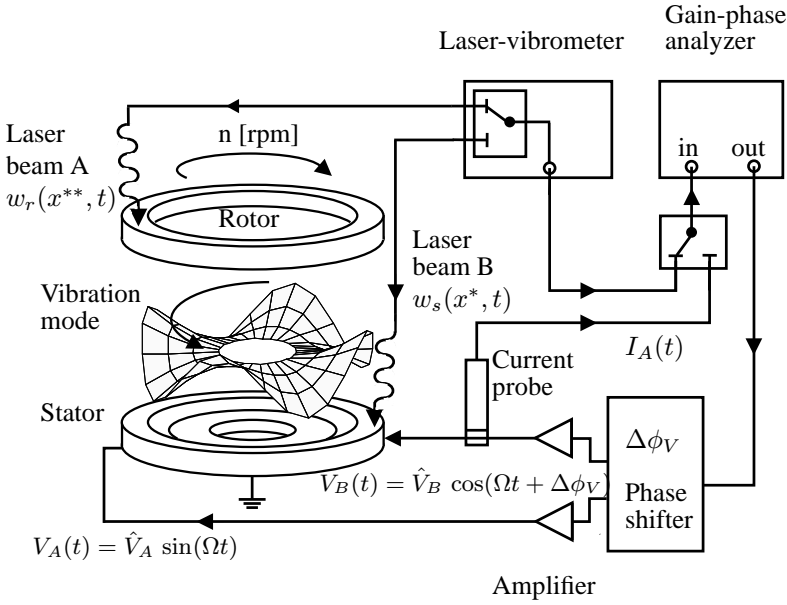


Figure 4.2: Sketch of the setup for measuring frequency response plots

recorded. The first one is the frequency response plot of the electric admittance (see Fig. 1.10)

$$\underline{Y}_{el_i}(\Omega) := \frac{\underline{\hat{I}}_i(\Omega)}{\underline{\hat{V}}_i}, \quad \text{for } i = \{A, B\} \quad (4.2)$$

where the underscore represents a complex quantity and Ω is the circular excitation frequency. The second frequency response plot is that of the stator's displacement. Transfer functions such as

$$\underline{Y}_{elmech_i}(\Omega; x^{**}) := \frac{\underline{\hat{W}}_{s_i}(\Omega; x^{**})}{\underline{\hat{V}}_i}, \quad \text{for } i = \{A, B\} \quad (4.3)$$

are measured since the used Laser-Vibrometer detects velocities. Substituting (4.1) into (4.3), the expression for the frequency response of the stator's displacement becomes

$$\underline{\hat{W}}_{s_i}(\Omega; x^{**}) = \underline{Y}_{elmech_i}(\Omega; x^{**}) \frac{\underline{\hat{V}}_i}{j\Omega}. \quad (4.4)$$

Frequency responses are recorded at room temperature and without mechanical load-torque. In a first stage this is sufficient to describe the qualitative behavior of the motor at different parameter settings. The experiments indicate that the temperature influence in most cases results in a shift of the measured curves with respect to the excitation frequency, but not that much of a change of the qualitative behavior. However, in some USM applications the motors are used for short term actuation with long term phases at rest. Under such applications the temperature rise is only moderate.

4.2.1 Resonance behavior of the stator

As a first measurement (Fig. 4.3), the electric admittance of the stator over a broad frequency range had been recorded. The resonance peak at 39 kHz has a significant drop

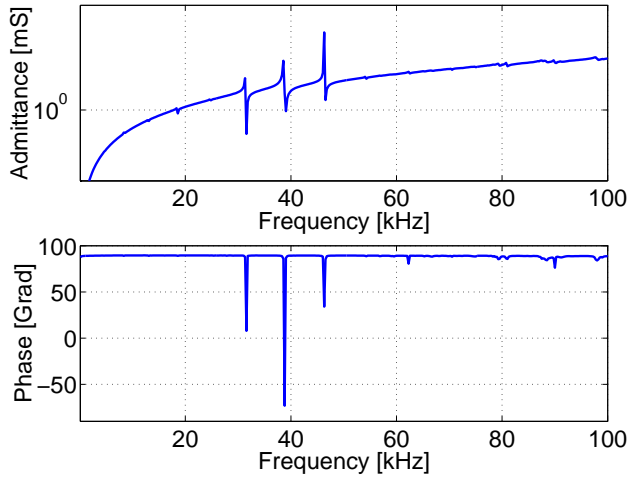


Figure 4.3: Electric admittance, $\underline{Y}_{el_i}(\Omega)$, frequency response plot of the stator

in the phase. This indicates a high mechanical quality factor so that it is reasonable to assume this vibration mode to be the operational mode of the motor. The operation mode with nine nodal lines and zero nodal circles at the resonance of approximately 39 kHz has been confirmed by scanning the stator's surface with the Laser-Vibrometer. In a second experiment the degeneracy of the operation modes has been investigated. Therefore, the electric admittances for both electrode systems, $\underline{Y}_{el_A}(\Omega)$ and $\underline{Y}_{el_B}(\Omega)$ are plotted near the resonance frequency, Fig. 4.4. The two frequency response plots coincide almost perfectly, giving two degenerated vibration modes. Notably, the electric admittance in Fig. 4.4 shows a resonance peak at 38.7 kHz and an antiresonance peak at 38.9 kHz, which typically is a usual phenomenon of electromechanical systems. The resonance in the electric admittance corresponds to the mechanical resonance. Measuring the frequency response plots of the stator displacements $\hat{W}_s(\Omega; x^{*/**})$, Fig. 4.5 shows the mechanical resonance at 38.7 kHz. Again, the two plots coincide well and by comparing Fig. 4.4 with Fig. 4.5 it is seen that their resonance frequencies correspond.

The electric admittances in Fig. 4.4 and the displacements in Fig. 4.5 have been measured at low voltage input signals of approximately 2 V. During the experiments it had been observed that at higher voltage amplitudes the resonance behavior of the stator becomes nonlinear. The resonance curves show a backbone behavior and a jump phenomenon occurs. Fig. 4.6 presents these effects at different excitation voltage levels. It is seen that with increasing voltage amplitudes the admittance show

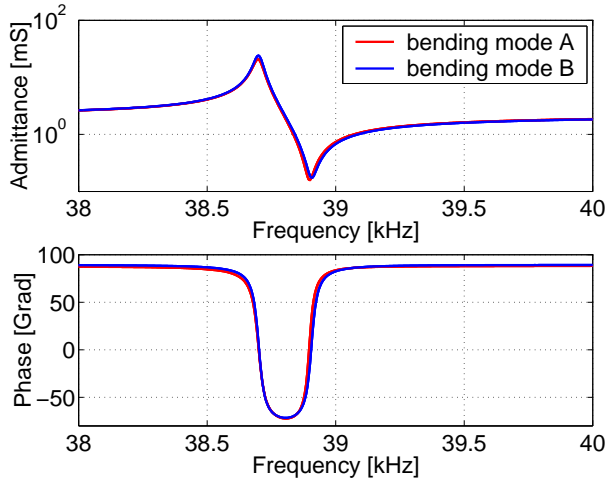


Figure 4.4: Enlarged view of the frequency response of the electric admittance from Fig. 4.3 near the operation frequency

a softening behavior and their maximum values decrease. Furthermore, with increasing voltage levels the jump frequencies between sweep up and sweep down curves increase as well. Although the distance between resonance and antiresonance jumps expand the phase response shrinks in between both resonances. At a voltage level of 5 V the phase plot comes down to -60° but at 150 V the phase minimum only reaches approximately 0° . This effect may come from an increase in internal damping. The mechanism of this behavior is not obvious but may have significant influences on the power electronics. If there is no zero crossing in the phase of the electric admittance, an operation without reactive power is not possible. Besides that, a strong nonlinear vibration behavior produces subharmonic vibration components, which may influence the vibrational behavior of the motor. It is remarkable too, that the resonance frequency in Fig. 4.6 shifts about 2 kHz corresponding to 5% with respect to the resonance frequency of the free vibrating stator at a low voltage signal, see Fig. 4.4. The measurement of the frequency response of the stator displacement in Fig. 4.7 yields on quantifying the stator's vibration amplitudes in the nonlinear regime. Usually, USM are driven with stator vibration amplitudes in the micron range. Voltage excitations of 150 V/mm are also reasonable quantities in USM applications. Thus, considering the resonance amplitudes in Fig. 4.7 an influence of this nonlinearity on the motor dynamics can not be neglected a priori. This effect has not been measured or discussed in literature of USM design, yet. Such a nonlinear resonance behavior is well known from literature (see HAGEDORN (1988 [16]), for example) A softening type DUFFING-oscillator with a cubic stiffness term gives the same qualitative resonance behavior. More detailed investigations, carried out by NGUYEN (1999, [37]), explain that the softening behavior in the electric admittance

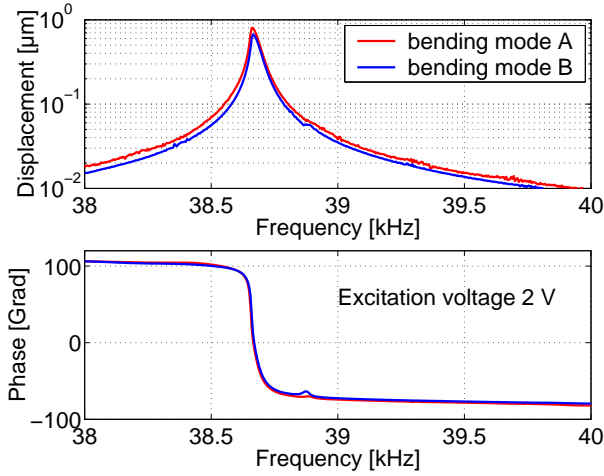


Figure 4.5: Frequency response of the stator's bending mode displacement $\hat{W}_{s_A}(\Omega; x^*)$ and $\hat{W}_{s_B}(\Omega; x^* + \frac{\lambda}{4})$ near the operation frequency of 38.7 kHz

belongs to the piezoceramic material only, and not as one could assume from the bonding between piezoceramic and stator. However, the bonding can have a strong influence on the efficiency of the electromechanical power conversion. Investigations on this have been carried out by SEEMANN & SATTEL (1999, [55]). Here, a pure piezoceramic rod sample (PZT181, PI Ceramics) of a square cross section with a polarization in axial direction has been used to confirm both, the softening behavior as well as the jump phenomenon which originates from the material nonlinearity in piezoceramic. The length of the sample was a few cm. First, frequency response plots of the electric admittance and the rod's longitudinal displacement had been measured at a low voltage excitation signal with the laser-vibrometer. The results are presented in Fig. 4.8. The resonance peaks correspond to the first longitudinal vibration mode of a rod with free-free boundary conditions. The curves look qualitatively similar compared to those measured for the stator, see Fig. 4.4 and 4.5. Notably, the distance between the resonance and the antiresonance frequency of the rod sample is significantly larger than that of the stator from Fig. 4.4. This distance indicates the strength of the electromechanical coupling in a structure. Since the rod sample is made fully out of piezoceramic material, its electromechanical coupling naturally must be larger than the one of the stator. In Fig. 4.9, electric admittances of the rod probe at different voltage excitation levels are plotted. It turns out that a qualitatively similar nonlinear behavior exists likewise as seen for the stator. This points out that the mechanism of the nonlinearity originates from the piezoceramic material and not from the bonding layer. Detailed studies on this topic were conducted by NGUYEN (1999, [37]). However, in contrary to the admittance phase plot of the stator, the phase plots of the rod samples switch from $+90^\circ$ to -90° at

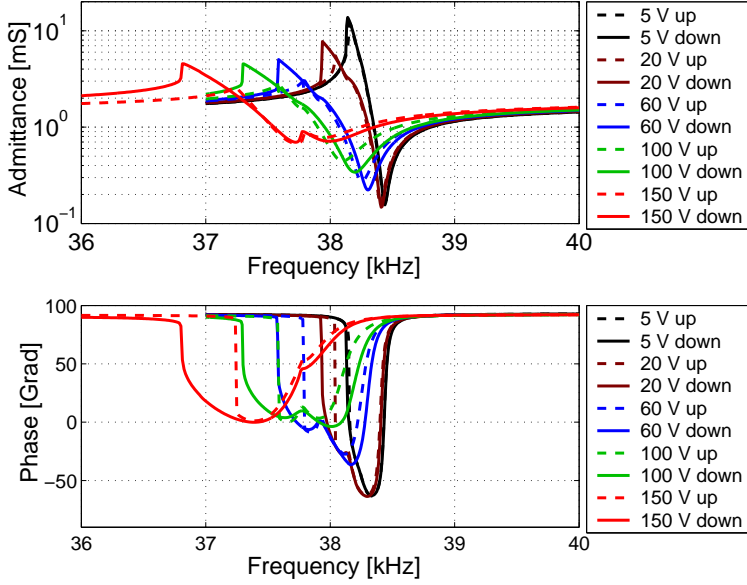


Figure 4.6: Nonlinear frequency response of the electric admittance, $\underline{Y}_{elA/B}(\Omega)$ of the stator; – solid line: sweep down, - - dashed line: sweep up

the resonance. From the frequency response plot of the rod's longitudinal displacement in Fig. 4.10 the jump phenomenon can be seen more clearly. The rod displacement was measured with the Laser-vibrometer focusing the laser beam at one of the free vibrating ends. This special kind of nonlinear resonance behavior has been investigated now for more than four decades. In UCHINO (1997, [56], p.169) the same resonance behavior as in Fig. 4.7 is shown for a piezoelectric resonator and it is argued that this non-linear phenomenon results from nonlinear elastic material behavior. This seems to be the evidence. BEIGE (1983, [4]) worked out experimental and analytical methods in the frequency domain for the identification of higher order material coefficients of piezoceramics acting in nonlinear regimes. Starting with an fully consistent expression for the free enthalpy upon terms of the order four, the following constitutive equations have been derived:

$$\begin{aligned}
 S_i &= s_{ij}^E T_j + d_{mi} E_m + s_{ijk}^E T_j T_k + 2d_{mik} T_k E_m + R_{mni} E_m E_n \\
 &\quad + s_{ijkl}^E T_j T_k T_l
 \end{aligned} \tag{4.5}$$

$$\begin{aligned}
 D_m &= d_{mi} T_i + \varepsilon_{mn}^T E_n + d_{mij} T_i T_j + 2R_{mni} T_i E_n + \varepsilon_{mnp}^T E_n E_p \\
 &\quad + \varepsilon_{mnpq}^T E_n E_p E_q .
 \end{aligned} \tag{4.6}$$

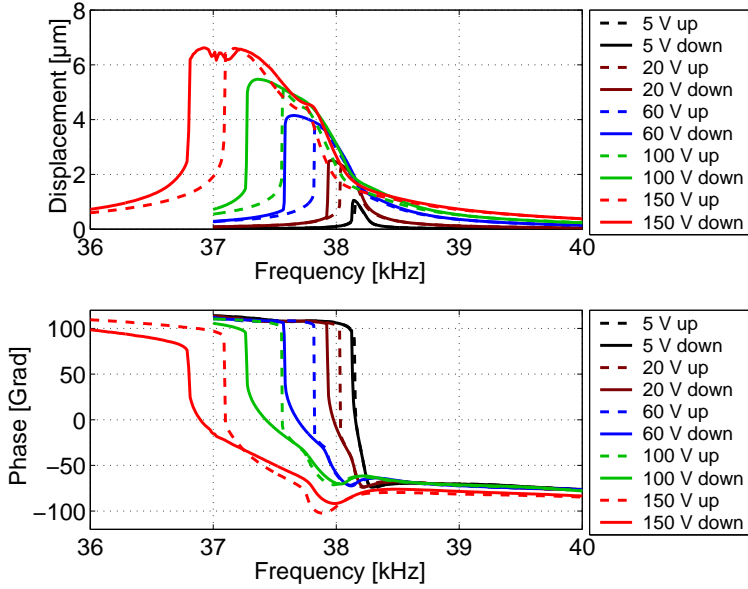


Figure 4.7: Nonlinear frequency response of the lateral displacement of the stator, $\hat{W}_{sA}(\Omega; x^*)$, $\hat{W}_{sB}(\Omega; x^* + \frac{\lambda}{4})$; – solid line: sweep down, - - dashed line: sweep up

The first two terms on the right side in (4.5) and (4.6) represent the linear piezoceramic material behavior. The softening behavior in the mechanical resonance of the rod sample (Fig. 4.9) can be explained by a cubic stress-strain relationship as described by the last term in (4.5). BEIGE (1983 [4]) measured and identified some of the non-linear elastic material coefficients at the mechanical resonance of a piezoceramic specimen, using measured electric admittances. More recently NGUYEN (1999, [37]) observed effects in a piezo-beam-system, stemming from of the same mechanism. In WOLF & GOTTLIEB (1999, [61]) a cantilever beam with piezoceramic layers was modeled, including cubic mechanical non-linearities in the material law. By utilizing a multiple-scale analysis, the nonlinear resonance curves with the softening behavior were obtained. Non-linear dielectric material coefficients were identified in BEIGE (1982, [3]). For these measurements a piezoceramic specimen is connected into series to a linear inductance so that the electrical resonance is far below the first mechanical resonance of the piezoceramic specimen. The measured electric resonance exhibited the same distortion in the resonance curve as for the mechanical resonance.

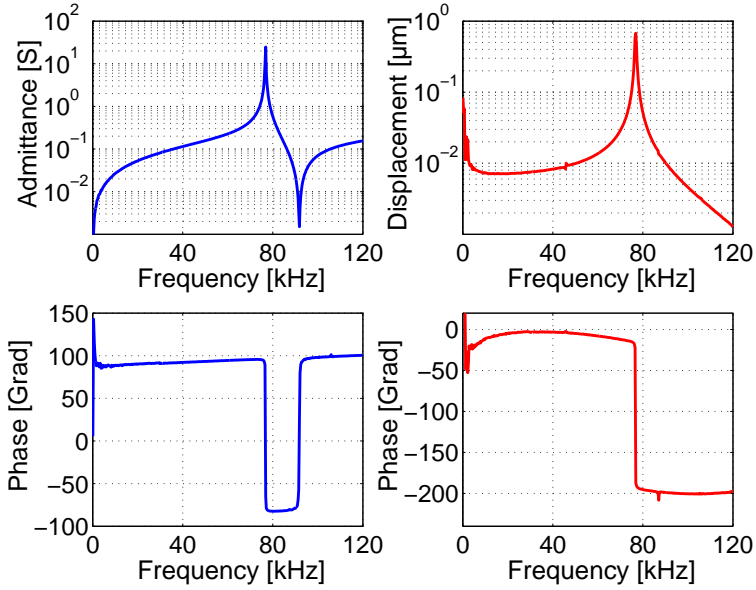


Figure 4.8: Frequency response of a piezoceramic rod sample; plots on the left: electric admittance, plots on the right: longitudinal displacement

4.2.2 Resonance behavior of the motor

In Section 1.1 the control parameters circular excitation frequency, Ω , driving voltage, V_A , and phase deviation $\Delta\phi_V$ for feedback control of USM have been discussed. The frequency responses, presented in the following, are measured at different driving voltages. Furthermore, it is distinguished between the two limiting cases of the phase deviation, the traveling wave operation $\Delta\phi_V = 0^\circ$ and the standing wave operation $\Delta\phi_V = 90^\circ$, Fig. 4.2 and (1.8).

The experimental characterization of the motor's resonance behavior is splitted into three categories. First, the non-linear resonance behavior of the motor is investigated, followed by a description of the well known jump phenomenon. The last part considers the vibration amplitude threshold of the stator vibration which has to be exceeded in order to drive the rotor.

Nonlinear resonance characteristics

In Fig. 4.11 the electric admittance of the motor is plotted for different axial preloads. The curves are recorded at a standing wave operation mode, i.e. for $\Delta\phi = 90^\circ$. Two

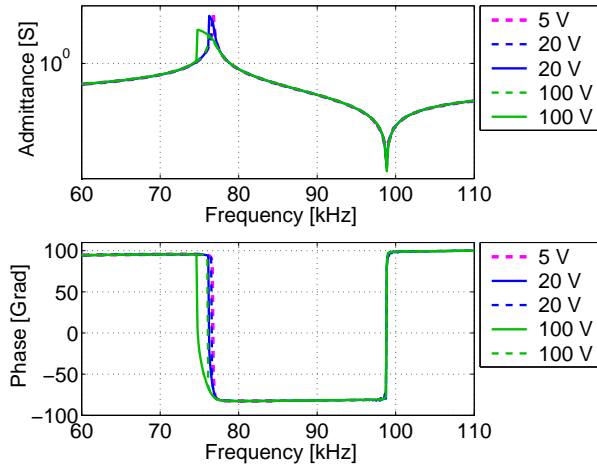


Figure 4.9: Frequency response of the electric admittance, $\underline{Y}_{el}(\Omega)$, of the piezoceramic rod sample near the resonance peak, Fig.4.8: –solid lines: sweep down, - - dashed lines: sweep up

aspects are worth to mention. First, with increasing axial preload the system stiffens, i.e. the resonance frequency increases from 39 kHz to 43 kHz. This stiffening effect may result from two basic mechanisms. On the one hand there is an increase of the penetration of both contact surfaces. Thus, the contact stiffness between both bodies increases with increasing preloads until the bulk stiffness of the system is reached. This mechanism depends on the surface roughness of both contacting bodies. On the other hand it may happen that rotor and stator partially loose contact in the vicinity of the resonance peak. With increasing axial preload the softening effect gets reduced and the resonance frequency increases. This would correspond to a softening effect during sweeping across the resonance. Notably, an axial preload of 250 N corresponds to an axial prestress of 0.7 N/mm^2 at full contact between stator and rotor. The second comment is on the dissipative losses in the motor. As it can be easily seen, the phase signals did not have a zero crossing. Frictional damping in the contact zone is relatively high.

Another measurement is shown in Fig. 4.12. Again, the electric admittance is plotted, but now with varying driving voltage and at a constant axial preload of 150 N. This preload is usually chosen for the operation of such motors. The plots were recorded at standing wave operation. Measuring frequency response plots at standing wave operation allows to compare them directly with those of the free vibrating stator in Fig. 4.6. Frequency response plots at traveling wave operation, i.e. with $\Delta\phi_V = 0^\circ$ will be discussed in the next paragraph. Several comments on the plots in Fig. 4.13 can be made. For driving voltages up to 75 V, the magnitude of the electric admittance decreases

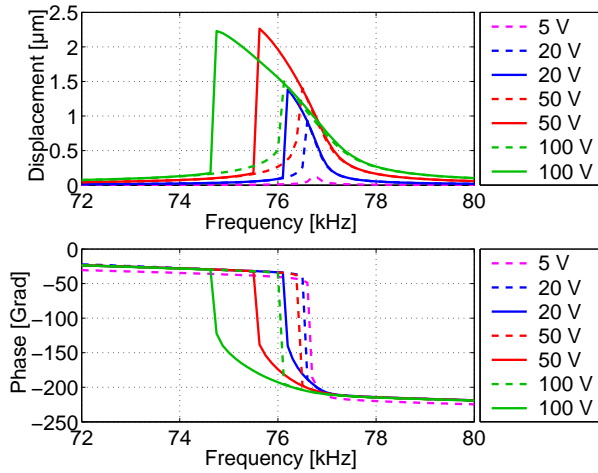


Figure 4.10: Frequency response of the longitudinal displacement of the piezoceramic rod sample in the vicinity of the resonance peak, Fig.4.8: –solid lines: sweep down, - - dashed lines: sweep up

while the phase drop slightly shrinks. Besides this, the frictional damping mechanisms between stator and rotor seem to be relatively strong, since the drop in phase signal is only down to approximately 80° between the resonance and antiresonance frequencies. At somewhat higher voltages there is a turn around, the magnitude of the admittance increases and the phase drop tends to be stronger too. Following even higher driving voltages result in a jump of the electric admittance at the resonance frequency. This jump seems to be caused by the non-linear stator-rotor contact. The stronger drop down in the phase signal reveals a decrease in frictional damping effects. At a driving voltage of 150 V the resonance frequency is at 38.8 kHz. At full stator-rotor contact (contact length corresponding to the wavelength λ of the bending wave) the resonance frequency of the assembled motor is more than 43 kHz. Without stator-rotor contact, the resonance frequency is 38.7 kHz applying 2 V driving voltage, as it can be seen in Fig. 4.4. Thus, the resonance frequency of 38.8 kHz at 150 V driving voltage in Fig. 4.12 leads in a first instance to the assumption of a small contact length or equivalently to a small stiffening effect at resonance. The measurement of the frequency response plot of the stator displacement in Fig. 4.13 shall give more details on the resonance characteristics.

The resonance frequency at low voltages is at 43 kHz. With increasing driving voltage, resonance and antiresonance frequencies approach each other. The plots at 110 V and more show an analog resonance behavior as those in Fig. 4.12. Especially the vibration amplitude at high driving voltages is interesting to be looked at more closely. Values up to 4 μm are reached. At these stator amplitude levels the piezoceramics

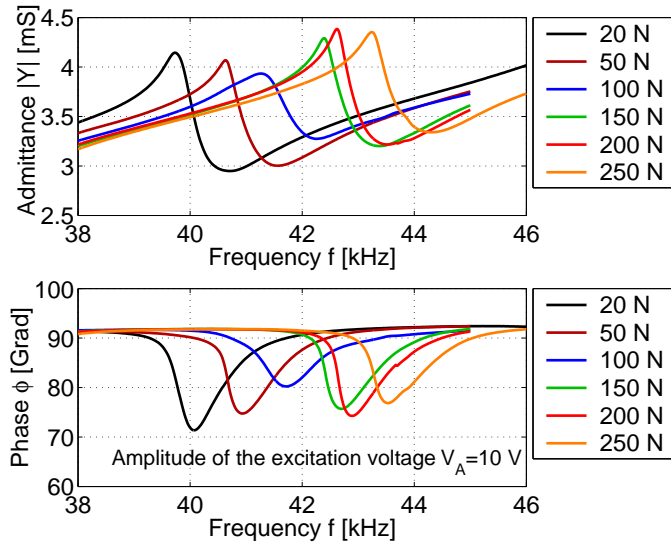


Figure 4.11: Frequency response of the electric admittance, $Y_{el_{A/B}}(\Omega)$, of the motor at constant driving voltage, standing wave operation mode and for different axial preloads

exhibit strong nonlinear resonance behavior, reconsidering the measurement of the free vibrating stator in Fig. 4.7. For a free vibrating stator with vibration amplitude of $4 \mu\text{m}$, the resonance frequency shifts down to 37.5 kHz. In Fig. 4.14 the frequency response plots of the free vibrating stator and those of the assembled motor at similar vibration amplitudes are shown. Coming back to what has been stated about the contact length in the discussion of Fig. 4.12, the following comment can be made. The resonance frequencies of stator and assembled motor at the same level of stator displacement differ approximately about 1 kHz. By no means, it can be argued that there is a weak stator-rotor interaction at resonance as it was supposed by comparing the resonance frequency of the stator at low driving voltage (38.7 kHz) with the resonance frequency of the assembled motor at high driving voltage (38.8 kHz).

The amplitude of the stator's electric admittance, $Y_{el_{A/B}}(\Omega)$, in Fig. 4.14 has a slightly lower level, a sharper antiresonance peak and a greater jump in the resonance. The high frictional damping in the assembled motor is obvious by the almost vanishing antiresonance peak and the low resonance amplitude in the admittance plot. However, the most important conclusion out of the measured frequency responses is that it is not possible to decide from these plots, whether the jump in the resonance frequency is due to the nonlinear stator-rotor contact or due to the nonlinear piezoceramic material behavior!

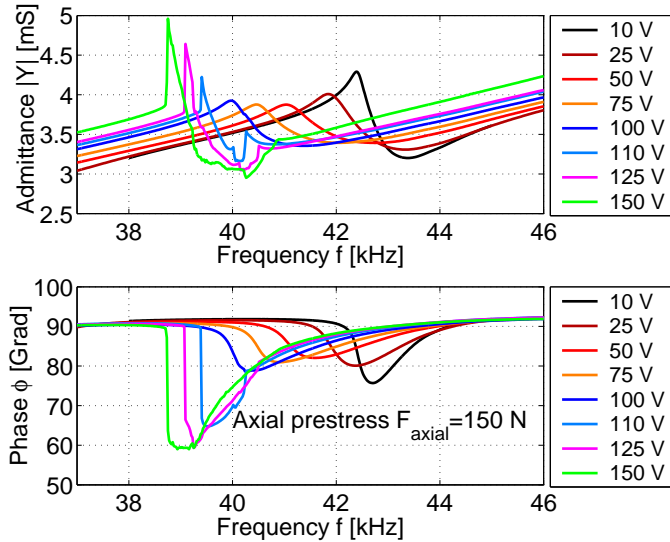


Figure 4.12: Frequency responses of the electric admittance, $Y_{el_{A/B}}$ (Ω) of the motor at different driving voltages and constant axial preload; standing wave excitation: $\Delta\phi_V = 90^\circ$, sweep down

Jump phenomenon

In the preceding paragraph the frequency responses of the assembled motor have been measured at a standing wave excitation. In the following experiments the motor is operated using a traveling wave, $\Delta\phi_V \approx 0^\circ$, see Fig. 4.15. At such an operation mode, the initiation of the rotor motion and the increase in the rotational speed at approaching the resonance frequency can be observed. Both, sweep up and sweep down frequency response plots are recorded. The resonance frequencies between the jumps of sweep up and sweep down curves differ about 2 kHz. The arrow on the right side in the upper plots of Fig. 4.15 indicates the begin of the rotor motion, the arrow on the left shows the end of the rotor motion. The rotation starts at 43 kHz with a relativ small rotational speed (below 1 rpm) and increases rapidly (depending on the sweep rate) to more than 100 rpm. The frequency response plot for the stator displacement at traveling wave operation (left side of Fig. 4.15) is qualitatively similar to the plot recorded at standing wave operation (Fig. 4.13). In contrast, the admittance response plots between both operation modes (Figs. 4.12 and 4.15) differ in their qualitative behavior. The phase response at traveling wave operation drops much more, here down to 20° and has no plateau. In conclusion to the results of the admittance response plots, it can be stated that zero crossing of the phase signal is difficult to reach, if not impossible. To this point, a significant improved contact mechanism between stator and rotor would be

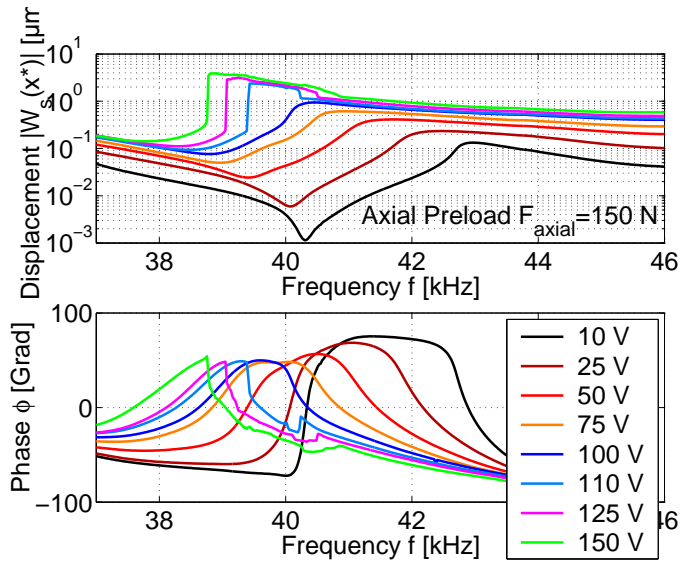


Figure 4.13: Frequency responses of the lateral displacement of a stator surface point at different electric voltage excitations; standing wave excitation: $\Delta\phi_V = 90^\circ$, sweep down

necessary. One possibility would be to take the radial vibration component of the stator into account, which causes dissipative effects only (see (1.2)).

Another conclusion is with respect to the motor operation at low rotational speed. In Section 1.1 it was mentioned that there are three concepts to control rotor speed, changing the driving voltage amplitude \hat{V}_A , the circular excitation frequency Ω or the phase deviation $\Delta\phi_V$. The phase signals of the electric admittance in Figs. 4.12 and 4.15 indicate to prefer a variation of the phase difference instead of the excitation frequency.

Vibration amplitude threshold

Each axial preload has a critical stator vibration amplitude which must be achieved to set the rotor into motion. In Fig. 4.16 the stator vibration amplitude threshold at different axial preloads is prescribed. The rotor motion starts at points, where the curves fluctuate and stops at points, where the curves are smooth again. The fluctuating curves indicate that the motor is not in a steady-state condition during frequency sweeps. This is due to the low integration time adjusted in the gain analyzer and the low rotational speed together with motor imperfections. The start and stop frequencies depend on the axial preload, too. For this particular motor design, the increase in the amplitude threshold is not proportional to the increase in the axial preload.

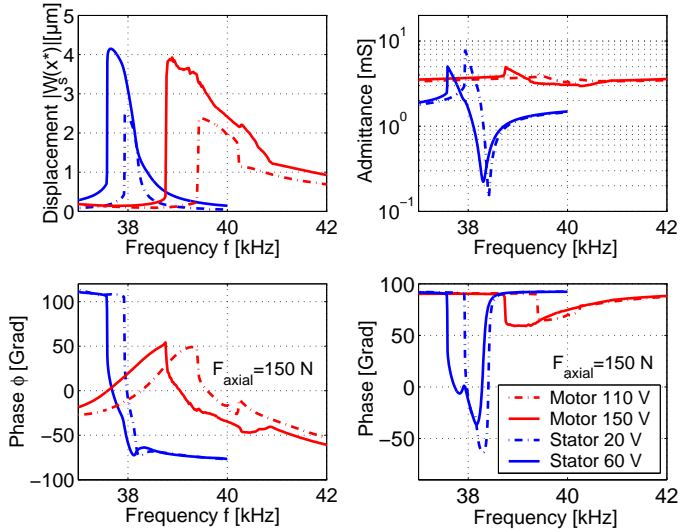


Figure 4.14: Comparison of the frequency responses of the stator displacement for the free vibrating *stator* and the assembled *motor*; standing wave excitation: $\Delta\phi_V = 90^\circ$, sweep down at constant axial preload F_{axial}

4.3 Temperature dependence

The operational behavior of an USM strongly depends on the temperature also. This is well known in USM research since the early stages of the invention of the various motors. The inherent frictional driving mechanism heats up the various motor components. The components most sensitive to temperature in USM are the piezoceramic, the friction layer and perhaps the "third body" layer i.e. the material layer between the contacting surfaces. But also the stator and rotor material parameters can exhibit a relevant temperature dependency. The main temperature effects are a shift of the resonance frequency of the assembled motor and the drift of its output torque. The first effect is demonstrated in Fig. 4.17, showing the electric admittance, $\underline{Y}_{elA/B}$, of the fully assembled motor. The resonance frequency shifts by several hundred Hz. In addition, the level of the admittance drops. In Fig. 4.18 the temperature dependent drift of the motor output torque is illustrated. These data have been recorded at a relatively low load of approximately 10 Ncm. The excitation frequency has been set to only 100 Hz above the resonance frequency at 60°C, which was 38.7 kHz. Within the recorded time of 100 s the temperature rises from 63°C up to 73°C. The motor's rotational speed has been controlled by the test bed's speed controller. The first 20 s the rotational speed was held constant slightly above an average value of 150 rpm. After 20 s the rotational speed was lowered and held constant for further 70 s. Within these 70 s the motor's

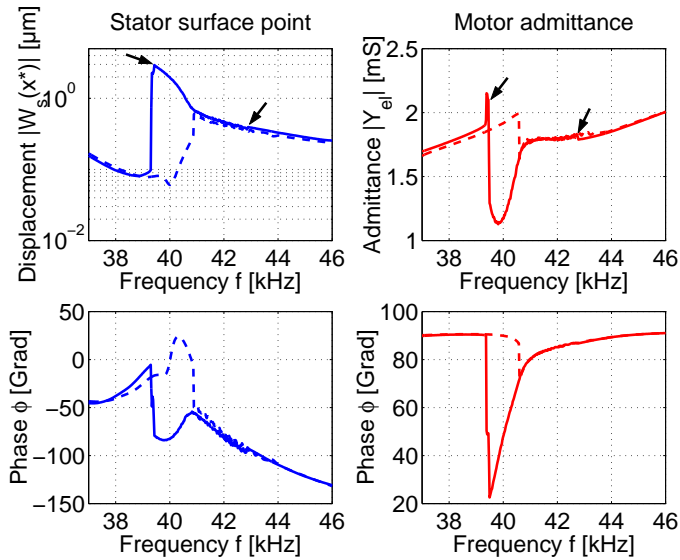


Figure 4.15: Typical jump phenomenon of ultrasonic motors; – solid line: sweep down, - - dashed line: sweep up, traveling wave excitation: $\Delta\phi_V = 0^\circ$

output torque signal declines with a rate of 0.13 Ncm/s. Then the rotational speed was lowered again. However, it should be mentioned, that the motor operation conditions used above are at the motor's limit of capability for the no-load rotational speed. The stator's vibration amplitude was about several μm . The effect of the declining torque signal is probably caused by the temperature induced shift of the resonance frequency according to Fig. 4.17.

The aforementioned effects imply that the temperature influence may be drastic and cause a drift in the motor output quantities. In published data of measured speed-torque characteristics this effect is almost not mentioned or discussed.

4.4 Steady-state behavior of the motor

It is the objective of this section to get a deeper insight into the steady-state motor behavior than the literature provides. Short time fluctuations due to noise and other irregularities are always present in experimental setups. From an experimental point of view, steady-state motor operation is defined as that operation condition where rotational speed and torque did not show a temporal drift as e.g. in Fig. 4.18 and the stator and rotor vibrations have only Fourier components of the excitation frequency

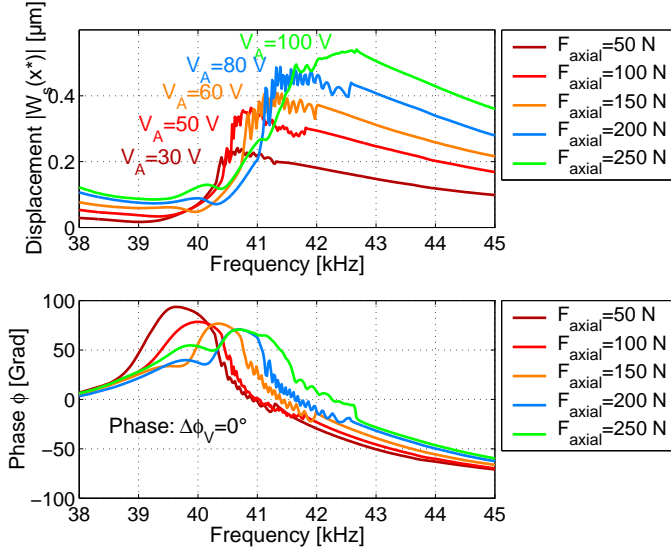


Figure 4.16: Typical vibration amplitude threshold phenomenon at different axial preloads for traveling wave excitation; sweep down

and multiples of it. For both, the rotational speed and the motor torque, the time signals have been recorded for a reasonable long time interval of 100 s. As a measure of the temporal fluctuations the standard deviation is chosen. All measured speed-torque characteristics have been obtained at speed-controlled operation mode of the test rig. Several internal motor quantities (e.g. rotor and stator vibration amplitudes) have been measured simultaneously during the motor operation. Vibration amplitudes of stator and rotor, $\hat{w}_s(x^*)$ and $\hat{w}_r(x^*)$, have been measured as depicted in Fig. 4.2. The electric currents $I_A(t)$ and $I_B(t)$ have been obtained by utilizing two current probes. The motor operation was restricted to a pure traveling wave operation mode, i.e. keeping the phase deviation of the electric voltage signals $V_A(t)$ and $V_B(t)$ at $\Delta\phi_V \approx 0^\circ$. With the aforementioned internal motor quantities, various motor characteristics like power consumption, reactive load and the efficiency were computed. The speed-torque characteristics were measured varying two parameters, namely the excitation frequency and the axial preload. The driving voltage signals were chosen to be sinusoidal.

4.4.1 Speed-torque characteristics: four quadrant operation

In Fig. 4.19 two measured speed-torque characteristics are plotted in a four-quadrant diagram. The two curves correspond to a clockwise and counter-clockwise motor operation. Both curves are point-symmetric to each other in a qualitative sense. This was

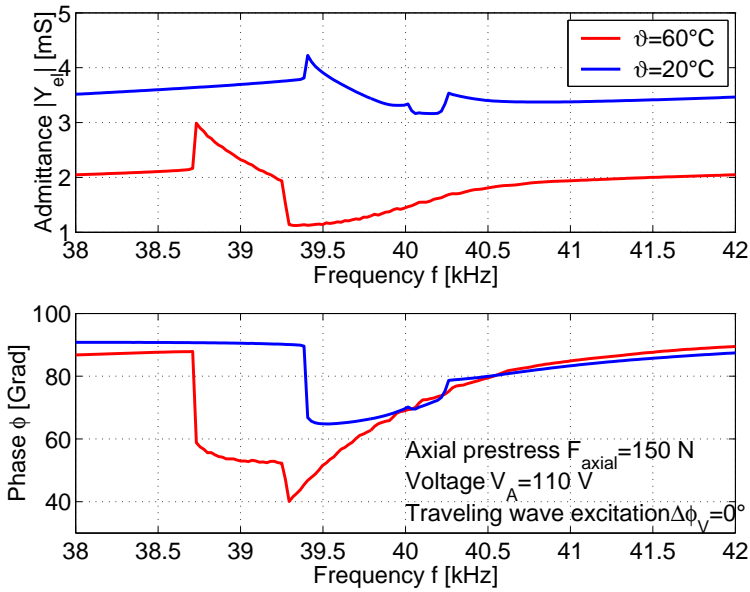


Figure 4.17: Typical temperature effect on the resonance frequency, sweep down

a general observation during all the measurements. Thus, in the subsequent plots it is sufficient to specify only the clockwise or counterclockwise characteristics. The explanation of the speed-torque diagrams is given in Section 1.1. The vertical and horizontal line segments at each operation point in Fig. 4.19 describe the standard deviation in the rotational speed and motor output torque signals, respectively. The characteristics are measured in a sweep down mode, i.e. starting in the dragging quadrant near the no-load speed (e.g. Point 1) and decreasing the rotational speed beyond the stall torque into the braking quadrant. The excitation frequency was approximately 400 Hz beyond the resonance frequency. Approaching the excitation frequency closer than 100 Hz to the resonance frequency causes squealing in the motor. Despite a distance of 400 Hz from the resonance frequency, the excitation voltage was high enough to produce a large no-load rotational speed. This again produces rapid heating up in the motor. Slightly above 80°C a steady-state condition was reached at point 2. At Point 1 the fluctuations in the torque are relatively high, no steady-state operation was possible. The time signals are depicted in Fig. 4.20. The upper two graphs are the time signals within a time interval of 30 s whereas the lower graphs are enlarged views of the zoom windows marked on the upper graphs. For every measurement in the dragging quadrant the qualitative result was similar. Details on the stator and rotor vibrational behavior in the dragging quadrant will be discussed in Section 4.4.5. Following the speed-torque characteristics along the arrow, one finds a temperature rise until Point 13, beyond which it remains

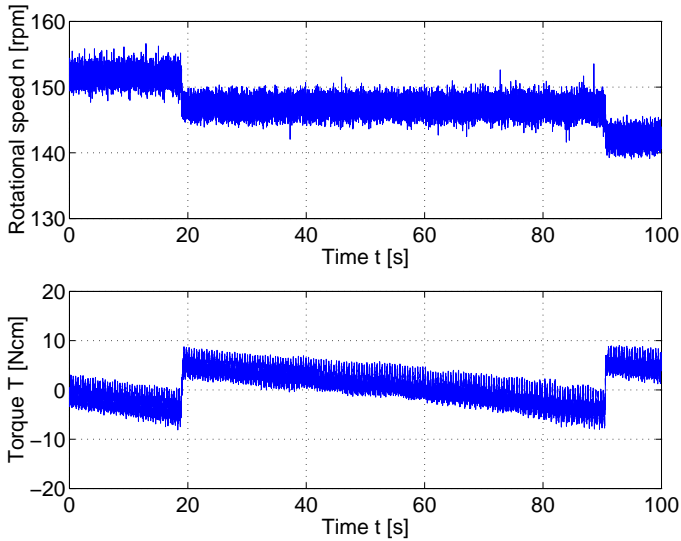


Figure 4.18: Typical time dependent temperature effect occurring at certain operation conditions

constant at 106°C . Up to Point 8 the motor remains in a steady-state condition. The time histories of rotational speed and torque between Points 2 and 11 are qualitatively similar to those shown for Point 2 in Fig. 4.21. An FFT was applied for the speed and torque time signals at operation point 2. The results are depicted in Fig. 4.22. The FFT of the torque signal shows a fundamental peak at 2.1 Hz. This frequency component is related to the rotational speed of the motor. Other peaks are multiples of the fundamental peak. Apparently the motor has an imperfection which produces frequencies that are correlated to the rotational speed of the motor. Such an imperfection could be caused by a rotor with tilt. This means that the axial prestress between stator and rotor is not constant in circumferential direction. HERZOG (1993, [22]) already reported this phenomenon.

An interesting phenomenon in the speed-torque characteristics in Fig. 4.19 is the occurrence of an overhang. So far, such a phenomenon has not been reported in literature. A discussion of this effect is given in Sections 4.4.2 and 4.4.4. It should only be mentioned, that from existing models in literature such a particular behavior of the motor cannot be predicted. The available models are not sophisticated enough to capture unsteady motor behavior such as those between Point 8 and Point 19. Exemplary, the time histories of the speed and torque signals in the braking quadrant (Point 19) are plotted in Fig. 4.23. The speed signal is under good feedback control and the torque signal switches between 60 and 70 Ncm in a more or less regular manner. Since this is not a steady-state motor condition it may not surprise that the motor output torque is sig-

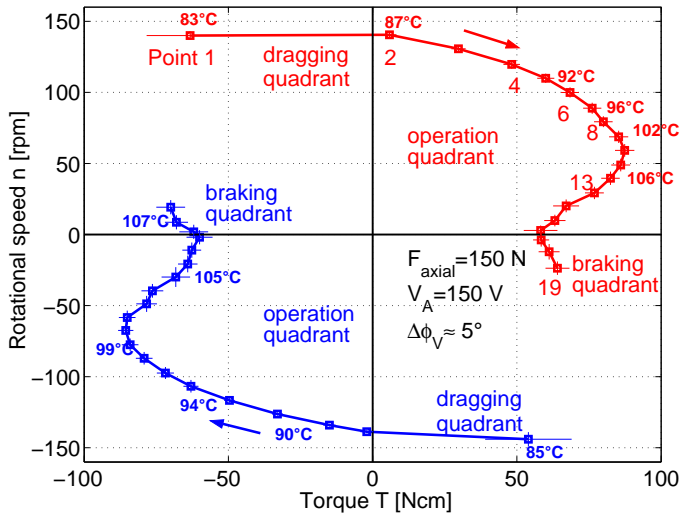


Figure 4.19: Example of typical speed-torque characteristics in four-quadrant motor operation

nificantly lower than its maximum. More detailed results on the overhang phenomenon and unsteady motor operation will be presented in the following sections.

4.4.2 Speed-torque characteristics: influence of excitation frequency

The excitation frequency is one of the control parameters for the motor operation. Its influence on the speed-torque characteristics is shown in Fig. 4.24. The resonance frequency (jump frequency) at this particular axial preload of 150 N is approximately 39.3 kHz. When the excitation frequency approaches towards the resonance frequency, the no-load rotational speed increases. The stall torque stays nearly unchanged. The important phenomenon are the overhanging curves. The key issue is that for these curves the maximum output torque is significantly greater than the stall torque. Too many variables are involved to draw a simple picture of such a phenomenon. For example the influence of the temperature on the contact layer behavior can not be estimated. To each of the curves belongs a slightly different average temperature level. Along the curve for $f = 39.5$ kHz (excitation frequency) the temperature raise is from 82°C to 102°C . Other important variables are the stator and rotor vibrations, which are mainly responsible for the stator-rotor contact state. It is evident, that a unsteady stator-rotor contact may cause this drop in the motor's output torque.

An insight on the time histories of the speed and torque signals at two different operating points is given by Figs. 4.25 and 4.26. In both operating points the speed

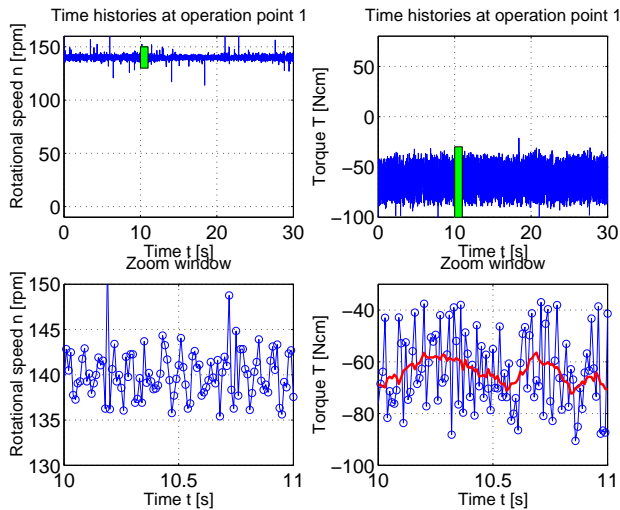


Figure 4.20: Speed and torque time histories at point 1 in the speed-torque characteristic of Fig. 4.19

is under excellent control. The torque signal in Fig. 4.25 shows only small temporal fluctuations. Such a torque time history is common for normal steady-state operating condition. Quite different is the temporal behavior of the torque signal in Fig. 4.26. The time signal shows a switching behavior, which occurs also in the torque signal in Fig. 4.23. The experiments revealed that this particular time behavior of the torque signal is always present if the motor squeals and operates in the vicinity of the stall torque. As it was mentioned above, the no-load rotational speed increases when the excitation frequency approaches the resonance frequency. The measurement depicted in Fig. 4.27 illustrates the relation between the rotational speed and the excitation frequency for a low load. The resonance frequency is at 39.3 kHz. Below 39.4 kHz the motor starts to squeal. From the graph it is seen, that a range of 3 kHz can be used to control the rotational speed from approximately 140 rpm down to nearly zero rpm.

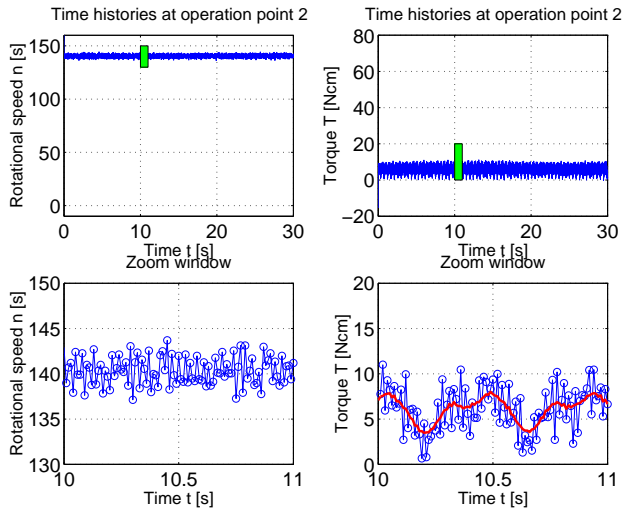


Figure 4.21: Speed and torque time signals at point 2 in the speed-torque characteristic of Fig. 4.19

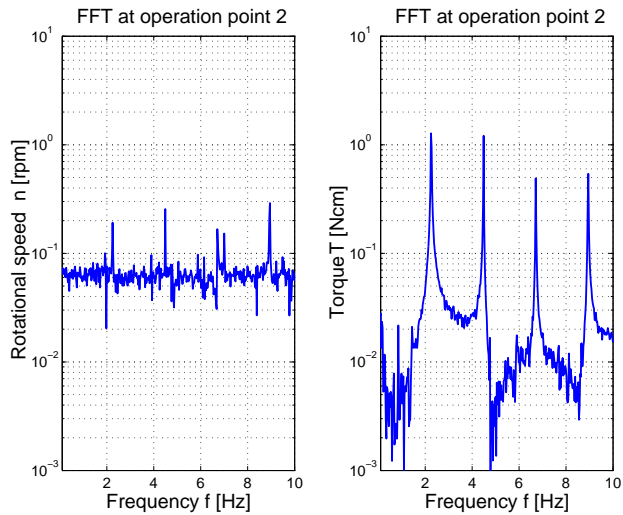


Figure 4.22: FFT of the speed and torque time signals in Fig. 4.21

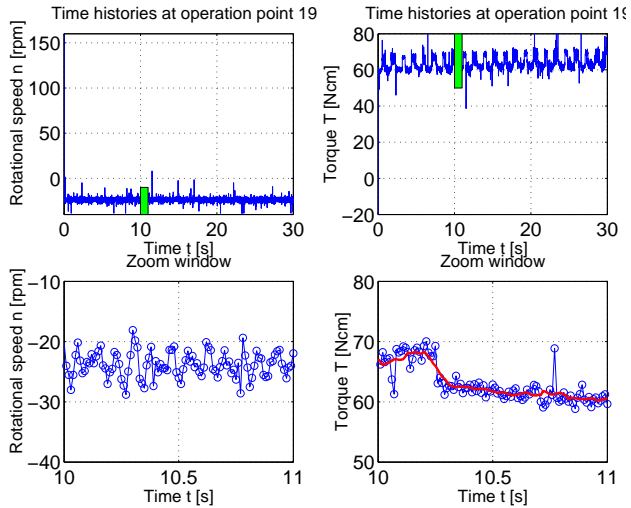


Figure 4.23: Speed and torque time histories of point 19 of the speed-torque characteristic in Fig. 4.19

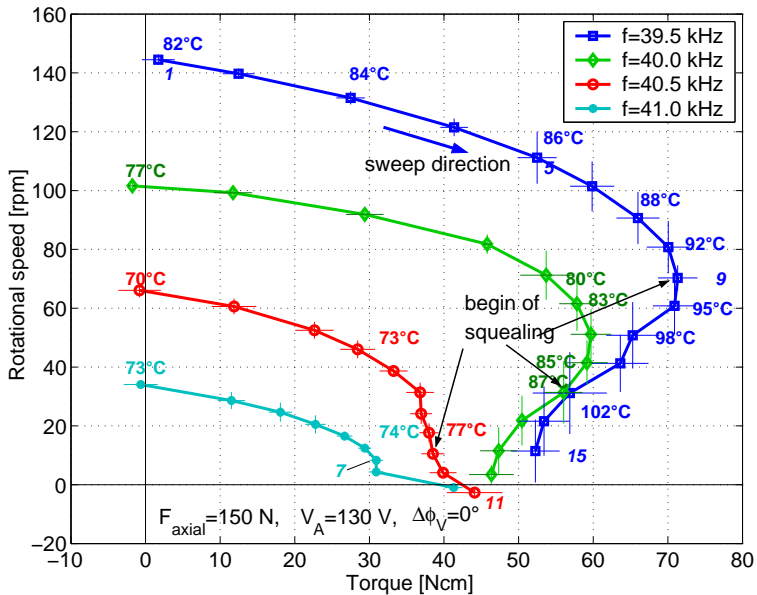


Figure 4.24: Speed-torque characteristics at different excitation frequencies

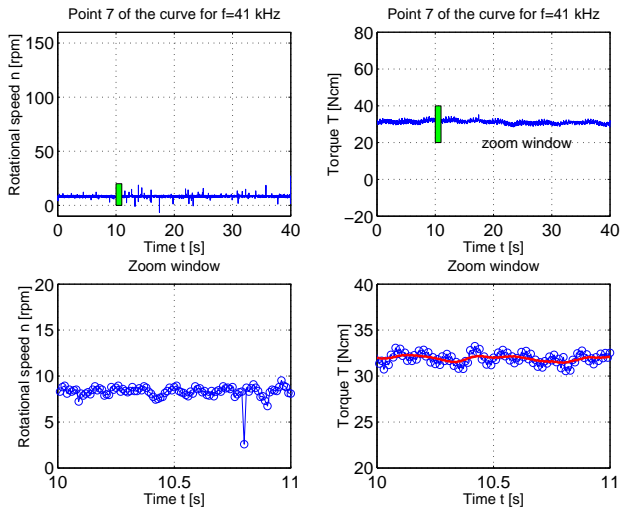


Figure 4.25: Speed and torque time histories of point 7 in the speed-torque characteristic at $f=41.0$ kHz in Fig. 4.24

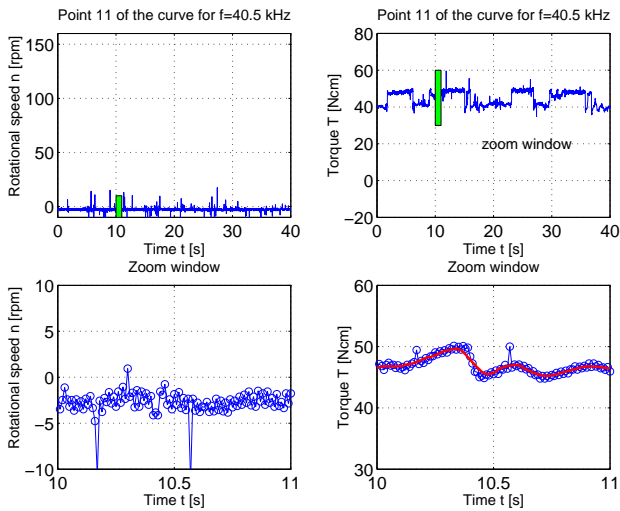


Figure 4.26: Speed and torque time histories of point 11 in the speed-torque characteristic at $f=40.0$ kHz in Fig. 4.24

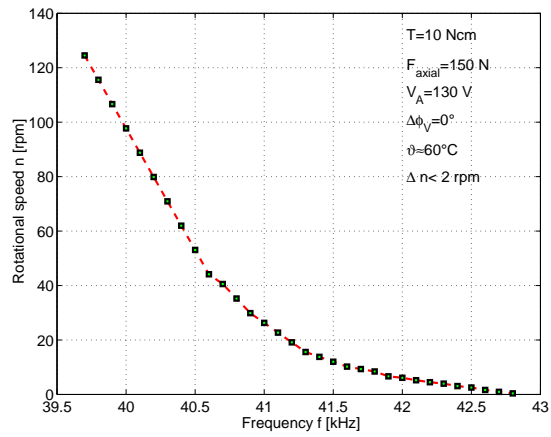


Figure 4.27: Rotational speed for different excitation frequencies

4.4.3 Speed-torque characteristics: influence of axial preload

The only design parameter of USMs which can easily be adjusted is the axial preload. How different the torque speed characteristics may look, like for different axial preloads at constant voltage excitation, is illustrated by the measurements presented in Fig. 4.28. All other parameters except the axial preload are held constant. The distance between

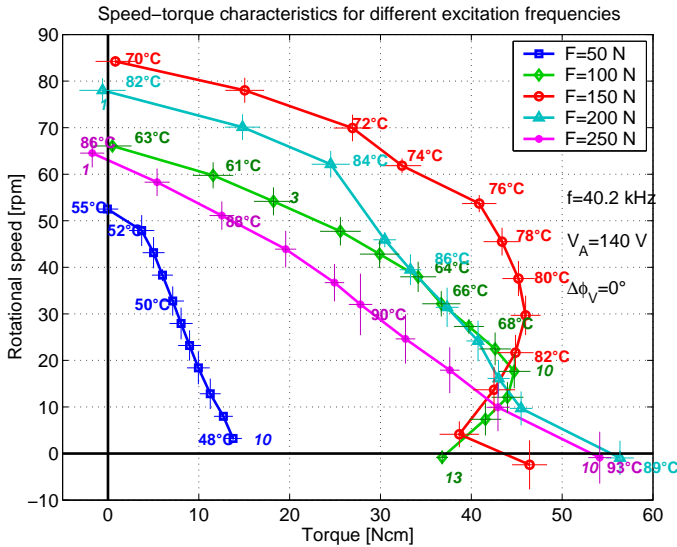


Figure 4.28: Speed-torque characteristics at different axial preloads

the excitation frequency and the resonance frequency depends on the axial preload and is listed in Tab. 4.29. From Fig. 4.28 one observes that the stall torque does increase with increasing the axial preload. And again, for some particular axial preloads overhanging curves exist. The change of the no-load rotational speed with the axial preload is shown in Fig. 4.30. From the model analysis it is expected that the no-load rotational speed decreases with increasing axial preload (see for example SATTEL *et al.* (2001, [49])). However, there is a maximum of the no-load rotational speed, which is a somewhat sur-

axial preload	50 N	100 N	150 N	200 N	250 N
frequency distance	100 Hz	200 Hz	900 Hz	1000 Hz	1000 Hz

Figure 4.29: Distance of the resonance frequency from the excitation frequency at different axial preloads

prising result. Moreover, a FFT of the time histories of stator and rotor vibrations only

show spikes at the excitation frequency and at second harmonics. The vibration amplitudes of neither stator nor rotor show any unusual behavior. Thus, the peculiarity in the variation of the no-load rotational speed is inexplicable from the available experimental data.

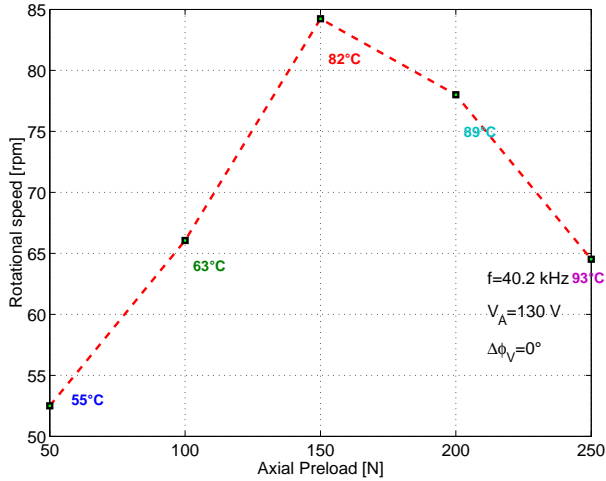


Figure 4.30: No-load rotational speed for different axial preloads

4.4.4 Speed-torque characteristics: hysteresis behavior

In the preceding sections the overhanging speed-torque characteristics have been observed whose occurrences depend on the proximity of the excitation frequency with respect to the resonance frequency (see Fig. 4.24), i.e. on the vibration amplitude of the stator. All the speed-torque characteristics shown in the foregoing sections are measured in a sweep down mode, where the rotational speed has been decreased from the no-load value until the motor stopped. In a cyclic measurement procedure, comprising of a sweep down and a sweep up mode paths are relatively close to each other for curves without overhang. However, they follow distant paths in presence of an overhang (Fig. 4.31). The cycle at $F_{axial} = 200 \text{ N}$ shows two turning points, one at the maximum torque and the other at a somewhat lower rotational speed. This second turning point is present also at other curves but located at the stall torque position (see Figs. 4.19 and 4.24, for example). In some more detailed experimental studies data were taken inside the braking quadrant and they showed that the motor torque does not exceed the maximum torque obtainable in the operation quadrant. It seems that the motor can not resist more than the maximum torque in the operational quadrant. Thus, there must be a pure sliding condition at the maximum torque where the frictional contact

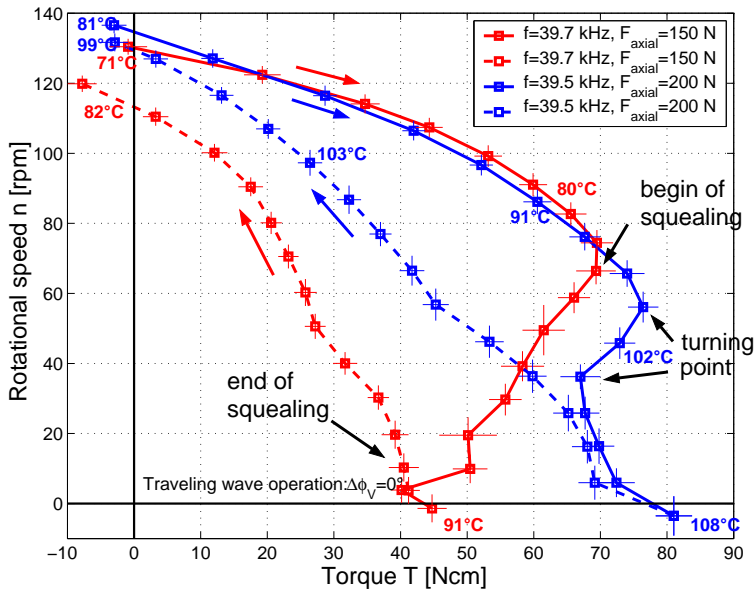


Figure 4.31: Hysteresis behavior for speed-torque characteristics

forces acting on the rotor within the contact zones are all driving forces. The decrease of the torque after the first turning point must either be caused by the onset of breaking contact forces or by the unsteady behavior of the stator and rotor vibrations. For the cycle at $F_{axial} = 150$ N squealing started at the maximum torque of the sweep down path (Point 9) and stopped at the sweep up path where both paths bifurcate. In the FFT diagram of the stator and rotor vibrations, additional peaks besides the regular ones were observed between Point 11 and 19. Naturally, it will be interesting to know the vibrational behaviors of the stator and rotor at the different points in one cycle. This is discussed in the next paragraph.

4.4.5 Vibrational behavior

The aim of this section is a more detailed experimental analysis of the stator and the rotor displacements and the electric currents at all operation points of the measured speed-torque characteristics. The results may be used to find the minimum parameters of motor models to capture the important features, to validate existing motor models and perhaps to find an interrelation between squealing, hysteresis and the vibrational behavior.

First, the time histories of the measured displacement and current signals at normal motor operation will be discussed. Then, two vibration phenomena will be described,

namely the beating and the squealing phenomenon. Last, the vibration amplitudes of stator and rotor along the various speed-torque characteristics are illustrated.

Normal operation behavior

At normal operation the motor works in a steady-state and the stator and rotor vibrations contain only the fundamental harmonics (40 kHz) and its multiples. In Fig. 4.32 typical time histories are shown at normal motor operation. Note that the stator and rotor speeds at surface points have been measured. The displacements can be computed as explained in Section 4.1.3. A deeper insight into the time histories can be obtained from

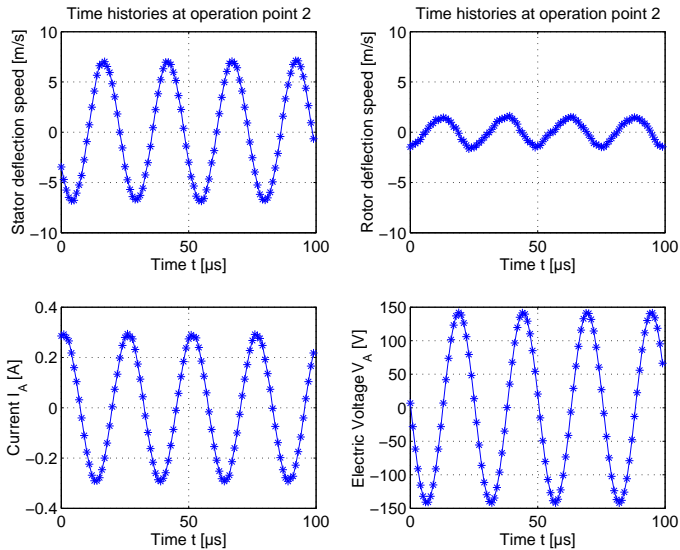


Figure 4.32: Typical time signals at normal operation of the motor, corresponding to point 2 of the speed-torque characteristic in Fig. 4.19

a FFT of the signals, which are presented in Fig. 4.33. As expected, all signals contain the fundamental frequency (excitation frequency) of approximately 40 kHz. The traveling bending waves run through these measuring points and cause the oscillations of the surface points which are detected by the laser-vibrometer. The frequency components in the FFT plot can be correlated with wave length as discussed below. The fundamental frequency component at 40 kHz is due to the traveling bending wave with the fundamental wave number in circumferential direction, which again corresponds in this particular design to a bending mode with nine nodal diameters (see e.g. Fig. 1.5). The frequency component at 80 kHz thus corresponds to the next higher wave number, i.e.

the next higher traveling bending wave component with 18 nodal lines. The occurrence of multiples of the fundamental mode originates from the stator-rotor contact. The contact between the stator wave crests and the rotor results in a periodic deformation of both, which is not necessarily harmonic. However, it is clearly indicated in the FFT

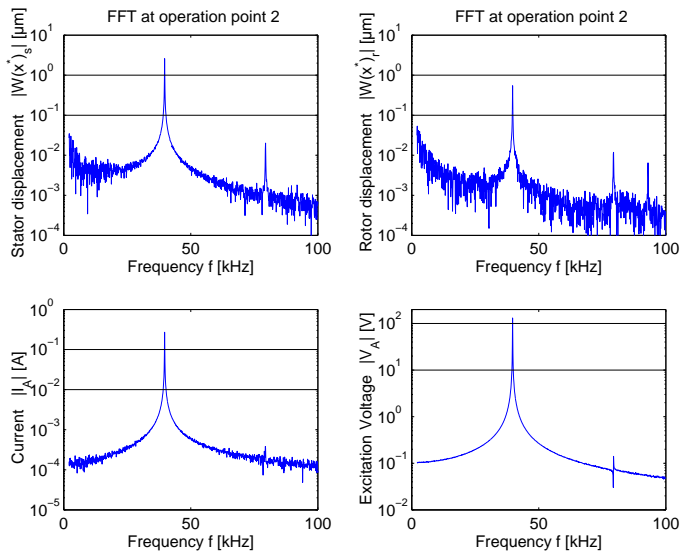


Figure 4.33: Typical FFT spectra of the time signals at normal motor operation; FFT of the time signals in Fig. 4.32.

diagrams that the higher harmonic components are not significant. In the current signals, the amplitudes of the second harmonic component are even an order of magnitude smaller than those of the displacement signals. Such an FFT diagram is typical at a normal operation condition.

Beating in the dragging quadrant

Operating a USM in the dragging quadrant is unusual and probably unwanted. Nevertheless doing so, a new insight into the vibrational behavior of stator and rotor can be gained as Fig. 4.34 illustrates. The beating vibrations occur every time the motor is driven in the dragging quadrant. Due to the electromechanical coupling of the stator vibration and the piezoceramic ring, beating is transmitted to the current signal as well. Even more interesting is that the current signal comes into a saturation beyond 0.5 A. This can be explained by the nonlinear admittance characteristics of the stator arising at high vibration amplitudes, respectively at high strains (Figs. 4.6 and 4.7). The maximum value of the stator speed in Fig. 4.34 is about 11 m/s, which corresponds to

a vibration amplitude of $4 \mu\text{m}$. The rotor oscillations show an irregular behavior with

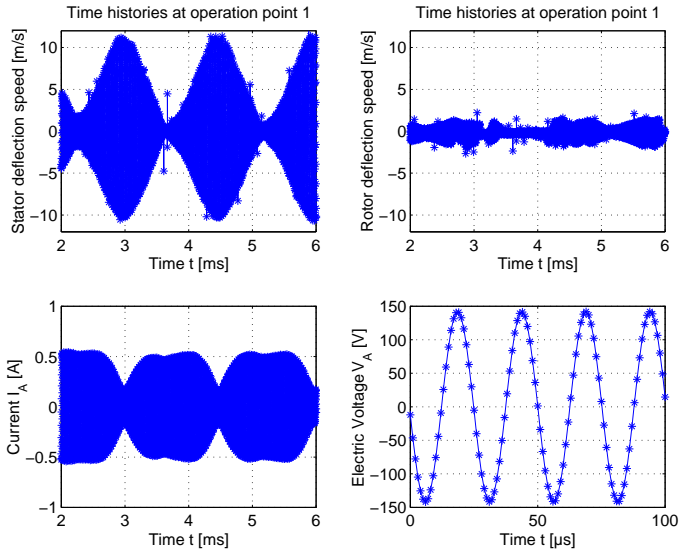


Figure 4.34: Beating phenomenon in the dragging quadrant of the speed-torque characteristic in Fig. 4.19, measured at operation point 1

much lower vibration amplitudes. The FFT diagram of the time signals is plotted in Fig. 4.35. One can vividly see the main peak at 40 kHz for the stator displacement with the two neighboring peaks which result in the beating oscillations. The three closely neighboring peaks are also present in the current signal.

Squealing phenomenon in the operation quadrant

Stator and rotor undergo irregular motion when the motor produces squealing. USMs like the Shinsei USR60 are usually operated far within their potential limits as can be seen comparing published data sheets specifying recommended ranges of operability with the results obtained in this work (Fig. 4.24). An important reason is due to the drastic increase in temperature close to the operation limit. Doubtless, another reason for this is the possible onset of squeal and irregular motion in the vicinity of the limiting values. However, the squealing effect is not only a problem when driving the motor at its operational limit, but also during the early stage of motor design. The geometry of stator and rotor, contact layer material parameters etc., all of them often make the design process difficult with the need of a vast amount of experiments. In the following, only an example is given regarding the squealing phenomenon. The time signals

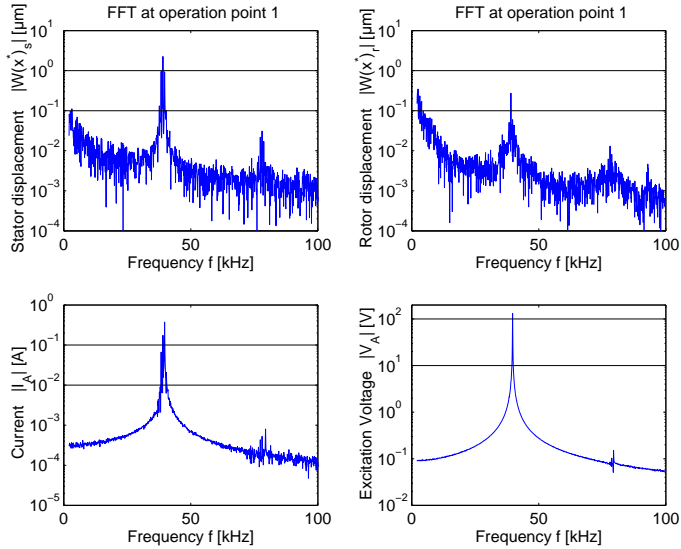


Figure 4.35: FFT of the time signals in Fig.4.34

shown in Fig. 4.36 are typical after the onset of squealing. In Fig. 4.37 the FFT's of the time signals are shown. Note that the time signals and the corresponding FFT diagrams are only snapshots. There are temporal fluctuations in the time signal, i.e. the magnitudes of some of the frequency components may change. Moreover, it may happen that frequency components appear or vanish during a long term run, say, of several milliseconds. Also, the laser beams are focused at one surface point on the outer circumference of stator and rotor. One has to keep in mind, that the time signals and the FFT diagrams may look different at other surface points. In the following, vibrational components with frequencies different from the fundamental operation frequency - and multiples of it - are called parasitic vibrations. Those operation points at the measured speed-torque characteristics where squeal and parasitic frequency components in the FFT diagram appear are listed in Tab. 4.2. Parasitic vibrational components which may occur in the inner part of stator and rotor have not been detected. From the table it follows, that the onset of squealing is before first of appearance of parasitic peaks in the FFT diagram. Generally, the amplitude of parasitic vibrations in the stator-rotor contact region are at least one order of magnitude smaller than the fundamental peak at 40 kHz. Having a closer look at which position in the speed-torque characteristics squealing show up, there is no characteristic operation state where this happens. In curve No. 1 in Tab. 4.2 squeal occurs before the turning point is reached, whereas in curve No. 4 it starts at the turning point. For curves No. 3 and 6, on the other hand, squealing appears after the turning point is exceeded. But it should be stated clearly, that there

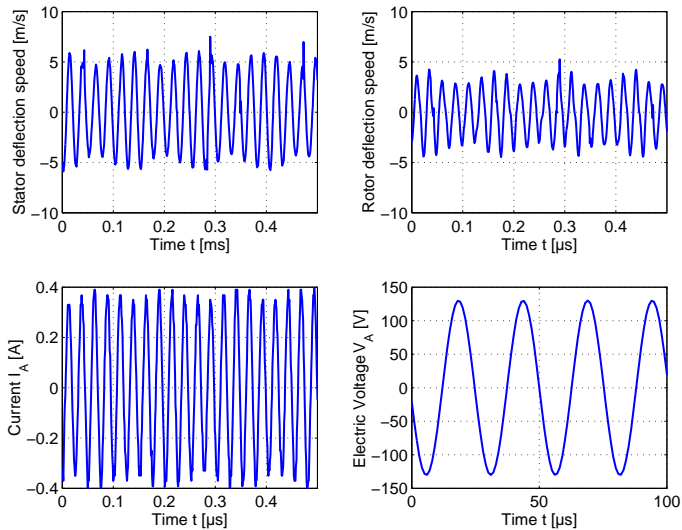


Figure 4.36: Beginning of squealing at point 9 of the speed-torque characteristic with excitation frequency $f=39.5$ kHz; Fig. 4.24

speed-torque characteristics			begin of	begin of parasitic	main parasitic
			squal at	vibrations at	vibrations in
No.	Figure	curve	Point No.	Point No.	kHz
1	4.19		8	13	47, 55
2	4.24	40.5 kHz	9	11	47, 55
3	4.24	40.0 kHz	9	9	47, 55
4	4.24	39.5 kHz	9	9	55
5	4.28	50 N	9	11	47, 55
6	4.28	150 N	9	11	47, 55

Table 4.2: Summary of the occurrence of squealing and parasitic frequency components in the FFT diagrams

is no distinct relation between the onset of squeal and the occurrence of overhang in speed-torque characteristics. For the overhanging curve corresponding to $F_{axial} = 100$ N in Fig. 4.28 no squeal occurs, but appears for curves No. 2 and 5, where no overhang exist. Looking at curve No. 1, for example, the onset of parasitic vibrations in the contact region take place after the turning point, whereas the squealing shows up

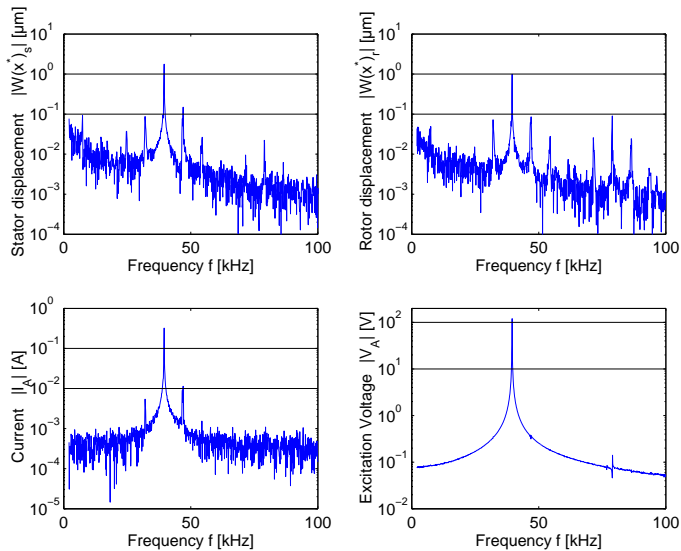


Figure 4.37: FFT of the time signals in Fig. 4.36 during heavy squealing in a motor

even before. All the aforementioned facts suggest that squealing in this motor and at the particular operation conditions (e.g. high operation temperature up to 90°C) is a side effect which does not influence the motor operation drastically, but causes uncomfortable noise. However, during the design of new motors, parasitic vibrations may cause not only unwanted noise, but also a drastic reduction of motor performance. The same can happen when operating a motor at low temperature (20°C , e.g.). For a more detailed investigation of the effect of squealing further information are required, as e.g. on the spatial distribution of the parasitic vibration modes or on the eigenmodes and eigenfrequencies of both, the stator and the rotor.

Vibration amplitudes along the speed-torque characteristics

In sections 4.4.1 to 4.4.4 the speed-torque characteristics of the motor were discussed. The typical vibrational signatures at different operation points for various speed-torque curves were also presented. Here, the vibrations of stator and rotor displacement and the fluctuations of the electric current along different speed-torque characteristics are discussed. It is expected that these information contribute towards a better understanding of the shape of the different curves as well as towards the validation of existing motor models. In Fig. 4.38 the vibration amplitudes along the speed-torque characteristics in the four-quadrant operation are plotted. The motor was excited at a constant driving voltage in a traveling wave mode. Following the curve from high to low rotational

speed, the amplitude of stator displacement, \hat{w}_s , decreased from $2.7 \mu\text{m}$ at no-load rotational speed by half at stall torque, whereas the amplitude of rotor displacement,

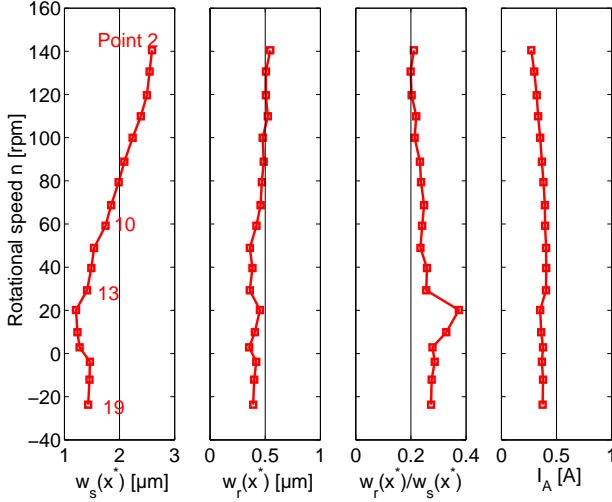


Figure 4.38: Vibration amplitudes of stator and rotor displacement, $\hat{w}_s(x^*)$, $\hat{w}_r(x^*)$, resp. and electric current \hat{I}_A for the speed-torque characteristics of Fig. 4.19

\hat{w}_r , decreased not that much. Thus, the ratio between the rotor and the stator amplitudes shows an increasing tendency, implying an enlargement of the area of contact between them. In the following, we shall try to explain the overhanging phenomenon in the speed-torque characteristics (Fig. 4.19) with the help of above results on vibrations along the sweep down path. At the operating point 10, the maximum motor torque is achieved. This corresponds probably to a contact state where the tangential contact stresses acting on the rotor are all oriented towards the rotor motion, i.e. they are all driving stresses (no change in sign in the tangential stress distribution). Exceeding the maximum motor torque at Point 10, braking contact stresses must take place in order to reduce the motor torque.

In Fig. 4.39 the vibration amplitudes are depicted for the speed-torque characteristics at different excitation frequencies. The stator vibration amplitudes reduce with decreasing rotational speed, i.e. with increasing load-torque. The rotor vibrations, however, do not follow this behavior distinctly. Nevertheless, the ratios between the rotor and the stator vibration amplitudes tend to increase with increasing mechanical load. Two of the curves, at 39.5 kHz and 40 kHz, belong to speed-torque characteristics with an overhang. The explanation for the occurrence of the overhang phenomenon, given in the previous paragraph, holds also for the curves in Fig. 4.39.

In Fig. 4.31 a strong path dependent behavior in the speed-torque characteristics

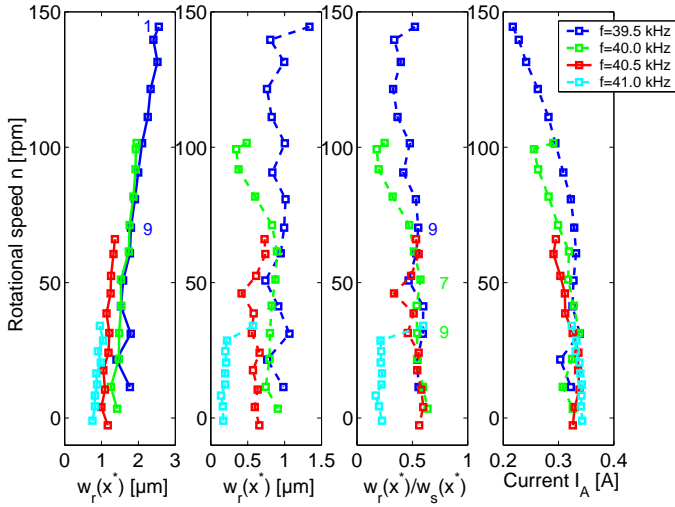


Figure 4.39: Vibration amplitudes of stator and rotor displacement, $\hat{w}_s(x^*)$, $\hat{w}_r(x^*)$, respectively and electric current \hat{I}_A for the speed-torque characteristics of Fig. 4.24

was observed. The strength of this hysteresis phenomenon depends on the strength of the overhang. An interesting question arises immediately: whether the low motor torque along the sweep up curves could be explained by the stator and rotor vibration amplitudes. For the speed-torque cycle at $F_{axial} = 150$ N in Fig. 4.31 the vibration amplitudes are plotted in Fig. 4.40. The sweep down path starts at Point 1, reaches the stall torque Point 17 and follows then the sweep up path to Point 30. At Point 18 both speed-torque characteristics bifurcate (Fig. 4.31). Surprisingly, there is no significant difference between the vibration amplitudes along both paths. Up to Point 23 in Fig. 4.40 both curves coincide quite well and beyond it the stator vibration amplitude along the sweep up path is slightly lower. The rotor vibration amplitudes are almost equal along both paths. However, the current signal between both paths shows a distinct difference. Thus, the electric input power between both paths is different too. In conclusion, the stator and rotor vibration amplitudes alone can not explain the hysteresis behavior in the speed-torque cycles with respect to the rotational speed. Since the vibrational behavior along the sweep up path is a steady-state one, an obvious hypothesis is, that the tangential contact force distribution causes this hysteresis behavior. One line of argument could be that the tangential contact force distribution depends on the path history and on the initial conditions. However, further model analysis and experiments would be necessary to check this hypothesis.

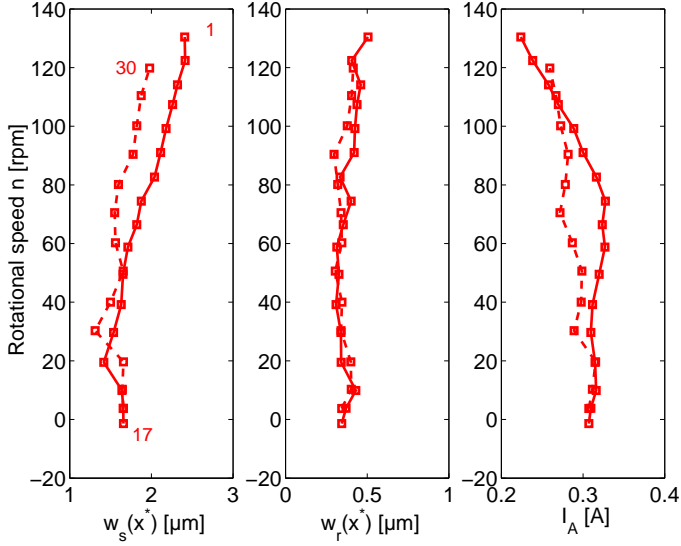


Figure 4.40: Vibration amplitudes of stator and rotor displacement, $\hat{w}_s(x^*)$, $\hat{w}_r(x^*)$, resp. and electric current \hat{I}_A for the speed-torque characteristics with significant hysteresis in Fig. 4.31

4.4.6 Power and efficiency

Important motor properties which have not been considered yet are the power quantities and the motor efficiency. With the rotational speed, $n(t)$, the motor torque, $T(t)$, the electric voltages, $V_A(t)$, $V_B(t)$, and the electric currents, $I_A(t)$, $I_B(t)$, different power quantities and the motor efficiency could be computed. The general definitions of different power quantities have been stated in (2.106)-(2.109). Since the time signals are available in a discrete form, the power quantities are computed practically in a different way as expressed by the definitions. The recorded values of the different time signals are stored in vector format. Using MATLAB style formulas the power quantities are calculated as following. The electric input power yields

$$\langle P_{in} \rangle = \langle P_{in} \rangle_A + \langle P_{in} \rangle_B = \text{mean}[\mathbf{V}_A \cdot * \mathbf{I}_A + \mathbf{V}_B \cdot * \mathbf{I}_B] \quad (4.7)$$

and the mechanical output power results in

$$\langle P_{out} \rangle = \text{mean}[\mathbf{T} \cdot * \mathbf{n}] , \quad (4.8)$$

with \mathbf{n} in rad/s. For the calculation of the reactive power $\langle Q_{f\Omega} \rangle$ according to (2.109) the effective voltages and the effective currents are needed

$$V_{\text{eff}i} = \text{sqrt}[\text{mean}[\mathbf{V}_i \cdot ^2]] , \quad I_{\text{eff}i} = \text{sqrt}[\text{mean}[\mathbf{I}_i \cdot ^2]] , \quad i = \{A, B\} . \quad (4.9)$$

In Fig. 4.24 the speed-torque characteristics at various excitation frequencies were plotted. The corresponding power and efficiency curves are illustrated in Fig. 4.41. As expected, the average input power level increases when the excitation frequency approaches the resonance frequency (approximately 39.3 kHz). The reverse is valid for the reactive power component. It is important to note that for this particular motor design there is always a reactive power component, which can be more than four times the average input power! Such a high reactive power component needs sophisticated power electric design to avoid reactive loading of the transistors. The other possibility

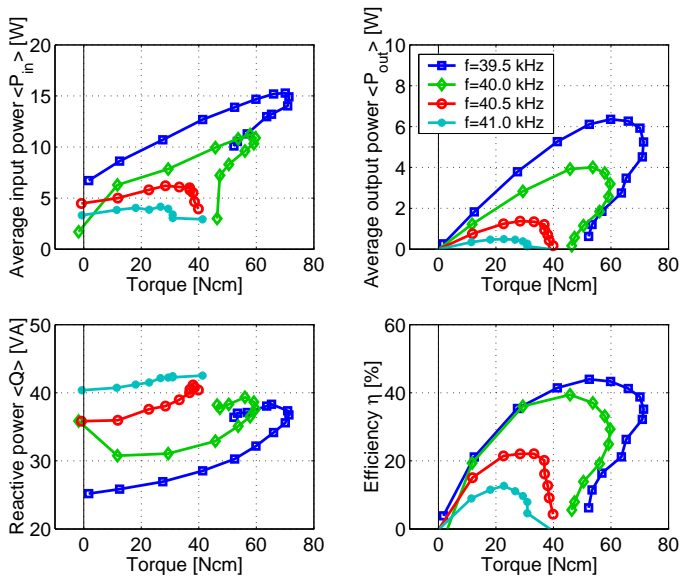


Figure 4.41: Average input power, average output power, reactive power and motor efficiency at different excitation frequencies, see Fig. 4.24

to avoid such a reactive loading may be achieved if the phase response of the electric admittance has a zero crossing in the resonance (compare Figs. 4.4 and 4.6). One design measure would be to increase the electromechanical coupling in the motor which corresponds to an increase of the distance between resonance and anti-resonance frequency. Comparing the admittance curves of the rod sample in Fig. 4.9 with those of the stator in Fig. 4.6 shows clearly the influence of the distance between resonance and anti-resonance on the phase response. Since the rod sample is solely made of piezoceramic material, there is a high electromechanical coupling and thus a larger distance between resonance and anti-resonance. In the motor design, illustrated in Fig. 1.1, the high electromechanical coupling is realized by a stator fully made of piezoceramic material. Additionally it is important to choose a proper vibration mode in the stator. This was pointed out by BERG (2001, [5]). However, one has to keep in mind, that a sta-

tor fully made of piezoceramics has also disadvantages. The temperature dependence of the piezoceramic material parameters is more distinct and shifts the design problem to the feedback control of the motor's resonance. Another result follows from the efficiency curves in Fig. 4.41. The dependence of the efficiency on the excitation frequency recommends to operate the motors in the vicinity of the resonance frequency.

In the previous sections it was mentioned that the motors were operated in the traveling wave mode. The stator is excited by the electric voltages $V_A(t) = \hat{V}_A \sin \Omega t$ and $V_B(t) = \hat{V}_B \cos(\Omega t + \Delta\phi_V)$, with $\Delta\phi_V = 0^\circ$ for a pure traveling bending wave excitation. Note, however, that a perfect transfer behavior of the stator and rotor is necessary to get a perfect traveling wave. The fundamental components of the electric

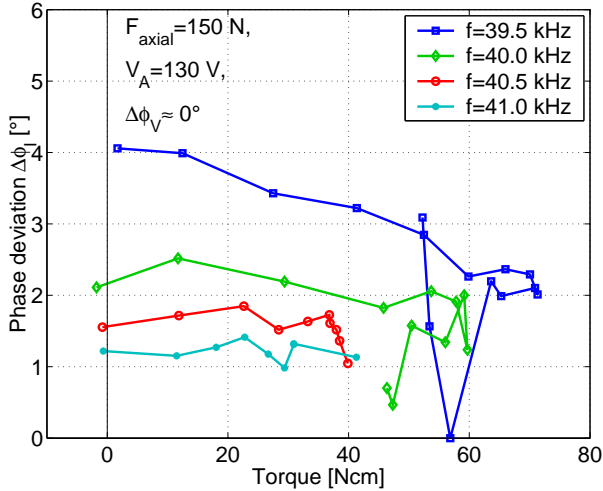


Figure 4.42: Phase deviation $\Delta\phi_I$ between the two current signals $I_A(t)$ and $I_B(t)$, see Fig. 4.24

current signals are

$$I_A(t) = \hat{I}_A \sin(\Omega t + \alpha_A), \quad \text{and} \quad I_B(t) = \hat{I}_B \cos(\Omega t + \alpha_B) \quad (4.10)$$

with the phase deviation

$$\Delta\varphi_I = \alpha_A - \alpha_B. \quad (4.11)$$

The phase deviation gives a measure for the purity of the traveling bending wave. Assuming the stator and rotor to be manufactured in good quality without significant imperfections, deviation from zero in $\Delta\varphi_I$ indicates standing wave components in the stator. Figure 4.42 shows the phase deviation for the speed-torque characteristics at different excitation frequencies in Fig. 4.24. The phase deviations are computed by

using the FFT of the time signals. The curves illustrate that the motor operates in a traveling bending wave mode in good approximation.

Besides the variation of the excitation frequency, the motor's characteristics are influenced also by the axial preload. This has been demonstrated in Section 4.4.3. The corresponding power characteristics are plotted in Fig. 4.43. The plot shows that

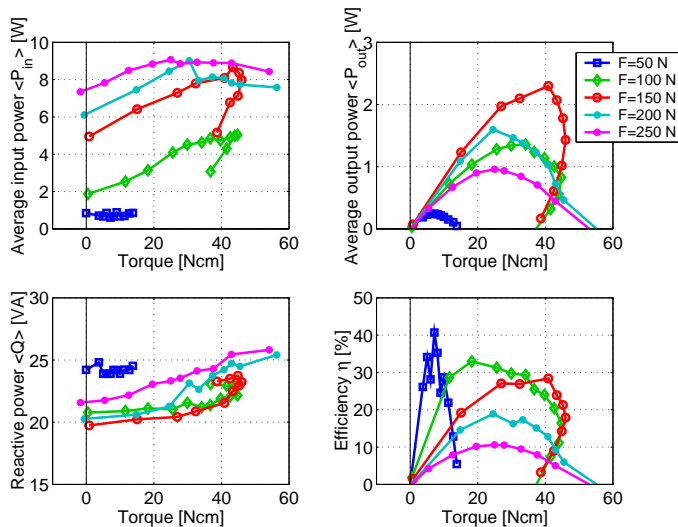


Figure 4.43: Average input power, average output power, reactive power and motor efficiency at different axial preloads, see Fig. 4.28

the level of the average input power increases with increasing axial preload, whereas the average output power curves has a maximum for an axial preload of 150 N. This behavior naturally comes along with the behavior of the speed-torque characteristics at different axial preloads. The reactive power curves show no significant effects. For all operating points along the speed-torque characteristics the traveling bending wave operating mode is in good approximation, as Fig. 4.44 illustrates. A change in the axial preload has no influence on this mode.

Following a sweep up and down path along a speed-torque curve, the motor characteristics exhibit a hysteresis effect. Such a phenomenon is most visible for curves with significant overhang. In Fig. 4.45 the power behavior of a typical hysteresis curve is illustrated. The power consumption along the sweep up path is much smaller than along the sweep down path in some regions. This effect cannot be explained by the differences in the vibrational amplitudes of stator and rotor along both paths (see Fig. 4.40). The differences are too small. The tangential contact behavior must have a strong influence on the motor characteristics along the sweep down path. There is evidence that two

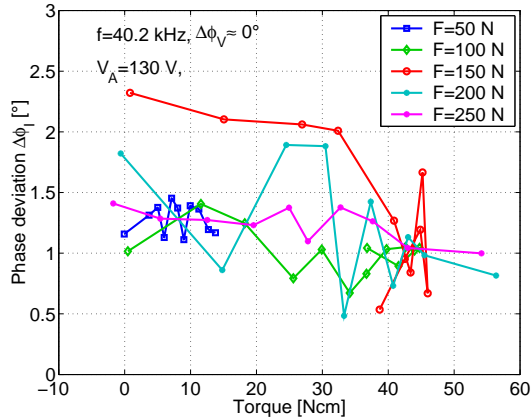


Figure 4.44: Phase deviation $\Delta\phi_I$ between the two current signals $I_A(t)$ and $I_B(t)$; corresponds to Fig. 4.28

stable tangential contact states exist at the same motor torque, one on the sweep down path at higher rotational speed and the other on the sweep up path at lower rotational speed. Since it is difficult to find out experimentally what is going on inside the contact zones between stator and rotor, more detailed model analysis would be helpful. Finally, it should be noted, that the motor was operated in good approximation in a traveling wave mode along both paths. The phase deviations $\Delta\varphi_I$ were only a few degrees.

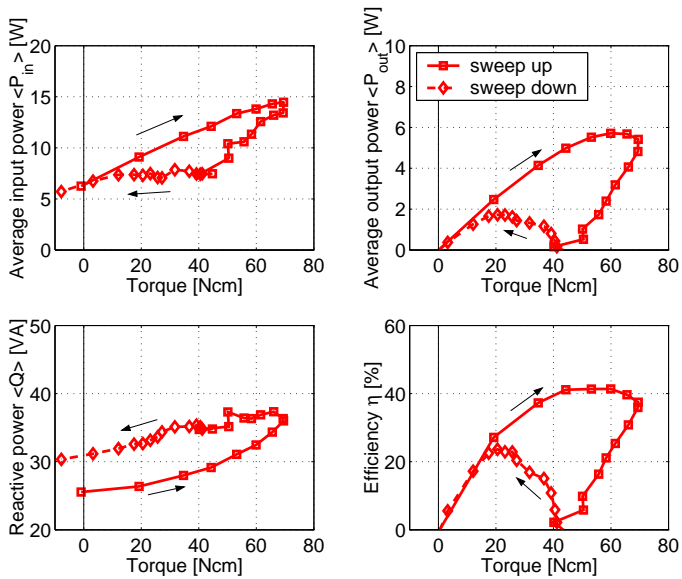


Figure 4.45: Average input power, average output power, reactive power and motor efficiency at different axial preloads; corresponds to Fig. 4.31

4.5 Summary

The experiments presented in this chapter give a comprehensive overview on the motor dynamics. They were focused on motor features which so far have not been investigated experimentally. Some new and perhaps interesting insights into the motor behavior were obtained from a dynamics point of view. The measurements had been carried out with a typical USM, which has a potential for further miniaturization and optimization of the torque to volume ratio. During all measurements the motors were driven without feedback control and without resonant power electronics, in contrary to most other published works. The focus has been on the plant behavior. Additionally, the temperature rise due to the frictional contact between stator and rotor was recorded. In the following, the most important results will be summarized.

Depending on the axial preload and on the position of the excitation frequency with respect to the resonance frequency, the temperature rises to different levels. The closer the excitation frequency at the resonance frequency, the higher the no-load rotational speed and the temperature rise. Within a few minutes of operation the temperatures reaches up to 80°C -90°C.

An interesting but surprising effect was observed in the resonance characteristics of the stator itself and the motor. The motor shows a softening type of nonlinearity and jump phenomenon in it's resonance curves (see Figs. 4.12 and 4.13). In many works this well known effect is supposed to originate from the nonlinear stator-rotor contact interaction, i.e. from a geometric nonlinearity. But measurements of the free stator vibrations (without rotor) revealed the same softening and jump phenomenon at vibration amplitude levels reasonable for the motor operation (see Figs. 4.6 and 4.7). In the stator, however, these effects result from a material nonlinearity in the piezoceramics. Thus, it seems that it is not possible yet to clearly indicate from which effect the jump in the resonance of the motor originates, from the material nonlinearity of the piezoceramic or from the geometric nonlinearity of the stator-rotor contact or from both. This is pointed out in Fig. 4.14, where a comparison of the jump phenomenon in both stator and rotor is given. From a motor design perspective the jumps are unwanted effects. Especially as it is desirable to drive the power electronic device near resonance to avoid reactive loading. Therefore, it is interesting to know the cause of the jump phenomenon in the resonance curves to estimate in advance their importance in the motor design or to avoid them. The softening behavior in piezoceramic samples is accompanied by an increase in the internal "damping", as can be seen by inspecting the phase of the electric admittance in Fig. 4.12. It is not obvious whether this "damping" effect originates from hysteresis due to a change of the net polarization or from mechanical damping mechanisms in the piezoceramic.

Using a special test rig, several speed-torque characteristics also with the phenomenon of overhang have been observed (see Fig. 4.19). Its occurrence depends on

the excitation frequency and the axial preload. Following a sweep down mode along the speed-torque characteristics (e.g. Fig. 4.19), the parasitic vibrations in both, stator and rotor, occur at different operating points, in most of the cases at or beyond the maximum output torque. Additional experimental and analytical studies would be necessary to explain this effect. Driving the motor in the dragging quadrant causes a beating phenomenon in the stator vibrations with high vibration amplitudes. This severe motor operation condition may produce high strain in the piezoceramics and high frictional loading. Therefore, such an operation should be avoided. Depending on the adjustment of the motor parameters, especially the excitation frequency and the axial preload, the speed-torque characteristics show a hysteresis behavior, i.e. the operation points of the motor depend on history. The curves produced by a sweep down and a sweep up of the rotational speed in the test rig are different. It is supposed that two different tangential contact stress distributions occur at the same excitation frequency, since the vibration amplitudes of the stator and the rotor are not significantly different between both paths, the knowledge of such a behavior may be important from a control perspective. Almost equal values for the control parameters may result in quite different motor output parameters.

A well-known effect in USM is the high reactive power component. The experiments show that the reactive power component can be more than four times compared to the average input power. Such a high amount of reactive electric current loads the transistors of the power electronic devices and demands for special power electronic design. To avoid reactive components in the electric current, there must be a zero crossing in the phase of the electric admittance at resonance. Whether the phase shows a zero crossing depends on the distance between the resonance and anti-resonance together with the amount of dissipative effects. Smaller distances between resonance and anti-resonance together with high dissipative effects lead to a low drop in the phase without zero crossing (Fig. 4.6). The experiments with a piezoceramic rod sample in Fig. 4.9 show, that with increasing electromechanical coupling, respectively increasing distance between resonance and anti-resonance, the phase drop in the electric admittance increases. Driving the motor with low reactive power components would be possible by using a stator totally made of piezoceramics, for example. But this may entail other negative effects, as e.g. a more distinct temperature dependence of the motor parameters.

Chapter 5

Discussion and future work

In the last years there has been considerable interest in new motor designs. However, the development of motor models, adequate for motor design and optimization is behind the technological state of the art of these motors. With more sophisticated motor models important design aspects may be considered, like those for choosing the proper rotor geometry and material parameters. The simple motor model proposed in Section 2.7 can be used with respect to such design problems by means of carrying out detailed parameter studies. Motor characteristics like speed-torque curves, resonance curves of the stator and rotor displacement, the electric admittance, the distribution of the contact forces along the contact zones as well as the power quantities at different motor operation points are the most interesting motor features at steady-state motor conditions.

The model framework presented here can be a guideline for an extension to three-dimensional problems. Especially the contact problem between stator and rotor plays an important role for further improvement of motor efficiency. The kinematics of some of the designed rotational motors show significant radial vibration components which contribute to dissipative effects only. Three dimensional motor models could help to analyze contact mechanism, which are difficult to investigate from an experimental point of view.

A problem in USM design is the occurrence of parasitic vibrations, sometimes noticeable in the audible frequency range. Comments have been made in literature about these effects but up to now there are no investigations on this. Since motor design follows a trial and error procedure, lots of experiments are necessary to give statements on design questions empirically. The mechanisms causing the unsteady operation in USMs and the influence of design parameters on its onset is a quite important but still unresolved problem. A stability analysis seems to be a promising direction for further research in USM modeling and analysis. Also the qualitative motor behavior for different rotor designs should be investigated. Design rules for the choice of rotor design

parameters for a given stator design aiming at "good" motor operation in a wide range of operation conditions are not available.

There is plenty of room for further experimental work in the future. Optimizing available motor designs, motor miniaturization, improving motor reliability and increasing the torque to motor volume ratio are the most important directions with respect to the mechanical parts. How can the present results be used in this sense? Often a trial and error procedure is used to build a motor. Surely, the stator design is done via FEM. But a motor model or a motor design procedure, including the flexible rotor, the piezoceramics and the power electronic components has not been established. Especially in the early stage of motor design the squealing problem often occurs. Our experimental experience with the design of various motors indicates that these trial and error procedures take plenty of time and cannot offer a deep insight into the contact mechanisms. Therefore, the experimental data can be used to verify more sophisticated mathematical motor models which include also rotor design parameters which cannot be accounted for in trial and error experiments. More detailed, future experimental work should investigate the resonance characteristics at different temperature levels and mechanical loads. It is also interesting to reveal the cause of the jump phenomenon in the motor's resonance. Up to now, it is not clear, whether the jump results from a material non-linearity in the piezoceramics, from the geometric non-linearity between the stator-rotor contact or from both. Besides that, the 3-D kinematics of the stator surface points is often neglected. The surface points of the plate-type stator in Fig. 1.5 move along an elliptic trajectory which is spatially declined in radial direction. Thus, there are radial frictional forces acting perpendicular to the driving direction. Depending on the particular motor design, such purely dissipative frictional forces can have an important influence on the motor efficiency. Special stator and rotor geometries and the choice of "good" vibration modes may improve the motor efficiencies. What has not been addressed in this work are the transient motor characteristics like the start and the stop behavior and precise positioning capabilities. Some work has been done on this, but a systematic overview with design rules is, to the best of our knowledge, still missing.

Appendix

A.1 Coefficient of the PDEs

The velocity of the traveling wave in the stator varies with the excitation frequency and is given by

$$v_w = \frac{\Omega}{n_s k} = \frac{[\Omega]}{n_s k} \bar{\Omega}.$$

In the following, the coefficients in the various PDE's are stated:
Coefficients of the stator equation:

$$\begin{aligned}
 S_1 &= \frac{6}{5} & S_8 &= \frac{6}{5} \left(\frac{v_w}{[\lambda][\Omega]} \right)^2 \\
 S_2 &= -\frac{18 h_s^2}{125 [\lambda]^2} & S_9 &= \frac{18}{125} \left(-\frac{h_s^2 v_w^2}{[\lambda]^4 [\Omega]^2} + \frac{E_s h_s^2}{\rho_s [\lambda]^4 [\Omega]^2} \right) \\
 S_3 &= -\frac{d_s}{h_s \rho_s [\Omega]} & S_{10} &= -\frac{[p]}{h_s \varrho_s [\hat{w}_s] [\Omega]^2} \\
 S_4 &= -\frac{12}{5} \frac{v_w}{[\lambda][\Omega]} & S_{11} &= \frac{3[p]}{5 \varrho_s [\hat{w}_s] [\lambda] [\Omega]^2} \\
 S_5 &= -\frac{36}{125} \frac{h_s^2 v_w}{[\lambda]^3 [\Omega]} & S_{12} &= -\frac{h_s \bar{h}_{31} [\hat{D}]}{10 \varrho_s [\hat{w}_s] [\lambda]^2 [\Omega]^2} \\
 S_6 &= \frac{k_s}{h_s \varrho_s [\Omega]^2} & S_{13} &= \frac{[p]}{h_s \varrho_s [\hat{w}_s] [\Omega]^2} \\
 S_7 &= -\frac{d_s v_w}{h_s \rho_s [\lambda] [\Omega]^2}
 \end{aligned}$$

Coefficients of the rotor rigid body equation:

$$\begin{aligned}
R_{r1} &= 1 + \frac{h_c \varrho_{rc}}{h_r \varrho_r} \\
R_{r7} &= -\frac{h_c(h_c + h_r) \varrho_{rc}}{h_r [\lambda] \varrho_r (\nu_{rc}^2 - 1)} \frac{v_w}{[\lambda] [\Omega]} \\
R_{r8} &= \frac{d_r [\hat{w}_s]}{h_r \varrho_r [\lambda] [\Omega]} \overset{\circ}{w}_r \\
R_{r11} &= \frac{1}{2} \frac{h_c \varrho_{rc}}{h_r \varrho_r} \\
R_{r13} &= -\frac{h_c \varrho_{rc}}{h_r \varrho_r} \frac{v_w}{[\lambda] [\Omega]} \\
R_{r15} &= \frac{E_{rc} [\hat{w}_s]}{\varrho_r 2 h_c h_r (1 + \nu_{rc}) [\lambda] [\Omega]^2} \bar{u}_c \\
R_{r16} &= \frac{h_c v_w^2 \varrho_{rc}}{2 h_r \varrho_r [\lambda]^2 [\Omega]^2} \\
R_{r17} &= -\frac{E_{rc} [\hat{w}_s]}{h_c h_r (\nu_{rc}^2 - 1) \varrho_r [\lambda] [\Omega]^2} (\bar{w}_c + \vartheta_{rc} [\Omega] \overset{\circ}{w}_c) \\
R_{r20} &= -\frac{[p]([\lambda] + [\hat{w}_s] \hat{u}'_c)}{h_r \varrho_r [\hat{w}_s] [\lambda] [\Omega]^2} \\
R_{r22} &= \frac{1}{h_r \varrho_r [\hat{w}_s] [\Omega]^2}
\end{aligned}$$

Coefficients of the rotor deformation equation:

$$\begin{aligned}
R_{f3} &= \frac{d_r}{(h_r \varrho_r + h_c \varrho_{rc}) [\Omega]} \\
R_{f4} &= -\frac{2v_w}{[\lambda] [\Omega]} \\
R_{f7} &= \frac{k_r}{(h_r \varrho_r + h_c \varrho_{rc}) [\Omega]^2} \\
R_{f8} &= \frac{d_r v_w}{(h_r \varrho_r + h_c \varrho_{rc}) [\lambda] [\Omega]^2} \\
R_{f9} &= \left(\frac{v_w}{[\lambda] [\Omega]} \right)^2 \\
R_{f11} &= -\frac{E_r h_r^2 (3h_c + h_r)}{12 (\nu_{rc}^2 - 1) (h_r \varrho_r + h_c \varrho_{rc}) [\lambda]^4 [\Omega]^2}
\end{aligned}$$

$$R_{f25} = \frac{[p]}{(h_r \varrho_r + h_c \varrho_{rc})[\hat{w}_s] [\Omega]^2}$$

$$R_{f26} = \frac{(2h_c + h_r)[p]}{2(h_r \varrho_r + h_c \varrho_{rc})[\hat{w}_s] [\lambda] [\Omega]^2}$$

Contact layer equation u:

$$L_{u9} = \frac{\vartheta [\Omega]}{1 - \nu_{rc}^2} \quad L_{u19} = -\frac{2h_c(1 + \nu_{rc})[p]}{E_{rc}[\hat{w}_s]}$$

$$L_{u13} = -\frac{\vartheta_{rc} v_w}{(\nu_{rc}^2 - 1)[\lambda]}$$

Contact layer equation w:

$$L_{w11} = \frac{\vartheta_{rc} [\Omega]}{1 - \nu_{rc}^2} \quad L_{w15} = -\frac{\vartheta_{rc} v_w}{(\nu_{rc}^2 - 1)[\lambda]}$$

$$L_{w14} = 1 \quad L_{w18} = \frac{h_c [p]}{E_{rc}[\hat{w}_s]}$$

Electric displacement Y_3 -direction:

$$P_1 = -\frac{s[\hat{V}]}{[\lambda]^2} \quad P_3 = \frac{sh_s^2 \bar{h}_{31}[\hat{w}_s]}{10[\lambda]^4}$$

$$P_2 = \frac{sh_s \bar{\beta}_{33}[\hat{D}]}{5[\lambda]^2}$$

Contact gap velocity:

$$G_2 = \frac{v_w}{[\lambda][\Omega]} \quad G_4 = G_6 = -\frac{v_w}{[\lambda][\Omega]}$$

Stick-Slip condition for tangential contact:

$$SS_1 = -\frac{h_p + h_s}{2[\lambda]} \quad SS_5 = \frac{2h_c + h_r}{2[\lambda]} \left(\frac{v_w}{[\lambda][\Omega]} \right)$$

$$SS_2 = \frac{(h_p + h_s)v_w}{2[\lambda]^2[\Omega]} \quad SS_7 = \frac{v_w}{[\lambda][\Omega]}$$

$$SS_4 = -\frac{2h_c + h_r}{2[\lambda]}$$

Bibliography

- [1] ANSI/IEEE Std. 176-1987. IEEE standard on piezoelectricity. Technical report, The Institute of Electrical and Electronics Engineers, Inc., New York, 1987.
- [2] Becker, E.; Bürger, W. *Kontinuumsmechanik*. B. G. Teubner, Stuttgart, 1975.
- [3] Beige, H.; Schmidt, G. Electromechanical resonances for investigating linear and nonlinear properties of dielectrics. *Ferroelectrics*, 41:39–49, 1982.
- [4] Beige, Horst. Elastic and dielectric nonlinearities of piezoelectric ceramics. *Ferroelectrics*, 51:113–119, 1983.
- [5] Berg, M. *Ein Wanderwellenmotor mit Zylindrischem Stator: Mathematische Modellierung und Experimentelle Untersuchungen*. PhD thesis, Darmstadt University of Technology, 2001. GCA-Verlag, ISBN 3-89863-091-9.
- [6] Berg, M.; Hagedorn, P.; Sattel, T. Comparison of experimental and simulation data of ultrasonic traveling wave motors. In *Actuator*, pages 253–255. 6th Intern. Conf. on New Actuators, 1998. P43.
- [7] Berlincourt, D. A.; Curran, D. R.; Jaffe, H. Piezoelectric and piezomagnetic materials and their function in transducers. In W. P. Mason, editor, *Physical Acoustics*, chapter 3, page 169. Academic Press, 1964.
- [8] Cao, X.; Wallaschek, J. Estimation of the tangential stresses in the stator/rotor contact of travelling wave ultrasonic motors using visco-elastic foundation models. In *Contact Mechanics II*, pages 53–61, Southampton, Boston, 1995. Computational Mechanics Publications.
- [9] Endo, A.; Sasaki, N. Investigation of frictional material for ultrasonic motor. In *Proc. 7th Symp. On Ultrasonic Electronics*, Kyoto, 1986. Japanese Journal of Applied Physics.
- [10] Furuya, S.-I. *et al.* Load-adaptive frequency tracking control implementation of two-phase resonant inverter for ultrasonic motor. *IEEE Transactions on power electronics*, 7(3):542–550, 1992.

-
- [11] Ferreira, A. Design and control of a mobile micromanipulator driven by ultrasonic motors with multidegrees of freedom. *Advanced Robotics*, 12(2):115–133, 1998.
- [12] Flynn, A.M. *Piezoelectric Ultrasonic Micromotors*. PhD thesis, MIT Artificial Intelligence Laboratory, 1997.
- [13] G.A. Maugin. *Continuum mechanics of electromagnetic solids*. Elsevier Science Publishers B.V., Amsterdam, 1988.
- [14] Ghandi, K. *Nonlinear Modeling and Characterization Techniques for Phase Transition in Electro-Mechanically Coupled Devices*. PhD thesis, MIT, Department of Aeronautics and Astronautics, 1997.
- [15] Glenn, T.S.; Hagood, N.W. Development of a two-sided piezoelectric rotary ultrasonic motor for high torque. In *SPIE Vol. 3041*, pages 326–338, 1998.
- [16] Hagedorn, P. *Nonlinear Oszillations*. Oxford University Press, New York, 2 edition, 1988.
- [17] Hagedorn, P. *Technische Schwingungslehre: Lineare Schwingungen kontinuierlicher mechanischer Systeme*. Springer-Verlag, Berlin, 1989. ISBN 3-540-50869-4.
- [18] Hagedorn, P.; Sattel, T. Simulationsmodell Zur Dynamik Eines Linearen Wanderwellenmotors. DFG-Report HA 1060/27-3, TU Darmstadt, July 2001.
- [19] Hagedorn P.; Sattel T.; Speziari D.; Schmidt J.; Diana G. The importance of rotor flexibility in ultrasonic traveling wave motors. *Smart Mater. Struct.*, 7:352–368, 1998.
- [20] Hagedorn P.; Wallaschek J. Travelling wave ultrasonic motors, part i: working principle and mathematical modelling of the stator. *J. of Sound and Vibration*, 155(1):31–46, 1992.
- [21] Hagood IV N.W.; McFarland A.J. Modeling of a piezoelectric rotary ultrasonic motor. *IEEE Trans. on Ultrasonics, Ferroelectrics, and Frequency Control*, 42(2):210–224, 1995.
- [22] Herzog, B. *Entwicklungsgrundlagen für modulare Ultraschallantriebe*. PhD thesis, Universität Stuttgart, 1993.
- [23] Honda, T.; Kato, K. Fundamental properties of friction and wear on friction drive by traveling wave type ultrasonic. *Japanese Journal of Tribology*, 47(7):1073–1084, 1993.
- [24] Ikeda, T. *Fundamentals of Piezoelectricity*. Oxford University Press, 1990.

- [25] Yuji Izuno. Adaptive control-based high-performance drive system implementation of traveling-wave-type ultrasonic motor. *Electrical Engineering in Japan*, 112(1):1147–1154, 1992.
- [26] Jackson, J.D. *Classical Electrodynamics*. John Wiley and Sons, Inc., 1975.
- [27] Johnson K.L. *Contact Mechanics*. Cambridge University Press, 1985.
- [28] Kamano, T. *et al.* Characteristics and model of ultrasonic motor. In *Japan. J. Appl. Phys.*, pages 189–191. Proc. 8th Symp. on Ultrasonic Electronics, 1988. Supplement 1.
- [29] Kanazawa, H. *et al.* Tribology of ultrasonic motors. *Japanese Journal of Tribology*, 38(3):315–324, 1993.
- [30] Kawai, Y. *et al.* High power travelling-wave type ultrasonic motor. *Japan. J. Appl. Phys.*, 34:2711–2714, 1995.
- [31] Le Letty, R. *et al.* Combined finite element-normal mode expansion methods in elctroelasticity and their application to piezoactive motors. *International journal for numerical methods in engineering*, vol. 40,, pages 3385–3403, 1997.
- [32] Le Moal P.; Minotti P. A 2-d analytical approach of the rotor/stator contact problem including rotor bending effects for high torque piezomotor design. *Eur. J. Mech., A/Solids*, 16(6):1067–1103, 1997.
- [33] Maas, J. *et al.* Model-based control of traveling wave type ultrasonic motors. In Wallaschek, J.; Lückel, J.; Littmann, W., editor, *Proc. Of 3rd Int. Heinz Nixdorf Symposium*. Heinz Nixdorf Institut, University of Paderborn, 1999.
- [34] Maas, Juergen. *Modellierung und Regelung Von Stromrichtergespeisten Ultraschall-Wanderwellenmotoren*. PhD thesis, University of Paderborn, Germany, December 1998. Faculty of Electrical Engineering.
- [35] Maeno T.; Bogy D. Effect of the hydrodynamic bearing on Rotor/Stator contact in a ring-type ultrasonic motor. *IEEE Ultrasonics Symposium Florida*, 1991.
- [36] Maeno T.; Takayuki T.; Miyaki A. Finite-element analysis of the Rotor/Stator contact in a ring-type ultrasonic motor. *IEEE Trans. on Ultrasonics, Ferroelectrics and Frequency Control*, 39(6):668–674, 1992.
- [37] Nguyen, M.N. *Non-Linear Dynamic Behavior of Piezo-Beam-Systems at Weak Electric Fields*. PhD thesis, Darmstadt University of Technology, Darmstadt, Germany, 1999. in german.
- [38] Nye, J.F. *Physical Properties of Crystals*. Clarendon Press, Oxford, 1985.

- [39] Oden J.T.; Martins J.A.C. Models and computational methods for dynamic friction phenomena. *Computer Methods in Appl. Mech. and Eng.*, 52:527–637, 1985.
- [40] Oestreich M. Untersuchung von schwingern mit nichtglatten kennlinien. *Dissertation Univ. Hannover; Fortschrittberichte VDI*, 11(258), 1998.
- [41] Rehbein. *Tribologische Untersuchungen Von Hochfrequent Schwingenden Gleitkontakten Für Den Einsatz in Reibkraftschlüssigen Antrieben*. PhD thesis, University of Paderborn, Germany, 1998. Title in English: Tribological investigations of surfaces at high vibration sliding contact for friction induced drives.
- [42] Rehbein, P.; Wallaschek, J. Friction and wear behaviour of polymer/steel and alumina/alumina under high-frequency fretting conditions. *Wear*, 216:97–105, 1998.
- [43] T. Sashida. Trial construction and operation of an ultrasonic vibration driven motor (in japanese). *Oyo Buturi*, 51:713–720, 1982.
- [44] Sashida T.; Kenjo T. *An Introduction to Ultrasonic Motors*. Clarendon Press, Oxford, 1993.
- [45] Sattel, T.; Hagedorn, P. A note on non-intermittend contact problems of a special class of ultrasonic motors. In *Proc. DETC'99*, pages 12–15, Las Vegas, Sept. 1999. ASME Design Engineering Technical Conference.
- [46] Sattel, T.; Hagedorn, P. On the contact between rotor and stator in an ultrasonic traveling wave motor. *ISROMAC*, 2000.
- [47] Sattel, T.; Hagedorn, P.; Berg, M. Simulation model used as design tool for traveling wave ultrasonic motors. In *Actuator 98*, pages 249–252, Bremen, Germany, 1998. 6th Intern. Conf. on New Actuators. P42.
- [48] Sattel, T.; Hagedorn, P.; Schmidt, J. The contact problem in ultrasonic traveling wave motors, part I: Modeling. *Journal of Applied Mechanics*, 2001. submitted.
- [49] Sattel, T.; Hagedorn, P.; Schmidt, J. The contact problem in ultrasonic traveling wave motors, part II: Numerical analysis. *Journal of Applied Mechanics*, 2001. submitted.
- [50] Schenker, P.S. *et al.* A composite manipulator utilizing rotary piezoelectric motors: new robotic technologies for mars in-situ planetary science. In *SPIE Vol. 3041*, 1997.
- [51] Schmidt, J. *Ein mechanisches Modell des Stator-Rotor-Kontaktes beim Ultraschall-Wanderwellen-Motor*. PhD thesis, Darmstadt University of Technology, Darmstadt, Germany, Dec. 1999.

- [52] Schmidt J.; Hagedorn P.; Bingqi M. A note on the contact problem in an ultrasonic travelling wave motor. *Int. J. Non-Linear Mechanics*, 31(6):915–924, 1996.
- [53] Schreiner, M. *et al.* Robotic wrist actuator with high torque piezoelectric traveling wave motor. In *Actuator 2000*, pages 375–378, Bremen, Germany, 2000. 7th Int. Conf. on New Actuators.
- [54] Schulte, T. *et al.* Control for ultrasonic motors with LLCC-resonant converter. In *Actuator 2000*, pages 367–370. Messe Bremen GmbH, June 2000.
- [55] Seemann, W.; Sattel, T. The influence of bonding on the efficiency of piezoceramic patches as actuators in smart structures. In *SPIE's 6th. Annual Int. Symp. On Smart Structures and Materials*, Newport Beach, 1999. vo. 3668.
- [56] Uchino, K. *Piezoelectric Actuators and Ultrasonic Motors*. Kluwer Academic Publishers, 1997.
- [57] Ueha S.; Tomikawa Y.; Kurosawa M.; Nakamura N. *Ultrasonic Motors Theory and Applications*. Clarendon Press, Oxford, 1993.
- [58] Wallaschek J. Contact mechanics of piezoelectric ultrasonic motors. *Smart Mat. Struct.*, 7:369–381, 1998.
- [59] Wallaschek, Joerg. Piezoelectric ultrasonic motors. *Journal of Intelligent Material Systems and Structures*, 6:?, January 1995.
- [60] Whatmore, R.W. Report on piezoelectric motors for nanoengineering and metrology. Technical Report GR/K89818/01, Cranfield University, Nanotechnology Group, Advanced Materials Department, 2001.
- [61] Wolf, K.; Gottlieb, O. Nonlinear dynamics of a cantilever beam actuated by piezoelectric layers in symmetric and asymmetric configuration. *Journal of Applied Physics*, 2002. accepted.
- [62] Wriggers P. Finite element algorithms for contact problems. *Archives of Computational Methods in Engineering*, 2(4):1–49, 1995.
- [63] Zharii O.; Ulitko A.F. Smooth contact between the running rayleigh wave and a rigid strip. *Trans. ASME*, 62:362–367, 1995.

Curriculum Vitae

Thomas Sattel

Gartenstraße 6 – 67105 Schifferstadt – Germany

- April 11, 1965 born in Speyer/Rh, Germany
- 07/1971 - 06/1975 Primary school, Schifferstadt
- 07/1975 - 06/1981 Secondary school, Schifferstadt
- 08/1981 - 06/1983 Training to Chemical Technician, BASF AG
- 07/1983 - 06/1985 Training to Chemical Laboratory Assistant, BASF AG
- 07/1985 - 06/1988 Chemical Assistant, BASF AG
- 07/1985 - 06/1986 Engineering School, Ludwigshafen
- 07/1986 - 06/1988 Upper School, Mannheim, receiving advanced technical college certificate (Fachhochschulreife)
- 07/1988 - 09/1989 Military Service AmphPiBtl 330 in Speyer/Rh.
- 10/1989 - 02/1991 Chemical Engineering, Polytechnic Institute Mannheim
Preliminary Diploma
- 03/1991 - 07/1991 Chemical Engineering, Polytechnic Institute Frankfurt
Preliminary Diploma
- 10/1991 - 09/1992 Mechanical Engineering, Darmstadt University of Technology
Preliminary Diploma
- 10/1992 - 10/1995 Applied Mechanics, Darmstadt University of Technology
Diploma
- 10/1994 - 07/1996 Mathematics, Darmstadt University of Technology
Preliminary Diploma
- 12/1995 - 04/1997 Research Fellowship of the State Hessen, Department of Applied
Mechanics, Darmstadt University of Technology
Topic: Biomechanics of the Inner Ear
- 05/1997 - 06/2001 Research Assistant at the Department of Applied Mechanics,
Darmstadt University of Technology
Topic: Dynamics of Ultrasonic Motors
- since 07/2001 Research Assistant in the *Mechatronics and Dynamics* research
group at the Faculty of Mechanical Engineering, University of
Paderborn
Topics: Nonlinear Dynamics, Design of Smart Actuators, Smart
Machining and Manufacturing Processes

